INVESTIGATION OF STRAIN AGING IN THE ORDERED INTERMETALLIC
COMPOUND β-NiAl

By

MARK LOVELL WEAVER

A DISSERTATION PRESENTED TO THE GRADUATE SCHOOL
OF THE UNIVERSITY OF FLORIDA IN PARTIAL FULFILLMENT
OF THE REQUIREMENTS FOR THE DEGREE OF
DOCTOR OF PHILOSOPHY

UNIVERSITY OF FLORIDA

1995

To Mom and Dad.

ACKNOWLEDGEMENTS

TABLE OF CONTENTS

Abstract of Thesis Presented to the Graduate School
of the University of Florida in Partial Fulfillment of the
Requirements for the Degree of Doctor of Philosophy

INVESTIGATION OF STRAIN AGING IN THE ORDERED INTERMETALLIC
COMPOUND β-NiAl

By

MARK LOVELL WEAVER

May, 1995

Chairman: Dr. Michael J. Kaufman
Major Department: Materials Science and Engineering

The phenomenon of strain aging has been investigated in polycrystalline and single crystal NiAl alloys at temperatures between 300 and 1200 K. Static strain aging studies revealed that after annealing at 1100 K for 7200 s (i.e., 2 h) followed by furnace cooling, high purity, nitrogen-doped and titanium-doped polycrystalline alloys exhibited continuous yielding, while conventional-purity and carbon-doped alloys exhibited distinct yield points and Lüders strains. Prestraining by hydrostatic pressurization removed the yield points, but they could be reintroduced by further annealing treatments. Yield points could be re-introduced more rapidly if the specimens were prestrained uniaxially rather than hydrostatically, owing to the arrangement of dislocations into cell structures during uniaxial deformation. The time dependence of the strain aging events followed a $t^{2/3}$ relationship suggesting that the yield points observed in polycrystalline NiAl were the result of the pinning of mobile dislocations by interstitials, specifically carbon.

Between 700 and 800 K, yield stress plateaus, yield stress transients upon a tenfold increase in strain rate, work hardening peaks, and dips in the strain rate sensitivity (SRS) have been observed in conventional-purity and carbon-doped polycrystals. In single crystals, similar behavior was observed; in conventional-purity single crystals, however, the strain rate sensitivity became negative resulting in serrated yielding, whereas, the strain rate sensitivity stayed positive in high purity and in molybdenum-doped NiAl. These observations are indicative of dynamic strain aging (DSA) and are discussed in terms of conventional strain aging theories. The impact of these phenomena on the composition-structure-property relations are discerned. Finally, a good correlation has been demonstrated between the properties of NiAl alloys and a recently developed model for strain aging in metals and alloys developed by Reed-Hill *et al.* [1-3].

CHAPTER 1
INTRODUCTION

Background

The development of more efficient gas turbine engines will depend upon the advancement of new high temperature materials with improved mechanical properties. These materials must have higher specific strengths and must maintain these strengths to higher temperatures than the nickel-base superalloys currently in use. Ordered intermetallic compounds are prime candidates to replace the superalloys. These materials form long range ordered crystal structures which are associated with the formation of strong A-B type bonds that typically result in high elastic moduli, high melting points, and high strengths. Furthermore, aluminide-based intermetallics exhibit good oxidation resistance and greater microstructural stability due to lower self-diffusion rates, another consequence of the strong bonding.

Of the many intermetallic systems, alloys based on β-NiAl are particularly attractive for development. NiAl has a simple B2 (CsCl) crystal structure which is similar to the body-centered-cubic (BCC) structure. It exists over a wide range of stoichiometries (greater than 20 at.% at 1673 K) which allows for significant alloying to improve its mechanical properties. In addition, it exhibits an appreciably higher melting point (~1950 K versus 1573 K), lower density (5.9 g/cm^3 versus 9.0 g/cm^3), and a thermal conductivity up to eight times greater than that of Ni-base superalloys. The potential benefits of using NiAl in gas turbine applications would include: (1) decreased cooling requirements; (2) decreased weight; and (3) higher operating temperatures resulting in increased operating efficiencies and higher thrust-to-weight ratios. In addition, NiAl has been used for years as an oxidation resistant coating on turbine blades [4]. Like most intermetallics, however,

1

NiAl is not currently a suitable replacement for superalloys due to its meager high temperature strength (above $0.45T_{mp}$) and its poor fracture resistance and ductility below its brittle-to-ductile transition temperature (BDTT).

NiAl undergoes a dramatic brittle-to-ductile transition at temperatures between 400 and 1000K with the actual transition temperature varying strongly with alloy composition, processing history (*i.e.*, thermal or mechanical), strain rate, bulk form (*i.e.*, polycrystal or single crystal), and orientation in single crystals. In polycrystals for example, Noebe *et al.* [5] have reported a 200K increase in the BDTT coinciding with a three order of magnitude increase in strain rate. Lahrman and coworkers [6] have reported similar increases in the BDTT of "hard" [001] oriented single crystals. In "soft" non-[001] orientations however, the BDTT was found to be less strain rate sensitive.

The BDTT in polycrystals and hard single crystals have been attributed to the onset of localized dislocation climb processes driven by short circuit diffusion [5]. In soft single crystal orientations however, the mechanism responsible for the BDTT is not as obvious. In crystals with soft orientations the BDTT occurs as low as $0.25T_{mp}$ and, as mentioned above, is much less sensitive to strain rate [6]. Possible explanations for the BDTT in soft orientations include enhancement of cross-slip leading to slip homogenization the operation of thermally activated deformation processes as in the other forms of NiAl or the unlocking of dislocations from point defects or impurities [7]. These explanations are only speculative and remain to be proven. Considering the peculiarly low BDTT in soft single crystals, an understanding of the mechanisms responsible for the BDTT in soft single crystals could reveal methods to lower the BDTT and lead to the development of more ductile alloys.

At ambient temperatures, research has shown that NiAl deforms predominantly by dislocation glide on the <100>{011} and <100>{001} slip systems of which only three are independent [8]. According to the Von Mises criterion, at least five independent slip

systems are required for macroscopic plastic deformation in a polycrystalline body; this may account for the lack of ductility in polycrystalline NiAl [9-13].

In single crystals, limited tensile ductilities (≤2%) are also observed. However, recent efforts have resulted in room temperature tensile elongations of up to 6% in conventional-purity binary NiAl annealed above the BDTT and rapidly cooled to room temperature [14,15] and in ternary NiAl crystals containing microalloying additions of Fe, Mo and Ga [16]. The mechanism behind this increased ductility is currently unknown but is suspected to be related to a gettering phenomenon since it is realized that some substitutional elements and interstitial impurities can cause significant embrittlement in BCC metals [17] and B2 ordered compounds such as NiAl [18]. Recent observations are consistent with this viewpoint. For example, room temperature tensile elongations of up to 5% have been observed in low interstitial binary NiAl single crystals [19] and the ductility and fracture strength in biaxial bending of high purity NiAl was found to be significantly greater than for commercial purity crystals [20]. Still, the effects of particular substitutional and interstitial elements on the mechanical behavior of NiAl is relatively unknown and the mechanisms by which various elements may enhance or hinder tensile ductility still remain a matter of conjecture.

Hack [14,15] attributes the profound effects of heat treatment on mechanical properties to the creation mobile dislocations and suggests that the low ductilities reported in other studies are due to strain age embrittlement in which interstitial atoms segregate to mobile dislocations at moderate temperatures. The interstitials then pin the dislocations resulting in a lower density of mobile dislocations. Evidence in support of a strain aging effect are provided by the observation of serrated yielding [15,21-26], plateaus in the temperature dependence of yield strength, and low strain rate sensitivities near the BDTT and in the temperature regimes where serrated flow is observed [27-29]. In addition, strain aging has also been reported in Ni-rich NiAl [22], stoichiometric polycrystalline NiAl [30], mechanically alloyed NiAl [30], NiAl deformed under hydrostatic pressure [23,31], and in

other B2 intermetallics [32-34]. These phenomena are similar to those commonly observed in mild steels and BCC refractory metals [21,35-43]. However, the species responsible for this behavior in NiAl or other ordered alloys (*i.e.*, interstitials, substitutional impurities, precipitates, vacancies, etc.) are currently unknown. A comprehensive understanding of these factors is required to fully discern the flow behavior of NiAl.

Thus, the objectives of this investigation are to examine, in a systematic fashion, the phenomenon of strain aging and it's influence on the mechanical behavior of near stoichiometric NiAl.

Approach

In order to examine the effects of strain aging, several nominally stoichiometric polycrystalline and single crystal alloys containing varying interstitial contents were subjected to static strain aging (SSA) experiments and strain rate change experiments to reveal the temperature dependence of the strain rate sensitivity (SRS). The resulting data were then used to determine activation energies for deformation processes and to determine the species responsible for strain aging in NiAl. The resulting data was also analyzed using a recently developed theory by Reed-Hill *et al.* [1,3].

CHAPTER 2
LITERATURE REVIEW

Introduction

In the sections that follow, the physical metallurgy of NiAl alloys and the general aspects of static and dynamic strain aging phenomena are described. As the physical metallurgy of NiAl alloys has been described in detail in recent review articles [7,18,44], only a summary of the properties pertinent to the deformation of NiAl is provided.

Physical Metallurgy of NiAl and NiAl Alloys

Physical/Thermodynamic Properties

The ordered intermetallic NiAl is a Hume-Rothery β-phase electron compound with a valence electron-to-atom ratio of 3/2. As a result, NiAl crystallizes with a primitive cubic CsCl (*cP2*, B2) crystal structure which may be described as two interpenetrating primitive cubic unit cells where Al atoms occupy one sublattice and Ni atoms the second. This is illustrated in Figure 1. NiAl exists as a single phase ordered intermetallic over the composition range of 45 to 60 at.% Ni at 1000 K and has the highest melting temperature of any compound in the Ni-Al binary system although the melting point of the stoichiometric compound (*i.e.*, Ni-50 at.%Al) is in dispute. For example, the phase diagram of Singleton *et al.* [45] (Figure 2) indicates that stoichiometric NiAl melts congruently at 1911 K. More recent evaluations, however, place the melting temperature of stoichiometric NiAl near 1955 K [46]. It has been suggested that the lower value might be attributed to the steep drop-off in melting temperature with deviation from stoichiometry or to unintentional contamination by ternary elements [7]. In addition, NiAl exhibits a high

5

degree of thermodynamic stability, as indicated by it's large negative heat of formation (approximately -72 kJ/mol) [47].

Lattice Parameter, Density and Defect Structures

Lattice parameter and density have been investigated thoroughly and have been used to deduce the types of defect structures occurring in the NiAl lattice [48-50]. Nickel, being smaller and heavier than Al, should cause a reduction in the lattice parameter and an increase in the density when it is substituted for Al. This is consistent with observations for alloys containing more than 50 at.% Ni (Figure 3). In Al-rich alloys, however, both the lattice parameter and the density decrease with increasing Al content and the decrease is more rapid than would be expected by replacement of Ni atoms by Al. This behavior is rationalized by the creation of vacancies on the Ni-sublattice rather than by substitutional defects as observed in Ni-rich alloys. In addition to influencing the lattice parameter and density, the defect structures induced due to deviations from stoichiometry also dramatically influence the mechanical behavior. For example, Vedula and Khadkikar [50] have shown that the yield strength shows a minimum at the stoichiometric composition. Furthermore, Hahn and Vedula [9] have shown that deviations of less than 1% from stoichiometry result in brittle behavior at room temperature as well as an increase in the BDTT. The influence of stoichiometry on the yield stress of NiAl is described in more detail in the next section. In all cases, the yield stress decreases with increasing temperature. The behavior of near-stoichiometric polycrystals resembles that of soft-oriented single crystals while the strengths of off-stoichiometric alloys approach that of hard-oriented single crystals. Interestingly, the increases in 0.2% offset yield stress, $\sigma_{0.2}$, with deviation from stoichiometry are not equivalent on both sides of the stoichiometric composition [50]. For Ni-rich alloys, for example, the hardening rate was shown to be 120 MPa/at.% while in Al-rich alloys the hardening rate was approximately 350 MPa/at.% [18]. The greater hardening rate on the Al-rich side of stoichiometry suggests that Ni

vacancies provide more resistance to dislocation motion than antisite atoms. These strength increases, however, become irrelevant above 1000 K where stoichiometric NiAl becomes stronger than nonstoichiometric compositions [51,52] primarily due to diffusional deformation.

In addition to the constitutional vacancies described above, another type of vacancy defect can exist in NiAl. These are thermal vacancies which can be introduced by rapid quenching from elevated temperatures. Bowman *et al.* [53] have shown that a 50-fold increase in cooling rate from temperatures above 1000 K can increase the compressive yield stress by almost 30 percent for near-stoichiometric binary NiAl. However, when the material is microalloyed with Zr, the dependence of strength on cooling rate disappears. Similarly, Nagpal and Baker [54] have shown that deviations from stoichiometry reduce the sensitivity of the binary alloy to cooling rate. Cooling rate has been shown to similarly influence the yield stress of NiAl single crystals [55].

Elastic Properties

The elastic behavior of NiAl has also been studied in some detail and has been shown to vary with processing technique and temperature. For example, Rusovic and Warlimont [56] have summarized the single-crystal elastic constants for NiAl as a function of temperature, cooling rate and stoichiometry showing the overall elastic properties of NiAl to be anisotropic with an anisotropy factor, E_{100}/E_{110}, close to 3.3 [57] and showing a mild temperature dependence but a strong stoichiometry dependence. This is illustrated in Figure 4a along with the recent results of Walston and Darolia [46] which shows the single crystal dynamic Young's moduli, E, for near-stoichiometric NiAl for a variety of orientations. It has also been shown that minor alloying additions have relatively little influence on the dynamic Young's modulus of <001> single crystals [46]. In polycrystals, Young's modulus is relatively insensitive to stoichiometry, but is very dependent on processing technique [58-60] (Figure 4b); extruded materials exhibit higher moduli and

different temperature dependencies than conventional cast and homogenized ingots or hot-pressed prealloyed powders. This can be rationalized, in comparison to single crystals, in terms of the crystallographic texture that develops during processing. Extruded NiAl-based materials commonly exhibit a preferred <111> orientation [61,62], whereas cast or hot-pressed materials are not expected to exhibit a strong preferred orientation. As a result, cast or hot-pressed materials have lower moduli in comparison to the higher moduli observed in <111>-textured material.

The remaining physical properties have not been characterized to the same degree as the lattice parameter, density or the elastic modulus. However, it has been reported that alloying NiAl with Ti and Re significantly reduces the thermal conductivity, whereas additions of 2.5 at.% Hf had minor effects, decreasing the thermal conductivity of NiAl single-crystals by only 15% [46]. These and other properties have been reviewed recently [7,18,44].

<center>Flow and Fracture Behavior</center>

Slip Systems

The operative slip systems in NiAl single crystals and polycrystals are described in detail in recent review articles by Miracle [44] and Noebe *et al.* [7,18]. NiAl single crystals exhibit two different types of slip behavior depending upon crystal orientation. In NiAl, the shortest translation vector that will maintain the B2 structure is that along the cube edge (*i.e.*, in the <100> crystallographic direction). For single crystals in "soft" orientations and in polycrystals, the dominant slip vector is <001>. However, if the loading direction is along [001], the "hard" orientation, then the operative slip vector at low and intermediate temperatures is <111>, and at elevated temperatures is a combination of <110> and <100>. Soft orientations include all non-<001> loading directions where <100> slip dominates. Orientations near [001] are considered hard because <001> Burgers vectors have a zero or

near-zero resolved shear stress resulting in the operation of alternative slip systems at very large yield stresses.

Early slip system determinations between 300 and 1273 K were completed by Ball and Smallman [51,63] who identified a <001>{110} slip system in all soft oriented single crystals. In addition, they also observed cross slip or pencil glide on orthogonal {110} planes. Shortly afterward, Wasilewski *et al.* [64] reported duplex cube slip, <001>{100}, in [110] single crystals. This observation was later confirmed by Field *et al.* [65]. Cube slip was also reported by Loretto and Wasilewski [66] in [112] crystals deformed between 77 and 1053 K. Only <001> slip is observed in soft oriented single crystals due to the nondissociated, compact structure of the <001> dislocation core [67] making <001> dislocations much more mobile than those with other slip vectors. In addition, it has been observed that NiAl in soft orientations deforms by <001> slip on either {100} or {110} slip planes in accordance with Schmid's law whereas for hard orientations, Schmid's law fails [68]. In hard oriented single crystals, <100> slip does not occur because the resolved shear stress for <100> slip approaches zero. As a result, deformation occurs by non-<001> dislocations giving rise to elevated yield stresses at low temperatures [64] and enhanced creep strengths at elevated temperatures [69].

Deformation in polycrystals occurs in accordance with that in soft-oriented single crystals. Investigators have reported the operation of <001>{110} and <001>{100} slip systems [53,70,71]. Isolated dislocation segments with non-<001> Burgers vectors have been identified in as-extruded NiAl [72,73]; their presence is attributed to interactions between <001> dislocations due to the extensive deformation that occurs during the extrusion process [74]. The operation of <100> slip vectors on planes other than {001} and {011} has been reported [75,76] under conditions of constrained flow, but are not a common aspect of the deformation of NiAl.

Yield Strength

Similar to BCC transition metals, the yield and flow behavior of NiAl is extremely sensitive to temperature and composition. At low temperatures, the yield stress exhibits a strong temperature dependence. This temperature dependence is attributed to a high Peierls stress. At intermediate temperatures, a yield stress plateau is observed where the yield stress is mildly temperature dependent. Finally at high temperatures, the yield stress again drops with temperature. Some results for single crystal and polycrystalline NiAl are shown in Figure 5. As shown in Figure 5a, the yield stress of single crystals exhibits a strong dependence on orientation. The yield stress versus temperature curves for soft oriented single crystals is similar to those observed for low yield strength polycrystalline NiAl.

At low temperatures, hard oriented single crystals, on the other hand, exhibit yield stresses several times larger than those for other orientations and exhibit a lower dependence on temperature. When the temperature is increased above approximately 600 K, however, the yield stresses of these crystals become extremely temperature dependent exhibiting a sharp decrease in yield stress over a narrow range of temperatures. In this regime, the slip vector has been shown to change from <111> to <001> and <011> [77]. Finally, at temperatures exceeding 1000 K, bulk diffusional processes dominate resulting in yield strengths similar to those observed in soft-oriented single crystals and in polycrystalline NiAl.

Ductility and Fracture

Tensile behavior

Single crystals of nominally stoichiometric NiAl exhibit different behaviors depending on crystallographic orientation. Hard-oriented single crystals exhibit essentially zero plastic strain to failure in tension at room temperature but undergo a sharp BDTT at temperatures near 600 K [78,79]. Similarly, soft-oriented single crystals also exhibit a

sharp BDTT ranging from 475 to 525 K [6,80]. In hard-oriented crystals, the BDTT corresponds to the temperature where the steep decrease in yield stress begins with increasing temperature. This decrease has been attributed to a change from <111> slip to climb of <100> and <110> dislocations. Initially, it was reported that soft-oriented single crystals also exhibited extremely low plastic strains to failure (on the order of one percent) at room temperature [68,80]. Slightly above the BDTT, anomalously large tensile elongations (greater than 100 percent) have been reported for soft-oriented single crystals while at even higher temperatures the ductility decreased to approximately 45 percent [6,78,80,81]. Takasugi *et al.* [80] attributed this increase to a balance between work hardening caused by glide and relaxation processes due to climb resulting in a large resistance to necking.

More recently, however, tensile elongations approaching seven percent have been measured in soft-oriented binary single crystals of low interstitial high purity NiAl [19], conventional purity NiAl [14,15,28] and in nearly stoichiometric crystals doped with approximately 1000 appm of Fe, Mo or Ga [16,26]. In the conventional purity material, the dramatic increase in ductility occurred after rapid cooling from elevated temperatures (1573 K) whereas the increased ductility in the low interstitial, high purity material was not dependent on heat treatment and cooling rate. The influence of the ternary dopants is illustrated in Figure 6. Interestingly, the ductility passes through a maximum at small alloying additions and the benefits of doping vanish as the dopant level exceeds 0.5 at.%. It has been suggested that the ductilizing effect is due to the gettering of interstitials, although, the real reasons for this behavior remain unknown. Interestingly, similar alloying schemes in polycrystalline alloys have been unsuccessful [82,83]. This is not really surprising since deformation occurs by <001> slip with only three independent slip systems available for deformation [63], rather than the five required for extensive uniform deformation of a polycrystal, leaving little room for significant room temperature ductility, independent of the other factors.

Fracture toughness

Room temperature fracture toughness of notched NiAl bend samples has been reported to be in the range 7 to 12 MPa$\sqrt{m}$ when the notch is cut normal to the <100> direction and in the range 4 to 6 MPa$\sqrt{m}$ when the notch is cut normal to the <110> direction [84,85]. In notched polycrystalline bend samples of nominally stoichiometric single phase NiAl, fracture toughness values have been observed to be independent of grain size, stoichiometry for Ni-rich alloys, and processing technique [86-89] with measured values in the range 4 to 7 MPa$\sqrt{m}$.

As mentioned previously however, Hack and co-workers [14,15,28] recently observed that the fracture toughness of commercial purity single crystals is extremely sensitive to heat treatment and cooling rate. In double cantilever beam specimens with the notch plane perpendicular to the <110> direction, single crystals rapidly cooled to room temperature from 1573 K exhibited fracture toughness values of nearly 16 MPa$\sqrt{m}$. When rapidly cooled specimens were subsequently re-annealed at 473 K and slowly cooled to room temperature, however, the fracture toughness dropped to 3 MPa$\sqrt{m}$. Comparable heat treatments had no influence on low-interstitial, high purity single crystals tested in four-point bending with the crack plane normal to <100>. There, fracture toughness values in the range 10 to 12 MPa$\sqrt{m}$ were observed independent of heat treatment [19]. More experiments using a miniaturized disk bend method [20,90] indicate that low-interstitial NiAl has an intrinsically larger room temperature ductility and fracture toughness than commercial purity material.

Influence of Microalloying Additions and Impurities

Finally, substitutional and interstitial elements appear to significantly influence the yield and flow behavior of NiAl. For polycrystals, abundant solid-solution alloying data exist. Some of the ternary and quaternary additions have included Be, B, C, Cr, Cu, Fe, Ga, La, Mo, N, Nb, Mo+Ti, V, Nb and Y to name a few (reviewed in references

[6,18,44,91,92]). In all cases, the flow stress was enhanced by the presence of solute and the hardening rate was generally shown to be dependent on solute size. This is illustrated in Figure 7.

In single crystals, a study [16] of the influence of Fe, Ga and Mo on the yield strength of <110> oriented single crystals showed Mo to be a potent solid solution strengthener with very limited solubility, while Ga exhibited a mild strengthening effect and Fe, at levels of less than 1 at.%, reduced the yield stress. In addition, recent studies indicated that the critical resolved shear stress in low-interstitial high purity single crystals is significantly lower than that for commercial purity material [55].

As discussed above, microalloying additions of Fe, Ga and Mo in the 0.1 to 0.2 at.% range consistently increase the room--temperature tensile ductility of soft-oriented single crystal NiAl. The mechanism(s) for this increase in ductility have not been determined, although it is speculated that it is the result of gettering of interstitials [16].

Strain Aging

Static Strain Aging (SSA)

The term strain aging characterizes a time-dependent strengthening or hardening process resulting from elastic interactions of solute atoms with strain fields of dislocations in plastically deformed metals and alloys [93]. Strain aging is most common in alloys containing interstitial or substitutional solute atoms capable of segregating to and pinning dislocations. The aging reactions can occur in either static or dynamic modes depending upon whether they occur prior to or during plastic deformation. Static strain aging (SSA) typically occurs in metals and alloys following prestraining, unloading (either partially or fully), aging for a prescribed time and then reloading at the same strain rate as the prestrain. A schematic illustration of SSA is provided in Figure 8. SSA is typically manifested by an

increase in yield stress or flow stress following aging and the return of a sharp yield point in the deformed alloy [94].

Mechanisms of SSA

In BCC metals, SSA can typically be separated into four processes: the Snoek effect, Cottrell locking, Suzuki locking and precipitate formation. Each mechanism is described below.

The Snoek effect. The Snoek effect is a strain-induced ordering of interstitial solute atoms around dislocations [95-97]. In the BCC lattice, interstitial atoms typically occupy octahedral sites at the center of cube edges and cube faces (Figure 9). However, the interstitial atoms are larger than the space available for them in an octahedral site. For example, an atom at position a (Figure 9a) will cause the substitutional atoms A and B to be displaced in the z direction. If four of the octahedral positions lying parallel to the z axis were to become occupied by interstitial atoms as illustrated in Figure 9b, then the unit cell would become elongated in the z direction and would assume a tetragonal shape. In the absence of an applied stress, a statistically equal number of interstitials will occupy sites parallel to each of the x, y and z axes. Thus, the unit cell remains cubic. The application of an external stress in the z direction, for example, causes the interstitial sites parallel to the z axis to enlarge while the openings perpendicular to the z axis decrease in size making it energetically more favorable for atoms in position a of Figure 9c to jump to position b. Schoeck and Seeger [97] have critically evaluated this mechanism and have concluded that, since no long range diffusion is required, this process occurs very rapidly and is normally completed within the time interval of one atomic jump of the species responsible for pinning. In addition, Nakada and Keh [98] have indicated that the apparent intercept of yield point return data plotted as $\Delta\sigma_u$ versus $t^{2/3}$ is positive when Snoek ordering occurs prior to Cottrell atmosphere formation. Rosinger [42] has found that the activation energy for this process in ferritic steels is approximately 60 kJ mol^{-1}.

Cottrell locking. Cottrell locking (also known as Cottrell atmosphere formation), which has been treated in detail by Cottrell and Bilby [43], involves the time- and temperature-dependent growth of solute atmospheres near dislocations. During atmosphere formation, elastic interactions between solute atoms and the strain fields of dislocations create a driving force for the diffusion of interstitial solutes toward the strain field. This mechanism results in a lowering of the total energy of the system and effectively locks the dislocations in the sites that they occupy during the process. The end result is an increase in the stress required to move a dislocation. Important characteristics of Cottrell locking are an aging time dependence for yield point return which follows a 2/3 power law and an activation energy for yield point return which is equivalent to the migration energy for the solute causing Cottrell locking. Though a 2/3 aging time dependence has been reported for several metals and alloys (for example, see reference [94]), the 2/3 power law often fails [99]. In ferritic steel, the activation energy for atmosphere formation is approximately 90 kJ mol^{-1} [42], which is equivalent to the activation energy for volume diffusion of interstitial solutes.

Suzuki locking. Suzuki locking has its origin in the chemical interaction between solute atoms and stacking faults [100]. This mechanism has been commonly observed in superalloys and is only expected to be significant in metals exhibiting low stacking fault energies in which stacking fault widths are large, *i.e.*, FCC and HCP metals and alloys. As NiAl exhibits a high stacking fault energy and no evidence of stacking faults before or after deformation, this mechanism inapplicable.

Precipitate formation. Precipitate formation only occurs when the metal is supersaturated with solute atoms. Strain aging occurs when interstitial or substitutional atoms, or compounds composed of those solutes (*e.g.*, carbides, nitrides, oxides, borides, etc.) precipitate on dislocations during aging, effectively pinning them.

Yield point return

Yield points that repeatedly return after aging are associated with the formation of solute atom atmospheres around dislocations. Mobile dislocations that were once active during deformation prior to unloading are pinned as a result of aging. For this pinning to occur, solute atoms must diffuse through the lattice to accumulate around dislocations. As a result, the reappearance of the yield point is a function of time which depends on the temperature since diffusion is a temperature-dependent function. Rosinger *et al.* [101] have shown that two plateaus are typically observed when the increment of yield stress, $\Delta\sigma$, observed after SSA is plotted versus the aging time t_a (Figure 10). The first plateau, which occurs at shorter t_a's, is associated with Snoek strain aging while the second plateau, which occurs at longer t_a's, is associated with Cottrell strain aging. The time corresponding to the first inflection point between the two stages has been shown to correspond to the time required for a single interstitial solute atom to undergo a single jump [101]. Easy identification of each regime can be made by plotting $\Delta\sigma$ versus $t_a^{2/3}$. The decrease in $\Delta\sigma$ observed after the second plateau is associated with saturation which occurs when the interstitial atoms have migrated to dislocations in sufficient numbers to either relieve the strain energy induced by dislocations in the lattice or to set up concentration gradients restricting the further migration of solute [43]. Saturation also occurs when the migration of interstitial atoms to dislocations results in the depletion of interstitial atoms in the surrounding lattice. At even greater times, the concentration of solute atoms about the dislocations may exceed the solid solubility limit of the solute in the solvent metal at that temperature. As a result, precipitates may form resulting in a decrease in $\Delta\sigma$, or softening [102].

Dynamic Strain Aging (DSA)

Dynamic strain aging is a phenomenon exhibited by many metals and alloys [103]. It is the result of interactions between diffusing solute atoms and mobile dislocations during

plastic deformation. This process tends to occur over a wide temperature range which is dependent upon strain rate $\dot{\varepsilon}$.

Dynamic strain aging is manifested by: the appearance of serrations, load drops, jerkiness or other discontinuities in the stress-strain curves obtained in constant-extension-rate tensile or compression tests; peaks or plateaus in the variation of flow stress, work-hardening rate, $\theta=\Delta\sigma/\Delta\varepsilon$, and Hall-Petch slope, k_ε, with temperature, T, and minima in the variation of ductility and strain-rate sensitivity, $s=\Delta\sigma/\Delta\ln\dot{\varepsilon}$ or $n=\Delta\ln\sigma/\Delta\ln\dot{\varepsilon}$, with T; and low or negative values of s and n in the temperature region of DSA [104]. Some of these manifestations are illustrated in Figure 11. These phenomena are associated with the dynamic formation and migration of solute atmospheres around dislocations during deformation.

<u>Serrated flow curves</u>

Serrations, load drops or jerkiness in the stress-strain curves obtained in constant-extension-rate tensile or compression tests are perhaps the best known manifestation of DSA. In creep tests under constant load or stress, or in constant-loading rate tests, DSA is manifested as staircase creep whereby sudden bursts of plastic strain periodically occur resulting in staircase-like creep curves [104].

Johnston [105] and Hahn [21] have proposed that load drops or yield point phenomena are related to an initially low mobile dislocation density and a low dislocation-velocity stress sensitivity. In reference to the latter, Gilman and Johnston [106,107] and Stein and Low [108] have demonstrated that the dislocation velocity V is related to the resolved shear stress according to the equation:

$$V = \tau D^m \tag{1}$$

where τ is the applied resolved shear stress and D and m are material properties. In tensile or compression tests, specimens are deformed at constant nominal strain rates $\dot{\varepsilon}$ such that

$$\dot{\varepsilon} = \dot{\varepsilon}_e + \dot{\varepsilon}_p \tag{2}$$

where $\dot{\epsilon}_p$ is the plastic strain rate in the specimen and $\dot{\epsilon}_e$ is the elastic strain rate of the specimen and the machine. For a load drop to occur during deformation, the plastic strain rate must exceed the imposed strain rate. Assuming that the plastic strain rate under dislocation glide obeys the Orowan equation

$$\dot{\epsilon}_p = \rho_m \bar{b} V \qquad (3)$$

where ρ_m is the mobile dislocation density, V is the average dislocation velocity and $\bar{b}$ is the Burgers vector; load drops or serrations can occur when there is an instantaneous increase in either ρ_m, V, or both. It is commonly accepted that the serrations observed during DSA are the result of repeated locking and unlocking of dislocations from solute atmospheres which results in a sudden increase in ρ_m. The solute atoms, however, repeatedly diffuse to form atmospheres resulting in repeated yielding (i.e., serrations). DSA is, therefore, expected to be more pronounced when V is equal to the drift velocity of solutes in the stress field of a dislocation. Furthermore, DSA can only occur in a range of intermediate strain rates and temperatures. At low temperatures and high strain rates, the solute velocity will be too small (compared to the dislocation velocity) to cause strain aging. At high temperatures and low strain rates, any solute atmospheres that form will be able to keep up with the dislocation velocity and the serrated flow will again disappear.

Types of serrations

Serrated flow can exhibit itself in a number of forms. Five types of serrations resulting from DSA have been identified (Figure 12) and were summarized by Rodriguez [104] as follows:

1. Type A serrations arise from periodic Lüders bands initiating at one end of the specimen and propagating along its gauge length. They are considered to be "locking" serrations and are characterized by an abrupt rise followed by a drop below the general level of the stress-strain curve. They occur in the low T, high $\dot{\epsilon}$ portion of the DSA regime.

2.   Type B serrations are oscillations about the general level of the stress strain curve. They also arise from the formation of Lüders bands, however, these bands do not propagate and are normally observed at higher temperatures and lower strain rates than type A bands; in other words they occur when there is an increased diffusion rate of solute atoms.

3.   Type C serrations, which occur at higher temperatures and lower strain rates than types A and B, are yield drops below the general level of the flow curve. These serrations are considered to be the result of dislocation unlocking.

4.   Type D serrations are plateaus in stress-strain curves due to the propagation of deformation bands with no work hardening or strain gradient ahead of the moving front. These serrations can occur alone or with type B serrations.

5.   Type E serrations develop from type A serrations at high strains. They resemble type A serrations but exhibit little or no work-hardening during band propagation.

As noted by Reed-Hill [109], regardless of the type of serrations observed, serrated flow is discontinuous and involves the immobilization of dislocations.

Often associated with the occurrence of serrations is a critical strain, ε_c, for the onset of serrated yielding. This strain is associated with the buildup of a sufficient dislocation density for serrated flow to occur and its value is dependent on both T and $\dot{\varepsilon}$. At higher strain rates and lower temperatures, ε_c typically increases with increasing strain rate and decreasing temperature [104]. However, in regions of higher temperature and lower strain rate, ε_c exhibits inverse behavior and increases with increasing temperature and decreasing strain rate [104]. This phenomenon is known as the inverse Portevin-Le Chatelier effect and is normally associated with type C serrations. Even though the occurrence of this "inverse" phenomenon has been substantiated, the reasons for its occurrence are unknown.

Theories of DSA

Several theories have been advanced to explain DSA phenomena and they typically fall into three main categories: solute drag models based on the model of Cottrell, "static" aging models based on the work of McCormick [110,111] and van den Beukel [112], and dislocation interaction models based on the work of Kocks [113,114]. These theories will be discussed below along with a theory recently advanced by Reed-Hill *et al.* [1-3,115,116].

The Cottrell model

The Cottrell model [43,117-119] considers DSA in terms of its most visible manifestation, the Portevin-Le Chatelier effect. This model assumes that serrated flow begins when the velocity of a dislocation exceeds the critical drag stress exerted by a solute atmosphere. The critical velocity, V_c, is given by:

$$V_c = 4D/\ell \qquad (4)$$

where D is the solute diffusion coefficient and ℓ the effective radius of the solute atmosphere. Above this velocity, the stress decreases with an increase in dislocation velocity making it logical to assume that V_c represents a critical condition for the appearance of serrations on a stress-strain curve.

If the Orowan equation is assumed valid, then V_c can be expressed as:

$$V_c = \dot{\varepsilon}/\phi b\rho_m \qquad (5)$$

or the equation may be rewritten as:

$$\dot{\varepsilon} = V_c\phi b\rho_m = 4D\phi b\rho_m/\ell \qquad (6)$$

where $\dot{\varepsilon}$ is the applied strain rate, ϕ is a Schmid orientation factor, b is the Burgers vector, ρ_m is the mobile dislocation density, D the solute diffusion coefficient, and ℓ the radius of the dislocation atmosphere. The dislocation density is normally considered to be a function of the strain, ε, such that:

$$\rho_m = N\epsilon^\beta \tag{7}$$

where N and β are constants. In the case of substitutional alloys, diffusion occurs by the vacancy mechanism such that the diffusion coefficient, D, is given by the relation:

$$D = D_0 \exp\left[-\left(\frac{Q_m + Q_f}{kT}\right)\right] = D_0 C_v^* \exp\left[-\left(\frac{Q_m}{kT}\right)\right] \tag{8}$$

where

$$C_v^* = \exp\left(-\frac{Q_f}{kT}\right) \tag{9}$$

and represents the thermal equilibrium concentration of vacancies, D_0 is the frequency factor, Q_m represents the activation energy for the movement of vacancies and Q_f is the work to form a vacancy. During plastic deformation, it is generally agreed that the total vacancy concentration increases with strain according the relation:

$$C_v = K\epsilon^m \tag{10}$$

where C_v is the vacancy concentration and K and m are constants. Based upon this, the diffusion equation can be rewritten as:

$$D = D_0 K\epsilon^m \exp\left(-\frac{Q_m}{kT}\right) \tag{11}$$

Substituting this relation back into the original Orowan equation yields:

$$\epsilon_c^{\beta+m} = \frac{\ell\dot{\epsilon}\exp Q_m/kT}{4\phi bNKD_0} \tag{12}$$

This equation suggests several experiments for determining the parameters $\beta+m$ and Q_m, but fails when it comes to predicting the critical strain itself [111].

The McCormick model

The inability of the Cottrell model to predict ϵ_c prompted McCormick to propose an alternative model [110,111]. The basis for this model is the assumption that dislocation movement is discontinuous as assumed in the dislocation arrest theory of Sleeswyk [120] who proposed that during the time when dislocations wait at obstacles, mobile solute atoms

can be drawn to them resulting in strain aging. According to this model the dislocation velocity, v, can be expressed as:

$$v = \frac{L}{t_w + t_f}$$

(13)

where L is the average spacing between obstacles, t_f the mean flight time between obstacles, and t_w the mean waiting time at an obstacle. In most cases, the average dislocation velocity is determined by the arrest time such that:

$$v = \frac{L}{t_w}$$

(14)

McCormick defined the aging time, t_a, as the time required to lock moving dislocations and proposed that serrations on stress-strain curves occur when $t_a \cong t_w$. When $t_a > t_w$, upon the onset of plastic deformation dislocations arrested at obstacles will not be locked and flow will be continuous. During straining, however, t_a can decrease due to vacancy production while t_w increases due to dislocation multiplication such that a critical strain will exist where $t_a = t_w$.

To evaluate t_a, McCormick assumes a Cottrell-Bilby [43] 2/3 power law where:

$$t_a = \left(\frac{C_1}{\alpha C_o}\right)^{2/3} \frac{kTb^2}{3U_m D}$$

(15)

and C_1 is the solute concentration at the dislocation required to lock it, C_o is the solute concentration in the alloy, U_m is the binding energy between the solute and the dislocation, D is the solute diffusion coefficient and α is a constant equal to about 3.

Assuming that both dislocation density and vacancy concentration are functions of strain as expressed above, McCormick arrives at an expression for the critical strain in substitutional alloys of the form:

$$\varepsilon_c^{m+\beta} = \left(\frac{C_1}{\alpha C_o}\right)^{3/2} \frac{\dot{\varepsilon}kTb\exp Q_m/kt}{3\phi NKU_m D_o L}$$

(16)

This expression can be simplified for BCC interstitial alloy systems where diffusion occurs independently of vacancy concentration. In this case, the equation becomes:

$$\epsilon_c^\beta = \left(\frac{C_1}{\alpha C_o}\right)^{3/2} \frac{\dot{\epsilon}kTb\exp(Q/kT)}{NLU_mD_o} \tag{17}$$

where D_o is the interstitial diffusion frequency factor and Q is the activation energy for the diffusion of interstitial solute atoms.

This theory has advantages in that it is able to accurately predict the critical strain for the appearance of serrated yielding as well as the temperature and strain rate dependence of ϵ_c. This theory, however, does not take into account other aspects of DSA such as the yield stress plateau, abnormal and rate dependent work hardening, flow stress transients that occur on changing the strain rate and the development of negative strain rate sensitivities.

The van den Beukel model

In an attempt to create a more universal theory of DSA, van den Beukel [112,121], starting with Sleeswyk's hypothesis [120], developed a theory based on the idea that a moving dislocation can be subject to strain-aging during its waiting time at an obstacle. The major advance in this model is the inclusion of the activation enthalpy, H, in the thermally activated strain rate equation:

$$\dot{\epsilon} = \dot{\epsilon}_o \exp\left(-\frac{H}{kT}\right) \tag{18}$$

where $\dot{\epsilon}$ is the strain rate, $\dot{\epsilon}_o$ is a constant and k and T have their usual meanings. It is assumed in this model that the activation enthalpy is a function of the effective stress, σ^*, and the local solute concentration at the dislocation, C. The value of C is a function of the time that the dislocation waits at an obstacle, t_w, and the rate of solute drift to the dislocation which is, in turn, a function of the diffusion coefficient or:

$$C=f(Dt_w) \tag{19}$$

He further shows the quantity Dt_w to be a function of the strain, strain rate and temperature and makes use of a $t^{2/3}$ relation between the concentration and the time formulated by Friedel [122] assuming that Dt_w is small. Thus we have:

$$C = C_0 + (KDt_w)^{2/3} \tag{20}$$

where C_0 is the nominal solute concentration of the alloy and K is given by:

$$K = \frac{3U_m}{b^2 kT}(\pi C_o)^{3/2} \tag{21}$$

In this equation U_m represents the binding energy between the solute and the dislocation.

By further considering H to be a function of the local solute concentration at the dislocation and the effective stress, van den Beukel obtained an activation enthalpy equation of the form:

$$H = -T \cdot V^* \frac{\partial \sigma^*}{\partial T} + T \frac{\partial H}{\partial C}\frac{dC}{dT} \tag{22}$$

where V^* is the activation volume. The first term on the right hand side of this equation assumes that a single thermally activated mechanism controls the flow stress [123] and is considered to give the activation enthalpy in the presence of DSA. The second term on the right hand side of the equation is considered to represent the DSA component of the activation enthalpy.

He also showed that the strain rate dependence of the flow stress could be expressed as:

$$\frac{\partial \sigma}{\partial \dot{\varepsilon}} = \frac{kT}{\dot{\varepsilon} V^*} - \frac{\partial H}{\partial C}Dt_w\frac{dC}{d(Dt_w)} \tag{23}$$

where the first term on the right side is the normal strain rate dependence in the absence of diffusion and the second is due to DSA.

Finally, van den Beukel obtained a relationship for the strain rate sensitivity by assuming that, upon an increase in strain rate from a low to a high rate, the change in activation enthalpy is given by:

$$\Delta H = -kT \cdot \ln \frac{\dot{\varepsilon}_{high}}{\dot{\varepsilon}_{low}} \tag{24}$$

which allowed him to write:

$$\frac{\Delta \sigma}{\Delta(\ln \dot{\varepsilon})} = \frac{kT}{V^*} + \frac{1}{V^*} \frac{\partial H}{\partial C} \frac{dC}{d\ln \dot{\varepsilon}} \tag{25}$$

In this equation, the first term on the right side corresponds to the strain rate sensitivity in the absence of DSA while the second term is the component due to DSA. It can be seen from these equations that any solute mobility makes a negative contribution to the total strain rate sensitivity and that this contribution increases with increasing strain. When the total strain rate sensitivity becomes negative, plastic flow becomes unstable and serrated flow is observed.

Van den Beukel further extends his investigation to show that the temperature dependence of the flow stress as well as the work hardening can be expressed by two additive terms; one friction term and one forest strength term. The friction term is assumed to be independent of strain but is said to be affected by aging while the forest strength term is assumed to be independent of solute concentration except through bulk material properties such as stacking fault energy [121] (i.e., the friction term is affected by DSA while the forest term is not).

Although this model represents an improvement over the earlier models of Cottrell and McCormick, it does have shortcomings:

1. Quantitative predictions depend upon a detailed knowledge of the variation of activation enthalpy with solute concentration near a dislocation. This data is generally not available.

2. The mathematical approach of this model makes visualization of the physics of DSA difficult.

3. This theory deals only with long range diffusion of solute atoms to dislocations.

The Reed-Hill model

The shortcomings of the Cottrell, McCormick and van den Beukel theories led Reed-Hill [1,3] to propose a new theory of DSA. In this model it is assumed that the total flow stress σ_t can be written as follows:

$$\sigma_t = \sigma + \sigma_{DSA} \tag{26}$$

where σ represents the stress in the absence of DSA and σ_{DSA} represents the stress associated with DSA. It is further shown that σ also has two parts, the internal stress, σ_E, and the thermally activated or effective stress, σ^*. Thus the total stress can be written as:

$$\sigma_t = \sigma_E + \sigma^* + \sigma_{DSA} \tag{27}$$

In BCC interstitial systems, however, it has often been demonstrated that σ_{DSA} may also consist of two additive parts due to Snoek and Cottrell aging such that:

$$\sigma_{DSA} = \sigma_{sn} + \sigma_{cot} \tag{28}$$

where σ_{sn} represents the Snoek component and σ_{cot} represents the Cottrell component. He also developed a new method to evaluate the internal stress [115,124] and demonstrated that the effective stress can be approximated by a power law of the form:

$$\sigma^* = \sigma_0^* \left(\frac{\dot{\varepsilon}}{\dot{\varepsilon}_0} \right)^{kT/H^o} \tag{29}$$

where σ_0^* is the effective stress at 0 K, $\dot{\varepsilon}$ is the nominal strain rate, $\dot{\varepsilon}_0$ and H^o are material constants with units of energy, and k is Boltzmann's constant.

The component of the flow stress attributed to DSA is given by the equation:

$$\sigma_{DSA} = \sigma_{s_{max}} \left\{ 1 - \exp\left[-\left(\frac{t_w}{\tau_s} \right) \right] \right\} + \sigma_{c_{max}} \left\{ 1 - \exp\left[-\left(\frac{t_w}{\tau_c} \right)^{2/3} \right] \right\} \tag{30}$$

where $\sigma_{s_{max}}$ and $\sigma_{c_{max}}$ are the isothermal maximum obtainable magnitudes of the Snoek and Cottrell contributions to the flow stress, respectively, and τ_s and τ_c are the relaxation

times for Snoek and Cottrell aging, respectively. The decrease in $\sigma_{s_{max}}$ and $\sigma_{c_{max}}$ due to dynamic recovery was achieved by multiplying the DSA component by the value:

$$\exp(B \times (T-T_0)) \tag{31}$$

where T_0 represents a temperature below the DSA regime and B is defined by:

$$B = \frac{R}{H^0} \times \ln\left(\frac{\dot{\varepsilon}}{\dot{\varepsilon}_0}\right) \tag{32}$$

It has been shown that this theory can model the temperature dependence of the flow stress and, when properly differentiated, the temperature dependence of the strain rate sensitivity in a wide variety of alloy systems [1-3,116].

Other models

Other models have been developed by Kocks and co-workers [113,114,121,125,126], and by Estrin and co-workers [127-130]. Kocks' model suggested that mobile dislocations are temporarily arrested at forest dislocations; solute atmospheres form on the forest dislocations and then drain by pipe diffusion from the forest dislocations to the mobile dislocations during their waiting times. Since this model relies on pipe diffusion rather than bulk diffusion, it allows for rapid atmosphere formation without the need for enhancement by vacancies. As a result, solute atmospheres need only pin portions of the dislocation line at the forest dislocation junctions rather than entire dislocation segments and the obstacle strength increases with waiting time. Like the van den Beukel model [112,121] described above, this model also assumes that the flow stress is composed of two additive terms but that the forest term rather than the friction term is influenced by aging. This assumption implies that the strength of the dislocation-dislocation interactions is altered. The model of Estrin and co-workers [127-130], is a further refinement of the Penning model [131] which is based on an N-shaped curve representing the strain rate dependence of the flow stress. Although both of these models have their merits and have been successfully used to model aspects of DSA [29,114,129,132], they will not be addressed here.

Static and Dynamic Strain Aging in Ordered Alloys

As mentioned above, most metals and alloys are subject to some sort of strain aging phenomenon [103]. And although several intermetallics have been shown to exhibit manifestations of strain aging (*e.g.*, FeAl [133,134], AgMg [33], CuZn [32], Ni_3Fe [135], NiAl [14,15,22,24-29,136-139], Al_3Ti-X [140-143], and TiAl [144,145]), the influence of strain aging on the mechanical behavior of intermetallic alloys and the species and mechanisms responsible for this behavior (*i.e.* Snoek effect , Cottrell aging, etc.) have, until recently, been essentially ignored.

A perfect example involves the $L1_2$ intermetallic alloys based on Al_3Ti. Yield point plateaus and serrated flow stress curves have often been reported for these compounds [25,140-142]. Lerf and Morris [142], however, initially elected to attribute the occurrence of serrations at intermediate temperatures to the repeated dissociation of <110> superdislocations into pairs of mobile superpartials with higher mobilities. As Potez *et al.* [141] pointed out, however, such an explanation would imply strain softening rather than strain rate softening via dynamic strain aging and, consequently, is insufficient to explain the related strain anomalies observed in these alloys. Potez *et al.* [141] indicated that oxygen might be the species responsible for DSA in Al_3Ti-Cu based on analysis of two Al_3Ti-Cu alloys with the same bulk compositions but different oxygen concentrations. However, it was later shown [146-149] that DSA in these alloys was actually the result of the precipitation of complex Al_2Ti-based precipitates on dislocations.

For the other intermetallic alloys mentioned above, the authors have often alluded to the occurrence of strain aging and speculated on the nature of the species responsible (*e.g.*, N and O in AgMg [33]); however, a detailed study of the species responsible and the resulting strain-aging mechanism in ordered alloys is lacking.
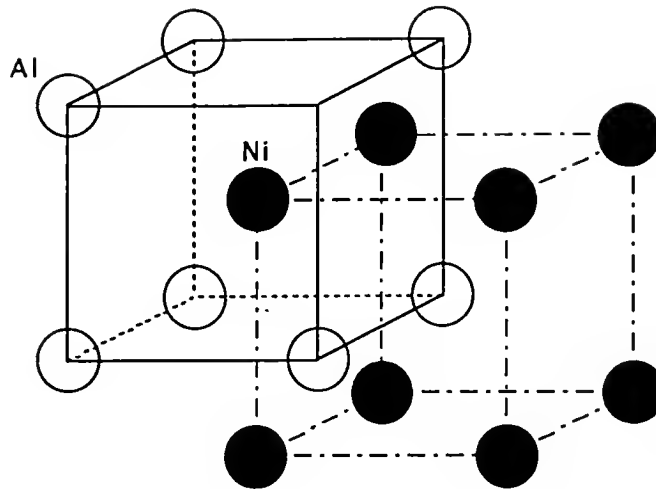
Figure 1.   The CsCl (*cP2*, B2) crystal structure of NiAl illustrating how this structure is composed of interpenetrating simple cubic sublattices of Ni and Al atoms.
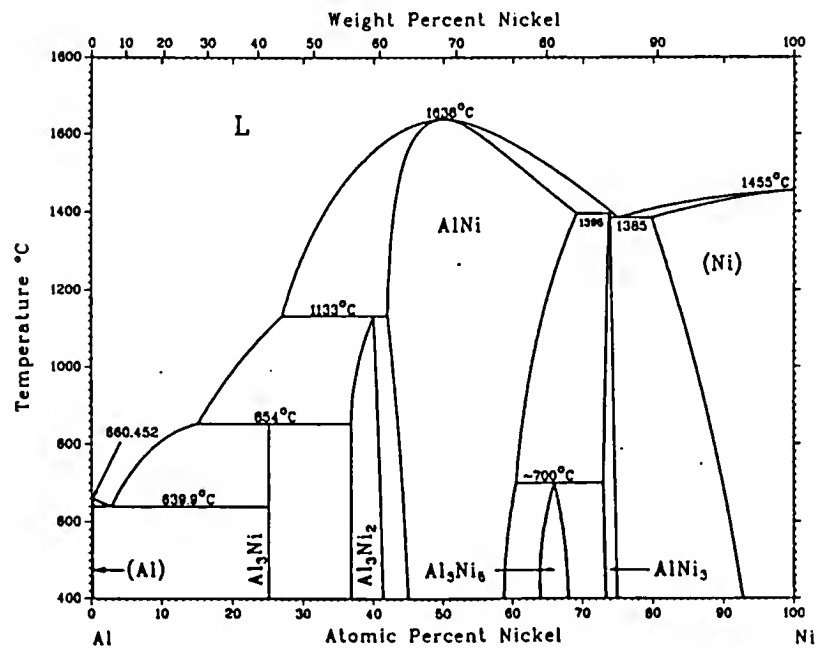

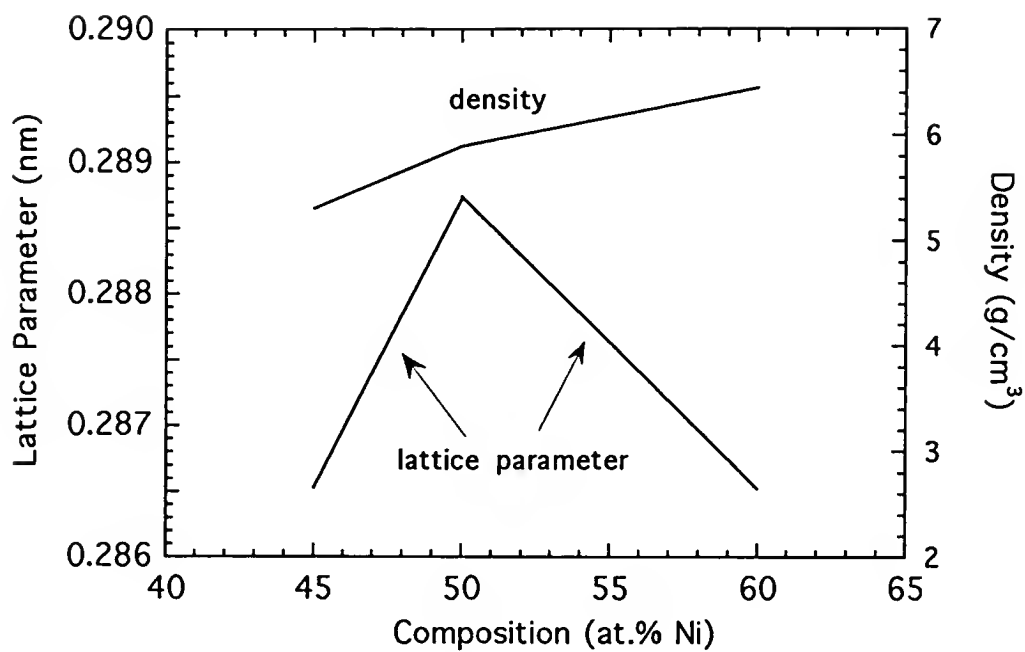
Figure 2.   The Ni-Al phase diagram [47].

Figure 3.   Variation in room-temperature lattice parameter and density of NiAl as a function of stoichiometry (Data compilation from [18]).
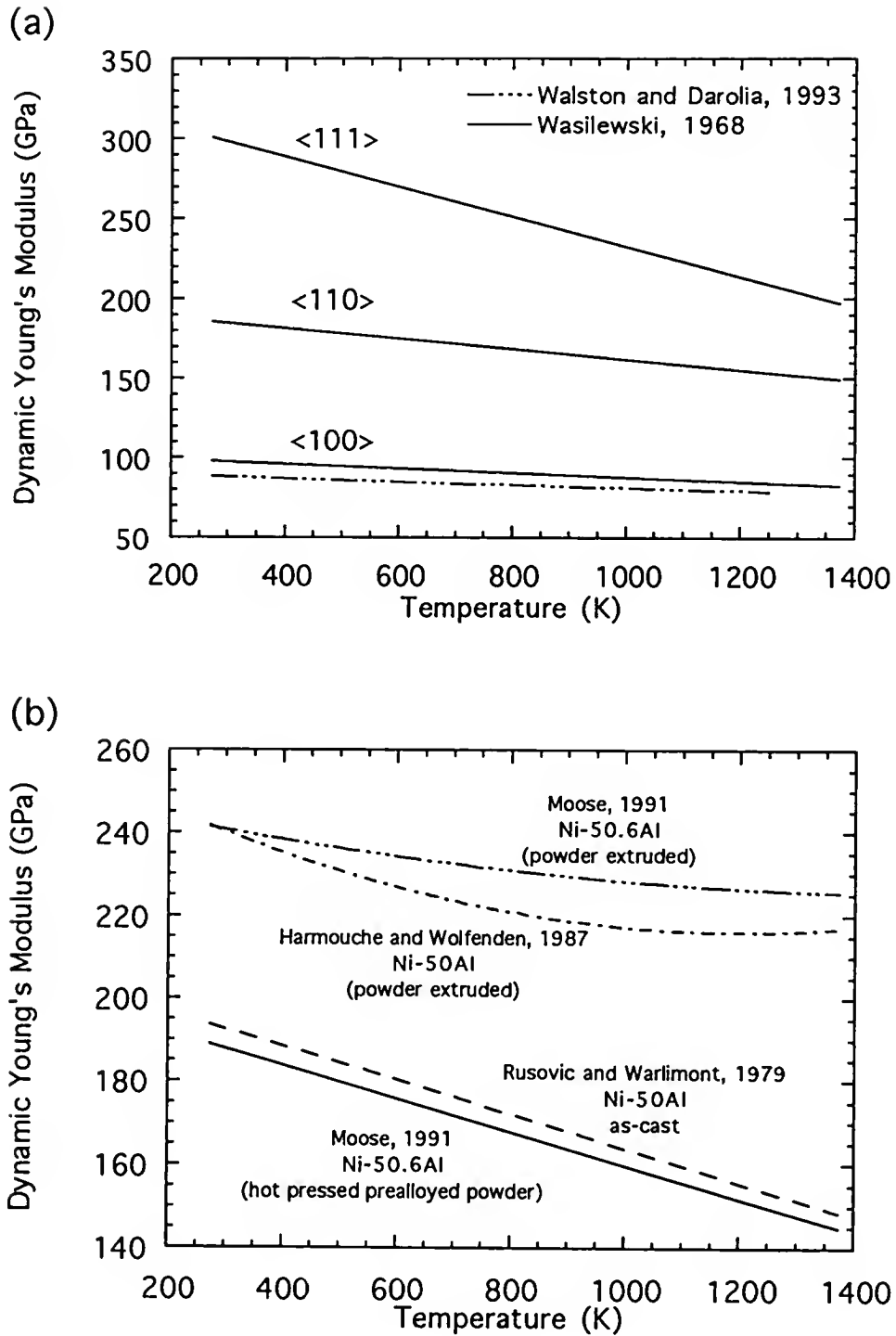
Figure 4. Elastic properties of single crystal and polycrystalline NiAl alloys: (a) single crystal NiAl as a function of orientation and temperature; (b) polycrystalline NiAl as a function of processing route and temperature (Data compilation from [7]).
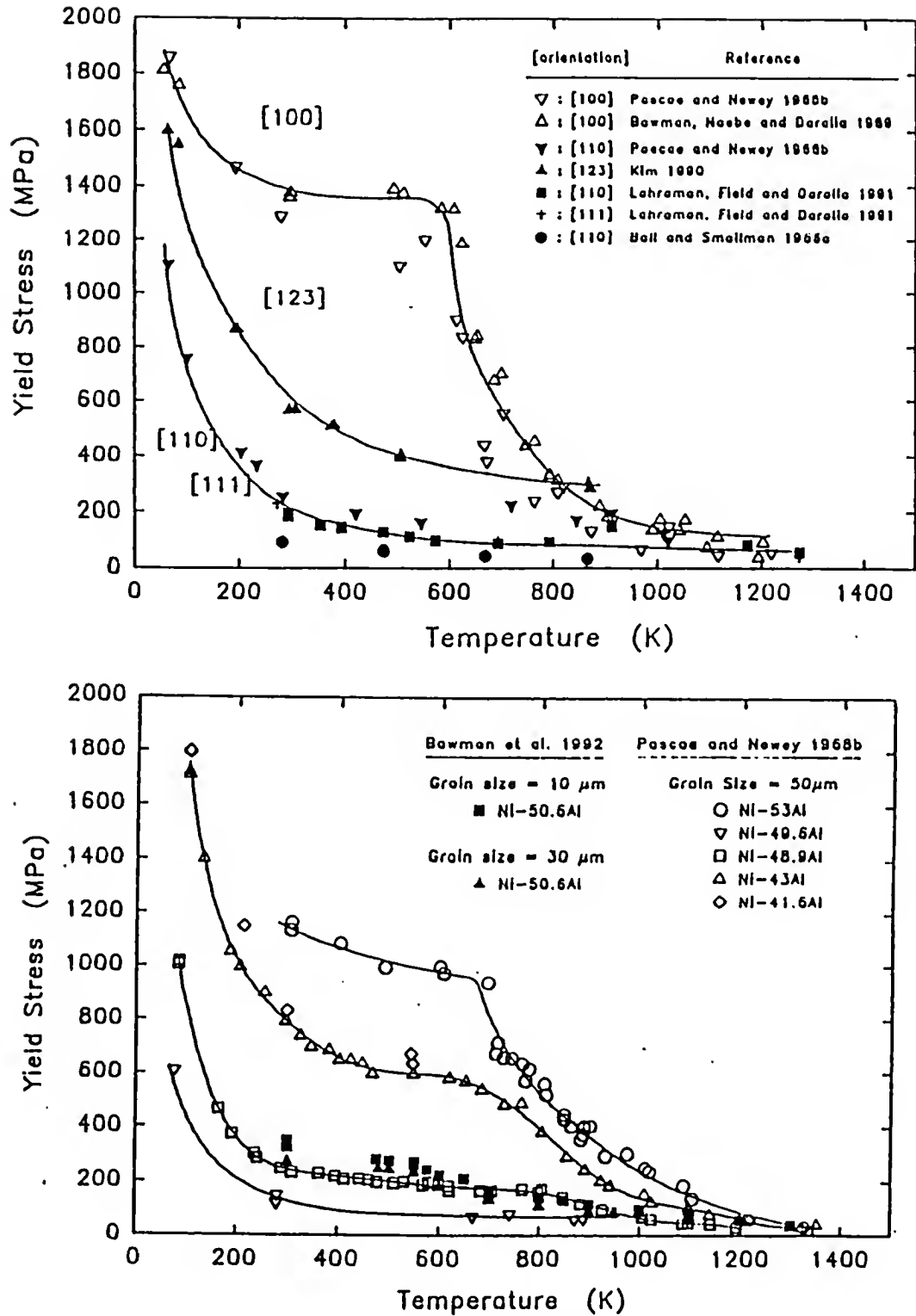
Figure 5. The variation in yield stress as a function of temperature for polycrystalline NiAl and for several different single crystal orientations: (a) single crystals and (b) polycrystals (Data compilation from [18]).
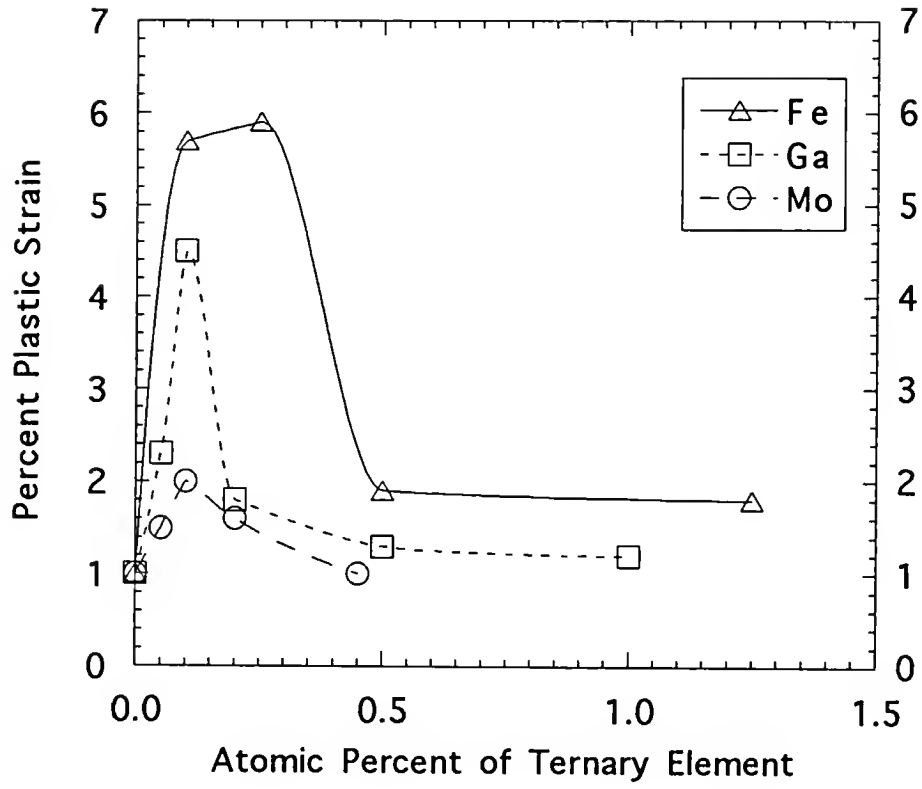
Figure 6.   Room-temperature tensile ductility of NiAl single crystals doped with iron, gallium or molybdenum [16].
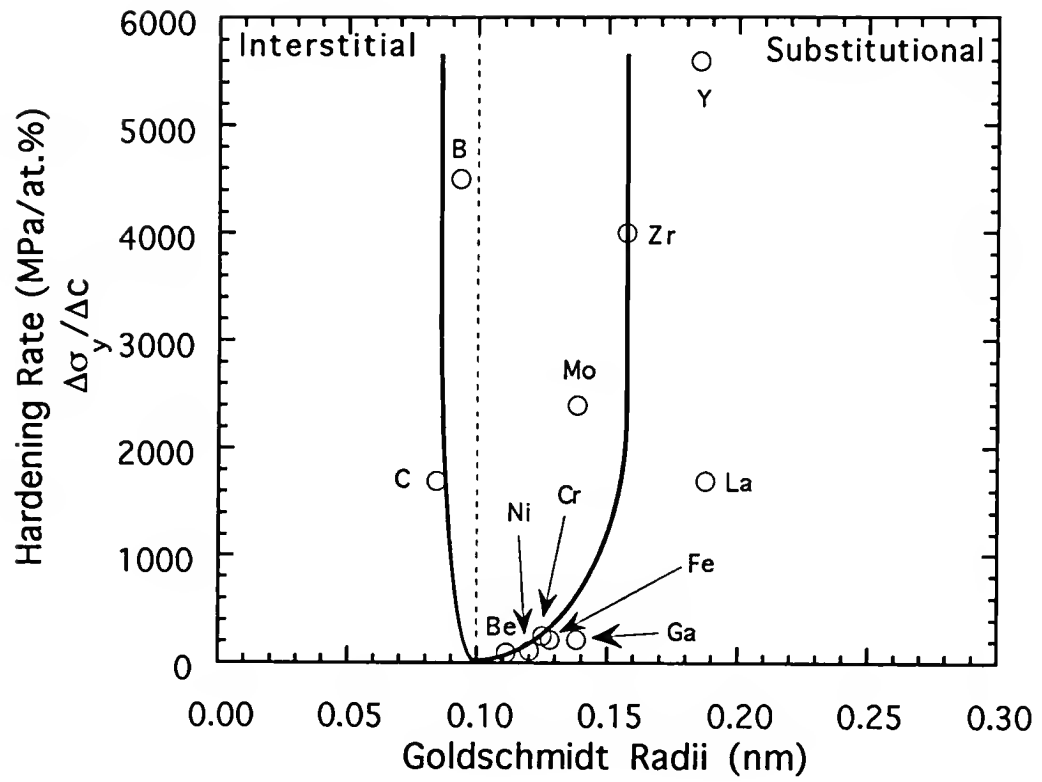
Figure 7.   Relationship between hardening rate and element size for various alloying additions in NiAl [7,18]
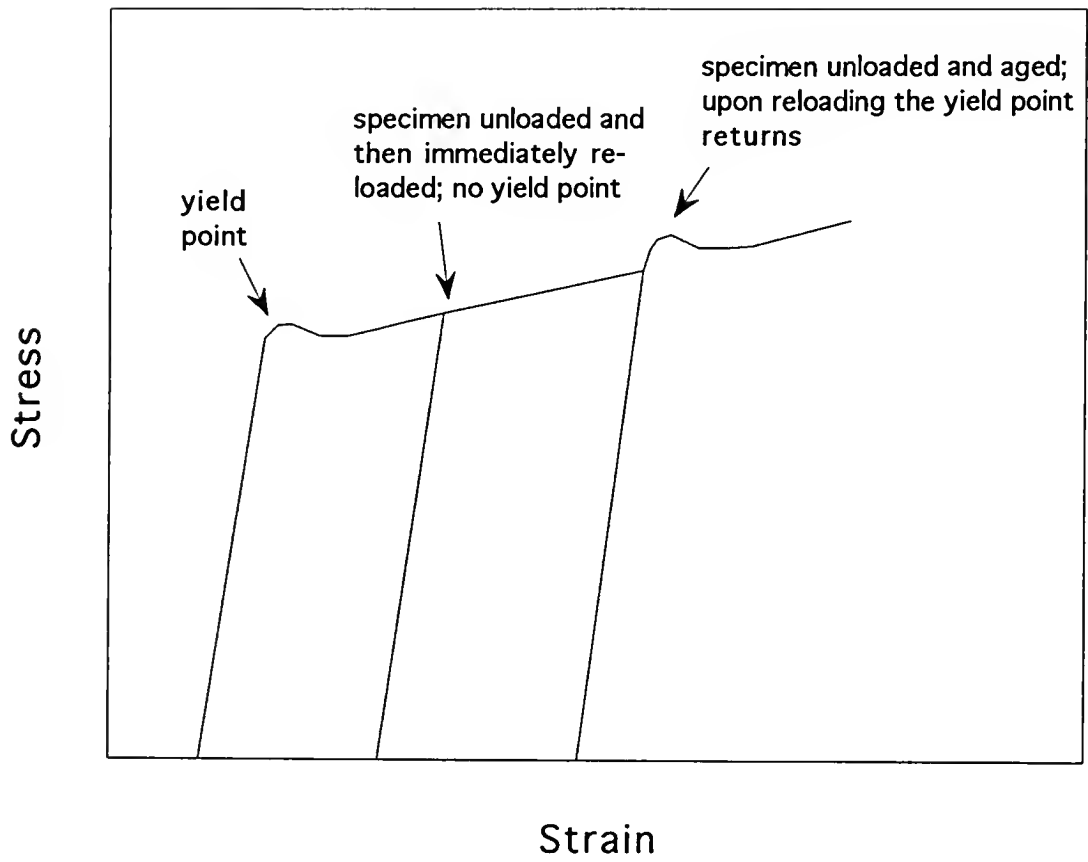
Figure 8.   Schematic illustration of static strain aging.
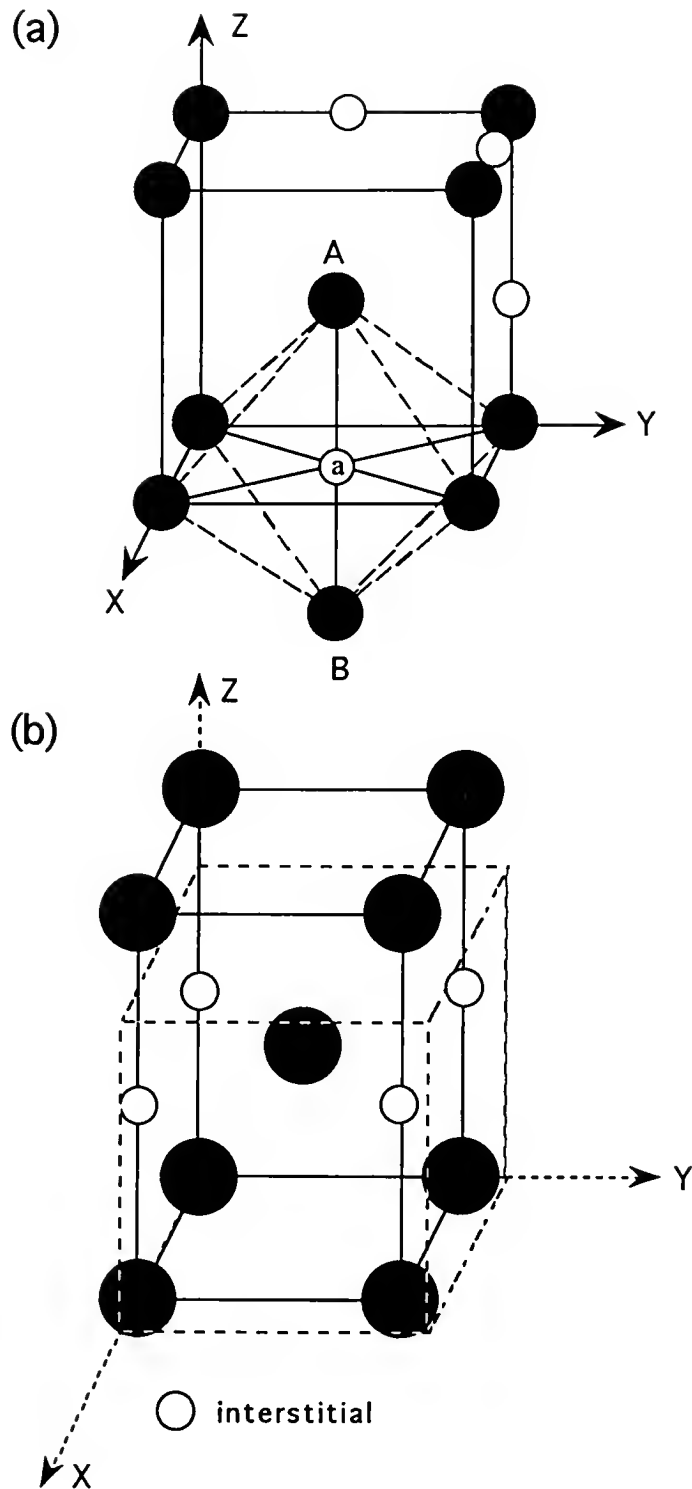
Figure 9.   Tetragonal distortion of the BCC unit cell due to the presence of interstitial atoms: (a) interstitial solute atoms occupying octahedral positions at the cube edges and faces; (b) four octahedral positions lying parallel to the z axis are occupied by interstitial atoms; (c) external stress applied parallel to the z axis causes atoms in position a to shift to more energetically favorable position b.

Figure 9 -- continued.

Figure 10.   Schematic illustration of the variation in the yield stress increment, $\Delta\sigma$, with aging time. The first plateau is due to Snoek strain aging while the second is due to Cottrell strain aging.

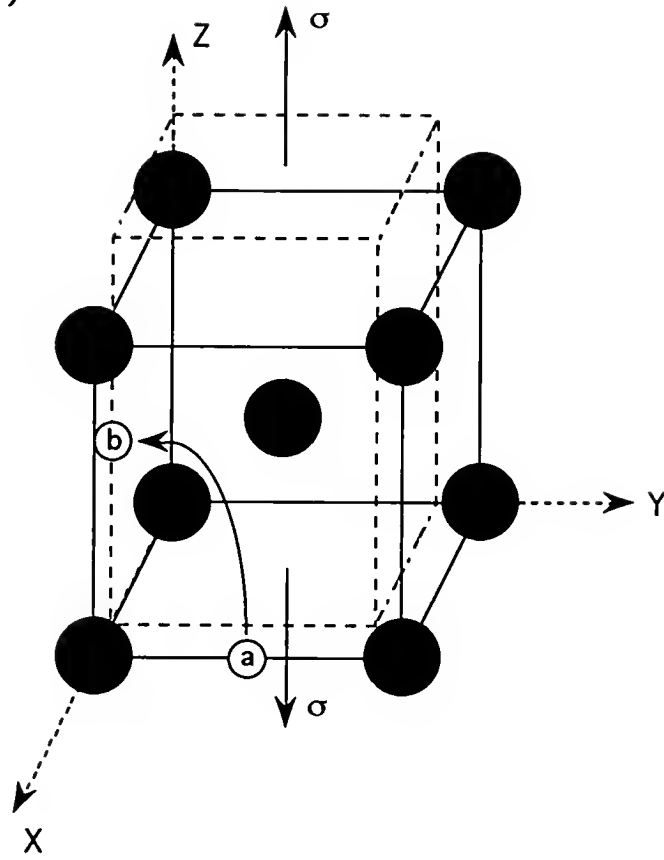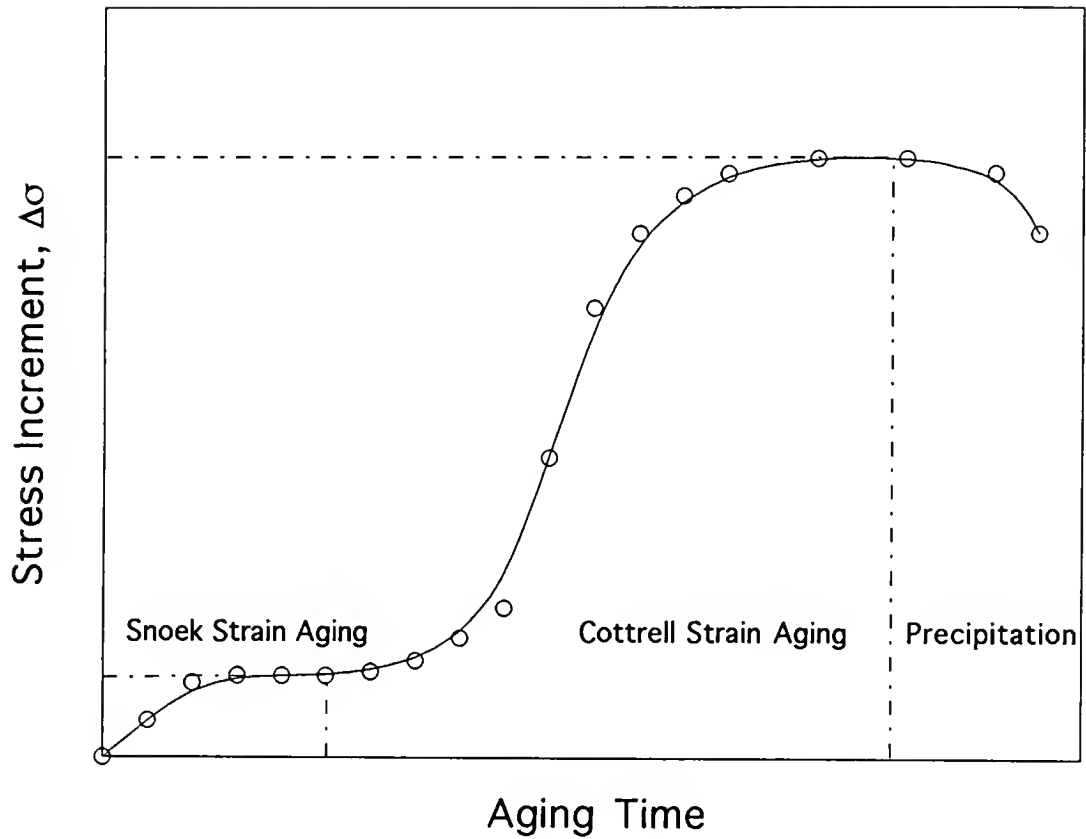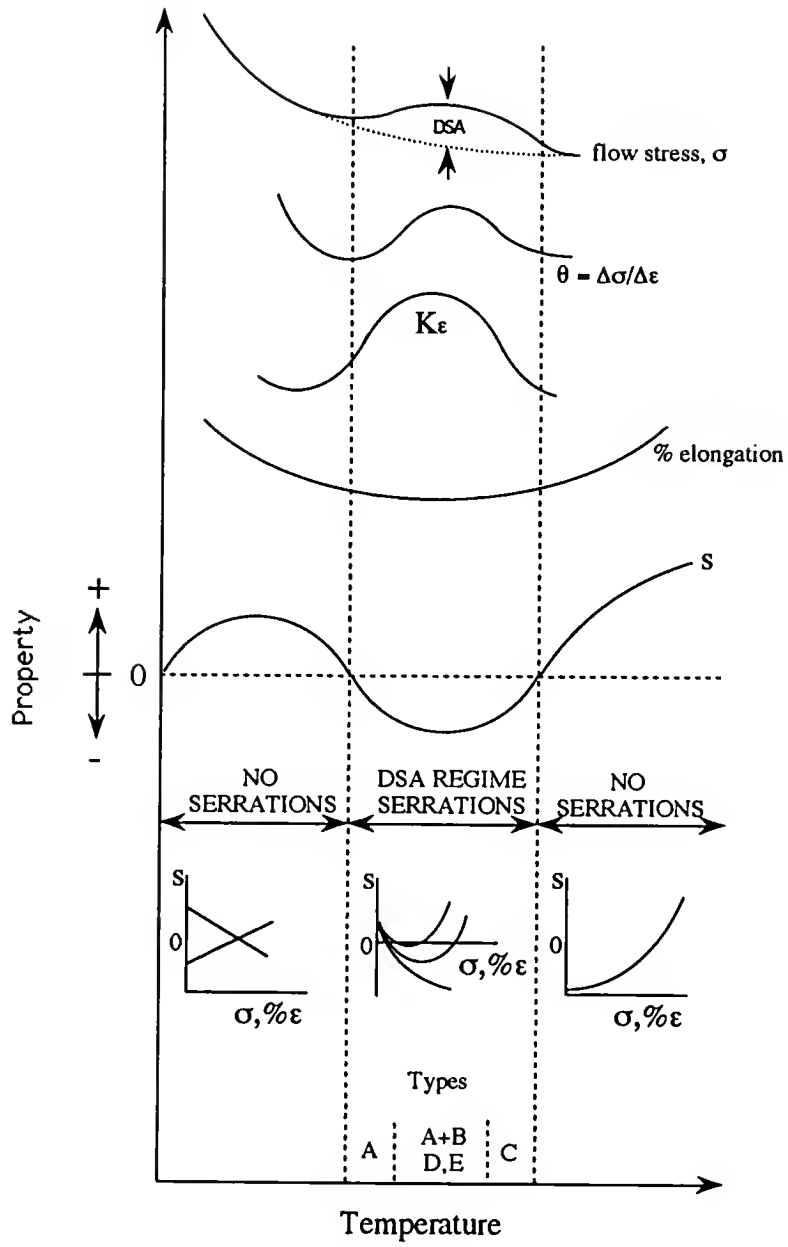Figure 11.   Manifestations of dynamic strain aging (after [106]).
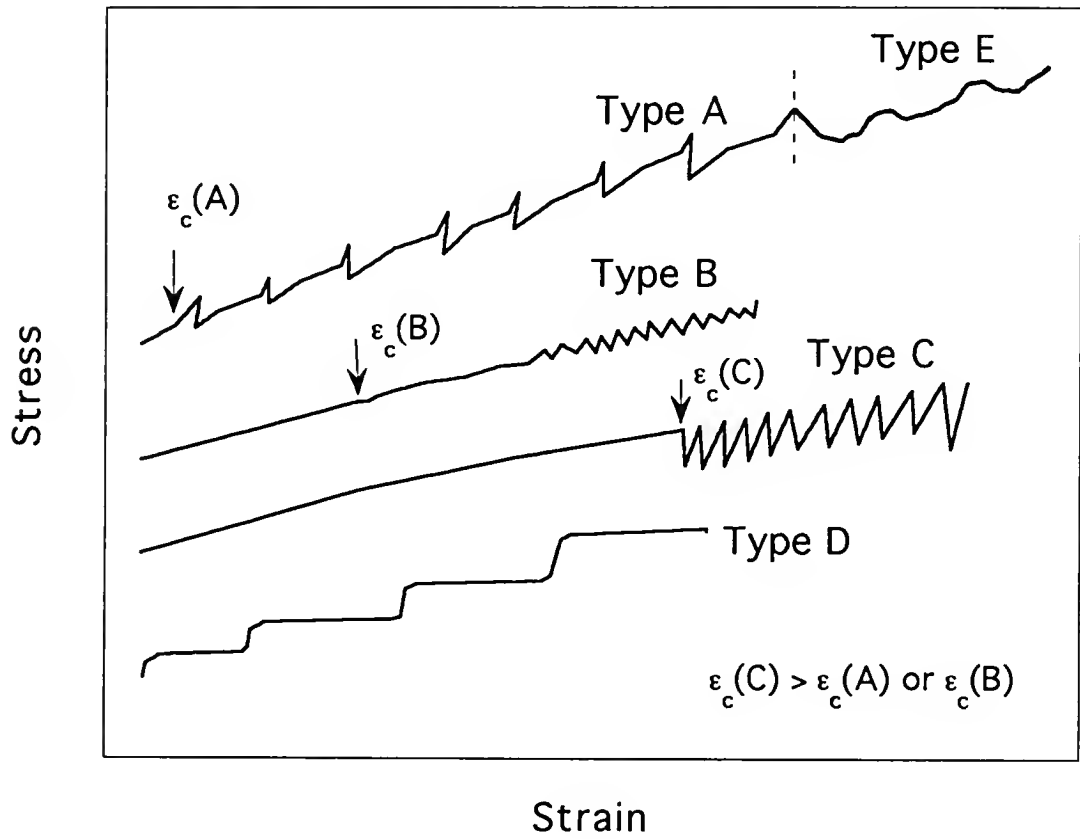
Figure 12.   Examples of the different types of flow stress serrations observed during dynamic strain aging (after [106]).

CHAPTER 3
THE EFFECTS OF PURITY ON THE MECHANICAL BEHAVIOR OF SOFT-ORIENTED NiAl SINGLE CRYSTALS

Background

Alloys based on the intermetallic compound NiAl are considered good candidates for high temperature structural applications due to their excellent oxidation resistance, low density and high thermal conductivity compared to nickel-base superalloys. In spite of these advantages, their development into a viable engineering material has been limited by low tensile ductility ($\leq 2\%$) at ambient temperatures. However, recent efforts have resulted in room temperature tensile elongations of up to 6% for doped NiAl single crystals containing microalloying additions of Fe, Mo or Ga [16,68]. The mechanism behind this increased ductility is unknown but may be related to a gettering phenomenon since it is realized that some substitutional elements and interstitial impurities can cause significant embrittlement in BCC metals [17,114] and B2 ordered compounds such as NiAl [7,18,150-152]. Current observations are consistent with this viewpoint. For example, room temperature tensile elongations of up to 5% have been observed in low interstitial binary NiAl single crystals [19] and the ductility and fracture strength in biaxial bending of high purity NiAl was found to be significantly greater than for commercial purity crystals [20]. Still, the effects of particular substitutional and interstitial elements on the mechanical behavior of NiAl are relatively unknown and the mechanisms by which various elements may enhance or hinder tensile ductility still remain a matter of conjecture. Consequently, the purpose of this chapter is to provide preliminary details concerning the effects of alloy purity on the mechanical properties of NiAl single crystals. To accomplish this goal, two stoichiometric NiAl single crystals with differing impurity contents were studied. In

addition, a NiAl alloy intentionally doped with Mo was investigated and a comparison of the mechanical properties of all three alloys is discussed in terms of relative compositions.

Experimental

Conventional purity (CP-NiAl) and Mo-doped (NiAl-0.2Mo) NiAl single crystal slabs, 25 mm x 32 mm x 100 mm, were grown in argon by a modified Bridgman procedure. The slabs were then homogenized at 1589 K for 48 h in argon and cooled at ~0.213 K/s by back filling the furnace chamber with gaseous argon. A high purity NiAl (HP-NiAl) single crystal, 25 mm diameter x 120 mm length, was produced by containerless float zone refining of a vacuum induction melted polycrystalline starter ingot of NiAl. A description of the equipment and process used to grow the low interstitial NiAl ingot has been presented in detail elsewhere [19,153].

Chemical analyses were conducted at the NASA-Lewis Research Center by the following techniques deemed to be the most accurate for the particular elements: Ni and Al were determined using analytical wet chemistry/titration techniques, Si was determined by ultraviolet/visible spectrophotometry, and Mo was determined by flame atomic absorption spectrophotometry. Oxygen, nitrogen, carbon and sulfur contents were determined by combustion techniques using LECO oxygen/nitrogen and carbon/sulfur determinators. The results of these analyses on the alloys studied are summarized in Table 1.

The crystals were oriented using the back reflection Laue technique and EDM wire cut into cylindrical compression specimens parallel to the <123> axis. Specimen dimensions were 3.0 mm and 6.4 mm for the diameter and height, respectively. Prior to testing, several CP-NiAl and HP-NiAl specimens were wrapped in Ta foil and annealed in argon at 1000 K for 2 h followed by either furnace cooling at ~0.083 K/s (FC) or water quenching (WQ) to room temperature. All compression tests were performed on an Instron Model 1125 load frame at a constant crosshead velocity corresponding to an initial strain rate of 1.4×10^{-4} s^{-1}. Tests were run in air between 300 and 700 K by heating the samples

in a clamshell type resistance furnace. True stress-strain data were calculated from the load-time plots and yield stresses were determined by the 0.2% offset method.

Table 1. Chemical Compositions of Single Crystals Examined

Alloy	at.%				Impurities (appm)			
	Ni[a]	Al[a]	Mo[e]	Si[b]	O[c]	N[c]	C[d]	S[d]
CP-NiAl	50.4±0.2	49.5±0.2	----	0.15	92	<31	169	<7
HP-NiAl	50.2±0.2	49.8±0.2	----	0.06	<27	<31	<36	<13
NiAl-0.2Mo	50.0±0.2	49.6±0.2	0.20	0.20	105	21	143	<4

[a] Analysis performed using analytical wet chemistry/titration techniques, relative accuracy ±1%

[b] Analysis performed on an Ultraviolet/Visible Spectrophotometer, Shimadzu, Model UV-160, relative accuracy ±10%

[c] Analysis performed on a Simultaneous Nitrogen/Oxygen Determinator, LECO Corp., Model TC-136 or Model TC-436, relative accuracy ±10%

[d] Analysis performed on a Simultaneous Carbon/Sulfur Determinator, LECO Corp., Model CS-244, relative accuracy ±10%

[e] Analysis performed on a Flame Atomic Absorption/Emission Spectrophotometer, Perkin Elmer Model 5000, relative accuracy ±5%

Samples for transmission electron microscopy (TEM) were cut from the tested compression specimens with a low-speed diamond saw and twin jet-electropolished in a solution of 70% ethanol, 14% distilled water, 10% butylcellusolve, and 6% perchloric acid at 273 K, 25V, and 0.15 mA. TEM examinations were conducted in JEOL 100C and JEOL 200CX microscopes operating at accelerating voltages of 120 kV and 200 kV, respectively.

Results

Within experimental accuracy, the Ni and the Al+Mo contents of the three alloys are not significantly different from each other. The major differences between the materials are the oxygen and carbon contents between the HP-NiAl and the other two materials and the addition of 0.2 Mo to one of the alloys. The Si contamination in the CP-NiAl and NiAl-0.2Mo alloys is the result of reaction with the ceramic mold walls during Bridgman growth

while the lower Si level in HP-NiAl is residual contamination from the original induction melting of the NiAl feed rod used for directional solidification.

Pronounced effects of alloy purity and thermal history (*i.e.*, prior heat treatment and subsequent cooling rate) on the compressive properties of NiAl were observed and are summarized in Table 2. First, the as-grown HP-NiAl samples exhibited yield and flow stresses similar to the as-received CP-NiAl samples but both binary NiAl alloys were much lower in strength than the as-received NiAl-0.2Mo crystal. Typical room temperature stress-strain curves for the three alloys are shown in Figure 13. Following identical treatments (*i.e.*, 1000 K(2h)+FC), both HP-NiAl and CP-NiAl experienced large decreases in yield strength (*i.e.*, >25%). It is evident from the data in Table 2 that the WHR in as-received HP-NiAl (13.8±0.7 MPa/%ε_p) and CP-NiAl (24.5±9.6 MPa/%ε_p) decreased to nearly equal values (~10.4 and 10.6 MPa/%ε_p, respectively) after this particular heat treatment. However, the yield stresses of the HP-NiAl specimens were nearly 30% lower than those of CP-NiAl. The yield stress and WHR of the Mo-doped NiAl were generally higher than those of the other alloys and were relatively insensitive to the thermal treatments employed in this study.

Table 2. Average Room Temperature Compressive Properties for <123> Oriented NiAl Single Crystals.

Alloy	0.2% Yield Stress (MPa)	Critical Resolved Shear Stress (MPa)	Samples Tested	Work Hardening Rate[*] (# Tested)
HP-NiAl: as-received	212.6±14.4	96.5±6.6	6	13.8±0.7 (3)
HP-NiAl: 1000K(2h)+FC	125.9±5.7	57.2±2.6	11	10.4±1.1 (4)
CP-NiAl: as-received	233.1±21.0	105.9±9.5	5	24.5±9.6 (3)
CP-NiAl: 1000K(2h)+FC	174.7±8.9	79.4±4.0	8	10.6±3.4 (4)
NiAl-0.2Mo: as-received	349.2±14.6	158.6±6.6	10	20.1±1.2 (4)
NiAl-0.2Mo: 1000K(2h)+FC	369.2±11.0	167.7±5.0	5	19.12 (2)

FC=furnace cooled at 0.083 K/s
[*] MPa/%ε_p at 4% plastic strain.

The temperature dependence of the yield stress for all three alloys in the as-received condition and the room temperature yield strengths for the annealed materials are presented in Figure 14 along with the data reported in previous studies of [123] oriented crystals [154,155]. As expected, the yield strength decreased gradually with increasing temperature. Figure 14 indicates that the yield stresses observed in other studies were higher than those observed for annealed HP-NiAl which suggests an influence of both purity and prior thermal history. It was shown above that low temperature heat treatments prior to mechanical testing at room temperature resulted in large yield strength drops for the binary alloys. This observation is confirmed and extended to tests run at elevated temperatures by the data of Takasugi *et al.* [155] who homogenized their single crystals at 1323 K for two days followed by furnace cooling at 0.368 K/s. The three NiAl alloys in this study exhibit slight plateaus in the yield strength vs. temperature data between 500 and 650 K. Similar behavior is frequently observed in BCC metals [17,114] and has been reported by Kim [154] for [123] oriented Ni-48Al and Takasugi *et al.* [80,155] for [123] oriented Ni-50Al single crystals. Considering the dependence of yield stress on temperature, it is convenient to represent the data in an Arrhenius form (Figure 15), *i.e.*, $\sigma_{ys}=Ae^{Q/RT}$, where A is a constant, R is the universal gas constant, Q is the activation energy, and T is the absolute temperature. In Figure 15, the changes in slope near 500 K for CP-NiAl, HP-NiAl, and NiAl-0.2Mo imply a change in deformation behavior and may be associated with the location of the brittle-to-ductile transition temperature (BDTT) [53].

Transmission electron microscopy of the dislocation microstructures revealed no differences from what has been previously reported. Prior to deformation, the overall dislocation density was low, consisting of randomly distributed $<001>\{110\}$ dislocations (Figure 16). The NiAl-0.2Mo alloy contained small α-Mo precipitates in the 10 to 30 nm size range. Following approximately 1% deformation at 300 K, the deformation

microstructure consisted of elongated dislocation cells and randomly distributed dislocation tangles (Figure 17). Once again only {110}<001> dislocations were observed.

Faceted voids were observed in all three alloys annealed at 1000 K(2h)+FC (Figure 18) but not in the as-received materials. Similar voids have been reported previously in rapidly solidified NiAl and in NiAl alloys annealed at lower temperatures after quenching from high temperatures [156-158]. These voids are attributed to the coalescence of thermal vacancies during heat treatment. All alloys exhibited <001> slip, consequently, alloy composition and purity had no effect on slip mode.

Discussion

Past studies have clearly shown that the yield stress and its temperature dependence for BCC metals can be significantly altered by either reducing or increasing the impurity contents or by causing a change in the point defect structures via irradiation and/or heat treatment [17,114,159,160]. Not surprisingly, this is also the case for NiAl. In agreement with prior studies of BCC metals, the yield stress of NiAl tends to increase as a function of interstitial and substitutional impurity contents [7,18], though great care to accurately measure composition is very rarely taken. Typically in BCC metals, interstitial solutes form Cottrell and Snoek atmospheres that pin dislocations resulting in increased strengths while substitutional additions such as Mo and Si result in solid solution hardening by increasing the frictional resistance of the lattice to dislocation motion [17,43,96,114].

Microalloying additions of Mo, Ga and Fe have been reported to decrease the BDTT of <110> oriented NiAl single crystals [16,68]. In polycrystals however, microalloying additions of Ga and Fe have been shown to increase the BDTT by as much as 250 K [82,83] while Zr additions have been shown to nearly double the BDTT to >1050 K [53,83]. In the case of Zr, the increase in the BDTT has been attributed to the pinning of extrinsic grain boundary dislocations due to grain boundary segregation of the microalloying addition [53,83].

Based on the Arrhenius plots, the BDTT for HP-NiAl and NiAl-0.2Mo appears to be the same as that for CP-NiAl at approximately 500 K which is consistent with a reported BDTT of between 473 and 573 K [16,155]. It is important to note that the assessment of the BDTT in this study is based solely on compressive data; tensile testing should be performed in order to validate this speculation. The mechanism for the BDTT in "soft" oriented single crystals is unknown although it has been proposed that the BDTT probably arises from the thermally activated climb of [001] dislocations [155], similar to what has been previously proposed for polycrystalline NiAl [53].

Heat treatment temperature and cooling rate are other important variables effecting the mechanical properties of NiAl. Previous studies have shown that high concentrations of thermal vacancies can be quenched into NiAl [161] and these vacancies result in increased yield stresses by providing resistance to the motion of dislocations [7,18,53,54,157]. Low temperature anneals, however, result in decreased yield strengths and may be attributed to reduced thermal vacancy content. This hypothesis is supported by the presence of faceted voids and significantly reduced yield stresses and WHR's in CP-NiAl and HP-NiAl following low temperature annealing. These voids form when alloys are annealed at high temperatures, rapidly cooled to produce a supersaturation of thermal vacancies, and subsequently re-annealed at intermediate temperatures resulting in the coalescence of the vacancies into faceted voids [18,156]. Low temperature heat treatments designed to produce similar defect contents in CP-NiAl and HP-NiAl result in a decrease in yield stress for both alloys and decreases in WHR to nearly equal levels. This suggests that WHR is dependent on the presence of thermal defects but independent of impurity content for the composition range encompassed in this study.

The effects of interstitial elements (*e.g.*, B, C, O, N, S, etc.) cannot be ignored when considering the mechanical properties of NiAl. Previously, it was mentioned that the CP-NiAl alloy exhibited higher yield stresses than the HP-NiAl alloy. The higher yield stresses of the CP-NiAl crystal are believed to be due to a solid solution strengthening

effect due to the presence of interstitial C and O impurities. The solid solution strengthening due to C and O in CP-NiAl relative to HP-NiAl is ~2500MPa/at.% C+O; this is in general agreement with the observations of George *et al.* [151] who reported the solid solution strengthening due to C in polycrystalline NiAl to be greater than 1700 MPa/at.% C.

As already mentioned, the NiAl-0.2Mo alloy exhibited higher yield stresses and WHR's than the binary NiAl alloys and was unaffected by the low temperature anneal. The higher yield stresses of the Mo-containing crystals are believed to be due to a solid solution strengthening effect as opposed to hardening due to the presence of the α-Mo precipitates. Mo was substituted in the place of Al (Table 1) and since all published phase diagrams [162] suggest that Mo preferentially substitutes on the Al sublattice, it is suspected that the positioning of Mo atoms on these sites leads to lattice strain and overall hardening. Furthermore, the formation of α-Mo precipitates may result in a shift in stoichiometry. Similar observations were reported recently by Cotton *et al.* [163] in the similar NiAl+Cr system. More convincing evidence in support of a solid solution strengthening mechanism is provided by the recent observations of Darolia *et al.* [16] who report the critical resolved shear stress for <110> oriented NiAl doped with 0.1% Mo to be 154 MPa which is virtually identical to the value (~159 MPa) reported for the <123> oriented NiAl-0.2Mo in this study. Specifically, if precipitation hardening were the cause of the increased strengths in Mo-doped NiAl, it would be expected that the alloy doped with 0.1%Mo would exhibit lower critical resolved shear stresses because it lies closer to the solubility limit for NiAl.

The reasons for insensitivity of the Mo-doped alloy to the lower temperature heat treatment is currently unclear. One possible explanation is that the NiAl/Mo interfaces could act as sinks for the thermal vacancies. For example, Locci *et al.* [156] observed crystallographic voids in stoichiometric NiAl melt spun ribbons subjected to intermediate temperature anneals. However, no such voids were observed in W-doped NiAl melt spun

ribbons subjected to the same heat treatments. The W-doped alloy contained fine W precipitates which were presumed to form effective sinks for the thermal vacancies thus allowing them to anneal out rapidly at the resulting W/NiAl interfaces. Thus, vacancy hardening of the as-received materials might be similar to that for the material given the low temperature anneal. An alternative explanation for the observed insensitivity to the low temperature anneal is the possible formation of Mo-vacancy pairs or clusters. Such interactions might preclude the formation of faceted voids as well as the annealing out of the thermal vacancies at 1000 K. However, neither mechanism is consistent with the observation of faceted voids in the annealed NiAl-0.2Mo alloy in similar densities as observed in the binary alloy.

<u>Summary and Conclusions</u>

Reductions in the interstitial and substitutional levels result in reduced yield strengths in NiAl. Heat treatment also results in reduced yield and flow stresses in both CP-NiAl and HP-NiAl due to a reduction in the concentration of thermal vacancies resulting from vacancy coalescence during heat treatment.

Conventional purity and HP-NiAl exhibit similar work hardening rates after similar heat treatments (*i.e.*, 1000 K(2h)+FC) which implies that the WHR might be dependent on the concentration of thermal vacancies and independent of purity level over the range encompassed by these alloys.

The yield stress and WHR of NiAl single crystals doped with 0.2%Mo exhibited no dependence on the pre-test heat treatment studied but displayed higher work hardening rates and yield stresses than both CP and HP-NiAl. These increases have been attributed to solid solution hardening effects due to the addition of Mo.
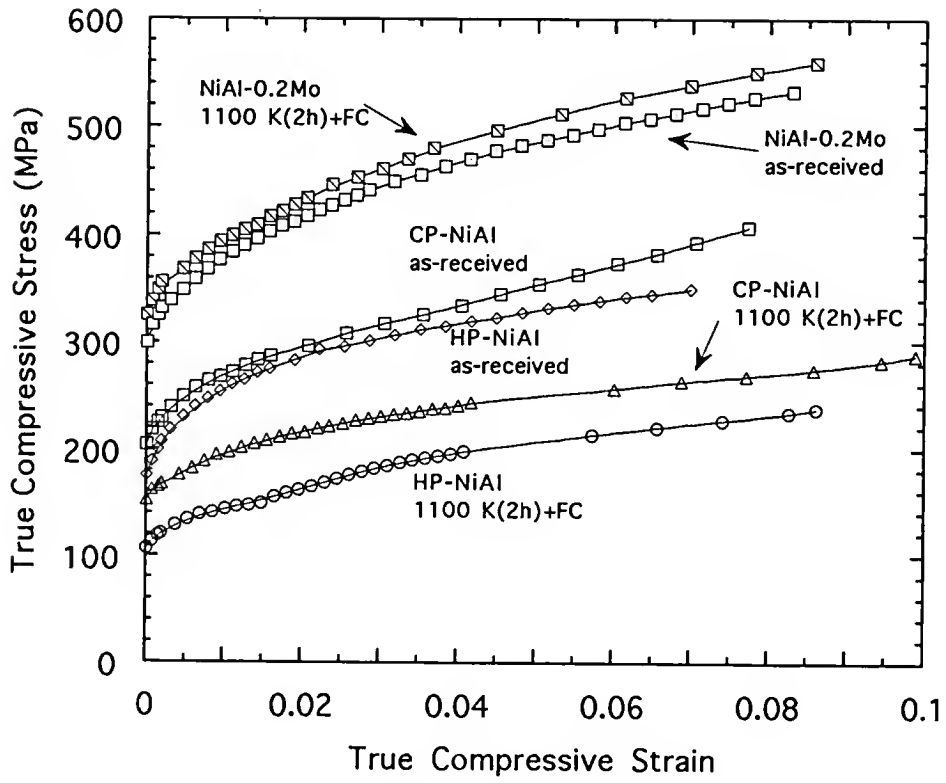
Figure 13.   Typical room-temperature compressive stress-strain response for HP-NiAl, CP-NiAl and NiAl-0.2Mo single crystals.
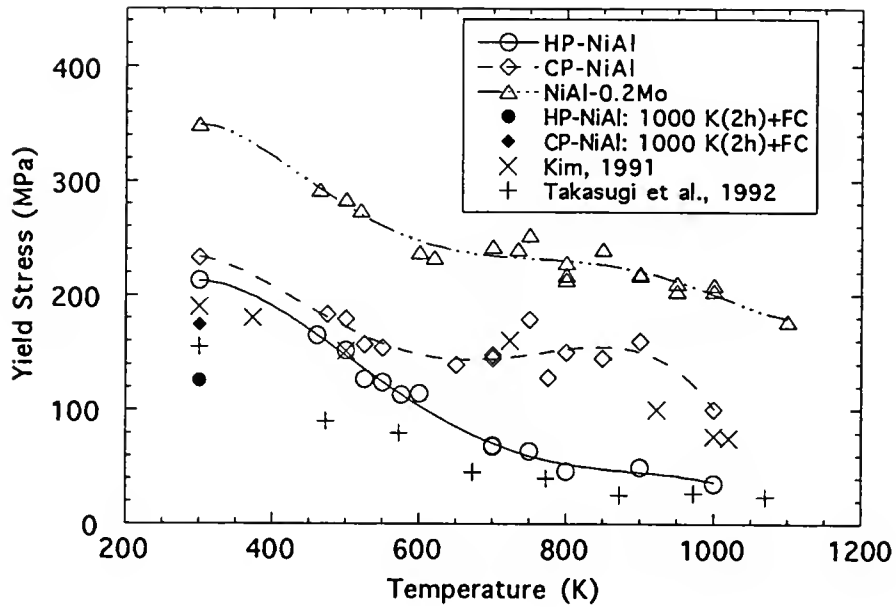
Figure 14.   The temperature dependence of the 0.2% offset yield stress for HP-NiAl, CP-NiAl, and NiAl-0.2Mo single crystals and additional data from the literature.
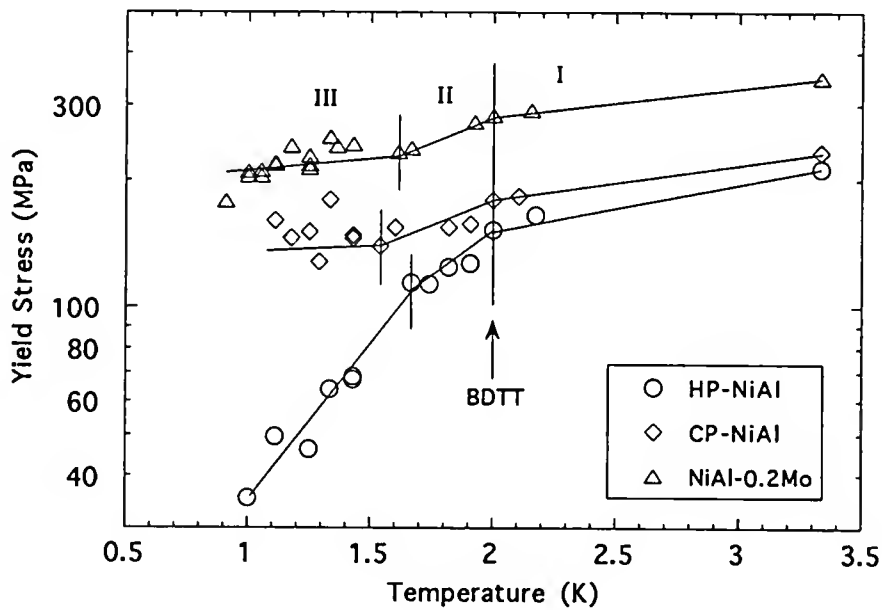

Figure 15.   Arrhenius representation of the compressive yield stress as a function of 1000/T for HP-NiAl, CP-NiAl and NiAl-0.2Mo single crystals.
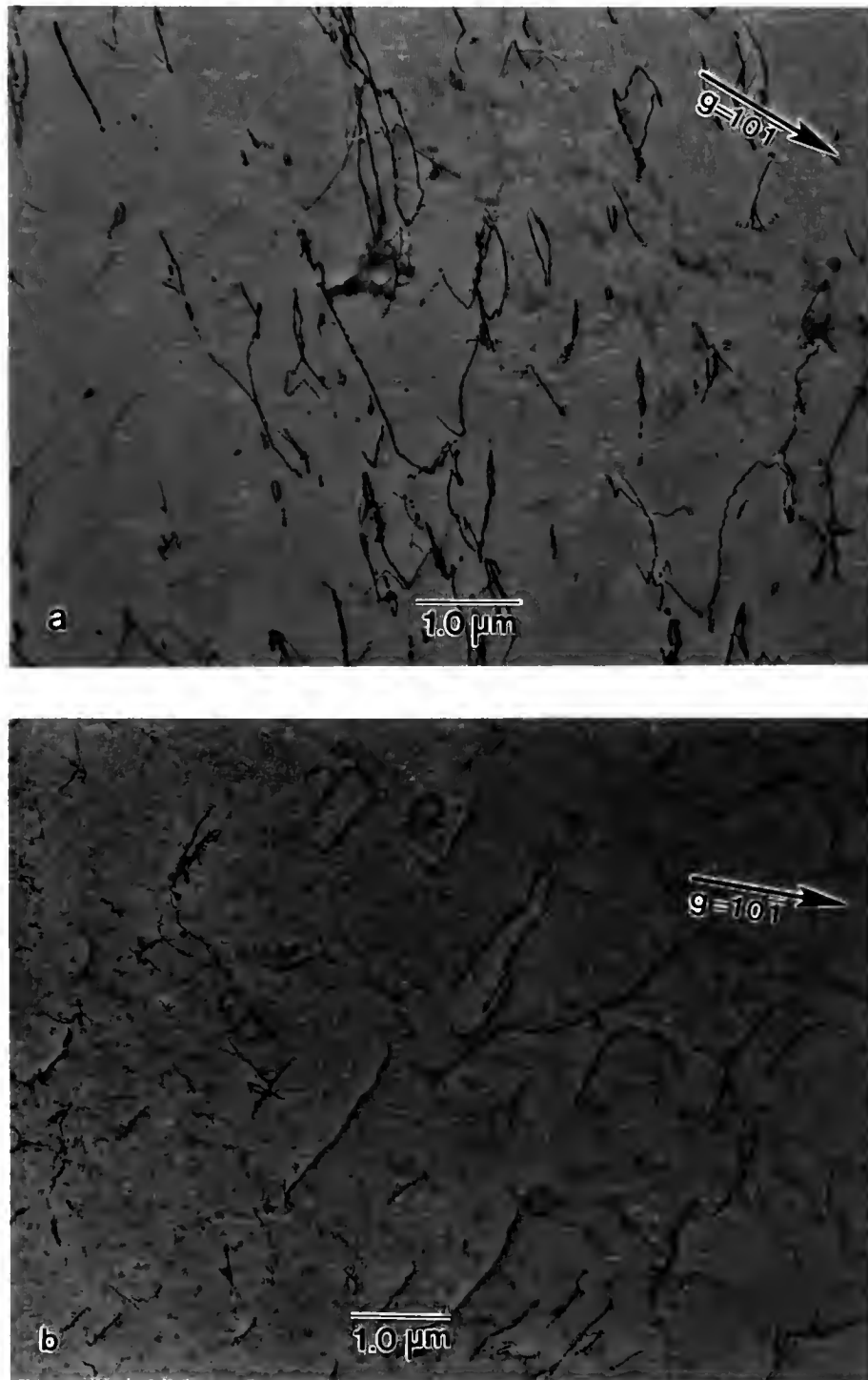
Figure 16. Bright Field TEM (BFTEM) micrographs of the dislocation morphology observed in NiAl alloys prior to deformation. (a) HP-NiAl, (b) CP-NiAl, and (c) NiAl-0.2Mo. Note the presence of a non=uniform distribution of 10 to 30 nm α-Mo precipitates (indicated by the arrows) in NiAl-0.2Mo.
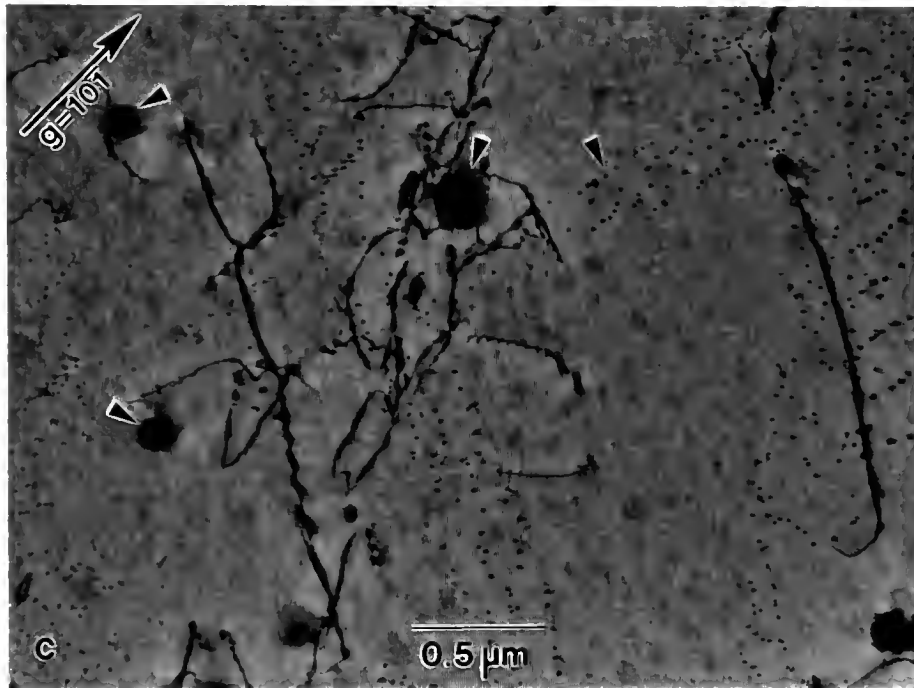
Figure 16 -- continued

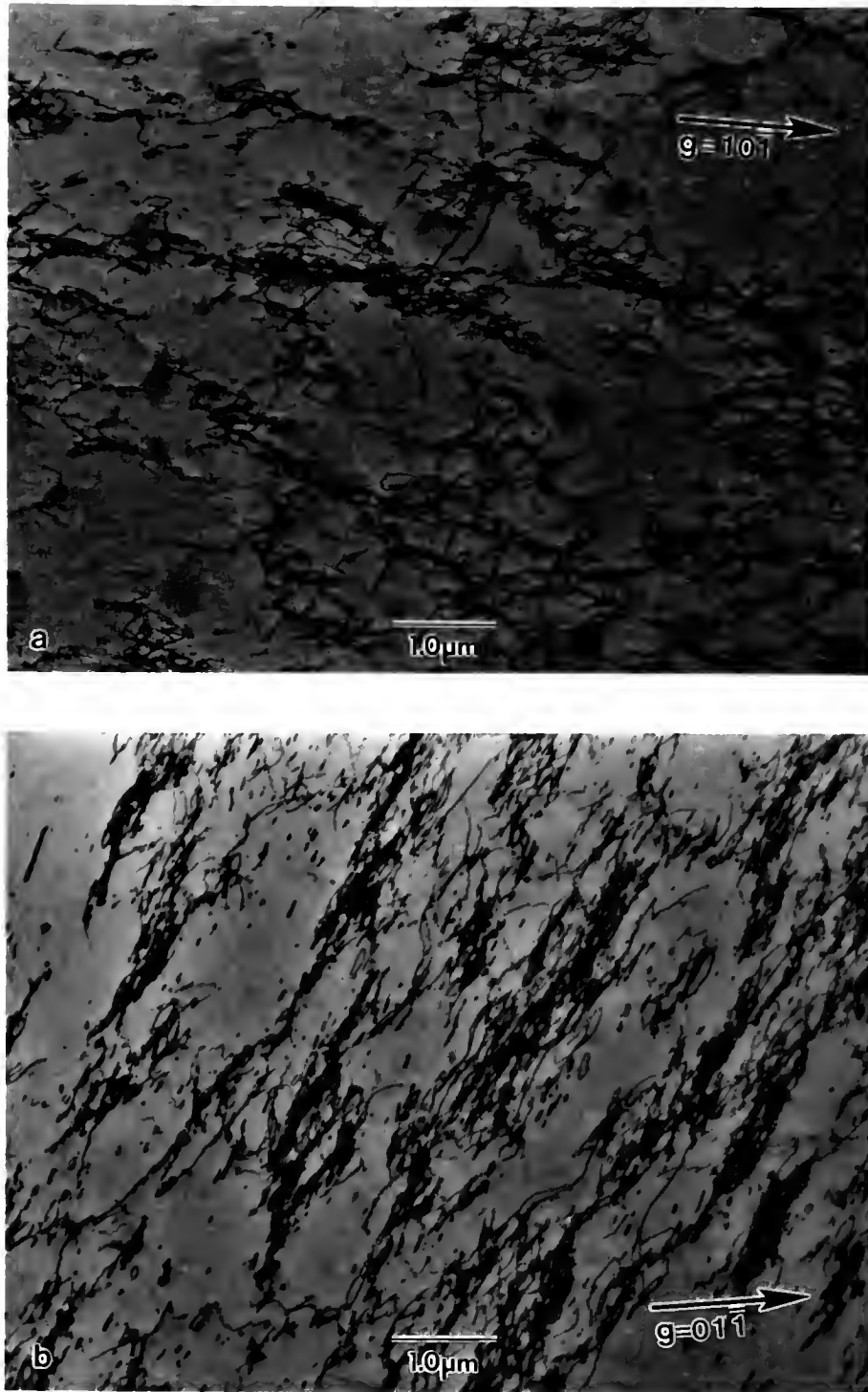Figure 17.   BFTEM micrographs showing the dislocation morphology observed in NiAl alloys after approximately 1% plastic strain in compression at 300 K. (a) HP-NiAl, (b) CP-NiAl, and (c) NiAl-0.2Mo.   Note the reduced tendency for cell formation in NiAl-0.2Mo.
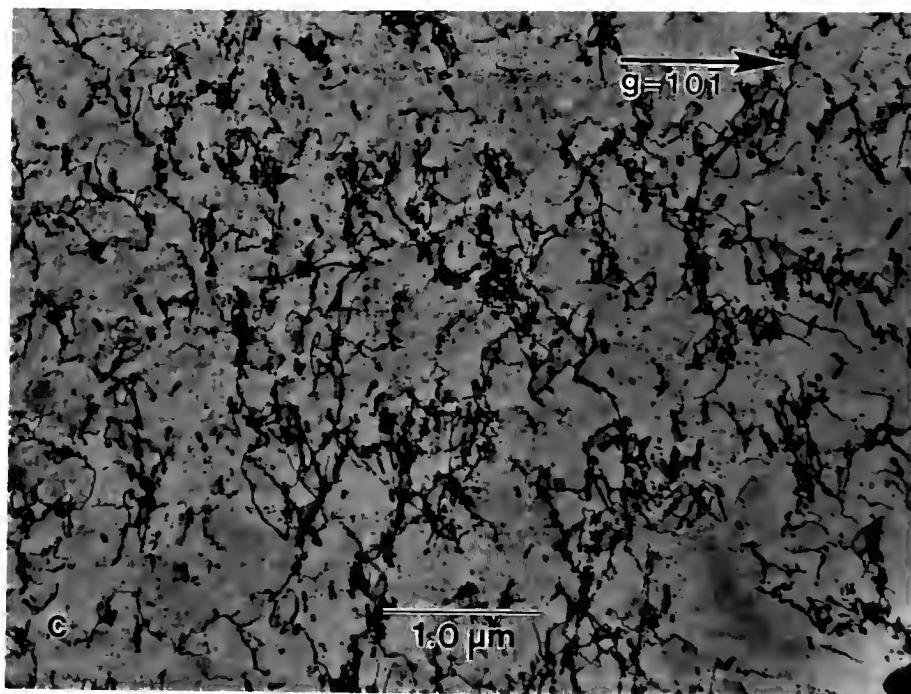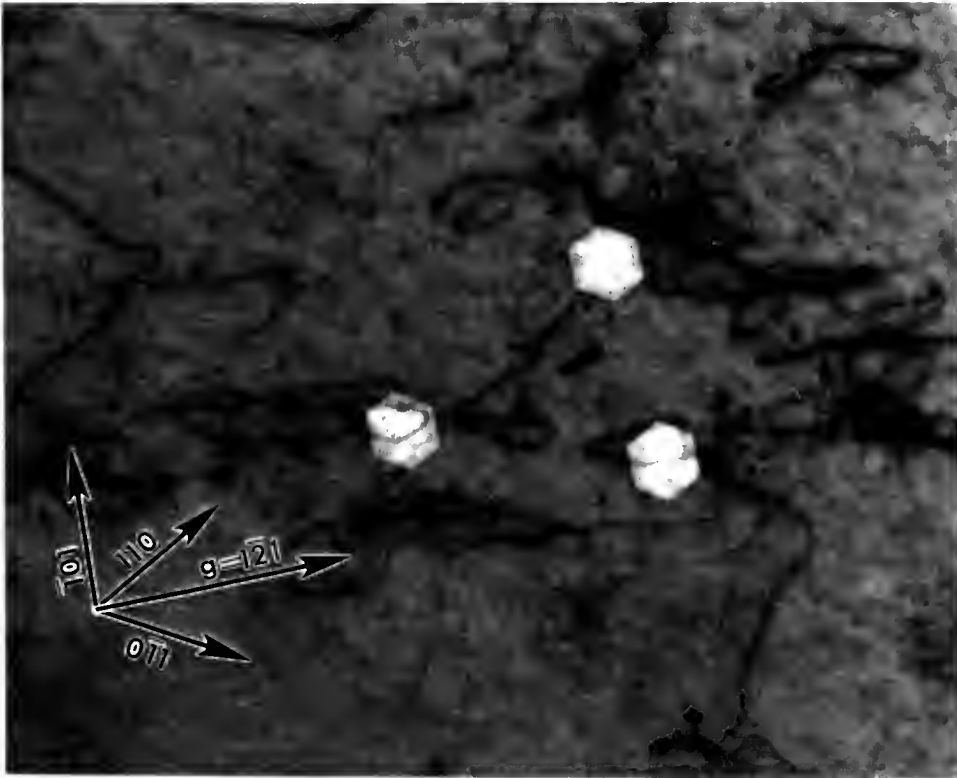
Figure 17 -- continued

Figure 18.   Faceted voids observed in HP-NiAl.   Voids result from point defect agglomeration during the 1000 K/2 h/FC anneal.

CHAPTER 4
THE EFFECTS OF INTERSTITIAL CONTENT, ANNEALING, AND PRESTRAIN ON THE TENSILE FLOW AND FRACTURE BEHAVIOR OF POLYCRYSTALLINE NiAl

Background

Body-centered cubic (BCC) metals and alloys exhibit an extreme sensitivity to (1) point defects introduced during processing and/or heat treatment, (2) the level and type of prestrain in the material, and (3) minute additions of interstitials which can lead to strain aging phenomena. Not surprisingly, several aspects of strain aging have been identified as playing a role in the deformation of polycrystalline and single crystal NiAl. They are the occurrence of yield points and serrated stress-strain curves [15,22,23,26,28,164,165], strain rate sensitivity minima [12,166], yield stress plateaus as a function of temperature [18] and flow stress transients on changes in strain rate [139,166]. In addition, extensive work by Margevicius *et al.* [23,167-169] has shown that a sharp yield point can be formed in binary NiAl following annealing at 1100 K and furnace cooling (FC). This yield point can be removed by subsequent prestraining of the material by hydrostatic pressurization prior to testing and recovered by aging the prestrained material for 7200 s (*i.e.*, 2 hours) at 673 K. Similarly, Pascoe and Newey [12] observed the formation of room temperature yield points in near stoichiometric NiAl annealed for 3600 s (1 hour) at 350 K following a uniaxial prestrain. In addition, preliminary investigations by Weaver *et al.* [138] have shown that these yield points can be removed by water quenching (WQ) from high temperature as opposed to FC. Despite these observations, no complete investigation of the interrelated effects of interstitial content, annealing and prestrain on mechanical behavior has been conducted on NiAl. The purpose of this chapter is to describe the interrelated

57

effects of interstitial content, annealing and prestrain on the tensile flow and fracture behavior of polycrystalline NiAl.

Experimental Details

NiAl alloys in the form of: (1) one titanium doped ingot (NiAl-Ti); (2) two conventional purity (CPNiAl-1, CPNiAl-2) ingots; (3) two carbon doped induction melted castings with varying carbon and oxygen concentrations (NiAl-100C and NiAl-300C); (4) two low interstitial high-purity zone refined ingots, one of which was subsequently zone leveled with carbon (HP-NiAl and HPNiAl-C respectively); and (5) a nitrogen doped powder (NiAl-N) were the basic starting materials used in this investigation. All starting materials were extruded at 1200 K at either a 12:1 or 16:1 reduction ratio. Descriptions of the equipment and processes used to fabricate the high purity, zone leveled and nitrogen doped alloys are presented elsewhere [19,92,153].

Material Characterization

Chemical analyses of the eight extrusions were conducted at the NASA-Lewis Research Center by the following techniques deemed to be the most accurate for the particular elements. Ni and Al were determined using analytical wet chemistry/titration techniques and Si was determined by inductively coupled plasma atomic emission spectroscopy. Oxygen, nitrogen, carbon and sulfur contents were determined by combustion techniques using LECO oxygen/nitrogen and carbon/sulfur determinators.

Optical, scanning electron microscopy (SEM) and transmission electron microscopy (TEM) were used to assess the microstructure of the materials. Polished optical microscopy specimens were etched by swabbing with a mixture of 0.10 kg MoO_3, 50 ml HF and 150 ml H_2O.

Samples for transmission electron microscopy (TEM) were cut from the gage of tested tensile specimens with a low-speed diamond saw and twin jet-electropolished in a

solution of 70% ethanol, 14% distilled water, 10% butylcellusolve and 6% perchloric acid at 273 K, 20-25 V and 0.15 mA. TEM examinations were conducted in either a JEOL 100C or a Philips EM420 microscope operating at accelerating voltages of 120 kV.

Fracture surfaces of selected tensile samples were examined using a Cambridge 200 scanning electron microscope. Quantitative fractography was performed to determine the percentage of intergranular fracture for most alloys. This was accomplished by taking at least five random micrographs of appropriate magnification relative to the grain size from each test specimen and using a point counting technique.

Tensile Testing

Round button-head tensile specimens were ground from the extruded rods so that the gage lengths of the samples were parallel to the extrusion direction. Sample dimensions were 3.1 mm for the tensile gage diameters and 30.0 mm for the tensile gage lengths. Prior to testing, all samples were electropolished in a 10% perchloric acid-90% methanol solution that was cooled to 208 K. Tensile tests were performed on an Instron Model 1125 load frame at a constant crosshead velocity corresponding to an initial strain rate, $\dot{\epsilon}$, of 1.4×10^{-4} s^{-1}. All tests were performed in air at 300 K. True stress-strain data were calculated from the load-time plots and yield stresses were determined by the 0.2% offset method.

The tensile testing was accomplished in four steps:

First, baseline mechanical properties were determined for all eight alloys by testing them as follows: (1) as-extruded and (2) as-extruded + 1100 K/7200 s/FC. (3) Four alloys (CPNiAl-1, HP-NiAl, HPNiAl-C, and NiAl-N), having received treatment (2), were prestrained via pressurization to 1.4 GPa. The prestrain pressurization treatment was selected based on the observations of Margevicius et al., [23,167-169].

Second, the temperature regime resulting in the maximum recovery of the yield point was determined for a series of CP-NiAl specimens, having received treatment (3).

Specimens were annealed at temperatures ranging from 500 K to 1100 K for times ranging between 60 s and 604,800 s (168 h) followed by FC, air cooling (AC) or WQ. Furthermore, some specimens were uniaxially prestrained in tension approximately 0.2% prior to annealing to determine the influence of heat treatment and type of prestrain on the baseline flow and fracture behavior of the eight alloys.

Third, some specimens were statically strain aged as follows: specimens were prestrained approximately 0.2% at room temperature, unloaded, aged *in situ* on the load frame for aging times varying between 50 s and 113,000 s (30 h), and then restrained at room temperature approximately 0.2%. Aging temperatures were selected based on the results from the test sequences described above. On several occasions, specimens were subjected to recovery anneals of 1100 K/1800 s (30 min.)/AC following an aging cycle. These procedures were repeated several times until fracture occurred in an effort to elucidate the influence of strain aging on flow and fracture behavior of NiAl. The results of one such experiment are presented in Figure 19 which shows the stress strain curves for an alloy following multiple strain aging cycles. A more detailed accounting of the test method used to study strain aging in NiAl is provided in references [137] and [138].

Experimental Results

Composition and Microstructure

The results of the chemical analyses of the eight alloys used in this study are shown in Table 3. Within experimental accuracy (± 0.2 at.% for Ni and Al), the Ni and Al contents of the eight alloys are not significantly different from each other. The major differences between the materials are the residual silicon, carbon, oxygen and nitrogen contents and the presence of Ti as an alloying addition to NiAl-Ti.

The microstructures of all the NiAl alloys were similar as observed by optical and transmission electron microscopy, and consisted of fully dense, recrystallized and equiaxed

grains as demonstrated in Figure 20. The only differences were the observation of semi-continuous stringers of nanometer-size precipitates in the NiAl-N (see reference [92]) and NiAl-Ti alloys (Figure 21). In the case of NiAl-N, previous studies have revealed the precipitates to be AlN [92]. Energy dispersive spectroscopic analysis in the TEM indicated that the stringers in NiAl-Ti were rich in Ti. The individual particles composing the stringers were, in general, too fine for analysis. On occasion, however, larger precipitates were observed within individual grains or along grain boundaries. These precipitates were typically elongated in shape as indicated in Figure 21. Analysis of microdiffraction patterns taken from these particles indicated that they were TiC precipitates which suggests that the Ti gettered C from the matrix in the NiAl-Ti alloy.

Table 3. Compositions and Grain Sizes of Polycrystalline NiAl-Alloys Investigated in This Study

Alloy (Heat)	Grain Size (µm)	at.%				appm		
		Ni	Al	Ti	Si	C	O	N
CPNiAl-1 (L2971)	18.7±1.5	50.1±0.2	49.7±0.2	----	0.15	147	550	<9
CPNiAl-2 (L3199)	18.0±2.0	50.1±0.2	49.8±0.2	----	0.02	186	94	<9
HP-NiAl (L2987)	51.4±2.3	49.9±0.2	50.1±0.2	----	0.02	43	32	<9
HPNiAl-C (L2988)	44.6±4.0	50.2±0.2	49.8±0.2	----	0.05	92	30	<9
NiAl-N (P1810)	4.0±0.3	50.1±0.2	49.7±0.2	----	0.02	57	347	904
NiAl-100C (L3218)	20.0±2.0	49.9±0.2	50.0±0.2	----	0.02	490	183	<9
NiAl-300C (L3217)	20.0±2.0	49.9±0.2	50.0±0.2	----	0.01	1153	131	<9
NiAl-Ti (L3215)	20.0±2.0	49.9±0.2	50.0±0.2	0.03	0.00	214	113	15

Mechanical Properties

The baseline mechanical properties are summarized in Table 4. Typical room-temperature stress-strain curves for each alloy are shown in Figures 22 through 26. From this data it is observed that the yield stress of each alloy generally decreased following the 1100 K/7200 s/FC anneal. In addition, a tendency for discontinuous yielding was apparent in the CPNiAl-1, CPNiAl-2, HPNiAl-C, NiAl-100C and NiAl-300C alloys but not in HP-NiAl, NiAl-N or in NiAl-Ti. Further decreases in yield stress and elimination of the tendency for discontinuous yielding were achieved in the CPNiAl-1 and HPNiAl-C alloys if the specimens were subsequently hydrostatically pressurized at 1.4 GPa whereas no additional decreases in yield stress or other apparent changes in flow behavior were observed in the powder processed NiAl-N alloy or in the HP-NiAl material (Figures 22-25). Pressurization treatments were not conducted on the remaining alloys. Recovery of the discontinuous yield behavior following pressurization could be accomplished by re-annealing pressurized specimens at 1100 K/2 h followed by furnace cooling (Figure 23). Interestingly, even though the yield stress could be reduced by annealing and in some cases by hydrostatic pressurization, these treatments had no obvious influence on the tensile ductility or fracture behavior of the various alloys. Similar observations have been recently reported by Margevicius and Lewandowski for single crystal and polycrystalline NiAl alloys [170]. Scanning electron micrographs of the fracture surfaces are exhibited in Figures 27-34. In all specimens, failure was always by a combination of intergranular separation and transgranular cleavage. Surprisingly, the HP-NiAl and NiAl-Ti exhibited a greater tendency for intergranular failure and lower tensile ductility than the other alloys.

Influence of Prestraining and Annealing on Baseline Properties

To determine whether the observed yield points resulted from the hold at temperature or during cooling from the annealing temperature, specimens of CPNiAl-1

previously prestrained hydrostatically, were reannealed at 1100 K/7200 s followed by AC or WQ. The resulting properties are summarized in Figure 35 and in Table 4. After WQ, only continuous yielding was observed while after AC, there was some evidence of a yield plateau which initially suggests that the yield points observed following FC are the result of the pinning of dislocations by mobile solute atoms during cooling through lower temperatures. As a result, annealing experiments were initiated at lower temperatures to determine the critical temperature for the migration of solute atoms to dislocations. The results of these experiments are summarized in Figure 36. It is observed that yield plateaus formed in CP-NiAl after hydrostatic prestraining followed by annealing treatments of 700 K/7200 s/FC but not following anneals of 500 K/7200 s/FC. Conversely, if the specimens were prestrained uniaxially, notable yield points formed readily after as little as 900 s (15 min.) at 522 K and in as little as 60 s (1 min.) at 700 K. Additionally, no yield points were observed when annealing temperatures exceeded 900 K.

TEM Observations of Deformed Specimens

Figure 37 shows a series of TEM bright field images of CPNiAl-1 that was deformed at room-temperature following anneals of 1100 K/2 h/FC. Tensile tests were interrupted at plastic strains of 0.05%, 0.31% and 2.04% corresponding to the yield stress peak, the Lüders region and after fracture respectively. At 0.05 and 0.31% strain (Figures 37a and b), the dislocation structure consisted of a low density of inhomogeneously distributed dislocations arranged into poorly defined cells and dense tangles. Some intercellular/inter-tangle dislocation debris was observed although the cell interiors remained largely dislocation free. As the strain was increased to 2.04% (Figure 37c), the dislocation density increased and the cells became more well defined. The dislocations observed were predominantly <100> dislocations of mixed character. The predominant slip plane was {011} although some dislocation debris lying on {001} slip planes was occasionally detected.

Table 4. Baseline Tensile Properties of NiAl Alloys

Material	Condition*	0.2% Yield Stress (MPa)	Fracture Stress (MPa)	Ductility (%)	Intergranular Fracture (%)	Observations #
CPNiAl-1	as-extruded	269	379	2.11	-na-	DY, YP
	as-extruded	275	368	1.83	36.0	DY, YP
	annealed/FC	184	301	2.08	36.1	DY, sharp YP
	annealed/FC	197	228	1.04	-na-	DY, sharp YP
	annealed/AC	154	309	2.26	-na-	DY, plateau
	annealed/WQ	143	228	1.13	46.2	CY
	pressurized	154	288	1.86	-na-	CY
	pressurized	159	317	1.81	37.5	CY
	pressurized	154	322	2.16	37.4	CY
CPNiAl-2	as-extruded	164	241	1.05	30.8	CY
	as-extruded	172	306	1.70	37.9	CY
	annealed	117	257	2.05	35.2	DY, sharp YP
	annealed	116	336	3.34	40.2	DY, sharp YP
HP-NiAl	as-extruded	166	214	0.79	57.5	CY
	as-extruded	157	235	1.16	60.4	CY
	annealed/FC	98	174	1.17	63.2	CY
	pressurized	118	176	0.92	58.2	CY
HPNiAl-C	as-extruded	170	201	0.59	43.4	CY
	annealed	113	157	0.68	-na-	YP
	pressurized	96	171	0.98	39.4	CY
NiAl-100C	as-extruded	155	255	1.35	37.5	DY, plateau
	as-extruded	151	319	2.25	33.0	DY, plateau
	annealed	113	342	3.29	41.9	DY, sharp YP
	annealed	115	285	2.35	40.1	DY, sharp YP
NiAl-300C	as-extruded	180	322	2.02	32.4	CY
	as-extruded	162	297	1.84	28.6	DY, plateau
	annealed	109	343	3.29	42.8	DY, plateau
	annealed	108	352	3.38	48.4	DY, plateau
NiAl-N	as-extruded	298	409	1.32	-na-	CY
	as-extruded	297	476	2.20	34.1	CY
	annealed/FC	265	468	2.45	31.9	CY
	pressurized	266	434	2.16	-na-	CY
	pressurized	274	352	1.03	33.5	CY
NiAl-Ti	as-extruded	170	235	0.86	57.5	CY
	as-extruded	176	176	0.20	56.2	CY
	annealed	123	256	1.76	64.7	CY
	annealed	124	265	1.81	64.3	CY

*annealed/FC or annealed = as-extruded + 1100 K/7200 s/FC

*annealed/AC = as-extruded + 1100 K/7200 s/AC

*annealed/WQ = as-extruded + 1100 K/7200 s/WQ

*pressurized = as-extruded + 1100 K/7200 s/FC + pressurize 1.4 GPa

#DY = discontinuous yielding, upper yield point, sharp yield drop

#YP = yield point; #CY = continuous yielding; -na- = not available

Intergranular fracture: accuracy = ±10%

Figure 37e shows the dislocation substructure observed in NiAl-N following hydrostatic prestraining to 1.4 GPa. In agreement with the reports of Margevicius and co-workers [168,169] for conventional purity cast and extruded NiAl, the dislocation substructures consisted of a more uniform distribution of long, straight dislocations generated from grain boundaries. Diffraction contrast analysis revealed that all of the dislocations were of <001> type. Similar microstructures were observed in CPNiAl-1 after hydrostatic prestraining.

Discussion

In agreement with the many prior studies of extruded near-stoichiometric NiAl in bulk form [71,171,172] and during *in-situ* TEM observations [173], the deformation substructure following straining at room-temperature consisted of a network of poorly defined dislocation cells, dense tangles and intercellular debris. Well defined deformation bands, were not observed by TEM nor was there evidence of coarse slip bands intersecting the specimen surfaces.

Species Responsible for Strain Aging in NiAl

A determination of the species most likely responsible for the strain aging effects in NiAl can be made by examination of the aging behavior of all eight alloys. Discontinuous yielding, in the form of yield points and yield plateaus, was observed in CPNiAl-1, CPNiAl-2, NiAl-100C, NiAl-300C and HPNiAl-C, while continuous yielding was observed in HP-NiAl, NiAl-Ti or NiAl-N following heat treatments known to produce yield points in conventional cast and extruded NiAl [167]. In NiAl-N, the oxygen and nitrogen contents were much higher than those observed in CPNiAl-1 or CPNiAl-2 while the C-content was much lower, which suggests that nitrogen and oxygen are not the species responsible for the observed yield points. When the excess interstitials were reduced sufficiently, as in the case of HP-NiAl, no yield points were observed; however,

doubling the carbon concentration (HPNiAl-C) resulted in a well-defined yield point. These observations are supported by the prior investigations of Noebe and Garg [92] who observed sharp yield points in powder processed conventional purity NiAl (C=143 appm, O=227 appm, and N=6 appm) but no yield points in powder processed nitrogen-doped NiAl (C=57 appm, O=347 appm, and N=904 appm). Also, in HPNiAl-C, it was observed [137,138] that longer aging times are required to achieve the same yield increment as observed in CPNiAl-1 and CPNiAl-2. It is believed that this behavior is a result of the significant reduction in the concentrations of interstitials, particularly C. Since there is less carbon to pin dislocations in NiAl-C, the carbon present must, presumably, diffuse longer distances to cause pinning. Finally, in NiAl-Ti, the bulk interstitial levels were equivalent to those observed in CPNiAl-2 which exhibited yield point behavior. However, no yield points were observed in NiAl-Ti which was shown to contain a TiC stringers; this suggests that the lack of a yield point in NiAl-Ti is due to the gettering of sufficient carbon from the NiAl matrix and that carbon is the species responsible for the observed yield points.

Influence of Prestraining

As noted in the Results, the return of a sharp yield point is much more rapid when the specimen has been prestrained uniaxially as opposed to hydrostatically. During uniaxial deformation of NiAl, dislocations cross-slip easily forming cell structures [53,92] that result in high work hardening rates at room temperature. As a result, the dislocations are in essence pinned. In contrast, samples pressurized hydrostatically show a more even distribution of dislocations which are not bound in cells [169]. In uniaxially prestrained samples, since some of the dislocations are already locked up in cell structures, fewer mobile dislocations are available. Thus, less solute is required to pin the available mobile dislocations. Since more mobile dislocations are available in hydrostatically prestrained samples, more carbon is required to cause pinning. As a result, longer aging times are required to achieve the same yield point increments observed after uniaxial prestraining. A

similar explanation has been applied to strain-aged steels prestrained in directions non-parallel to the original tensile direction [174].

The results of this study also revealed a further reduction in the yield stress of CPNiAl-1, HP-NiAl, and HPNiAl-C following pressurization to 1.4 GPa. However, no such effect was observed in NiAl-N. Prior investigations by Margevicius *et al.* [169] on pressurized NiAl alloys have shown that dislocation generation is enhanced by compositional differences between neighboring grains. This suggests that higher dislocation densities will be enduced in CPNiAl-1, HP-NiAl, and HPNiAl-C over NiAl-N due to the larger compositional variations between the neighboring grains.

Despite it's influence on the tensile flow behavior of NiAl alloys, prestraining, whether uniaxial or hydrostatic, had no observable influence on the tensile ductility and fracture behavior of NiAl. In CP-NiAl, for example, the fracture surfaces were approximately 37% intergranular regardless of how the specimens were prestrained or strain aged prior to testing. In HP-NiAl, however, there was an apparently higher propensity for intergranular fracture over transgranular failure. Interestingly, this alloy, although apparently closer to stoichiometry and free from high interstitial levels, exhibited lower tensile ductilities than the CP-NiAl and the NiAl-N alloys. This observation contradicts the observations in single crystals where soft-oriented specimens having low interstitial levels and high purity were shown to exhibit nearly 5% tensile ductility at room temperature, regardless of pretest treatments [19]. Although some of these observations can be related to the differences in grain size between the alloys, more thorough investigations of these issues are required.

Conclusions

The yield points observed in conventional purity and carbon-doped NiAl are the result of strong dislocation pinning by interstitial carbon. Oxygen and nitrogen levels

below 0.035 and 0.09 at.%, respectively, do not appear to pin dislocations in NiAl and, therefore, do not produce yield point phenomena.

Hydrostatic prestraining as opposed to uniaxial prestraining delays the kinetics of the yield point return by forming random networks of free unpinned dislocations which require more diffusion time for strong locking to occur.

Yield point phenomena can be removed by microalloying with sufficient levels of reactive elements such as Ti to getter carbon from the matrix by forming semi-continuous precipitates of TiC.

Despite their influence on the flow behavior of NiAl, prestraining and/or strain aging have no observable impact on the room-temperature fracture characteristics of NiAl alloys. In fact, fracture always occurs by a mixture of intergranular failure and transgranular cleavage.
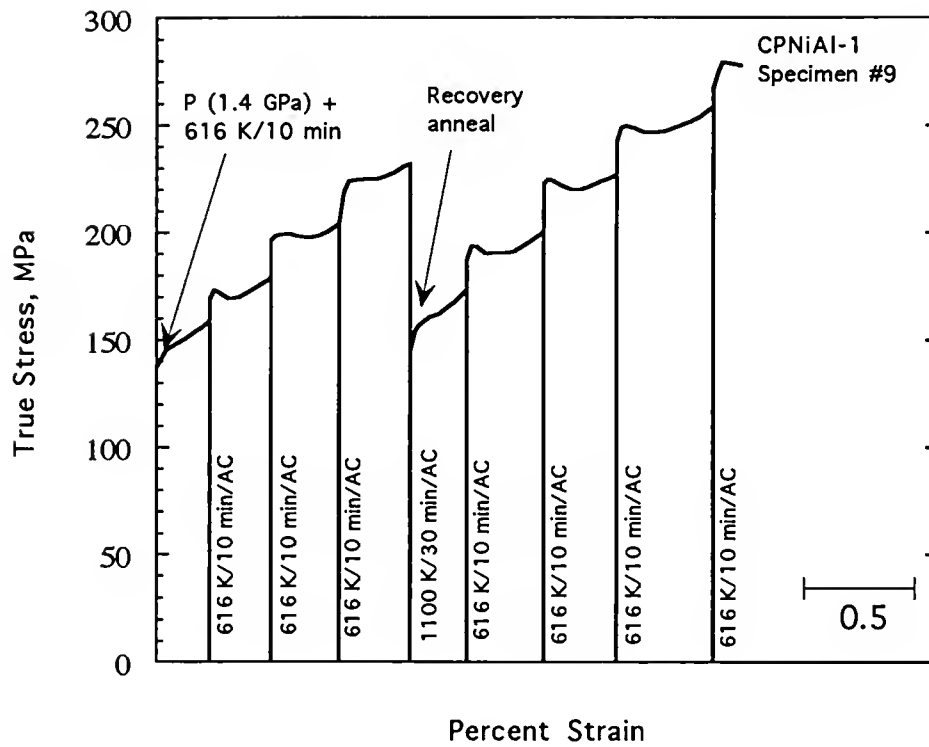
Figure 19.   Series of true stress-strain curves for CP-NiAl after multiple strain aging cycles.
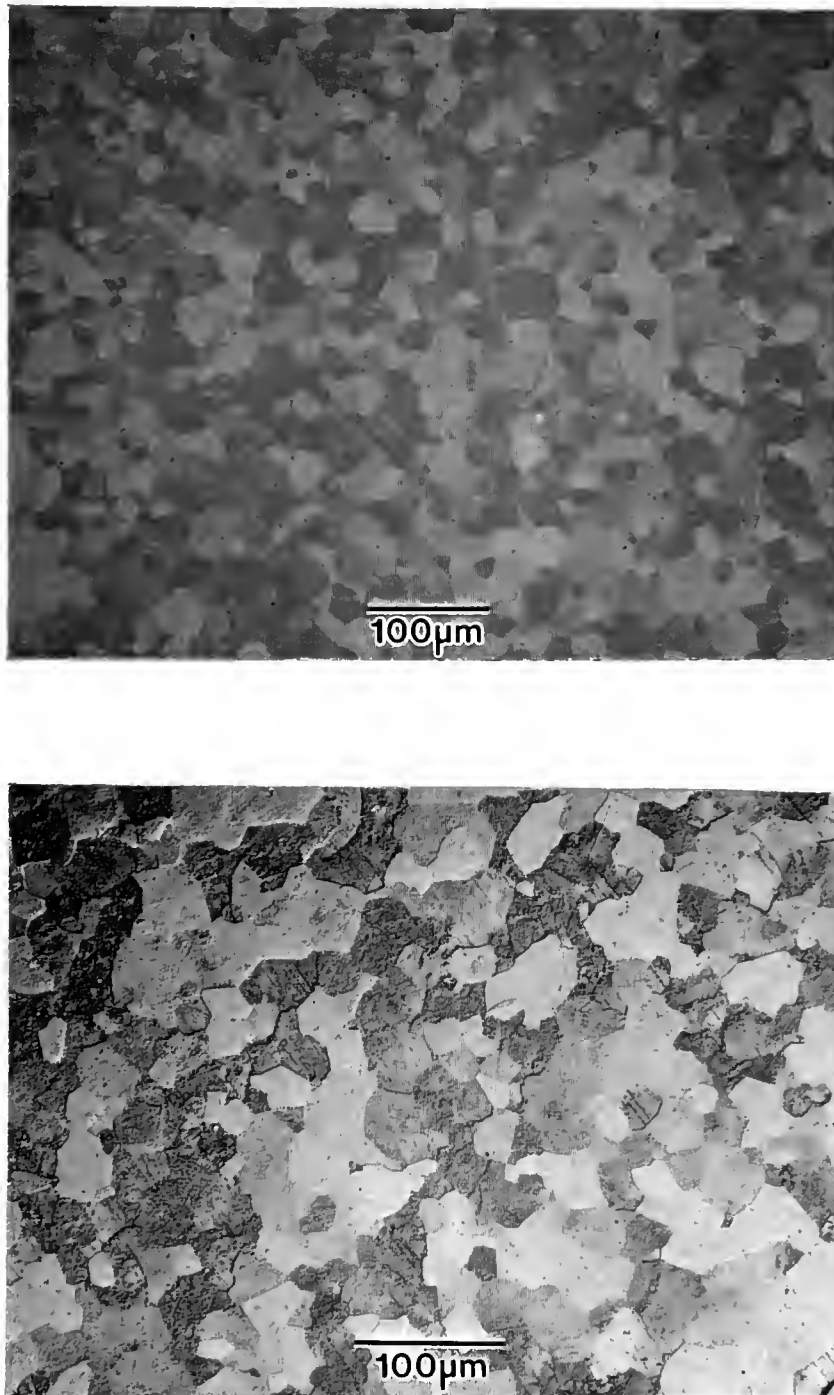
Figure 20.   Transverse sections of extruded material: (a) CPNiAl-1; (b) CPNiAl-2; (c) HPNiAl-C; (d) HP-NiAl; (e) NiAl-100C; (f) NiAl-300C; and (g) NiAl-N.
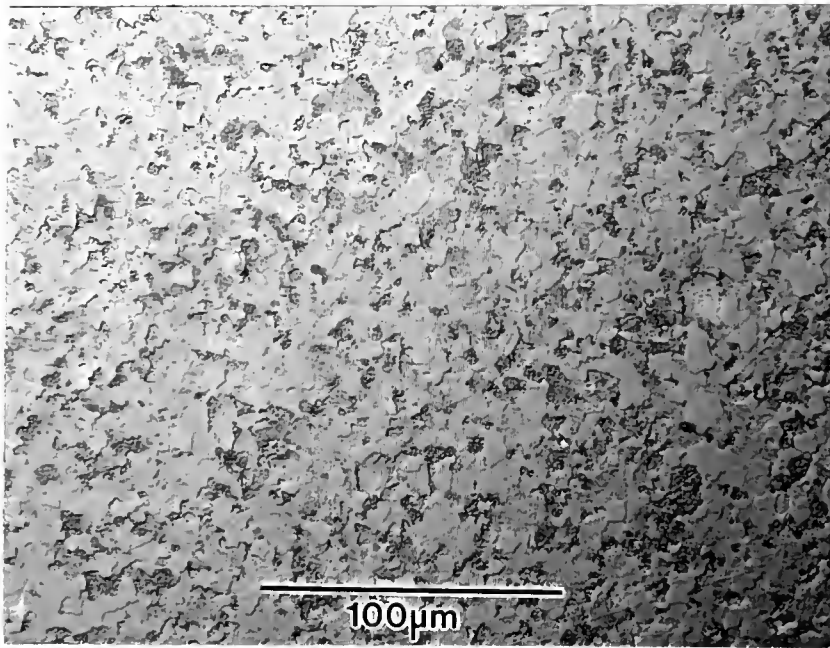
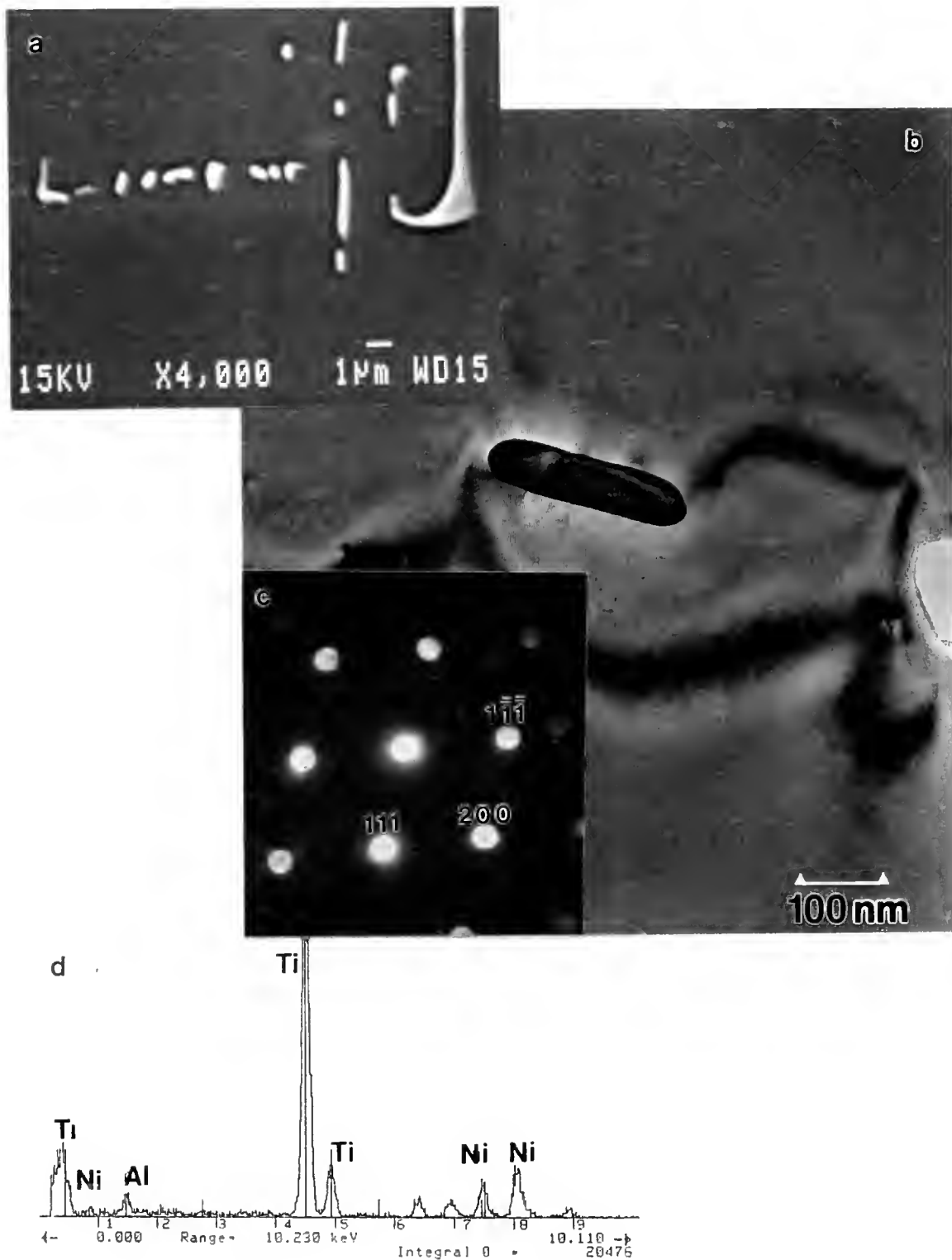Figure 20 -- continued

Figure 20 -- continued

Figure 20 -- continued

74
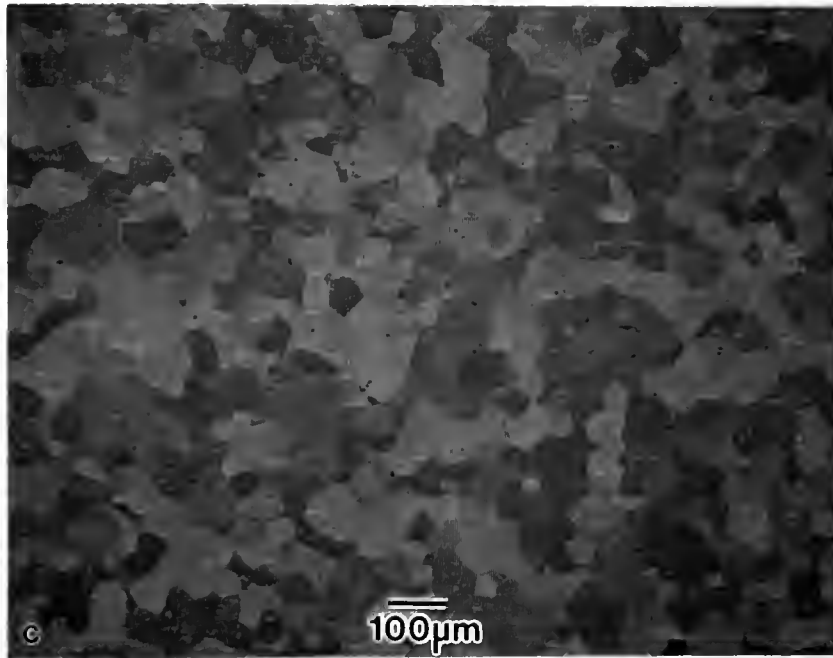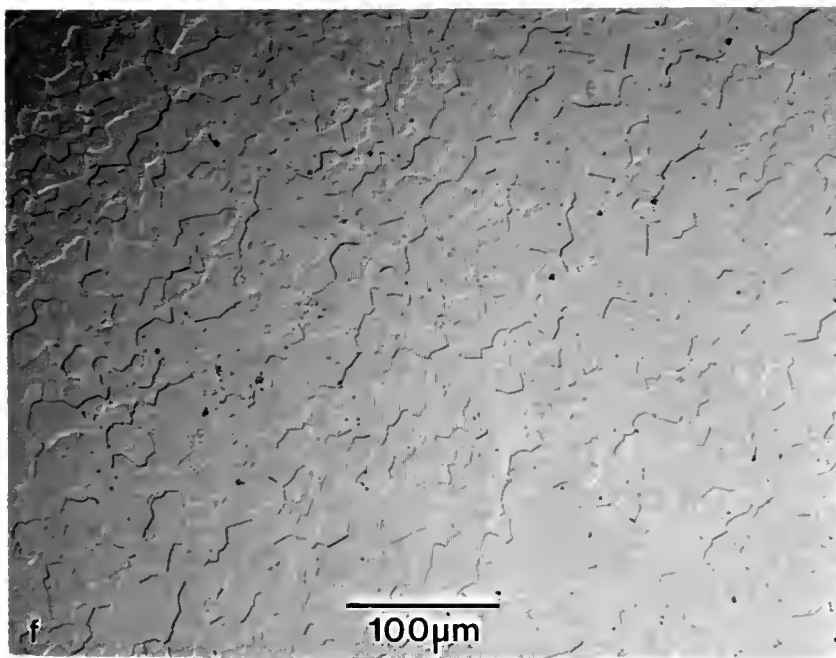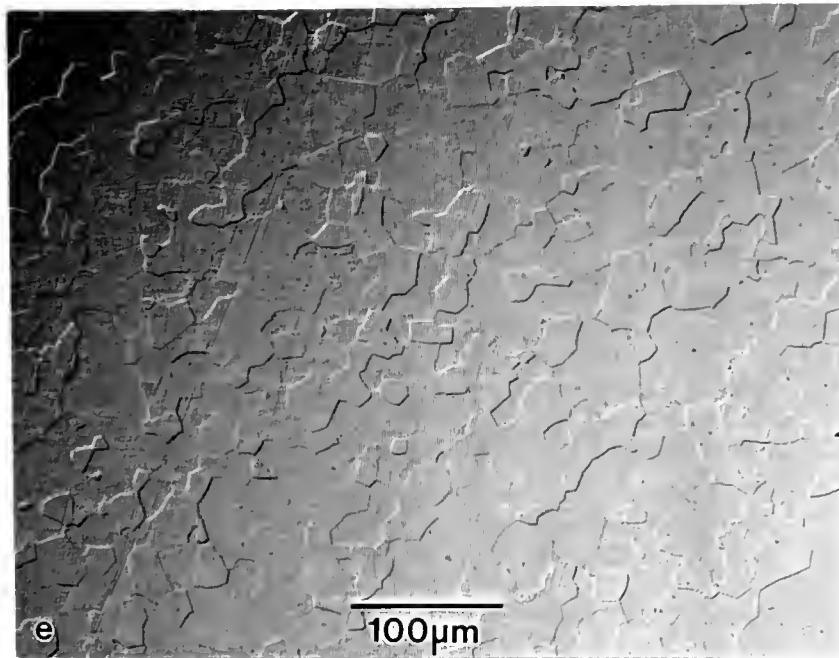
Figure 21. Stringers observed in NiAl-Ti: (a) Backscattered scanning electron micrograph of TiC stringers in NiAl-Ti; (b) BFTEM micrograph of a large TiC precipitate; (c) TEM microdiffraction pattern from the TiC precipitate ([01 $\bar{1}$] TiC zone axis); and (d) EDS spectra for the particle in (c) indicating the presence of Ti.
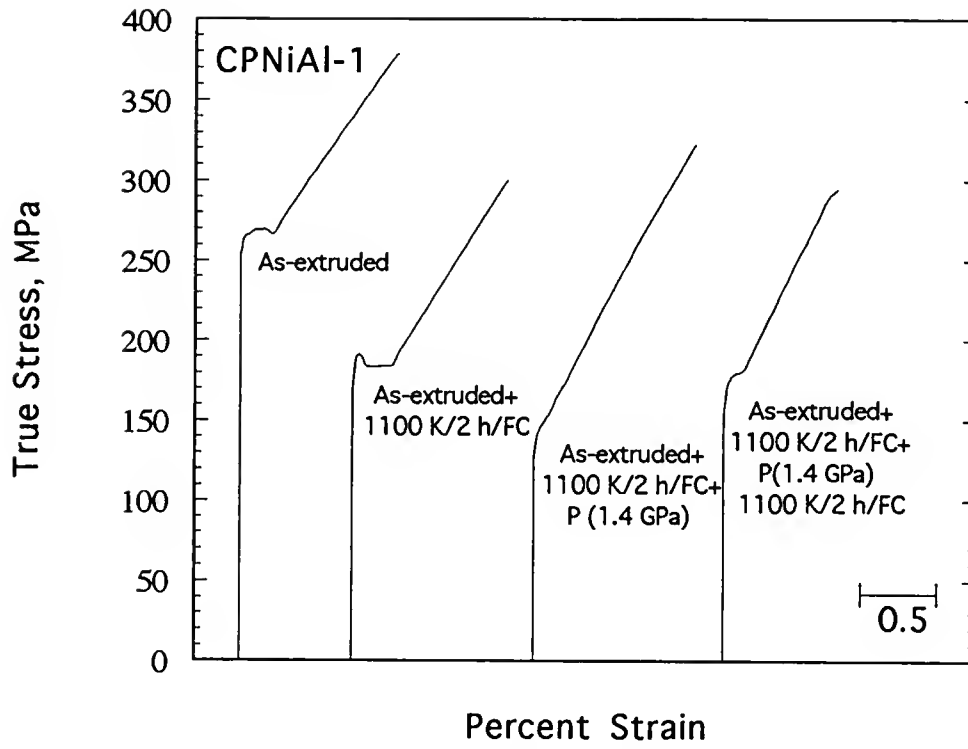
Figure 22.   Room-temperature tensile stress-strain curves for CPNiAl-1 in the as-extruded, annealed, pressurized and pressurized+annealed conditions.
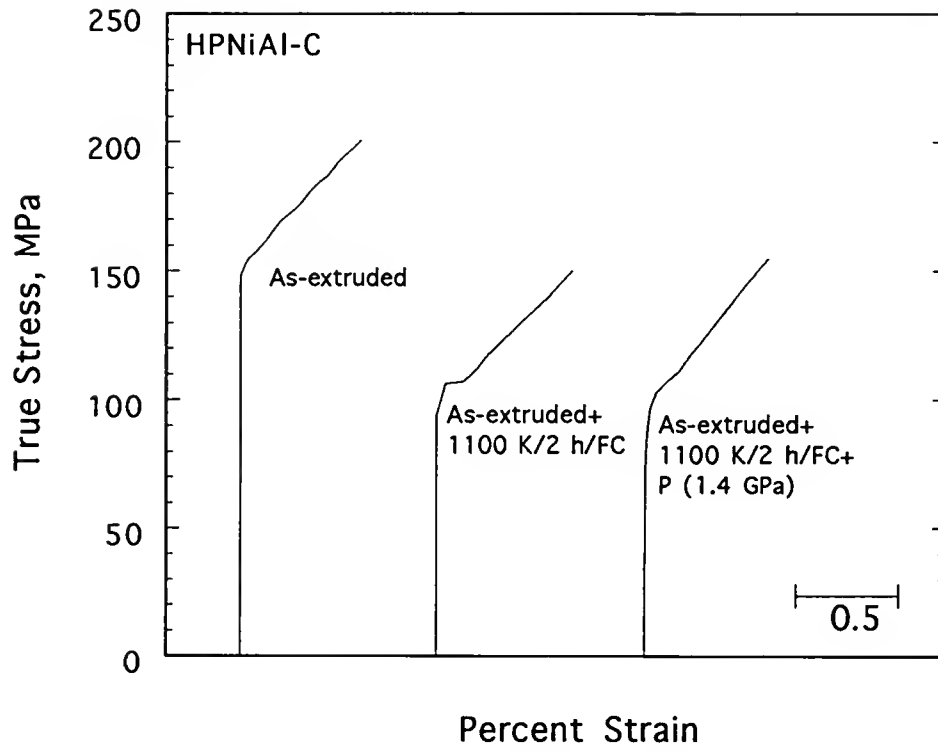
Figure 23. Room-temperature tensile stress-strain curves for HPNiAl-C in the as-extruded, annealed, and pressurized conditions.
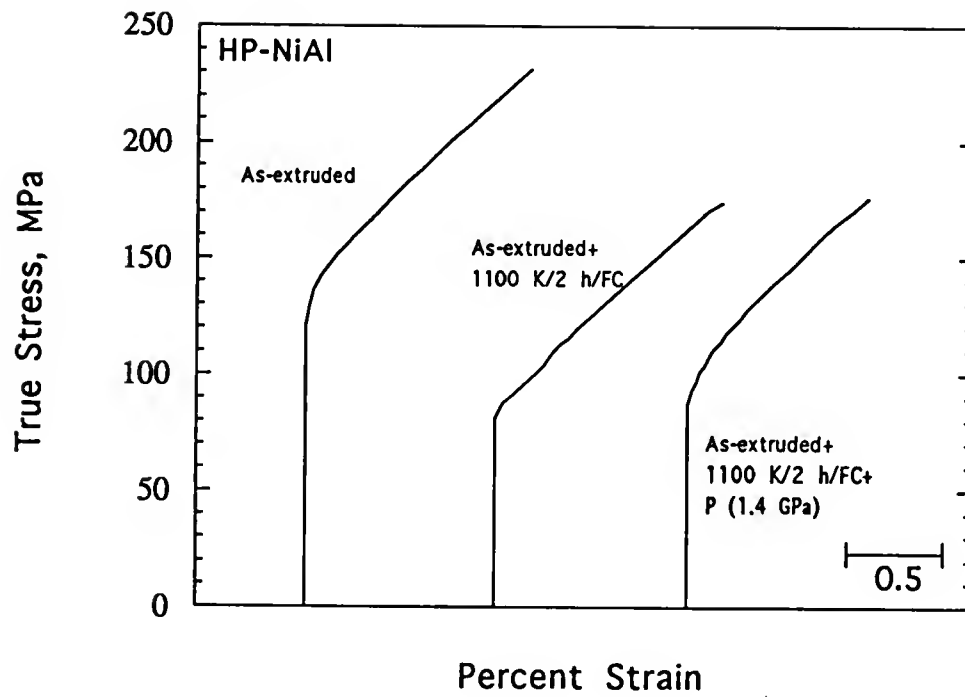
Figure 24. Room-temperature tensile stress-strain curves for HP-NiAl in the as-extruded, annealed, and pressurized conditions.
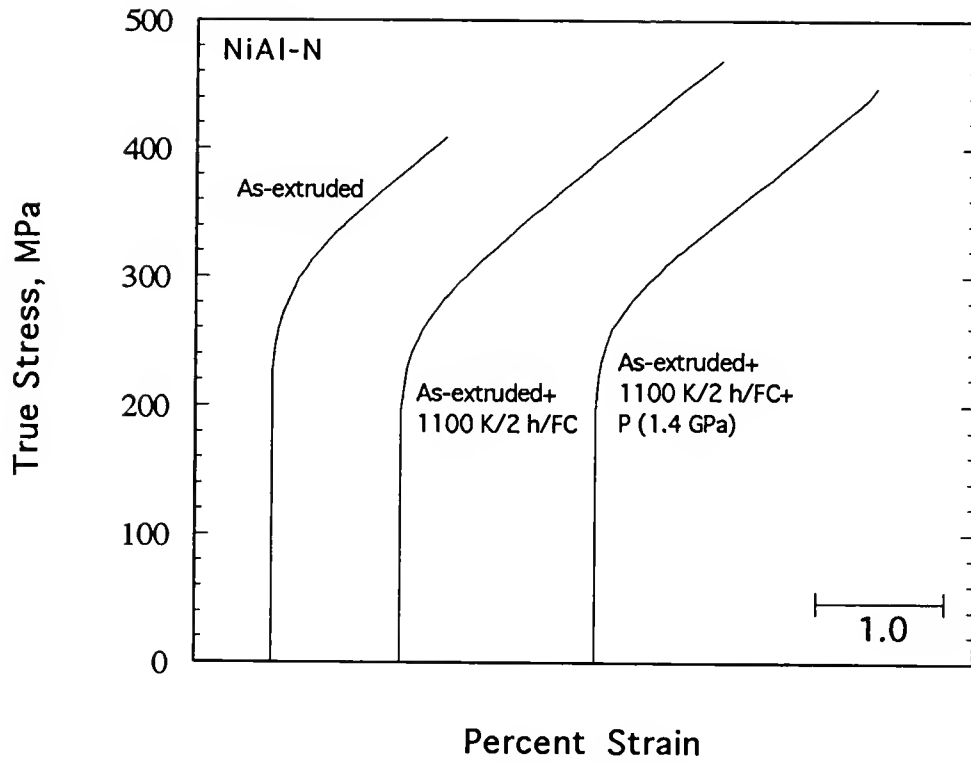
Figure 25. Room-temperature tensile stress-strain curves for NiAl-N in the as-extruded, annealed, and pressurized conditions
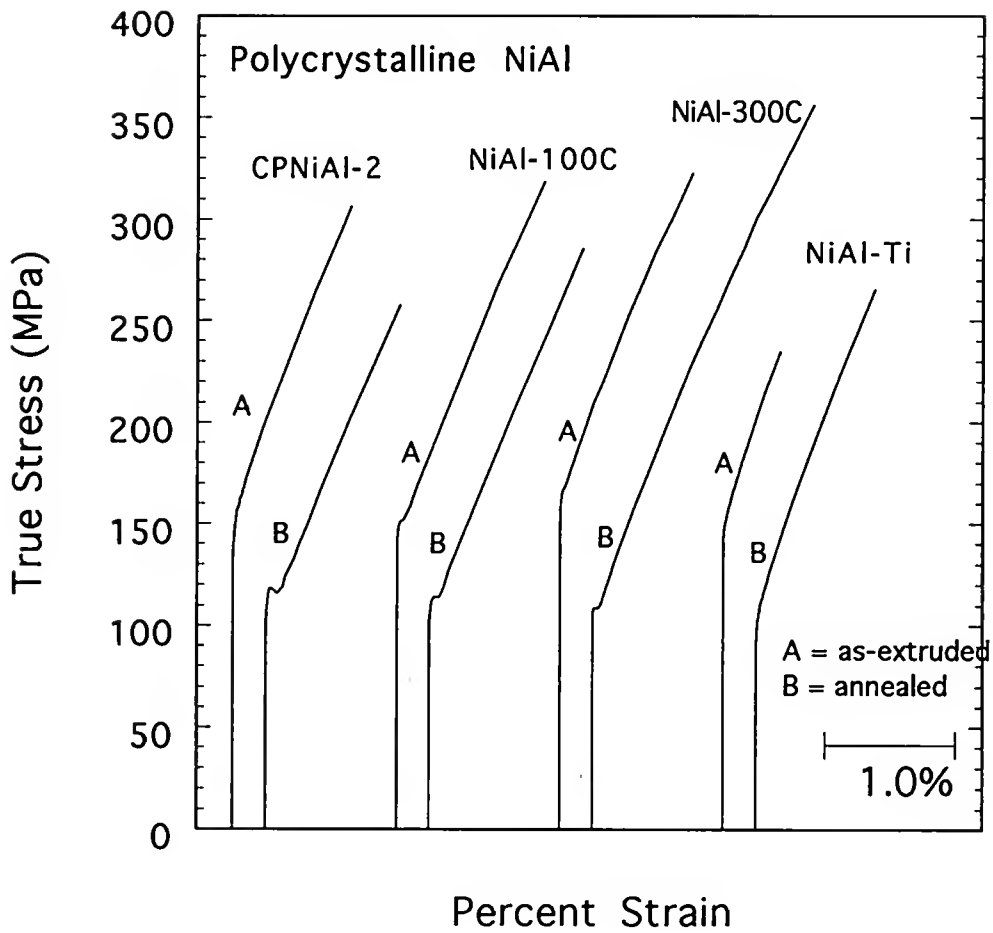
Figure 26.   Representative room-temperature tensile stress-strain curves for CPNiAl-2, NiAl-100C, NiAl-300C and NiAl-Ti
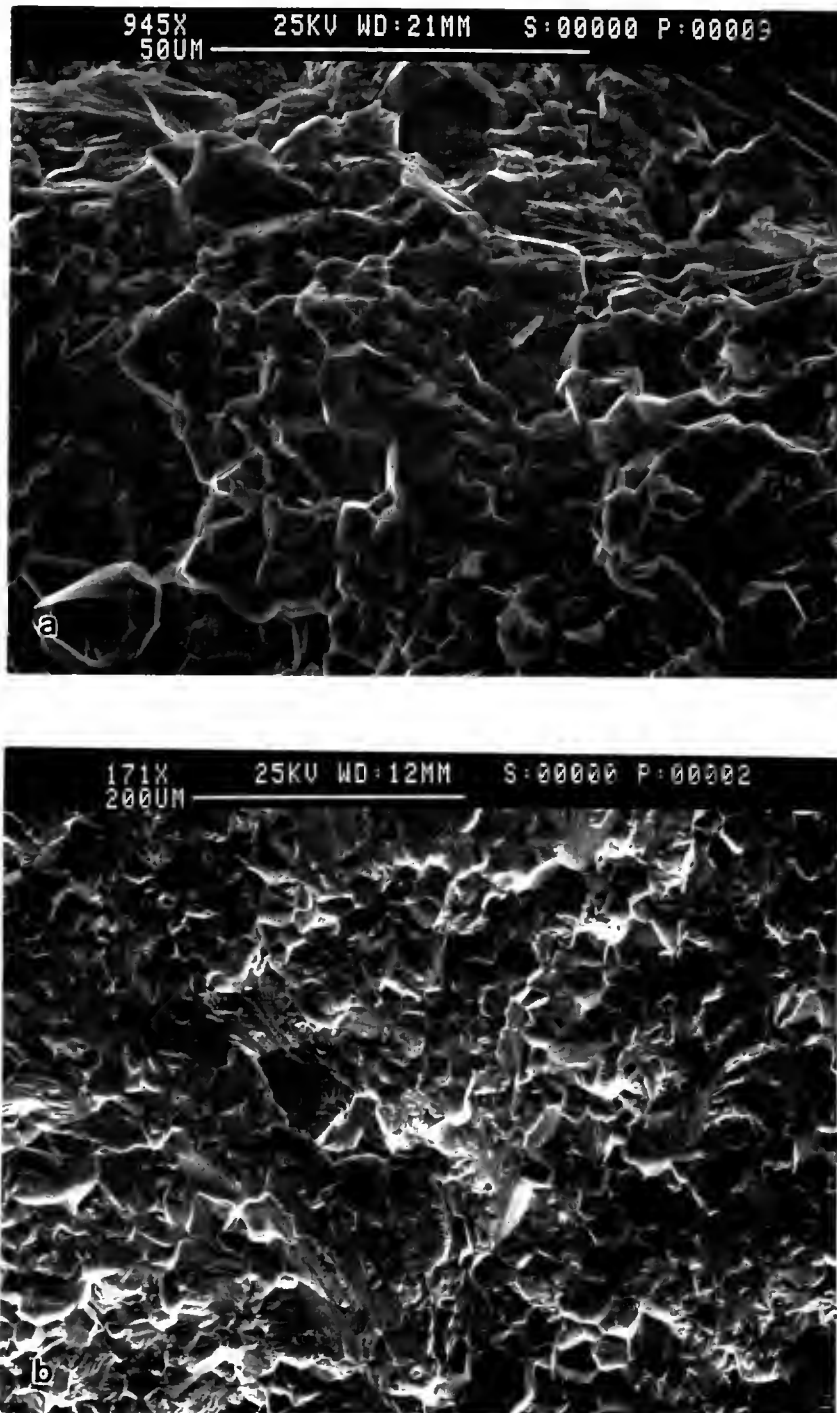
Figure 27.   Fracture surfaces of CPNiAl-1 samples tensile tested at room temperature: (a) as-extruded; (b) after annealing at 1100 K for 2 h followed by furnace cooling; (c) after annealing followed by subsequent pressurization.
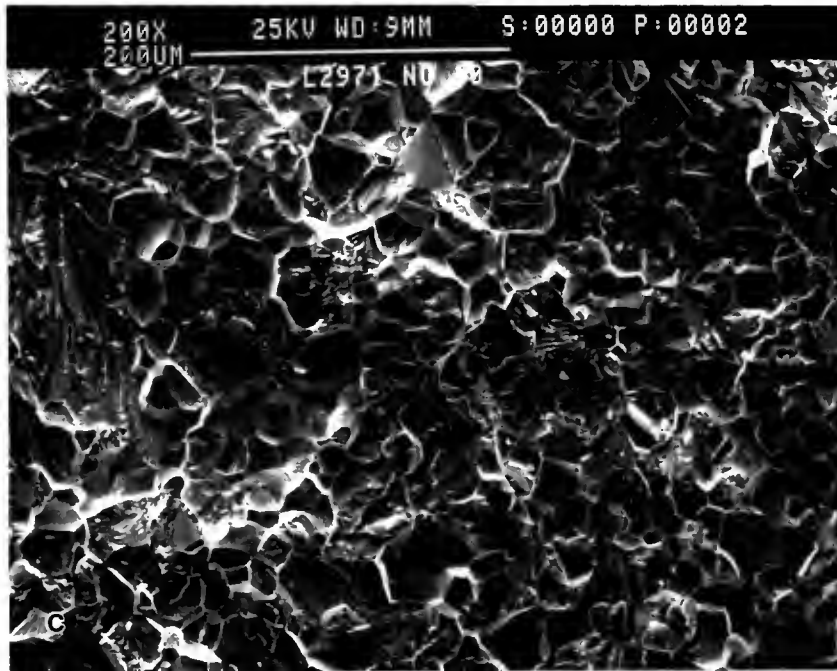
Figure 27 -- continued

Figure 28.   Fracture surfaces of HP-NiAl samples tensile tested at room temperature: (a) as-extruded; (b) after annealing at 1100 K for 2 h followed by furnace cooling; (c) after annealing followed by subsequent pressurization.

Figure 28 -- continued

Figure 29.   Fracture surfaces of NiAl-C samples tensile tested at room temperature: (a) as-extruded; (b) after annealing at 1100 K for 2 h followed by furnace cooling; (c) after annealing followed by subsequent pressurization.
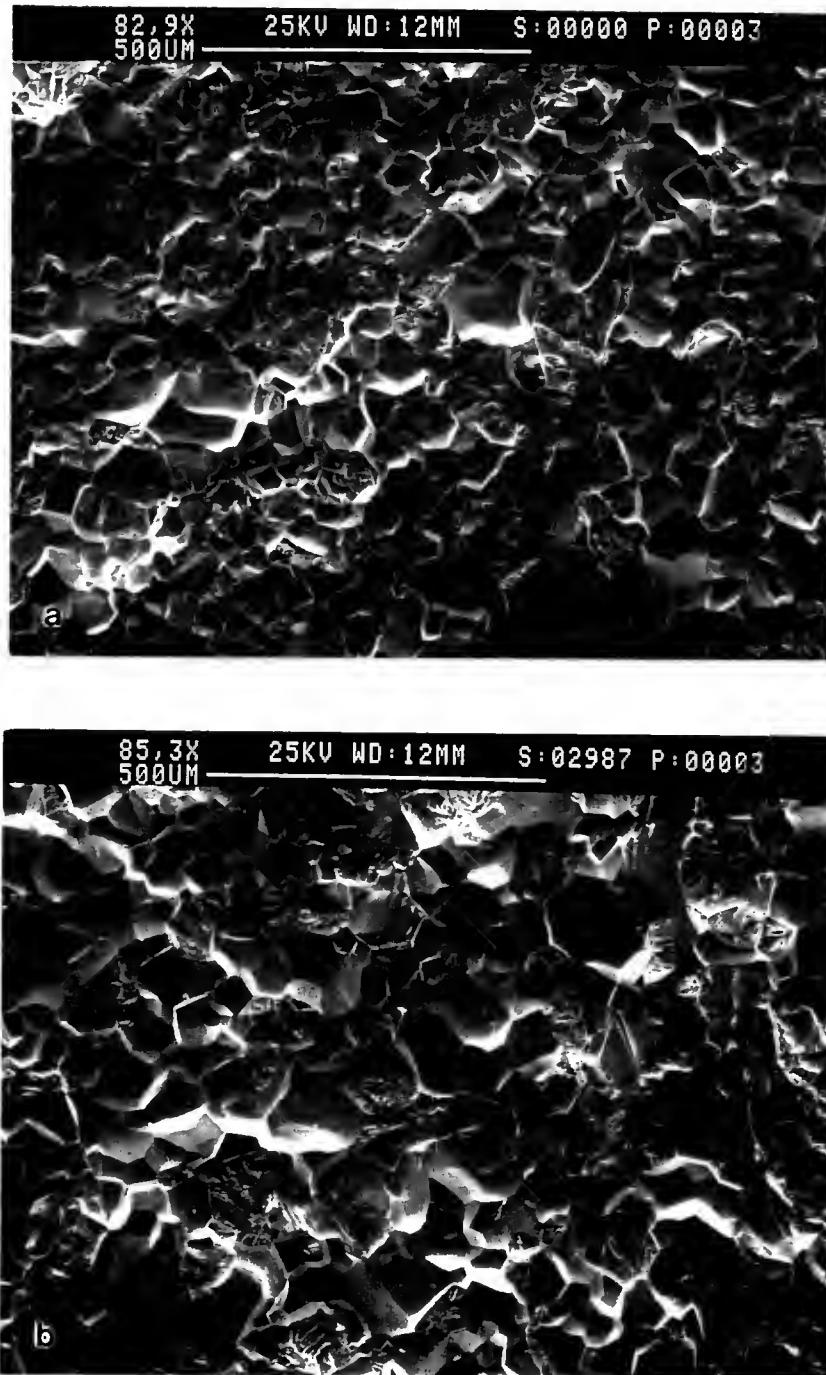
Figure 29 -- continued

Figure 30.   Fracture surfaces of NiAl-N samples tensile tested at room temperature: (a) as-extruded; (b) after annealing at 1100 K for 2 h followed by furnace cooling; (c) after annealing followed by subsequent pressurization.
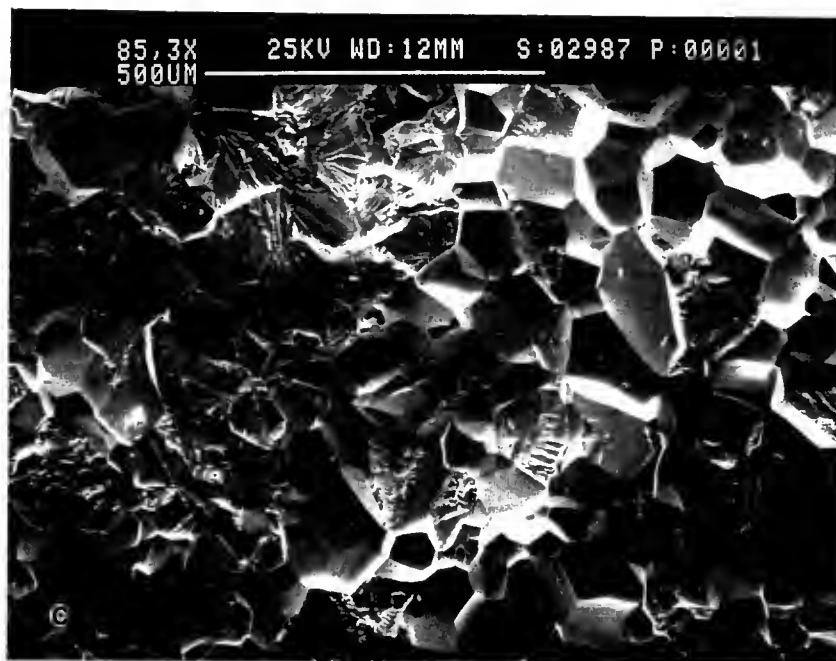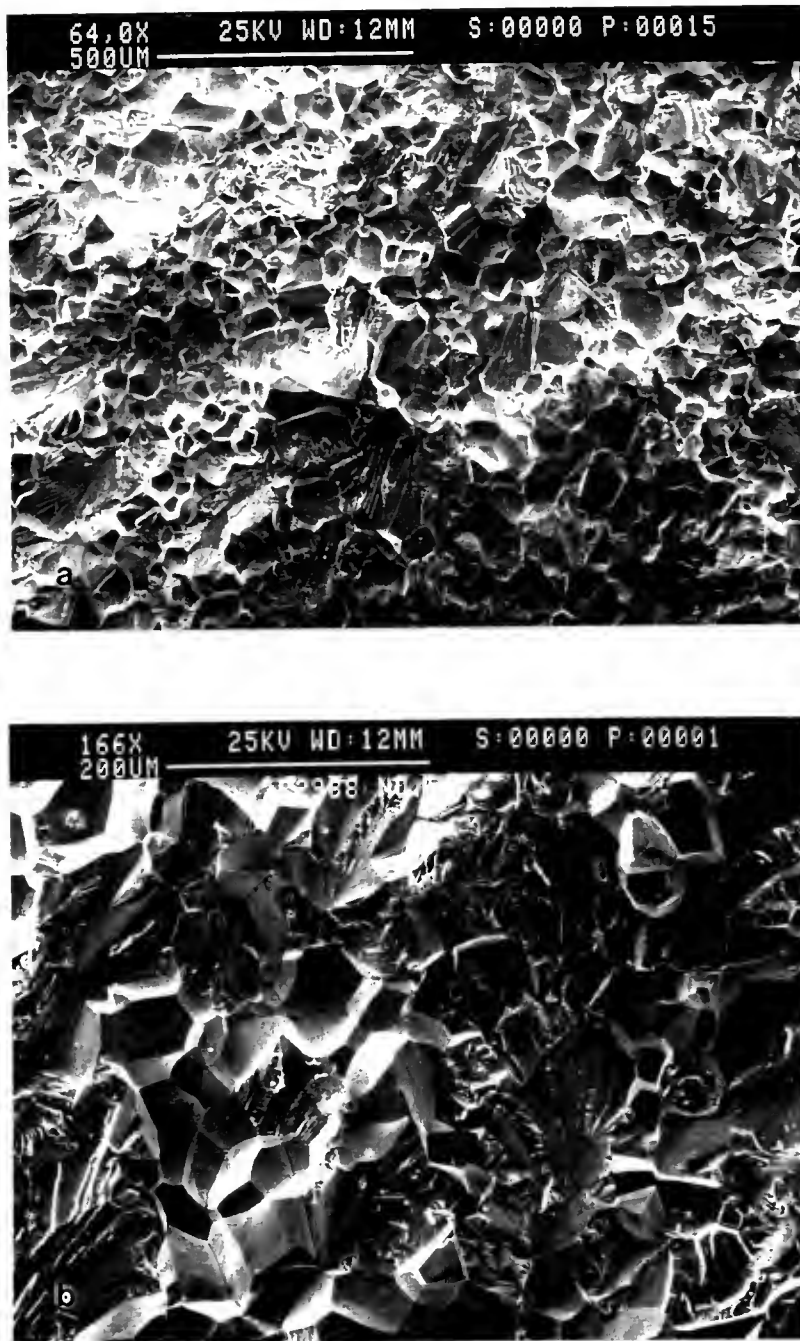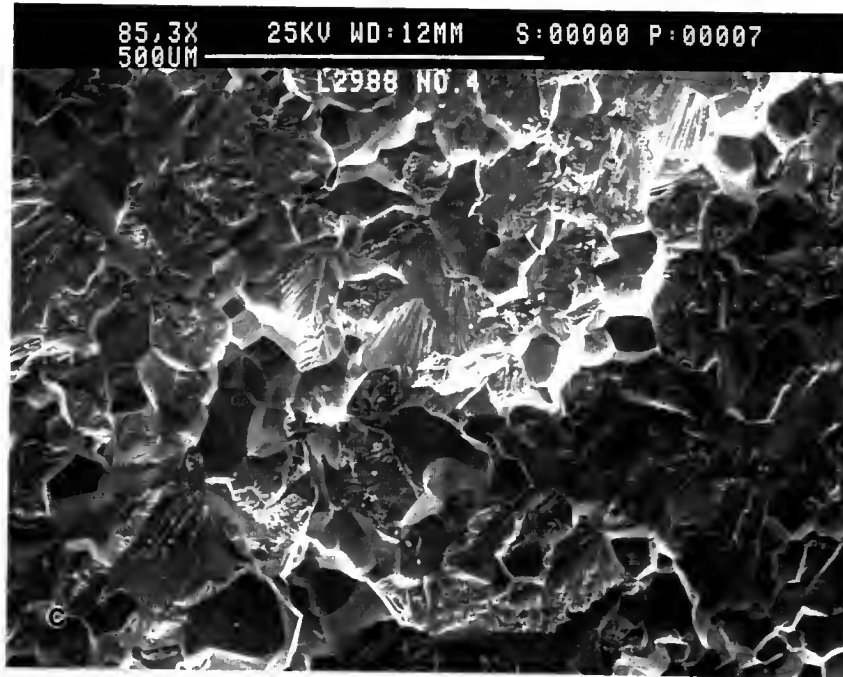
Figure 30 -- continued

Figure 31.   Fracture surfaces of CPNiAl-2 following tensile testing at room-temperature: (a) as-extruded and (b) after annealing at 1100 K for 2 h followed by furnace cooling.
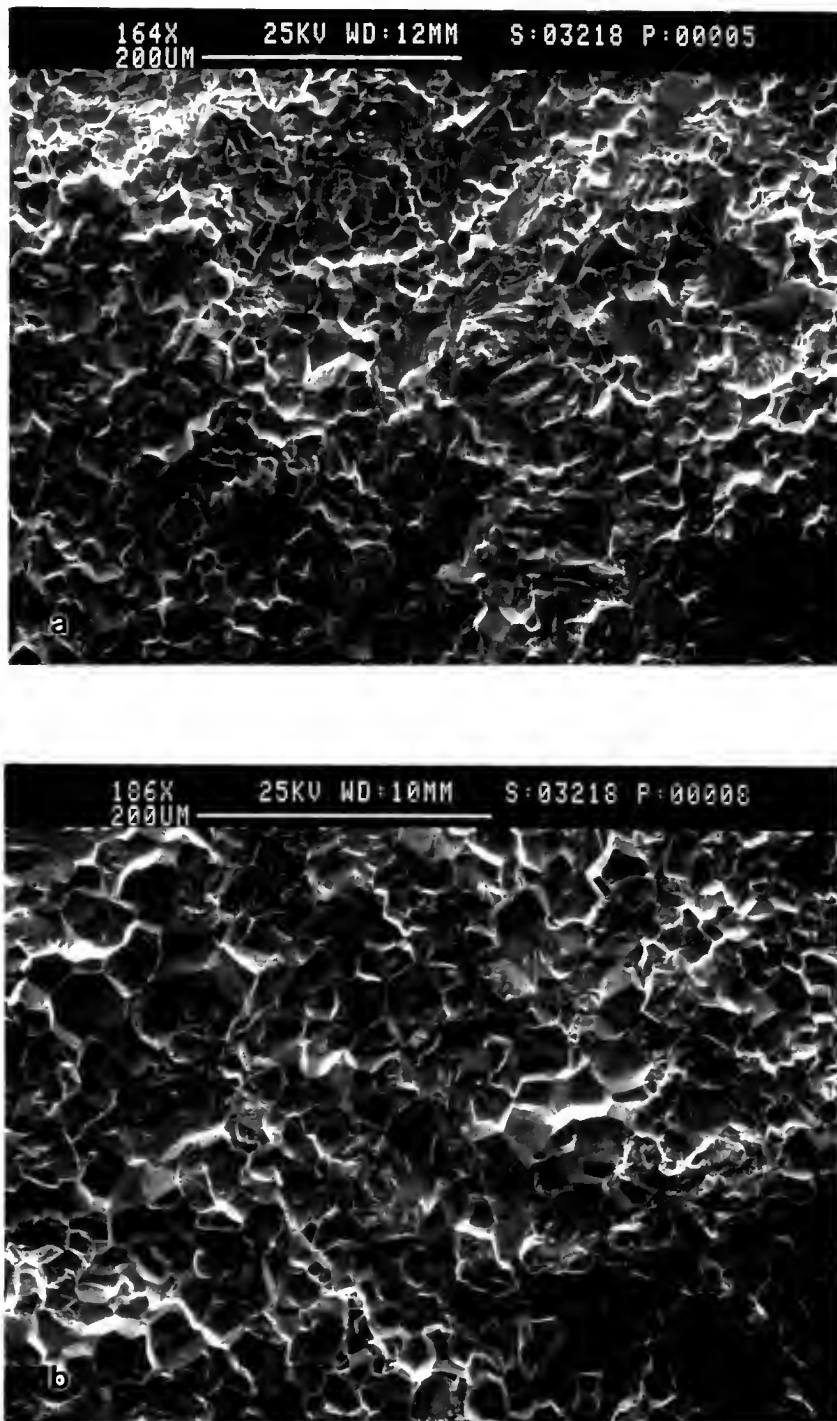
Figure 32.   Fracture surfaces of NiAl-100C following tensile testing at room-temperature: (a) as-extruded and (b) after annealing at 1100 K for 2 h followed by furnace cooling.
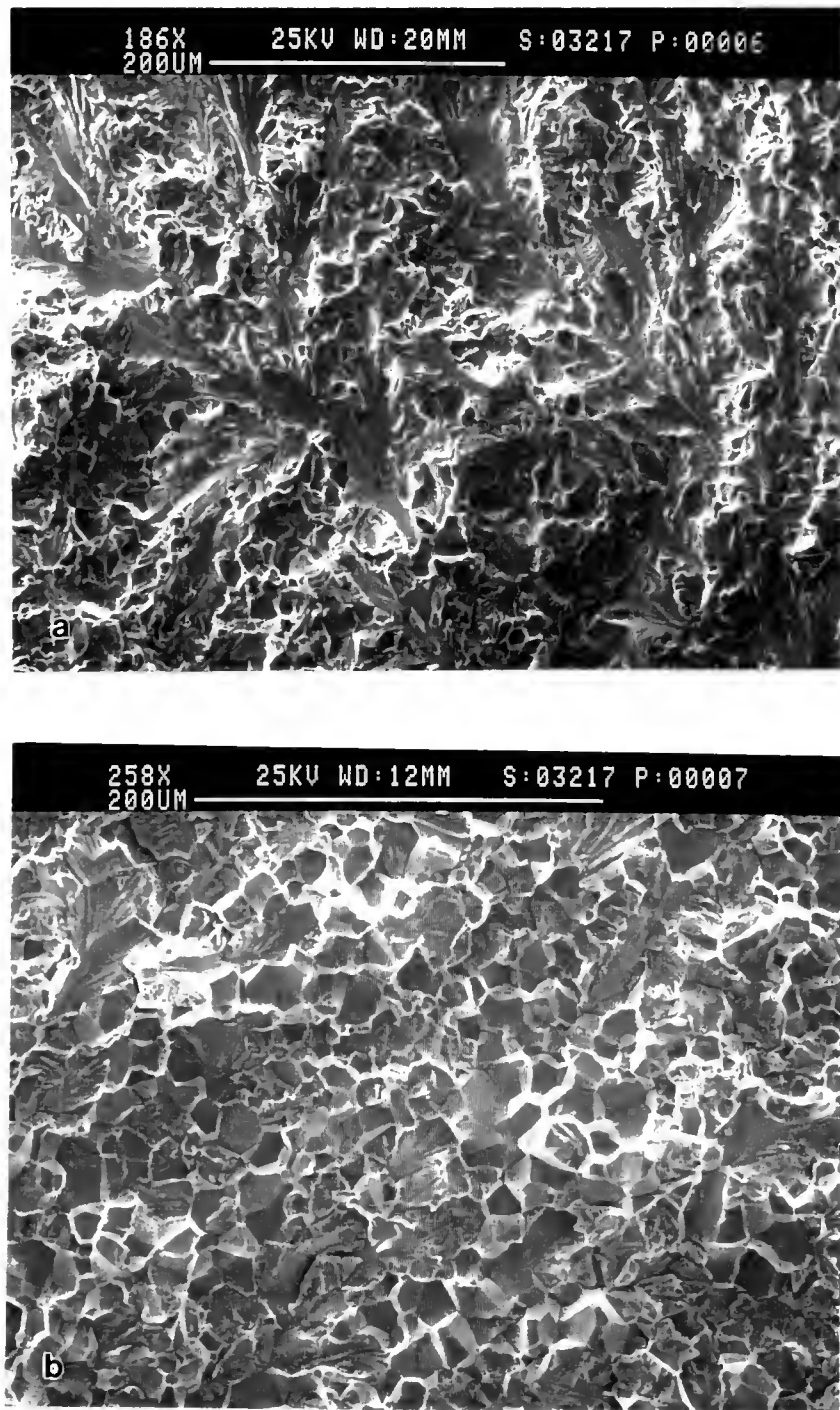
Figure 33.   Fracture surfaces of NiAl-300C following tensile testing at room-temperature: (a) as-extruded and (b) after annealing at 1100 K for 2 h followed by furnace cooling.
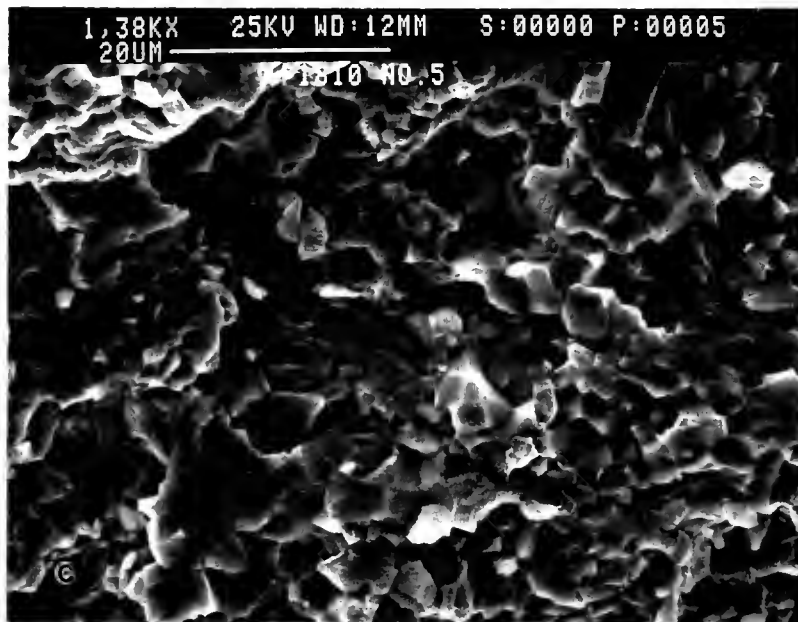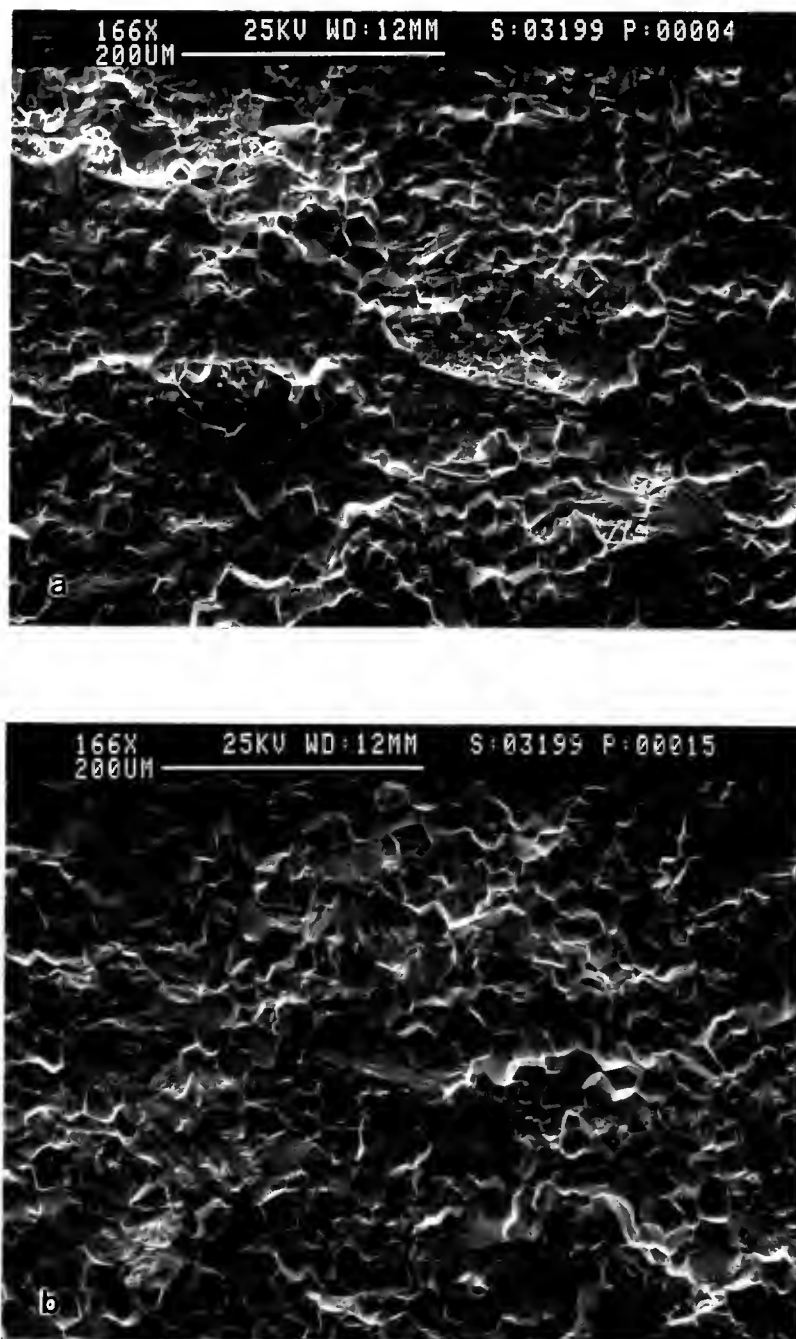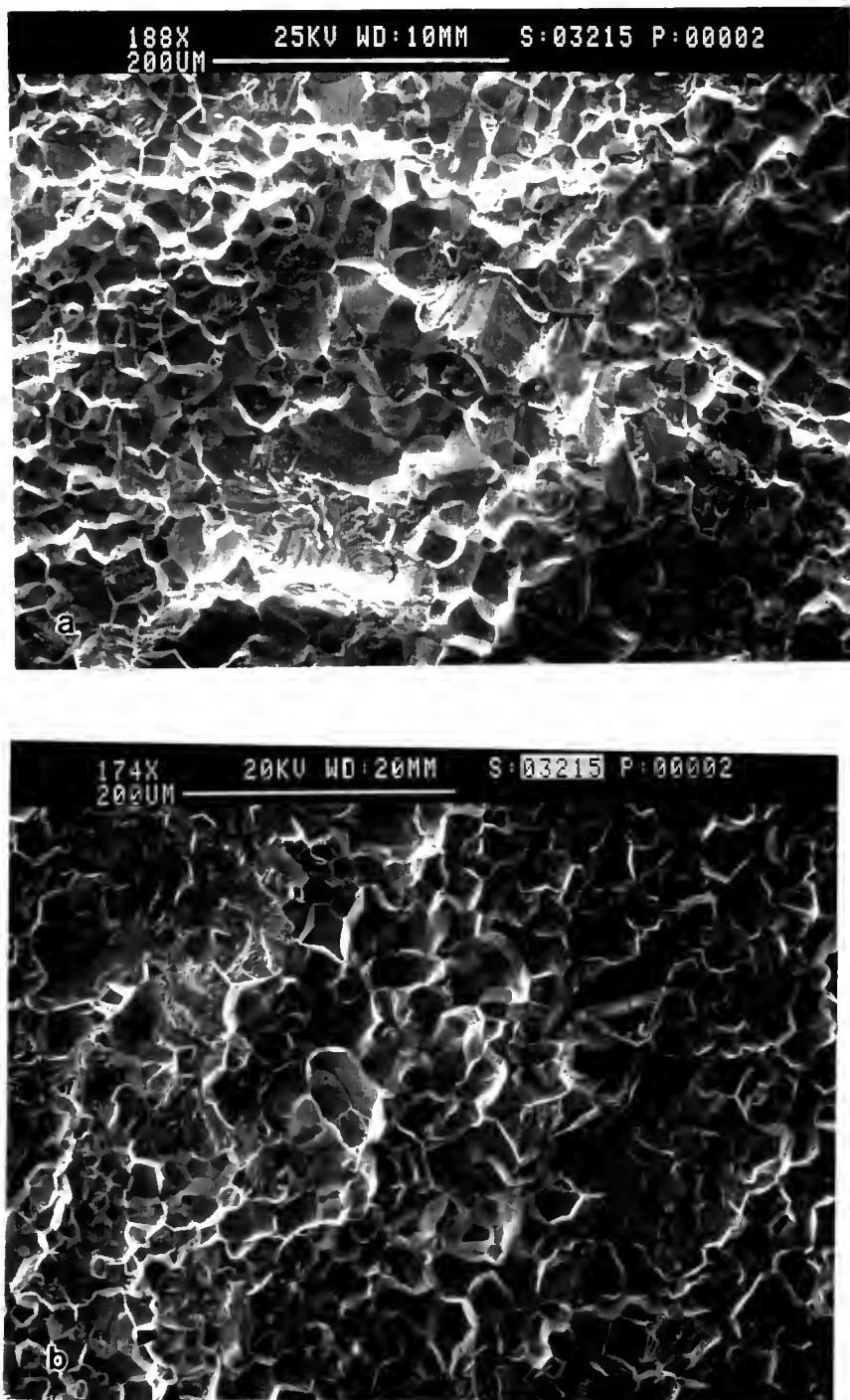
Figure 34.   Fracture surfaces of NiAl-Ti following tensile testing at room-temperature: (a) as-extruded and (b) after annealing at 1100 K for 2 h followed by furnace cooling.
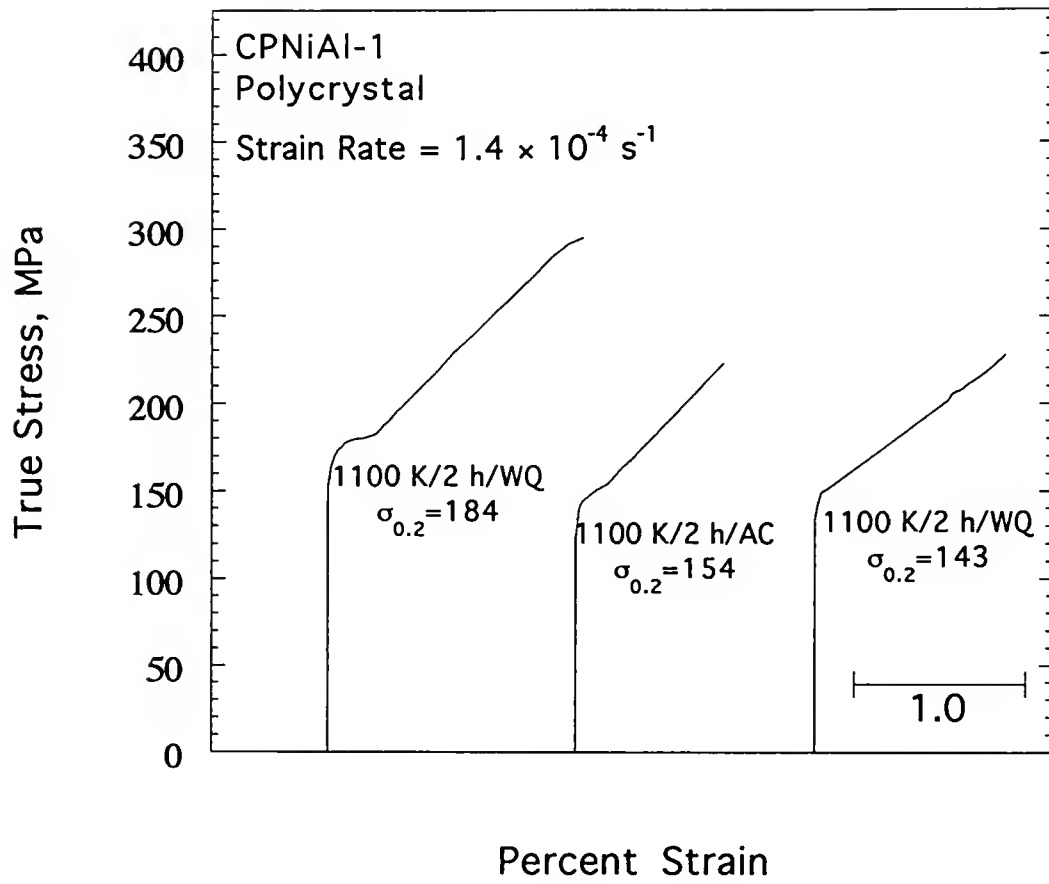
Figure 35.   Room-temperature stress-strain curves illustrating the influence of cooling rate on the tensile flow behavior of CP-NiAl.
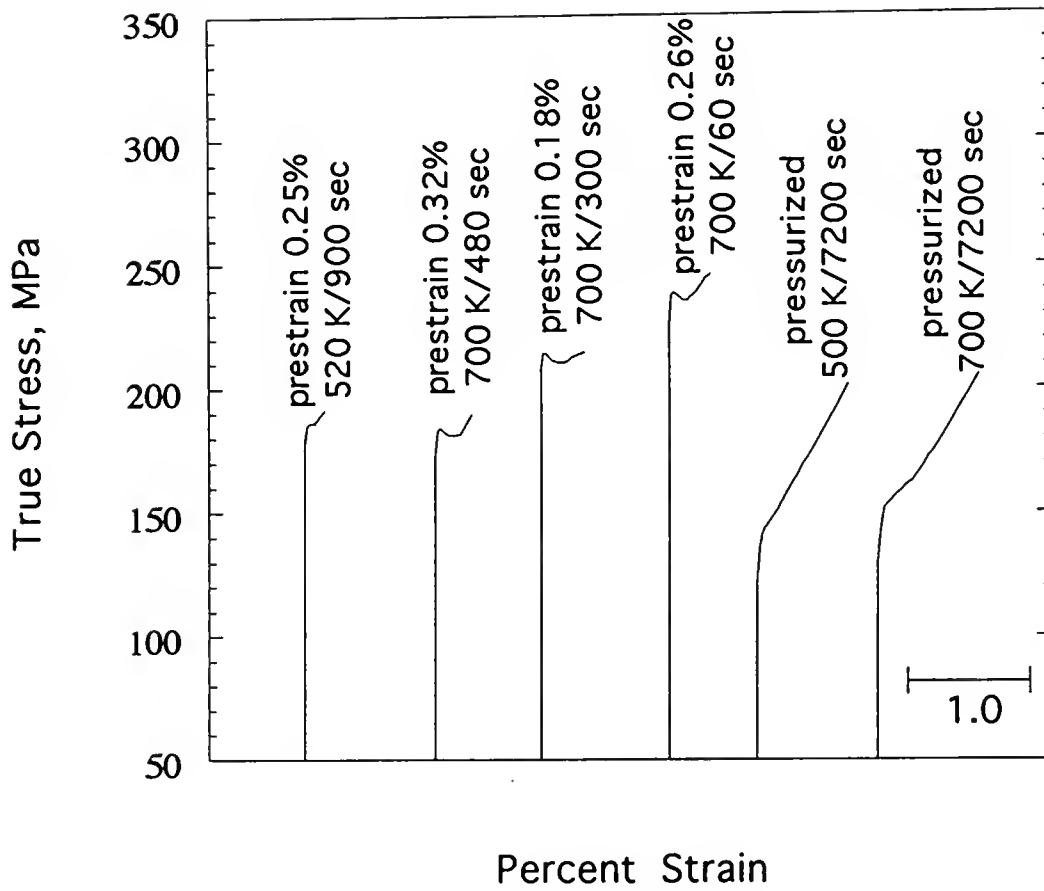
Figure 36.   Room-temperature stress-strain curves illustrating the influence of various prestraining and annealing treatments on the tensile flow behavior of CP-NiAl.
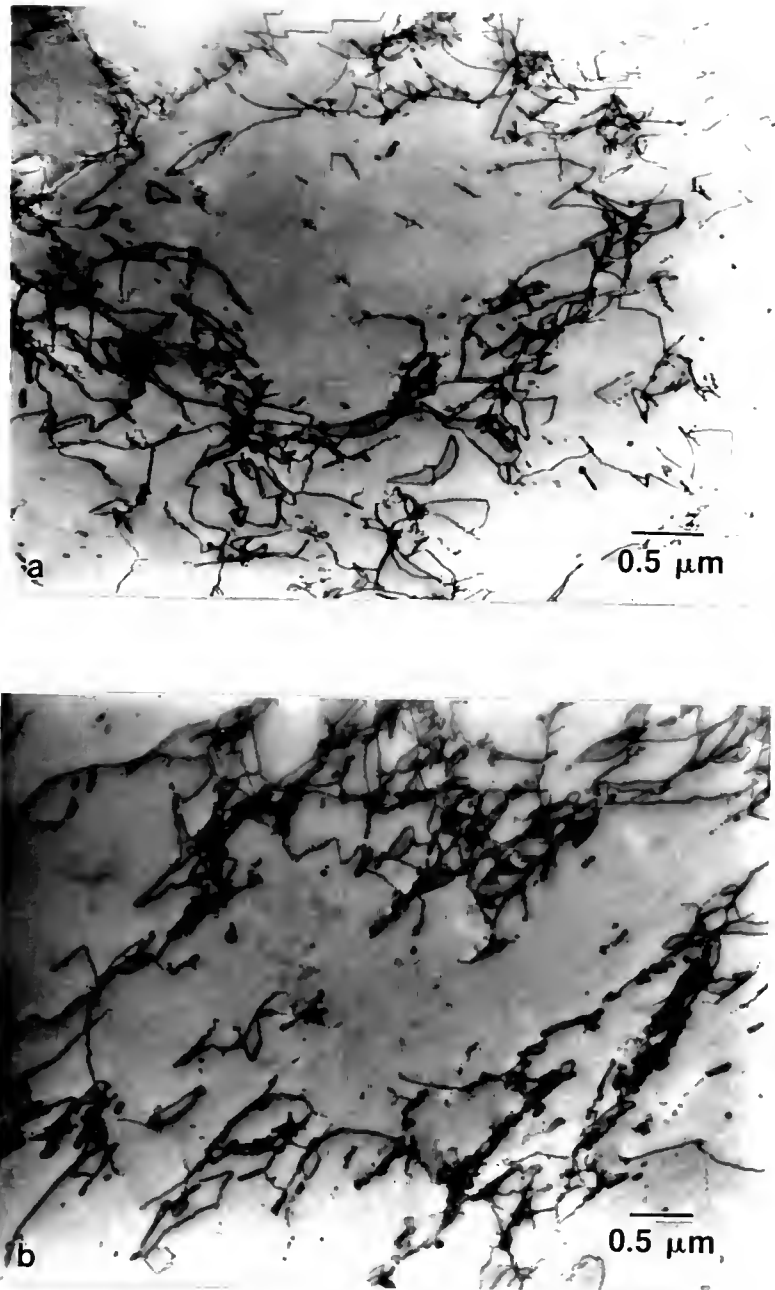
Figure 37.   Transmission electron micrographs of CPNiAl-1 and NiAl-N after uniaxial and hydrostatic prestraining at 300 K: (a) CPNiAl-1 prestrained uniaxially 0.05%; (b) CPNiAl-1 prestrained uniaxially 0.40%; (c) CPNiAl-1 prestrained uniaxially 2.04%; (d) schematic stress-strain curve showing stress-strain levels where specimens in (a)-(c) were taken from; (e) NiAl-N prestrained hydrostatically to 1.4 GPa.
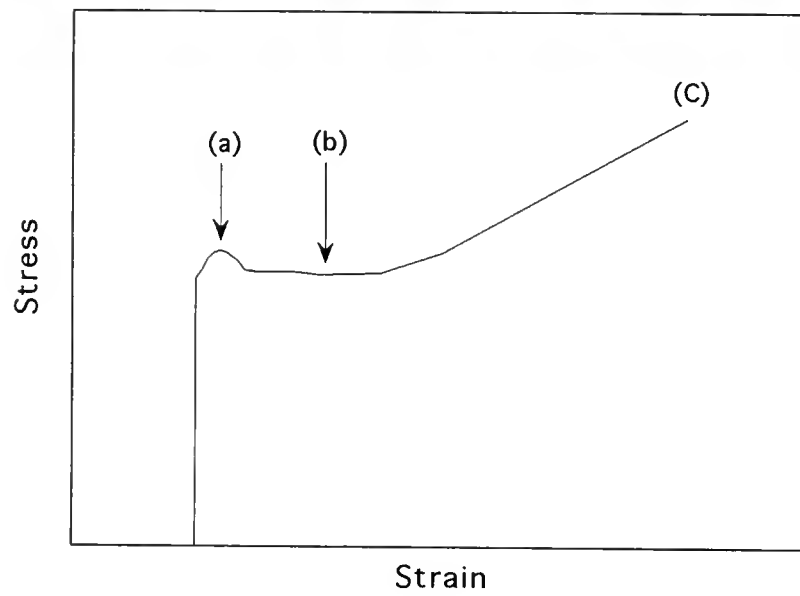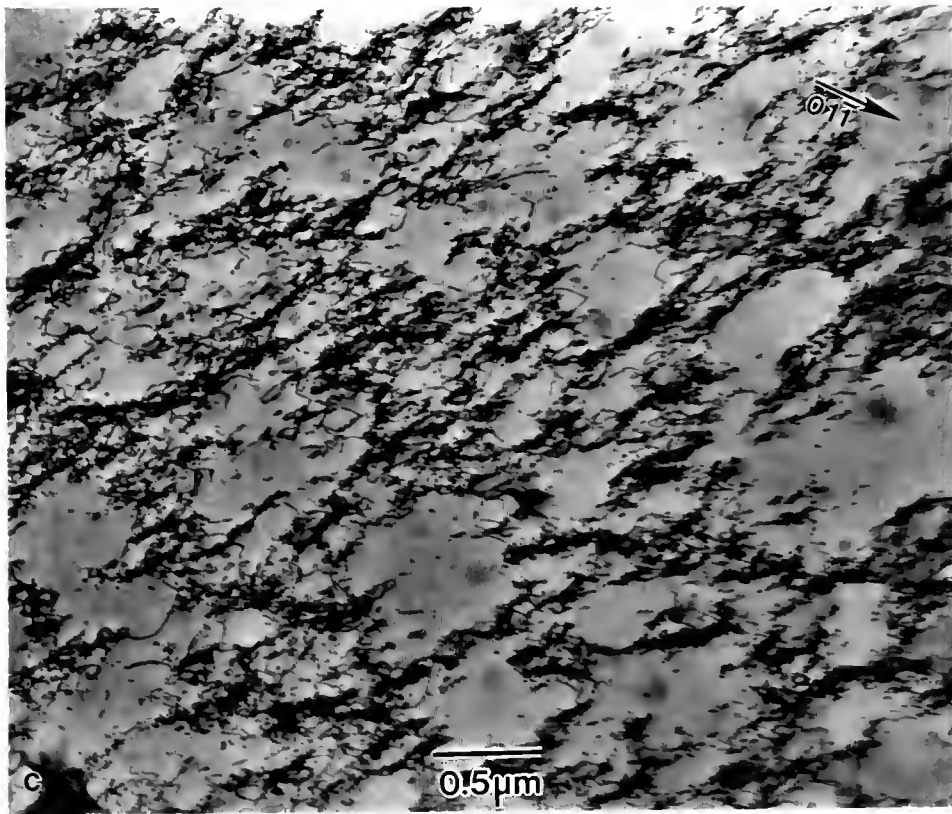
Figure 37 -- continued
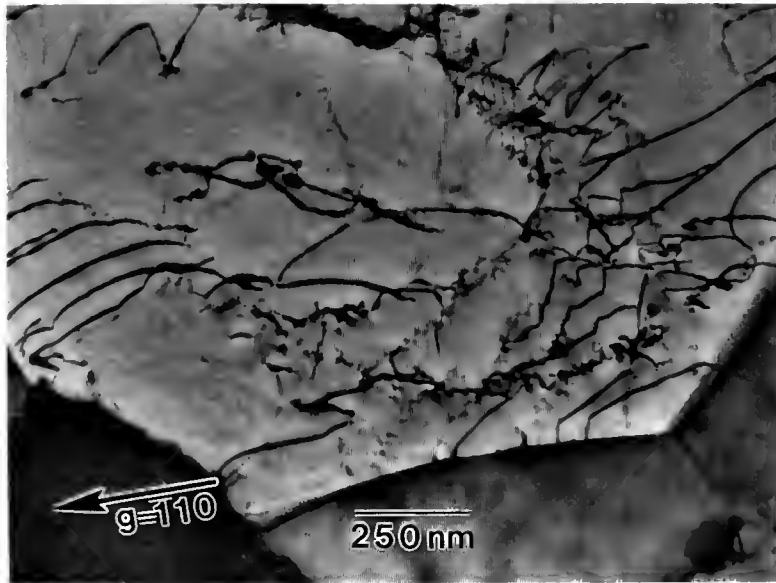
Figure 37 -- continued

CHAPTER 5
THE KINETICS OF STATIC STRAIN AGING IN POLYCRYSTALLINE NiAl-BASED ALLOYS

Introduction

It is generally accepted that BCC metals, in the presence of sufficient levels of interstitials, are subject to strain aging phenomenon caused by elastic interactions between interstitial atoms and dislocations. The specific mechanisms by which this behavior occurs may involve Snoek ordering [95,96], Cottrell aging [43], Suzuki locking [175], or precipitation on dislocations. In spite of the large number of papers dealing with strain aging, few discuss aspects of strain aging in ordered BCC alloys even though several manifestations of dynamic and static strain aging have been identified as playing a role in the deformation of polycrystalline and single crystal B2 intermetallic compounds.

In the intermetallic compounds AgMg, FeCo, FeAl, and NiAl, for example, the occurrences of sharp yield points and serrated stress-strain curves [15,22,23,26,28,29,33,133,134,164,165,167,176,177], strain rate sensitivity minima [12,27,178-180], yield stress plateaus as a function of temperature [18] and flow stress transients on changes in strain rate [139,166] have been reported. In addition, extensive work by Margevicius *et al.* [23,167-169] on NiAl has shown that a sharp yield point can be formed in binary NiAl following annealing at 1100 K and furnace cooling. This yield point can be removed by subsequent prestraining of the material by hydrostatic pressurization prior to testing and recovered by aging the prestrained material for 7200 s (*i.e.*, 2 h) at 673 K. Similarly, Pascoe and Newey [12] observed the formation of room temperature yield points in near stoichiometric NiAl annealed for 3600 s (1 hour) at 350 K following a uniaxial prestrain. Recent investigations of static [137,138] and dynamic [164] strain aging

97

have shown that observations of discontinuous yielding, in the form of yield points, yield plateaus and serrated yielding occurred in alloys containing high interstitial concentrations, particularly high carbon concentrations (see Chapter 4). These phenomena were not observed in low interstitial high purity, Ti-doped, or in nitrogen doped material (see Chapter 4) suggesting that strain aging in NiAl is the result of strong dislocation pinning by carbon atoms.

Despite these observations, no complete investigation of classical strain aging has been conducted on ordered BCC intermetallic alloys. Consequently, the purpose of this chapter is to describe the results of a detailed study of the kinetics of static strain aging in polycrystalline NiAl. Details of the influence of strain aging on the flow and fracture behavior of polycrystalline NiAl are provided in the previous chapter.

Experimental

Materials

The alloys used in this study were prepared by extrusion of (1) a nominally stoichiometric conventional purity induction melted ingot (CPNiAl-1) and (2) a carbon doped and zone leveled ingot (HPNiAl-C). The processing methods, chemistries and grain sizes are described in the previous chapter. The as-extruded microstructures were fully dense consisting of recrystallized and equiaxed grains.

Chemical analyses of the extruded materials were conducted at the NASA-Lewis Research Center by the following techniques deemed to be the most accurate for the particular elements. Ni and Al were determined using analytical wet chemistry/titration techniques and Si was determined by inductively coupled plasma atomic emission spectroscopy. Oxygen, nitrogen, carbon and sulfur contents were determined by combustion techniques using LECO oxygen/nitrogen and carbon/sulfur determinators. A

table containing the chemical analyses and additional details concerning materials processing and the chemical analysis techniques are presented in Chapter 4.

Round button-head tensile specimens were ground from the extruded rods so that the gage lengths of the samples were parallel to the extrusion direction. Sample dimensions were 3.1 mm for the tensile gage diameters and 30.0 mm for the tensile gage lengths. Prior to testing, all samples were electropolished in a 10% perchloric acid-90% methanol solution that was cooled to 208 K.

Mechanical Testing

Tensile tests were performed on an Instron Model 1125 load frame at a constant crosshead velocity corresponding to an initial strain rate of 1.4×10^{-4} s^{-1}. True stress-strain data were calculated from the load-time plots. All tests were performed in air at 300 K.

The kinetics of strain aging were investigated using the classic yield point return technique. Testing was conducted in two steps: (1) Initially, tensile specimens in the as-extruded condition were prestrained approximately 0.2%, unloaded to a stress of approximately 2 MPa, aged *in situ* on the load frame for aging times varying between 60 s and 113,000 s (30 hours), and then tested in tension at room temperature. This test method allows specimen alignment to be maintained and the stress level to be kept effectively constant during aging. After aging, the specimens were cooled by removing the furnace from the test frame and passing a forced stream of ambient air over the specimen and the tensile grips. This method of cooling resulted in average temperature drops of 500 to 1000 K during the first minute of cooling. The parameters generally used to evaluate the kinetics of strain aging are illustrated in Figure 38. These include the upper yield stress increment $\Delta\sigma_u = \sigma_u - \sigma_a$, the lower yield stress increment $\Delta\sigma_L = \sigma_L - \sigma_a$, and the Lüders strain ε_L, however, in this study the upper yield stress increment was used as the primary measurement of strain aging. (2) Single specimens were often aged several times to obtain

a $\Delta\sigma_u$-time relationship. A specimen previously tested or prestrained uniaxially was given a recovery anneal, typically 1100 K/1800 s (30 min.) /AC, prestrained approximately 0.2%, aged *in situ* and re-tested at room temperature. A typical series of stress-strain curves illustrating this procedure are shown in Figure 39. When this type of testing is adopted, the yield point exhibited during the original deformation of the material can be recovered as can the yield point increment observed during the previous test. This means that it is possible to recover the dislocation structure and obtain a reproducible $\Delta\sigma_u$ following the same strain aging (*i.e.* prestrain + annealing) treatment, justifying the use of multiple deformation experiments on single samples.

Results

Figure 40 shows the influence of prior strain on the resulting yield stress increment, $\Delta\sigma_u$, after aging of the CPNiAl-1 at 616 K. Increasing the amount of prior strain in samples aged at 616 K for 600 s, for example, leads initially to a rapid increase in $\Delta\sigma_u$ followed by an apparent plateau at prestrains exceeding 0.5%. Strain dependence of this type, which has been classified as type S by Kubin *et al.* [99], is commonly observed in BCC alloys and is often associated with elastic interactions between dislocations and solute atoms.

The time dependence, t, of $\Delta\sigma_u$ for the CP material is shown in Figure 41. The data is summarized in Table 5. The shapes of the aging curves up to the maximum value of $\Delta\sigma_u$ are comparable to similar curves reported for BCC metals [94]. Under type S conditions [99], $\Delta\sigma_u$ will increase proportionally with $t^{2/3}$ during the early stages of aging, assuming $\Delta\sigma_u$ is proportional to the amount of solute segregating to dislocations. At longer times, the dislocations will become saturated with solute leading to a plateau in $\Delta\sigma_u$ or even to a decrease in $\Delta\sigma_u$ due to precipitation. The strain aging time exponent, as determined by least squares analysis of the data prior to saturation in Figure 41, is in the range 0.57 to 0.67, which is close to the theoretical value of 2/3 predicted by Cottrell and

Bilby [43]. In confirmation of this result, $\Delta\sigma_u$ is plotted versus $t^{2/3}$ in Figure 42 demonstrating the satisfactory fit. Although experiments were only performed at 610 K for HPNiAl-C, a similar trend of higher $\Delta\sigma_u$ with increasing aging time was observed (Figure 43 and Table 6). In addition, the time exponent was found to be 0.59 in agreement with the observations for CP-NiAl.

Table 5. The temperature dependence of the yield stress increment for CPNiAl-1.

Aging Temperature, K	Aging Time, s	Yield Stress Increment, MPa
520	300	2.00
520	3,600	9.64
520	7,200	13.84
520	9,000	12.86
520	10,800	17.58
520	19,800	17.48
520	23,400	17.21
520	113,400	19.45
616	300	7.78
616	600	14.04
616	600	14.53
616	600	14.47
616	1,020	20.42
616	1,800	21.57
616	2,700	21.63
616	3,600	28.09
616	7,200	22.32
616	11,880	21.58
616	59,820	25.33
700	60	8.25
700	180	19.97
700	300	22.99
700	300	25.76
700	300	25.22
700	480	23.06
700	600	26.37
700	600	26.09
700	7,200	24.35
700	61,200	22.65

The $\Delta\sigma_u$ versus log time data for CPNiAl-1 and HPNiAl-C that were aged for various times at 616 and 610 K, respectively, are plotted together in Figure 43 to illustrate the influence of carbon concentration on the yield point return in NiAl. A significant

difference in the magnitudes of the $\Delta\sigma_u$'s is evident as is an increase in the time required for yield points to form in NiAl-C. In addition, the saturation stress increment is lower in HPNiAl-C than in CPNiAl-1. This behavior would be expected since HPNiAl-C has only about 60% of the C level of CPNiAl-1.

Table 6. Temperature dependence of yield stress increment for HPNiAl-C.

Aging Temperature, K	Aging Time, s	Yield Stress Increment, MPa
610	600	4.46
610	3,600	12.2
610	4,500	11.7
610	5,760	9.33
610	9,000	12.9
610	18,360	11.9

In an effort to establish a mechanism for static strain aging in NiAl, the activation energy for the return of the lower yield stress was determined by applying and Arrhenius equation that was derived from the expression of Cottrell and Bilby [43] for the number of atoms per length of dislocation line segregating to the vicinity of a dislocation in time t:

$$n(t) = \alpha N_0 \left(\frac{ADt}{kT} \right)^{2/3}$$

(33)

where, $\alpha \cong 3.5$, N_0 is the average volumetric concentration of defects in the lattice, D is the diffusivity of the defect at the aging temperature, T, k is Boltzman's constant and A is a term corresponding to the binding energy between the defect and a dislocation. If prestraining and subsequent reloading are conducted at the same temperatures and if these temperatures are sufficiently low that no aging occurs during testing, the number of defects required to pin a unit length of a dislocation line, $n(t^*)$, will be approximately constant. Thus, equation (33) becomes:

$$C_1 = \left(\frac{n(t^*)}{N_0 \alpha}\right)^{3/2} \left(\frac{k}{AD_0}\right) = \frac{t^*}{T} \exp\left(\frac{-Q}{RT}\right)$$

(34)

where D_0 is the pre-exponential factor for diffusivity of the defect and t^* represents the aging time for the reappearance of a yield point. Equation (34) can then be rewritten as:

$$\ln\left(\frac{T}{t^*}\right) = \ln\left(\frac{1}{C_1}\right) - \frac{Q}{RT}$$

(35)

The activation energy for diffusion of the pinning defect, Q, is determined from the slope of a plot of $\ln(T/t^*)$ versus $1/(RT)$. This method is illustrated in Figure 44. On this basis, an activation energy for the return of a lower yield point in CPNiAl-1 was determined to be in the range 72 to 76 kJ/mole (approximately 0.75 to 0.79 eV/atom), which corresponds to the activation energies for the migration of interstitials in many BCC transition metals [181].

As an alternate approach to the Arrhenius calculation, the activation energy was also determined by the method used by Hartley [38] who modified the Cottrell-Bilby relationship for the yield stress increment as follows:

$$\frac{\Delta\sigma_u}{\overline{\sigma}} = \frac{(\sigma_u - \sigma_a)}{\overline{\sigma}} = K_1 + K_2\left(\frac{t}{T_a}\right)^{2/3}$$

(36)

where, $\overline{\sigma} = \frac{1}{2}(\sigma_a + \sigma_u)$, K_1 is a constant, K_2 is a constant proportional to $D^{2/3}$, where D is the diffusivity, t is the aging time, and T_a is the aging temperature. Recalling that $D = D_0 \exp(-Q/RT)$, activation energies are calculated by first determining the slope S_1 of a plot of $\Delta\sigma_u/\overline{\sigma}$ versus $t^{2/3}$ and then by plotting $\ln(S_1 T^{2/3})$ versus $2/(3RT)$. This method is illustrated in Figure 45. Using this approach, an activation energy of 70 kJ/mol (0.73 eV/atom) was determined which is in good agreement with the values established using the Arrhenius method.

Due to the lack of diffusion data for any type of interstitial solute in NiAl, little can be said about the activation energies derived in this investigation except that these values lie

below the self diffusion energies for Ni and Al in NiAl and that they lie well below the activation energy for the creation and motion of vacancies [18]. However, the activation energies derived in this study are within the range for interstitial diffusion in BCC transition metals [181].

Discussion

Previously, it was shown that the discontinuous yielding observed in CPNiAl-1 and HPNiAl-C was the result of strong dislocation pinning by interstitial carbon (Chapter 4), whereas increased concentrations of oxygen and/or nitrogen had little or no influence on the properties of nominally stoichiometric NiAl. Therefore, C has been identified as the major solute responsible for strain aging effects in NiAl. In addition, it has been observed that longer aging times are required in HPNiAl-C (92 appm C) to achieve the same yield stress increment as observed in CPNiAl-1 (147 appm C) and that the yield increment after saturation is much greater in CPNiAl-1 than in HPNiAl-C. It is believed that this behavior is a result of the significant reduction in the concentration of interstitials, particularly C, in the HPNiAl-C alloy. Since there is less carbon to pin dislocations in NiAl-C, the carbon present must, presumably, diffuse longer distances to cause pinning.

At least four different mechanisms have been postulated to explain strain-aging in metals and alloys. These include (1) the formation of Cottrell atmospheres [43], (2) Snoek ordering [95-97], (3) Suzuki locking [175] and (4) the precipitation of solute on dislocations [100].

Cottrell locking or aging involves the diffusion of interstitial atoms to dislocations resulting in the formation of solute atmospheres around the dislocations. The driving force for this process is the reduction in total strain energy of the system. The resulting increase in yield stress is due either to an increased stress required to move the locked dislocations or an increase in stress necessary to nucleate new dislocations permitting macroscopic plastic flow. This often leads to yield point behavior when stresses are suddenly sufficient

to unlock the dislocations or nucleate new ones at a temporary rate greater than necessary to accommodate the applied strain rate on the material. The initial locking of dislocations requires long range diffusion of interstitials to the vicinity of dislocations and, as a result, requires many atom jumps. During the early stages of Cottrell locking, the kinetics of yield point return normally increase with time according to a $t^{2/3}$ power law. This relationship was originally deduced by Cottrell and Bilby [43] and has been confirmed for a number of systems involving interstitial atoms in transition metals including Nb-O, Ni-H, Fe-C and Fe-N [35,36,42,94,97,98,101]. The observed log t or approximate $t^{2/3}$ time dependence of $\Delta\sigma_u$ in NiAl due to carbon is consistent with the Cottrell-Bilby theory and suggests that Cottrell locking is the primary mechanism responsible for the observed yield points.

Snoek ordering of impurity atoms within the stress field of a dislocation remains a possible mechanism that may occur prior to the formation of a Cottrell atmosphere. This mechanism is best explained in terms of the Snoek effect as it occurs in BCC metals containing interstitial atoms in solution [95-97]. In the BCC lattice the tetrahedral sites are larger than the octahedral sites. However, interstitial atoms typically occupy the smaller octahedral sites at the center of cube edges and cube faces because the lattice strain caused by octahedral occupancy can be more easily accommodated by the lattice than that caused by tetrahedral occupancy. For example, the insertion of an interstitial atom into the 1/2, 1/2, 0 position in Figure 46 will cause atoms 1 and 2 to be displaced apart in the z direction resulting in a tetragonal distortion, whereas the insertion of an interstitial into the 1/2, 0, 0 position will cause a more uniform distortion of substitutional atoms 1-4. In the absence of an applied stress, a statistically equal number of interstitials will occupy octahedral sites parallel to each of the x, y and z axes. Thus, the unit cell remains cubic. The application of an external stress in the z direction, for example, causes the interstitial sites parallel to the z axis to enlarge while the openings perpendicular to the z axis decrease in size making it energetically more favorable for atoms at the 1/2, 1/2, 0 position, for example, to jump to the 1/2, 0, 1/2 position. This is known as the Snoek effect or Snoek ordering [95,96].

Since no long range diffusion is required, this process occurs very rapidly and is normally completed within the time interval of one atomic jump of the species responsible for pinning.

Similar behavior will be observed in B2 alloys. As in the case of BCC metals described above, an atom placed in an octahedral site results only in displacement of the two nearest atoms, whereas tetrahedral occupancy results in the distortion of the four neighboring atoms. Baker [182], however, indicates that in the B2 crystal structure, the octahedral sites are not equivalent. Assuming that the A metal atoms represent Ni and the B metal atoms represent Al (*i.e.*, $R_B > R_A$), the octahedral sites defined by Ni atoms will always be larger than those defined by Al atoms. In other words, an interstitial will prefer to occupy the octahedral position at 1/2, 1/2, 0 (face) in the B2 lattice illustrated in Figure 46 as opposed to the 1/2, 0, 0 (edge) position because this site is larger than the edge position and allows for easier accommodation of an interstitial atom. However, even if the interstitials prefer only half of the total octahedral sites, the effect of stress on these remaining sites would still be the same as that described in the previous paragraph and Snoek ordering should still occur. Nakada and Keh [98] have indicated that the apparent intercept of the $\Delta\sigma_u$ versus $t^{2/3}$ curves is positive when Snoek ordering occurs prior to Cottrell atmosphere formation. In Figure 42, a positive intercept of the $\Delta\sigma_u$ versus $t^{2/3}$ curves is observed which suggests that some degree of Snoek ordering does occur in NiAl prior to the aforementioned Cottrell locking.

Suzuki locking is inapplicable to the present investigation. This mechanism has its origin in a chemical interaction between solute atoms and stacking faults and is only expected to be significant in metals of low stacking fault energy in which the stacking fault widths are large. This is not the case in NiAl.

Precipitation on dislocations as a result of solute segregation is another possible mechanism for yield point formation, however, precipitates were not observed in thin foils made from specimens of CPNiAl-1 and HPNiAl-C aged at 1100 K/7200 s/FC or 610

K/7200 s/AC. In addition, the shapes of the aging curves for CPNiAl-1 and HPNiAl-C for aging times up to 61,000 s at 700 K (Figures 41 and 43) do not suggest the formation of precipitates since a decrease in $\Delta\sigma_u$ that could be attributed to overaging and coarsening of any precipitates present was not observed at longer aging times. This does not preclude such a mechanism in alloys containing higher levels of substitutional contaminants as well as interstitial carbon [90,183,184]. However, precipitation was not observed within the time-temperature range examined for alloys with the specific compositions studied in this investigation

Therefore, assuming a Cottrell type pinning mechanism does occur, additional kinetic information about C diffusion in NiAl can be obtained from the data generated during this study. Using the activation energies calculated above, it becomes possible to estimate the amount of enrichment at the dislocation core after strain aging. First, assume that the segregation of interstitials to a dislocation core is described by a Maxwellian distribution [122]. The solute concentration at the dislocation core, c, is determined according to:

$$c = c_0 \exp\left(\frac{-W_m}{RT}\right) \tag{37}$$

where c_0 represents the bulk solute concentration in the crystal, R is the universal gas constant, T is the absolute temperature and W_m is the dislocation-solute binding energy. Though W_m is currently unknown, a rough estimate can be obtained by substituting into equation (37) the temperature above which yield point phenomena are not observed, T_{max}, (approximately 900 K for CP-NiAl), and by setting c equal to unity. This results in an estimated W_m of 51 kJ/mol (0.5 eV/atom), which is a reasonable estimate when compared to similar numbers generated for BCC metals using the same assumptions [122,181]. Using this estimated value for W_m, an expression for the solute enrichment at the dislocation core after strain aging for time t_a at temperature T can be derived as follows [122]:

$$c - c_0 = \frac{\pi c_0}{b^2} \left[\frac{n(n+2)D|W_m|b^n t_a}{RT} \right]^{n/(n+2)} \qquad (38)$$

where b represents the Burgers vector of the dislocations and n is a material parameter used to characterize the type of dislocation-solute interaction. For interactions due to size effects, as in this case, n=1. The time required to saturate a dislocation at temperatures sufficiently low for stable saturation to occur is given by the condition $c=c_1 \gg c_0$ where c_1 is the critical solute concentration for saturation and is less than unity. Assuming that the carbon atoms (impurities) attract each other then $c_1 = 1/2$ and the saturation time, t_s, is related to the solute diffusivity as follows [122]:

$$t_s \cong \left(\frac{c_1}{\pi c_0} \right)^{\frac{n+2}{2}} \frac{RTb^2}{n(n+2)D|W_m|} \qquad (39)$$

Assuming that t_s corresponds to the minimum aging time required to induce yield point phenomena (*i.e.*, sharp yield points or pronounced yield plateaus in the stress-strain curves), it is possible to calculate an upper bound for the diffusion coefficients for carbon in NiAl using equation (39) and the T and t_s values determined during this investigation and listed in Table 7. The resulting D values are also listed in Table 7.

Table 7. Calculated diffusion coefficients for C in NiAl.

Temperature, K	t_s, s	D cm^2 s^{-1}
522	3,600	2×10^{-16}
616	300	3×10^{-15}
700	60	2×10^{-14}

A linear least squares fit of ln D versus 1/(RT) using the values in Table 7 yields:

$$D = (6 \times 10^{-9}) \exp\left(\frac{-Q}{RT} \right) \qquad (40)$$

where the activation energy, Q, turns out to be 74 kJ/mol (0.77 eV/atom), which is equivalent to the values derived from the $\Delta\sigma_u$ vs. t data in the Results. Furthermore, in the regime where static strain aging has been shown to occur in CP-NiAl, the calculated diffusivities of carbon in NiAl, are the right order of magnitude compared to the diffusivities of carbon in alpha iron within the strain aging regime (*i.e.*, approximately 10^{-17} cm^2/s at 298 K to approximately 10^{-10} cm^2/s at 573 K [185]).

Summary and Conclusions

The observed log t or approximate $t^{2/3}$ time dependence of $\Delta\sigma_u$ in NiAl due to carbon is consistent with the Cottrell-Bilby theory for solute atmosphere formation around dislocations. This suggests that Cottrell locking is the primary mechanism responsible for the observed yield points. In addition, positive intercepts on plots of $\Delta\sigma_u$ versus $t^{2/3}$ suggests that Snoek ordering also occurs prior to Cottrell strain aging.

Activation energies for yield point return ranging from 70 to 76 kJ/mol (0.73 to 0.79 eV/atom) have been calculated by three different techniques. These values are in the range for the diffusion of interstitials in BCC transition metals.

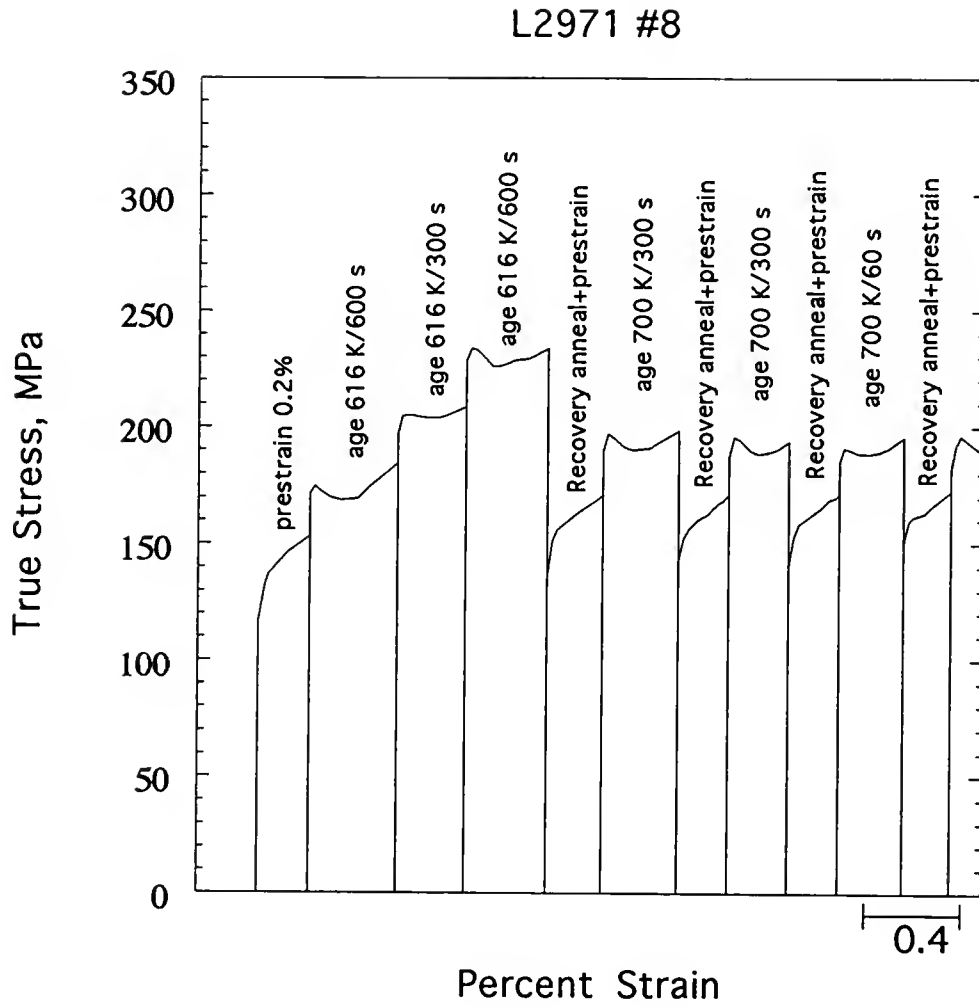Figure 38.   Definition of strain-aging parameters.

Figure 39.   Series of stress-strain curves illustrating the test method used to determine the strain aging kinetics in NiAl.
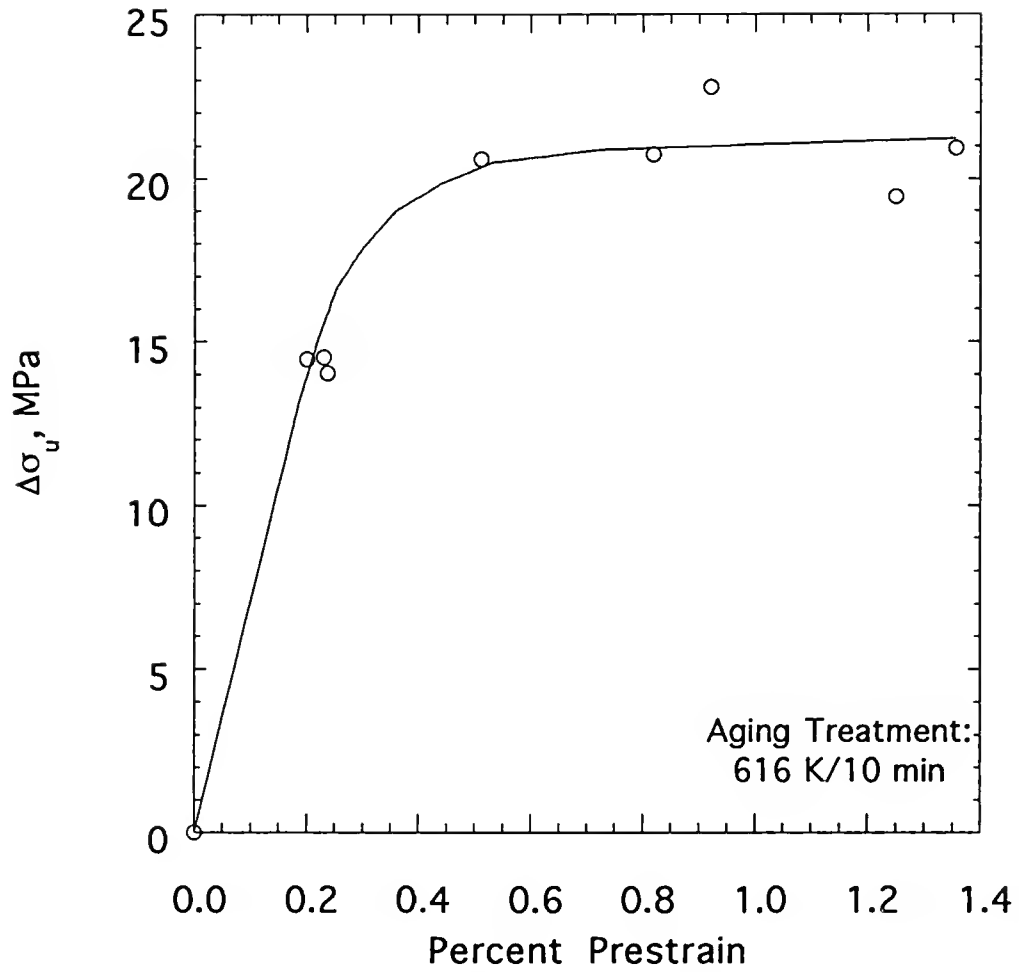
Figure 40. Influence of percent prestrain at room temperature followed by aging at 616 K/10 min. on the subsequent yield stress increment measured at room-temperature.
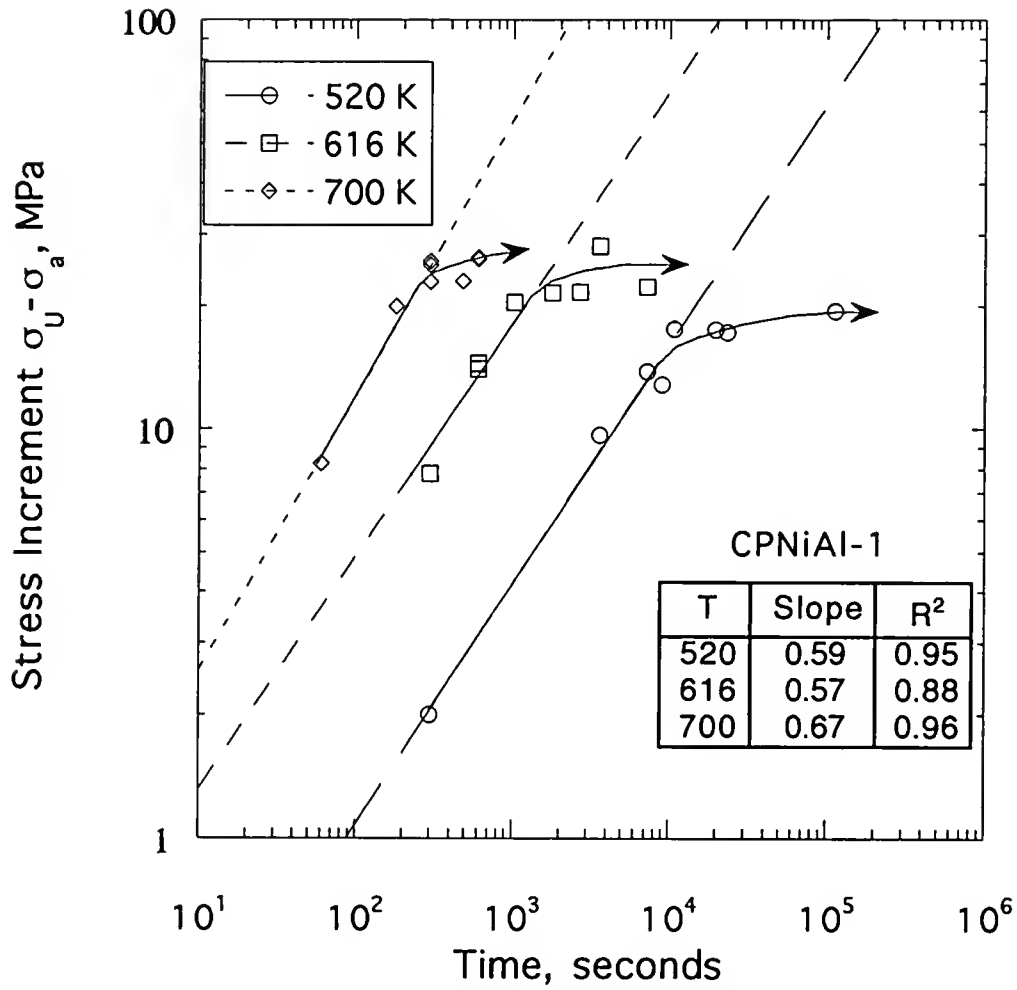
Figure 41.   Ln $\Delta\sigma_u$ vs. Ln t for CPNiAl-1 specimens. Specimens were prestrained uniaxially in tension to 0.2% prior to the strain aging treatments. The least squares parameters are indicated on the figure.
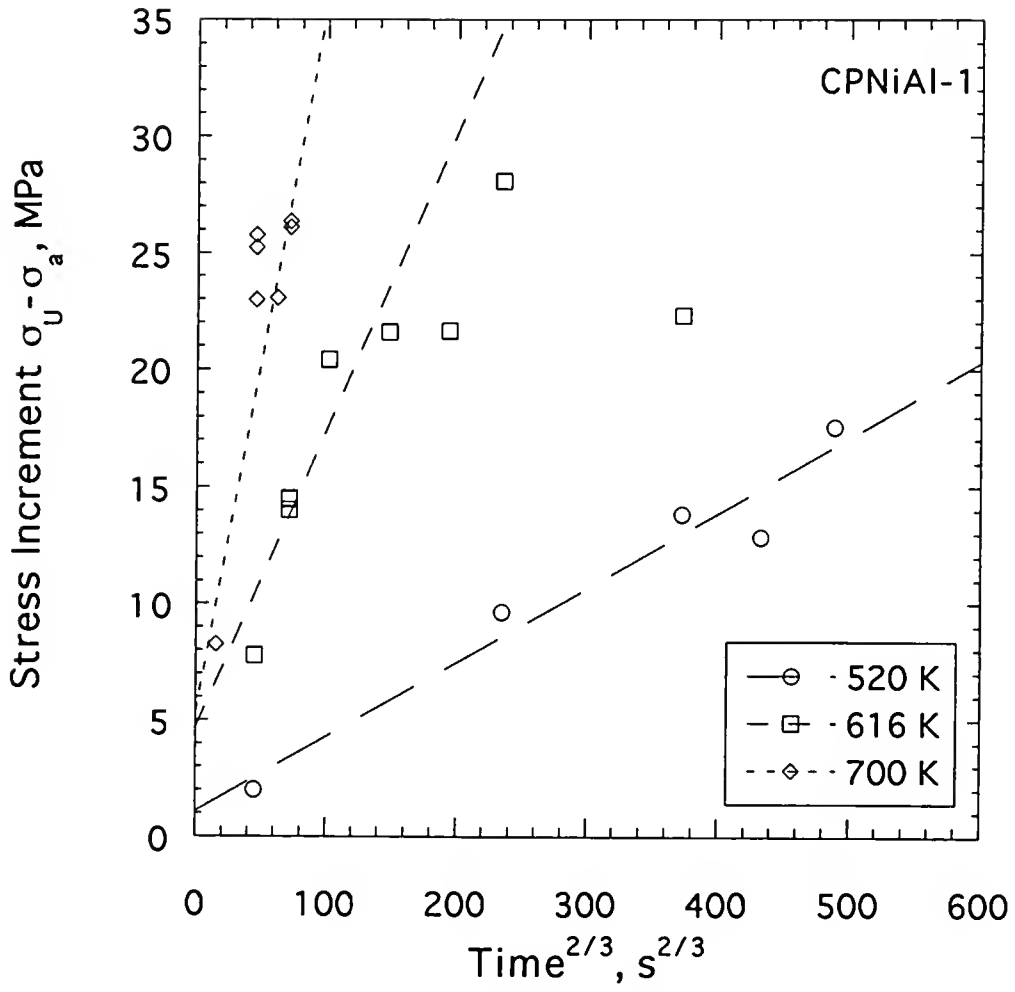
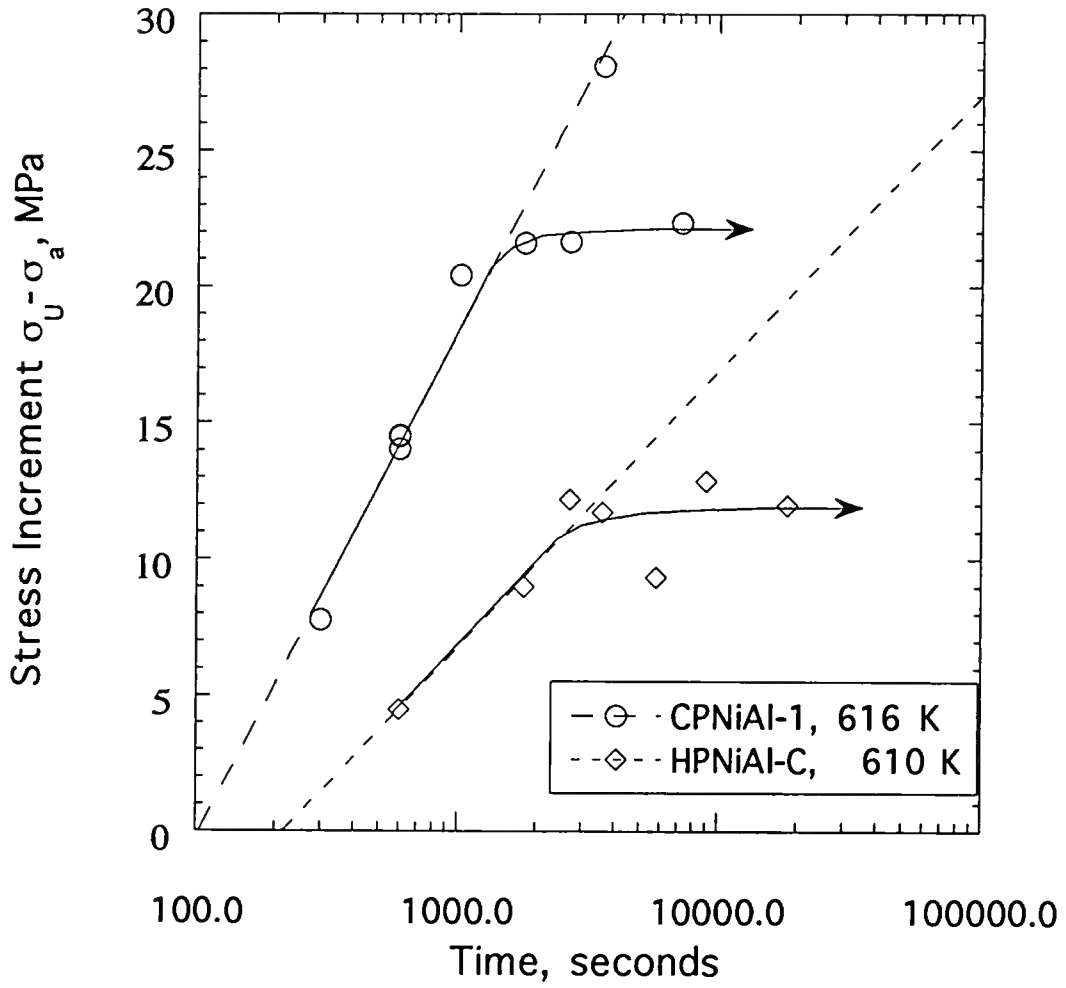Figure 42. Plots of $\Delta\sigma_u$ vs. $t^{2/3}$ for CPNiAl-1 aged at 520, 616, and 700 K.

Figure 43.   Plot of $\Delta\sigma_u$ vs. natural log t for CPNiAl-1 and HPNiAl-C at 616 K and 610 K, respectively.
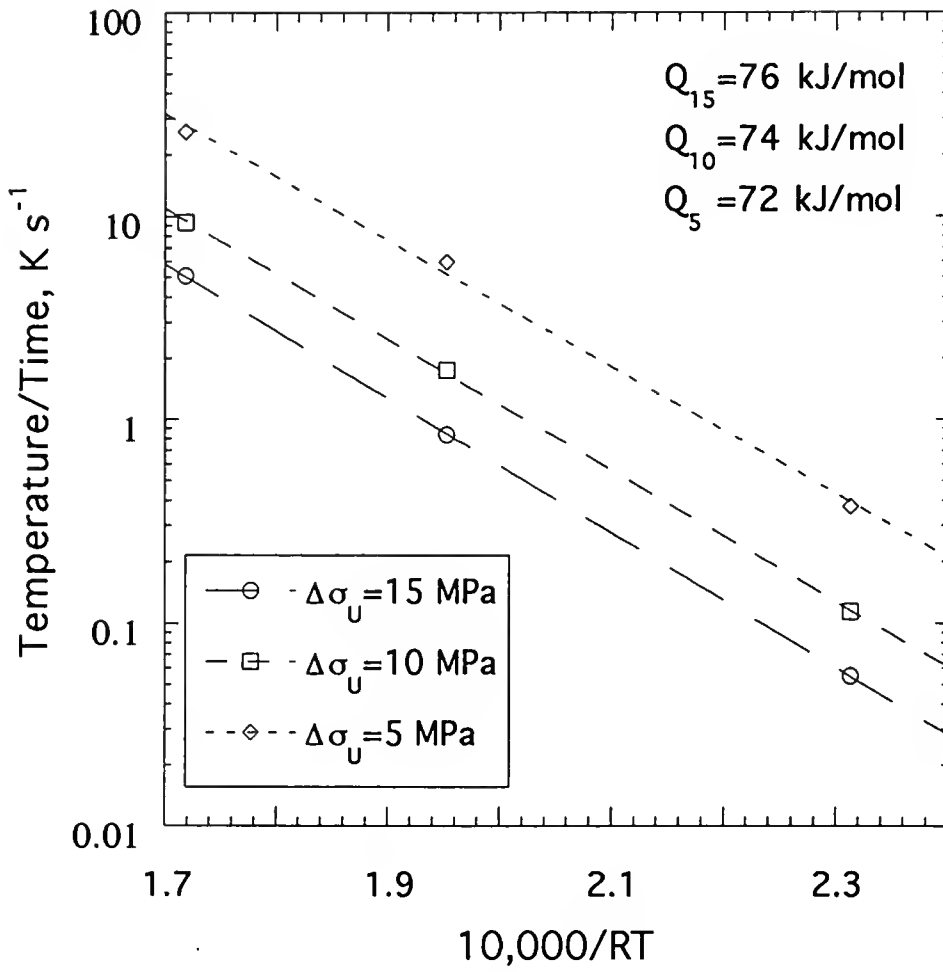
Figure 44.   Arrhenius representation of the strain aging data for CPNiAl-1.

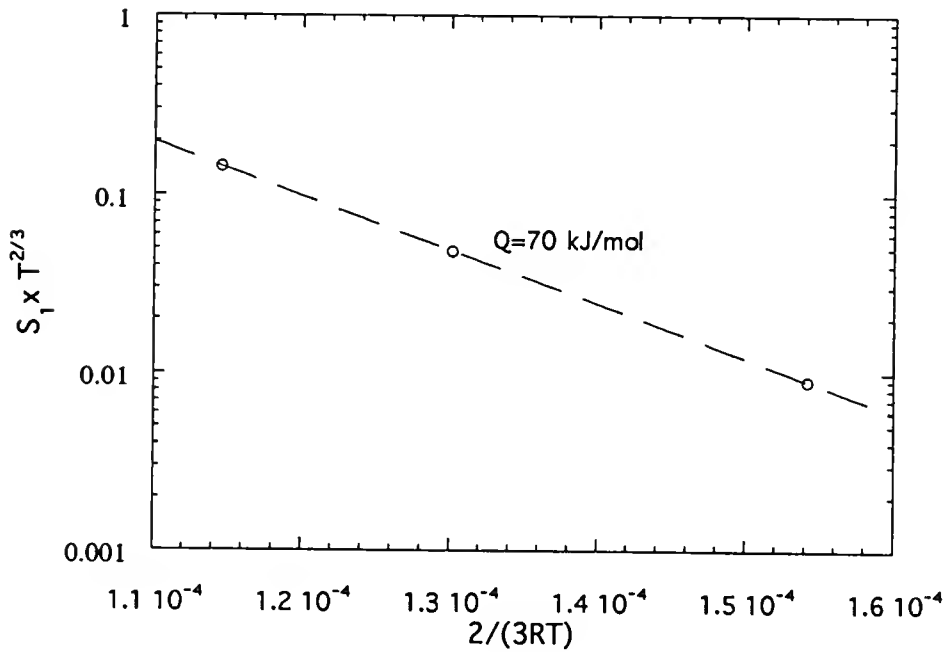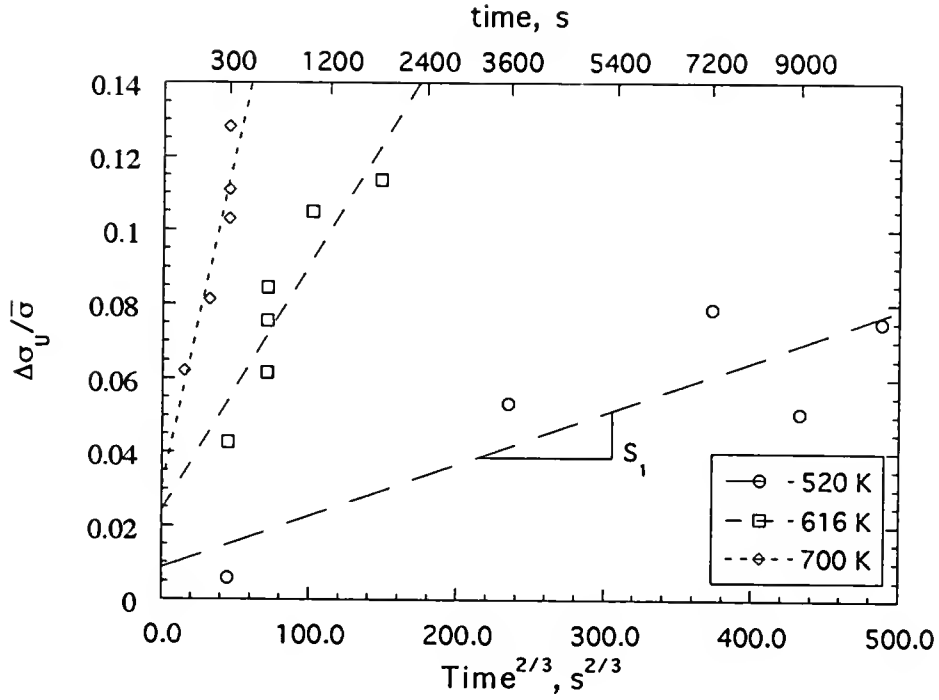Figure 45.   Demonstration of the Hartley method [38] for determination of the activation energy for yield point return. (a) Strain aging parameters versus $t^{2/3}$ for CPNiAl-1 aged at 520, 616 and 700 K; (b) determination of the activation energy for yield point return using the Hartley method.
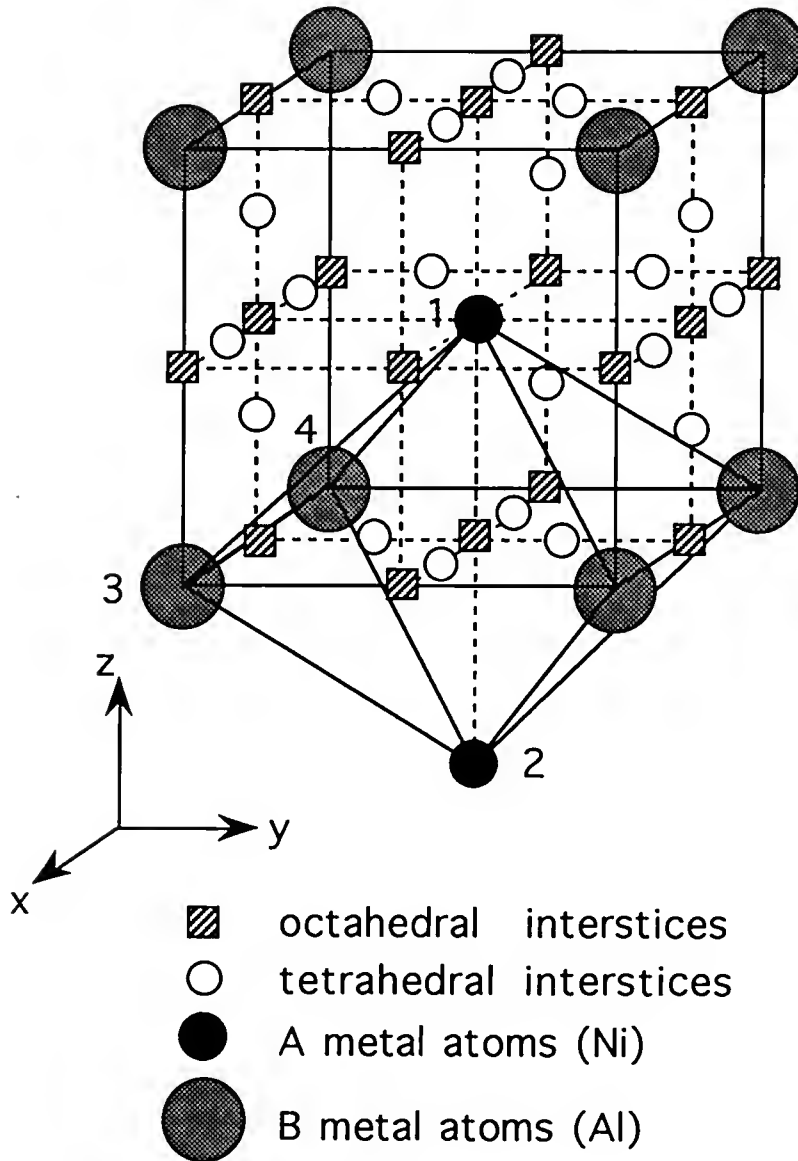
Figure 46.   Schematic illustration of the octahedral and tetrahedral interstitial sites in the BCC/B2 unit cell.

CHAPTER 6
MANIFESTATIONS OF DYNAMIC STRAIN AGING IN POLYCRYSTALLINE NiAl

Introduction

It is commonly accepted that BCC metals, in the presence of sufficient interstitial levels, are subject to the phenomenon of strain aging which can manifest itself as: (1) sharp yield points, (2) serrated stress-strain curves, (3) strain rate sensitivity minima, (4) maxima in plots of work hardening rate as a function of temperature, (5) yield stress plateaus as a function of temperature and (6) flow stress transients upon changes in strain rate (see reference [104]). Not surprisingly, several B2 intermetallic compounds have also been shown to exhibit some of the manifestations associated with strain aging. Despite these observations, the relative significance of strain aging and its influence on the mechanical properties of ordered intermetallic compounds has been largely ignored. The purpose of this chapter is to describe the results of a study of dynamic strain aging (DSA) in polycrystalline NiAl. To accomplish this goal, stoichiometric NiAl polycrystals with differing interstitial contents were studied. In addition, since dilute additions of reactive elements have been reported to retard strain aging in BCC alloys, an NiAl alloy intentionally doped with Ti was investigated to analyze the role of reactive ternary additions on the strain aging behavior of NiAl.

Materials and Methods

The five cast and extruded alloys (*i.e.*, CPNiAl-1, CPNiAl-2, NiAl-100C, NiAl-300C and NiAl-Ti) and the extruded nitrogen-doped powder alloy, NiAl-N, used to study static strain aging (SSA) in Chapters 4 and 5 were used here. In addition, two more carbon-doped alloys were induction melted prepared using the techniques described in

Chapter 4. The designations for the new carbon-doped alloys are described below. As before, post extrusion chemical analyses of the new ingots were conducted using the techniques deemed the most accurate for the particular elements. The results of these analyses are listed in Table 8 along with the compositions of the prior alloys for comparison. Cylindrical compression specimens and round button-head tensile specimens were ground from the extruded rods so that the gage lengths were parallel to the extrusion direction. Sample dimensions were 3.1 mm for the tensile gage diameters and 30.0 mm for the tensile gage lengths and 3.0 mm for the compression sample diameters and 6.4 mm for the lengths. All specimens were electropolished prior to testing in a 10% perchloric acid-90% methanol solution that was cooled to 208 K.

Table 8. Chemical Compositions of Extruded Alloys Examined in This Chapter

Alloy	at.%				appm			
	Ni	Al	Ti	Si	C	O	N	S
NiAl-100CO (L3249)	50.0±0.2	49.8±0.2	----	0.03	420	1283	22	<13
NiAl-300CO (L3216)	49.9±0.2	49.8±0.2	----	0.02	1072	1345	34	<12
Compositions of alloys used in Chapters 4 and 5 are listed below.								
CPNiAl-1	50.1±0.2	49.7±0.2	----	0.15	147	550	<9	<7
CPNiAl-2	50.1±0.2	49.8±0.2	----	0.02	186	94	<9	<7
NiAl-100C	49.9±0.2	50.0±0.2	----	0.02	491	180	<9	<7
NiAl-300C	49.9±0.2	50.0±0.2	----	0.01	1153	131	<9	<7
NiAl-N	50.1±0.2	49.7±0.2	----	0.02	57	347	904	<7
NiAl-Ti	49.9±0.2	50.0±0.2	0.03	0.00	214	113	<9	<7

Ni & Al   Analysis performed using wet chemistry/titration techniques, relative accuracy ±1%.

Ti   Analysis performed using Inductively Coupled Plasma Emission Spectroscopy, relative accuracy ±5%

C & S   Analysis performed on a Simultaneous Carbon/Sulfur Determinator, LECO Corp., Model CS-244, relative accuracy ±10%

N & O   Analysis performed on a simultaneous Nitrogen/Oxygen Determinator, LECO Corp., Model TC-136 or Model TC-436, relative accuracy ±10%

Si   Analysis performed on an Ultraviolet/Visible Spectrophotometer, Shimadzu, Model UV-160, relative accuracy ±10%

All tensile and compression tests were performed using an Instron Model 1125 load frame at constant crosshead velocities corresponding to an initial strain rate of 1.4×10^{-4} s^{-1}. Testing was accomplished in two steps: first, the temperature dependence of flow stress was determined by testing all as-extruded alloys in air between 300 and 1200 K by heating the samples in a clamshell type resistance furnace where temperature gradients were controlled to ± 2 K. Tests below room temperature were conducted in compression by cooling the specimens in liquid baths. During this phase of testing, the strain rate sensitivity (SRS) was also determined by increasing the strain rate by a factor of ten from the base strain rate at fixed plastic strain intervals. The quantity extracted from these experiments was the SRS, $s = \Delta\sigma/\Delta\ln\dot{\varepsilon}$. Second, alloys exhibiting room-temperature yield discontinuities after annealing were subjected to static strain aging (SSA) tests. A description of the SSA test procedure is provided in Chapters 4 and 5 and in reference [138].

Samples for transmission electron microscopy (TEM) were cut from the tested tensile and compression specimens with a low-speed diamond saw and twin jet-electropolished in a solution of 70% ethanol, 14% distilled water, 10% butylcellusolve, and 6% perchloric acid at 273 K, 25V, and 0.15 mA. TEM examinations were conducted in a JEOL 100C microscope operating at an accelerating voltage of 120 kV.

Results

Microstructural Characterization

The post-extrusion microstructure of all alloys consisted of fully equiaxed and recrystallized grains with nominal grain sizes of 20 μm exceept for the NiAl-N alloy that had a grain size of approximately 5 μm. The results of chemical analyses of the extruded alloys revealed that, within experimental accuracy, the Ni and Al contents of the eight nominally stoichiometric alloys are not significantly different from each other. The major

differences between the materials are the addition of 0.03 at.% Ti to NiAl-Ti and the varying carbon and oxygen interstitial levels. Chemical analysis of the new carbon-doped alloys revealed that, in addition to containing the desired levels of carbon, each contained five times as much oxygen as the first set of ingots. As a result, the new ingots were labeled NiAl-100CO and NiAl-300CO respectively.

Tensile Properties

Mechanical tests and strain rate change experiments were conducted in the temperature range of 77 to 1200 K. The temperature-dependent properties (*i.e.*, flow stress, work hardening rate and SRS) are summarized in Figures 47-49. Figure 47 shows the temperature dependence of the flow stress at 0.2% plastic strain. In agreement with previous studies [18], the flow stress generally decreased with increasing temperature. In all alloys except NiAl-Ti and NiAl-N, however, a definite plateau or slight hump was observed in the range 750-900 K.

The work hardening characteristics over the 0.2-1.8% plastic strain interval have been evaluated from the average work hardening rate, $\theta = (\Delta\sigma/\Delta\epsilon)$, and average work hardening exponent, n, as defined by the equation:

$$\sigma = K\epsilon^n \tag{41}$$

where K is a strength coefficient [186]. The resulting values for θ and n have been normalized with respect to the elastic modulus and are summarized in Figure 48. Much like the 0.2% yield stress, both θ/E and n/E decreased steadily with increasing temperature with all alloys except NiAl-Ti and NiAl-N exhibiting slightly anomalous work hardening behavior in the temperature range 600-700 K.

The temperature dependence of the strain rate sensitivity s is presented in Figure 49. The SRS remained positive for all alloys except CPNiAl-1 which exhibited negative s values at 600 and 700 K. For all alloys distinct minima were observed in the temperature

range 750-850 K with the minima in the carbon-doped alloys occurring at slightly lower temperatures than in CPNiAl-2 and NiAl-Ti. This behavior is analogous to soft-oriented single crystals which also exhibit SRS minima in this regime and which often exhibit negative strain rate sensitivities and serrated flow indicative of DSA [14,15,28,164,179,180]. Serrated flow was only observed in CPNiAl-1 and not in any of the other alloys studied here. However, yield stress transients in the form of sharp yield points were consistently observed in the temperature range of the flow stress plateau in all alloys except NiAl-Ti upon increasing the strain rate by a factor of 10. Examples of this behavior is illustrated in Figure 50. This is clearly indicative of DSA.

Limited SSA experiments were conducted on CPNiAl-1 and NiAl-100C. These experiments were conclusive in that significant yield points could be obtained for both alloys after aging. For example, in NiAl-100C significant yield points could be recovered after annealing for as little as 2100 s (35 min.) at 622 K, in agreement with the SSA results presented in Chapters 4 and 5.

Post-test TEM analysis of the NiAl-100C (Figure 51) alloy after deformation at its SRS minimum revealed a deformation structure consisting of randomly-distributed <001> dislocations and dislocation debris arranged into coarse tangles and poorly defined cell walls. The majority of the cell walls were oriented parallel to the <110> crystallographic directions indicating some propensity towards localized slip. Similar observations have been made in single crystal NiAl alloys and is discussed in more detail in Chapter 7. Conversely, in specimens deformed at room-temperature (see Chapter 4), dislocations were arranged into well developed cellular networks indicating the ease of cross-slip at this temperature. At elevated temperatures, more uniform dislocation distributions develop due to enhanced relaxation and recovery.

Discussion

The curves in Figures 47-49 have several common features. (1) In all alloys but NiAl-Ti and NiAl-N, the temperature dependencies of the flow stress, θ/E, and n/E increase anomalously in the temperature range 600 to 850 K. (2) For all of the alloys, the SRS's exhibit distinct minima in the temperature range 750-850 K but remain positive except for CP-NiAl1. These anomalies are generally observed at lower temperatures for carbon doped alloys followed by the conventional purity alloys and then by NiAl-Ti. Similar flow stress peaks and anomalous work hardening parameters have been observed in soft-oriented NiAl single crystals in this same temperature range as have SRS minima, negative SRS values, and serrated yielding [14,15,28,164]. These anomalies are attributed to the migration of interstitial carbon to dislocations. Confirmation that diffusion of solute atoms toward dislocations is occurring is provided by the static strain aging studies performed in this chapter and in Chapters 4 and 5.

In the present set of experiments, the flow stress and work hardening anomalies are shifted to higher temperatures compared with the minimum in SRS. This serves as further evidence in favor of DSA. Classical theory [111,127] dictates that the microscopic mechanism responsible for DSA is the thermally activated motion of dislocations through localized forest obstacles. This type of dislocation motion is characterized by a waiting time, t_w, during which dislocations temporarily arrested at obstacles in the slip path become pinned by diffusing solute atoms. As a result, the obstacles to dislocation motion become stronger with increasing waiting time (*i.e.*, strength increases with increasing temperature and decreasing strain rate in the DSA regime) resulting in an increased resistance to plastic deformation. Accordingly, SRS reaches a minimum when the time required to pin a dislocation, t_a becomes equal to t_w. At a given strain rate (*i.e.*, at a fixed t_w) strengthening saturates when the temperature becomes high enough that $t_a \ll t_w$. In other words, maximum strengthening will occur at temperatures higher than the SRS minima.

Some interesting observations in NiAl-Ti were: (1) the lack of a flow stress plateau or anomalous work hardening region; (2) the presence of a SRS minima; and (3) the lack of flow stress transients upon a change in strain rate. Normally, the temperatures at which DSA phenomena are observed tend to rise with increasing purity. Thus, the temperatures where the flow stress and work hardening anomalies are located should rise with decreasing solute content. Figures 47-49 show that the stress anomalies and SRS minima do indeed occur at lower temperatures for NiAl-100C compared to conventional purity NiAl alloys. NiAl-Ti, however, contains just as much C as CPNiAl-2. It is suggested, therefore, that the gettering of C by Ti, as reported in Chapter 4 reduces the DSA effects in NiAl-Ti. DSA is not eliminated entirely as evidenced by the SRS minima, either because the maximum solubility of C in the Ni-Al-Ti alloy is still greater than the concentration required to cause DSA or because there is not enough Ti present to getter all of the C. Interestingly, negative SRS and serrated flow was only observed in CPNiAl-1 even though it contained interstitial contents comparable to the other seven alloys used in this chapter. As a result, all extruded alloys were analyzed for the presence of Si, a common impurity in induction melted castings. The results of these tests are indicated in Table 9 along with the carbon contents. In CPNiAl-1, residual Si contents were much higher than those observed in any of the other alloys. This could suggest that silicon, rather than carbon, is the cause for strain aging in NiAl. The results from Chapter 4, however, indicated the presence of sharp yield points and broad yield plateaus in HPNiAl-C, CP-NiAl-2, NiAl-100C, and NiAl-300C after annealing (i.e., 1100 K/2 h/FC). Examination of Table 9 reveals that these four alloys contain between 0.01 and 0.05 at.% Si. HP-NiAl, NiAl-N, and NiAl-Ti, however, exhibit no yield points or plateaus despite the presence of approximately 0.02 at.% Si in HP-NiAl and NiAl-N. This suggests that it is the lower C levels, as reported in Chapter 4, rather than the presence of Si that causes DSA. The results for NiAl-Ti provide further support for this hypothesis. NiAl-Ti contains no Si, exhibits no yield points, but exhibits a dramatic SRS minimum indicative of some DSA at intermediate temperatures.

Prior investigations revealed that in this alloy some of the C is gettered by Ti. This indicates that Si alone cannot be the cause of the DSA observed in NiAl but serves to indicate that it may play an important role. One possibility is that Si increases the activity of C in NiAl resulting in an increased diffusivity of C. This suggestion is only speculative, however, and is addressed further in Chapter 7.

Table 9. Carbon and Silicon Compositions for all of the Polycrystalline Alloys Examined in This Dissertation (at.%)

Alloy	C	Si
HP-NiAl	0.0043	0.0228
HPNiAl-C	0.0092	0.0489
CPNiAl-1	0.0147	0.1458
CPNiAl-2	0.0186	0.0199
NiAl-100C	0.0491	0.0153
NiAl-100CO	0.0420	0.0261
NiAl-300C	0.1153	0.0137
NiAl-300CO	0.1073	0.0198
NiAl-N	0.0057	0.0200
NiAl-Ti	0.0214	0.0000

Summary and Conclusions

The occurrence of serrated yielding in CPNiAl-1, SSA, yield points during room temperature testing after annealing, yield stress transients upon changes in strain rate, and the occurrence of yield stress and work hardening anomalies confirm that DSA does occur in polycrystalline NiAl alloys. Evidence for DSA in the other alloys is more subtle and is indicated predominantly by SRS minima and anomalous yield strength-temperature behavior.

Preliminary analysis indicates that residual Si impurities can play a significant role in DSA and that the addition of dilute quantities of reactive metals can reduce the effects of DSA via a gettering mechanism.
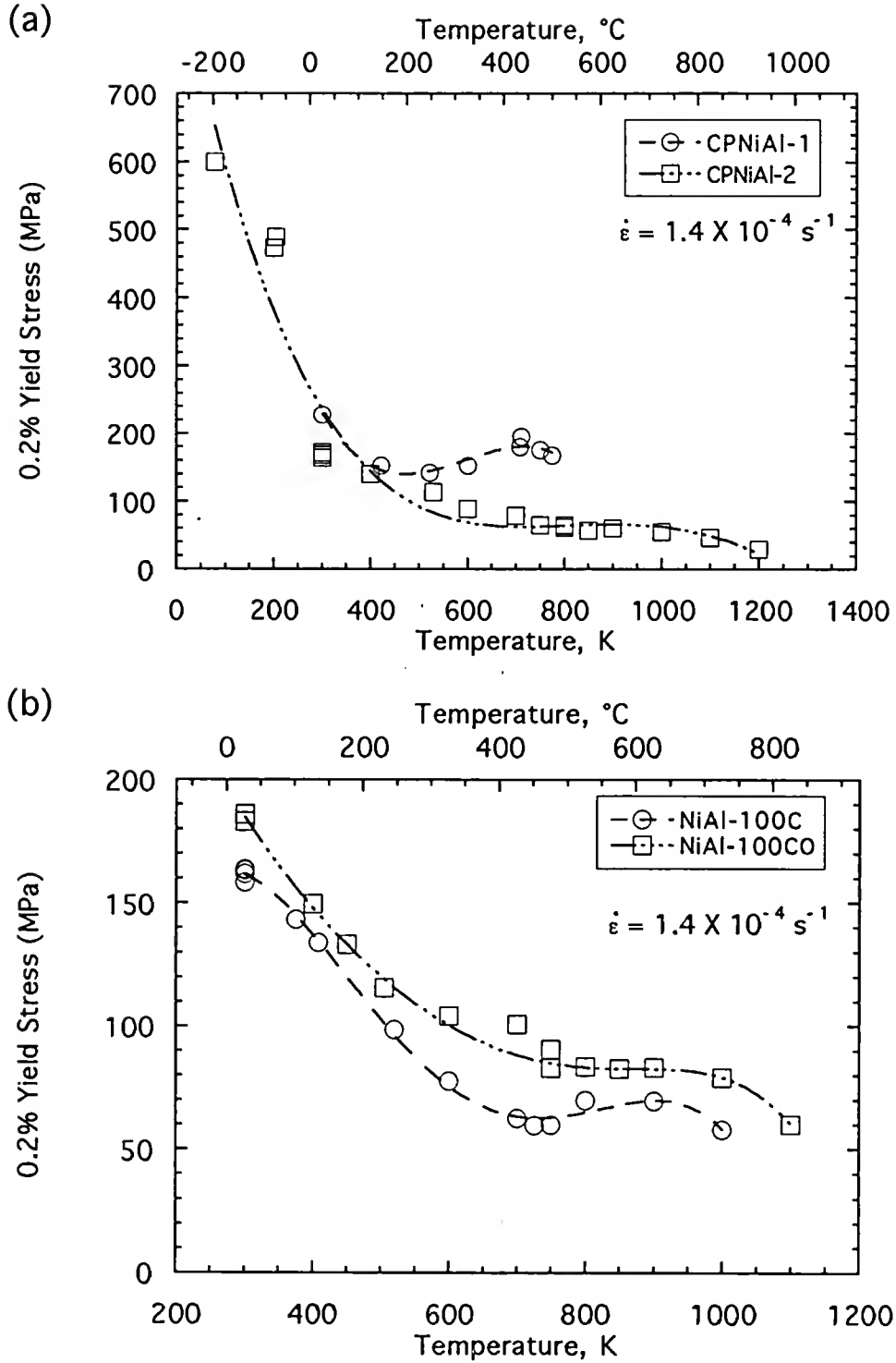
Figure 47. Temperature dependence of the 0.2% yield stress for NiAl Alloys: (a) CPNiAl-1 and CPNiAl-2; (b) NiAl-100C and NiAl-100CO; (c) NiAl-300C and NiAl-300CO; and (d) NiAl-N and NiAl-Ti.
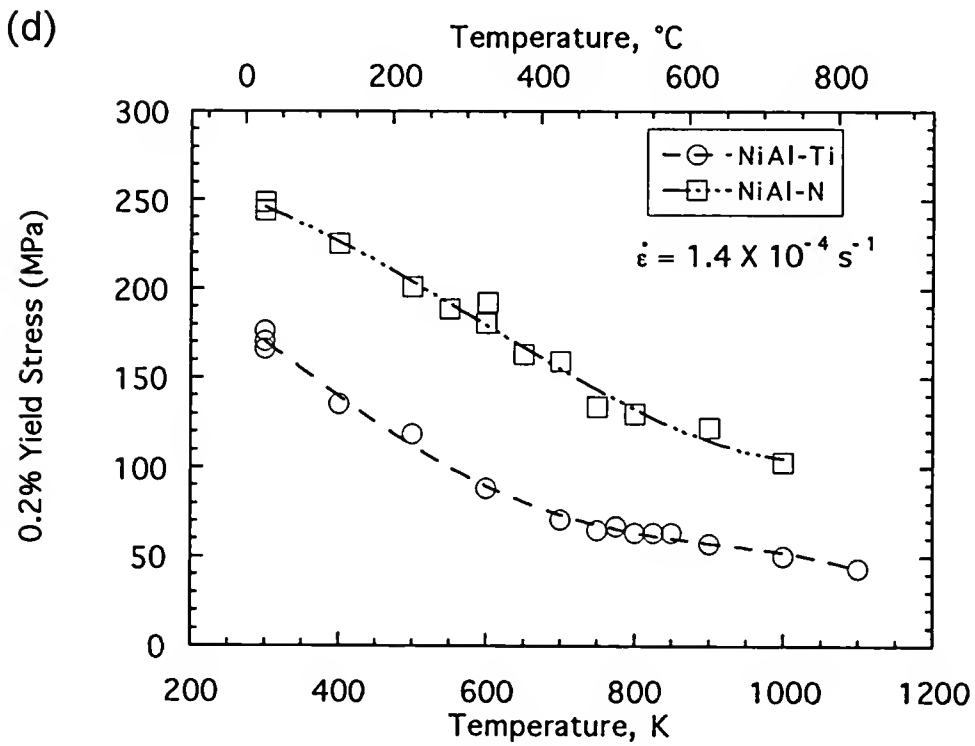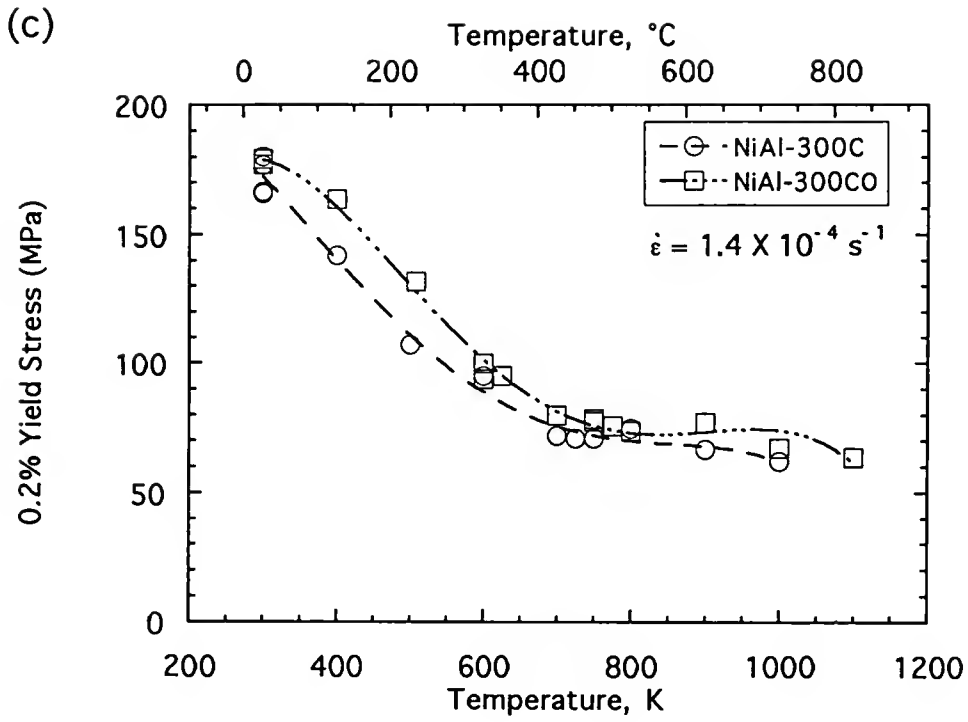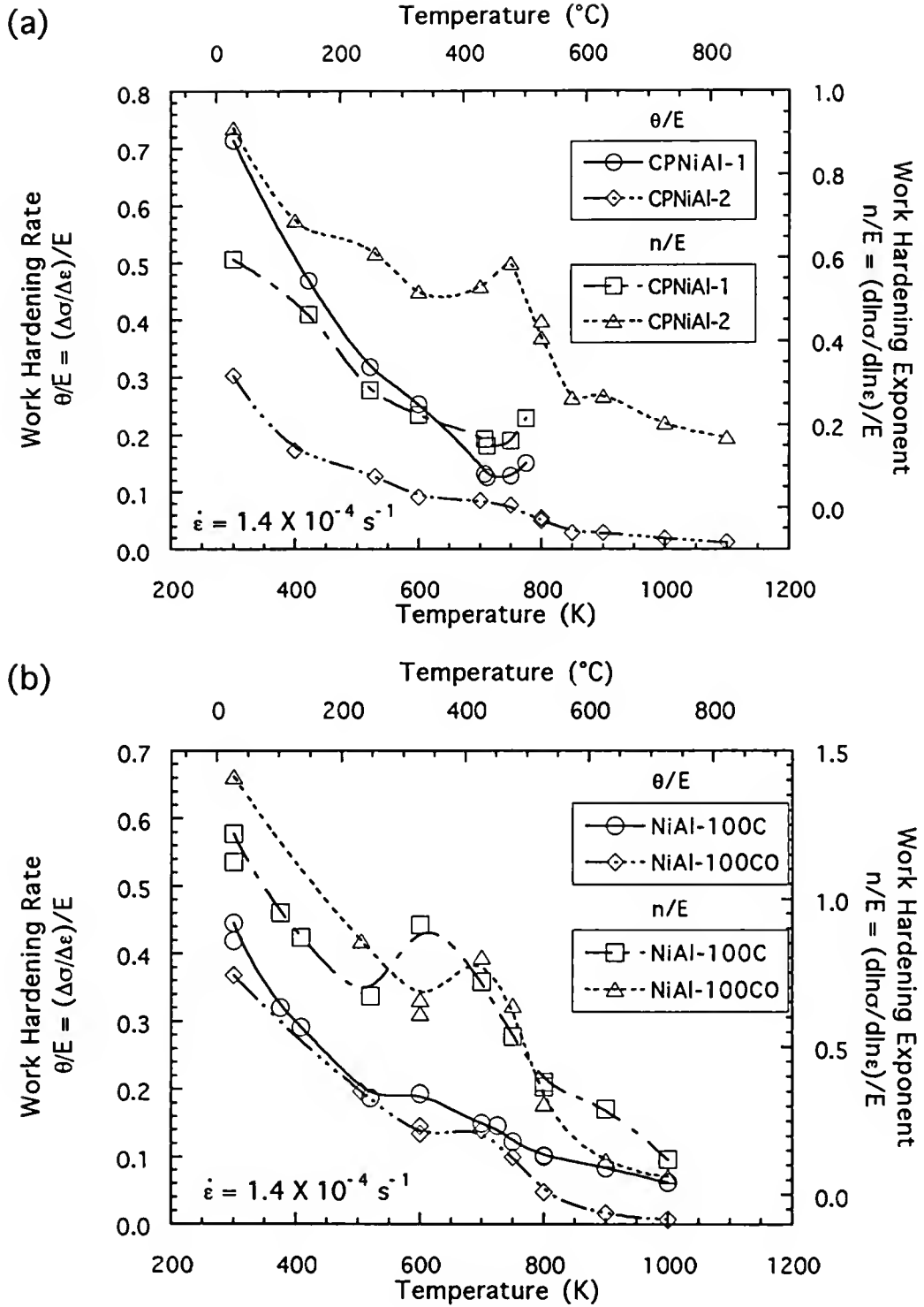
(c)

(d)

Figure 47 -- continued

Figure 48. Temperature dependence of the work hardening rate, θ/E=(Δσ/Δε)/E, and work hardening exponent, n/E=(dlnσ/dlnε): (a) CPNiAl-1 and CPNiAl-2; (b) NiAl-100C and NiAl-100CO; (c) NiAl-300C and NiAl-300CO; and (d) NiAl-N and NiAl-Ti.
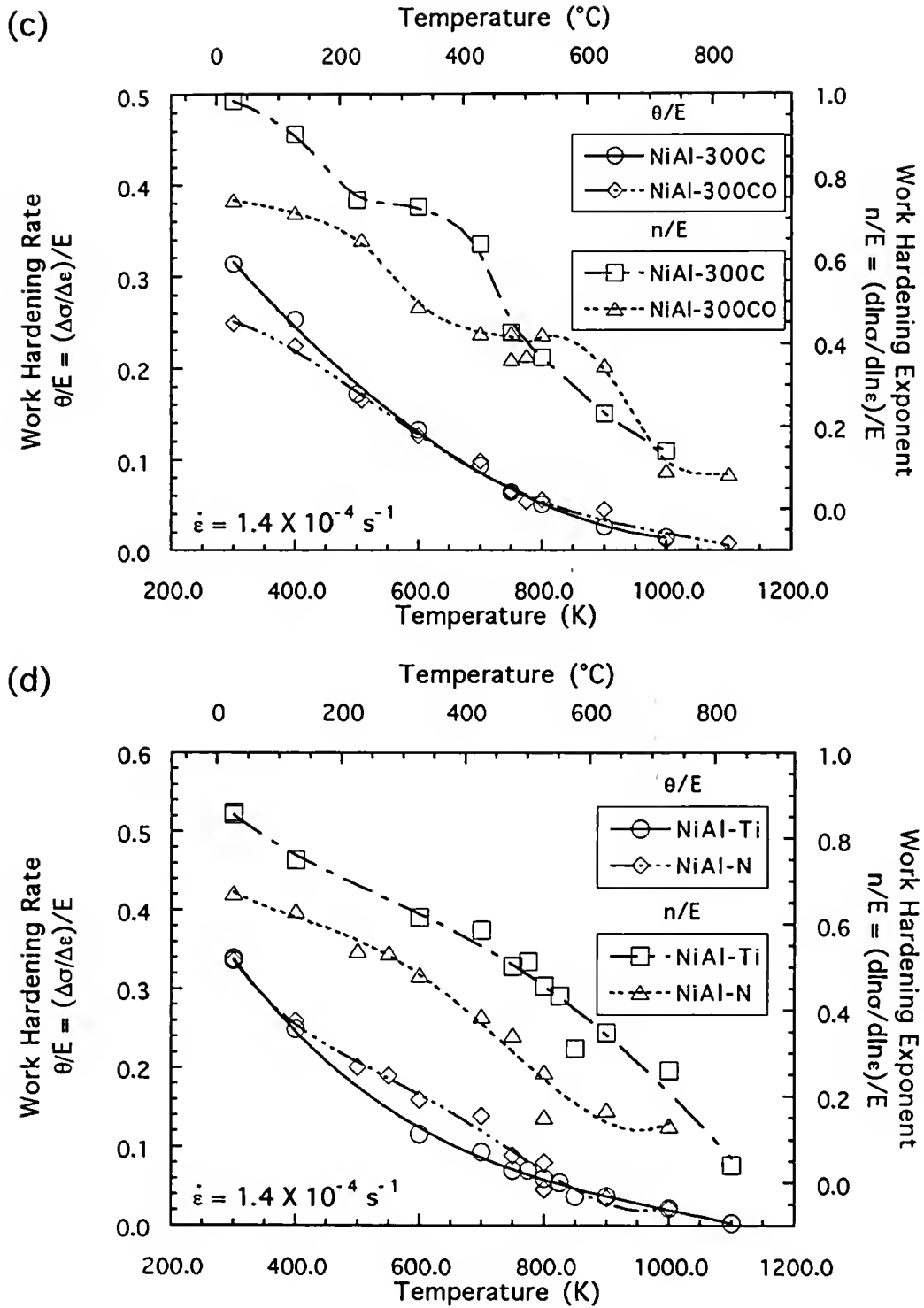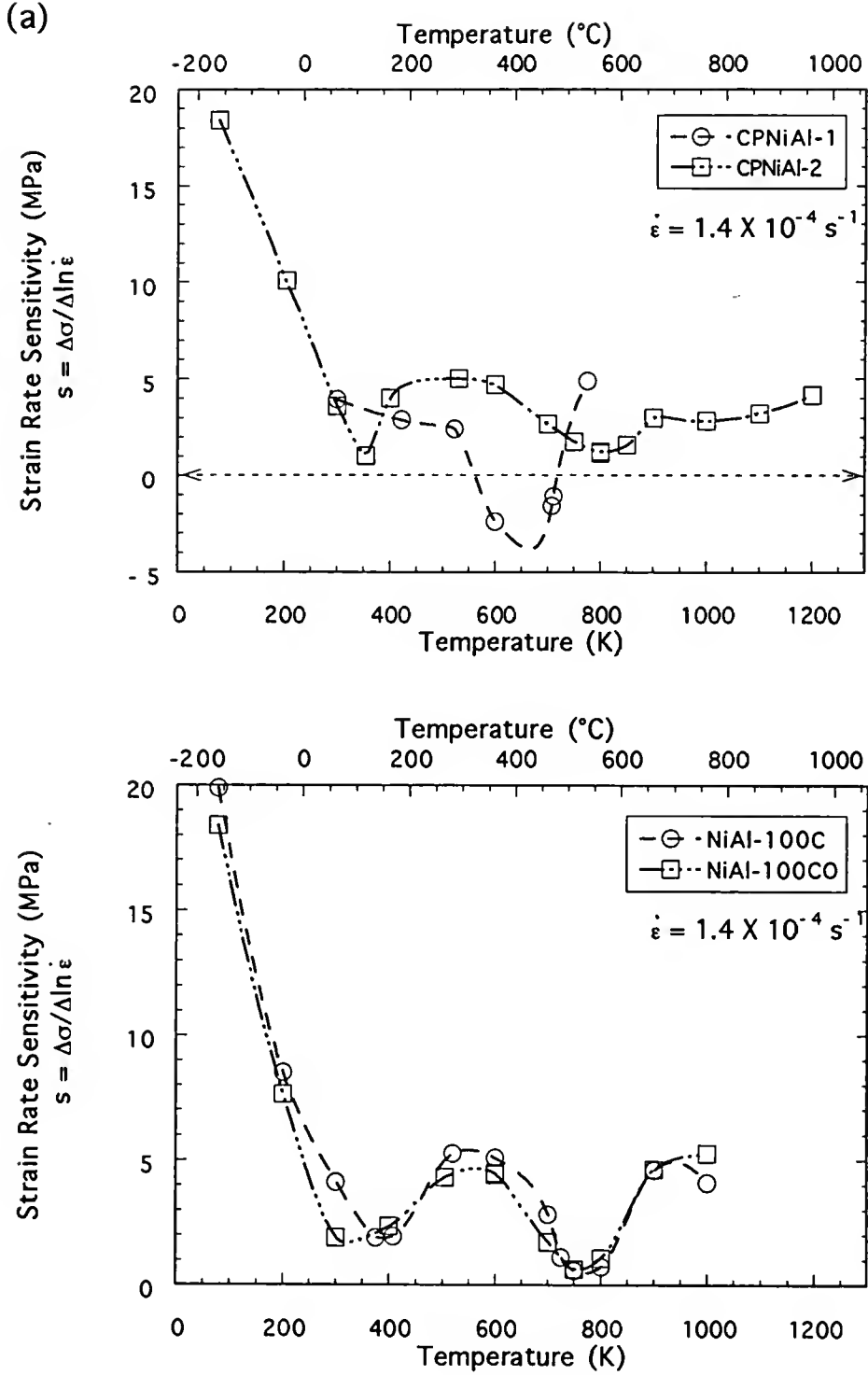
(c)

(d)

Figure 48 -- continued

Figure 49. Temperature dependence of the SRS, $s=\Delta\sigma/\Delta\ln\dot{\epsilon}$: (a) CPNiAl-1 and CPNiAl-2; (b) NiAl-100C and NiAl-100CO; (c) NiAl-300C and NiAl-300CO; and (d) NiAl-N and NiAl-Ti.
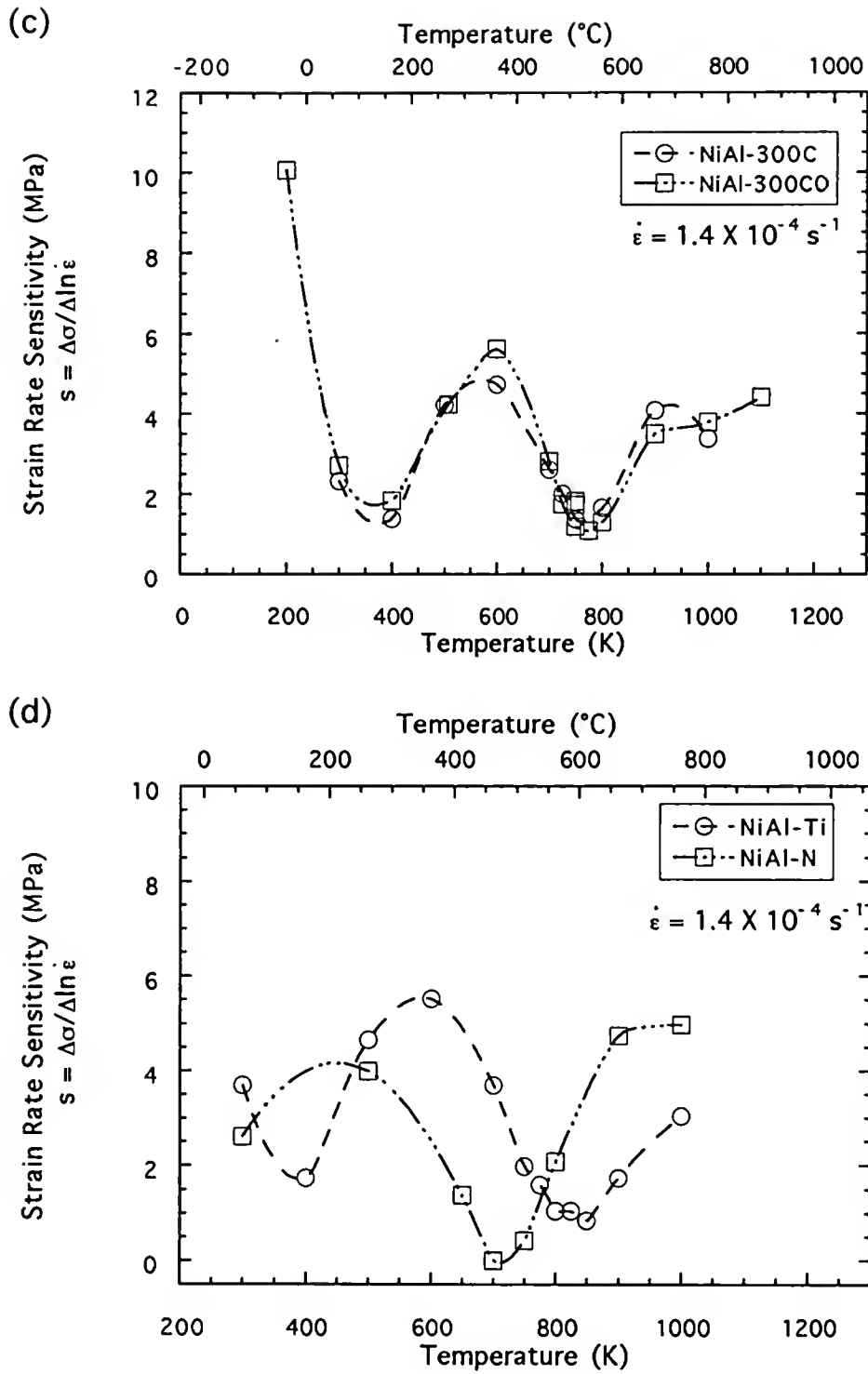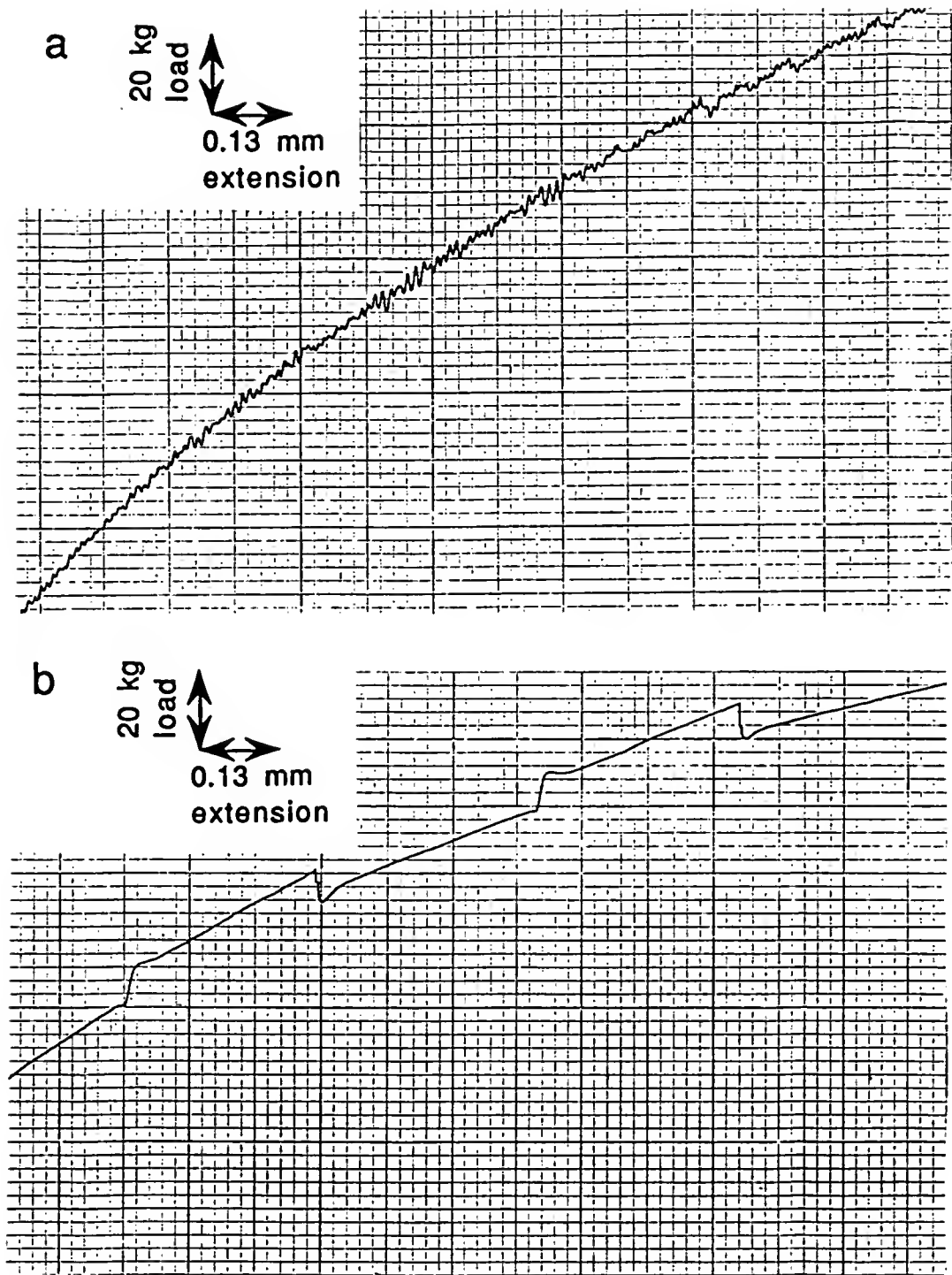
(c)

(d)

Figure 49 -- continued

Figure 50. Examples of serrations, stress transients, and the lack of stress transients observed in CPNiAl-1, NiAl-100C, and NiAl-Ti during testing near the SRS minimum. (a) CPNiAl-1 at 800 K, (b) NiAl-100C at 800 K, and (c) NiAl-Ti at 725 K.
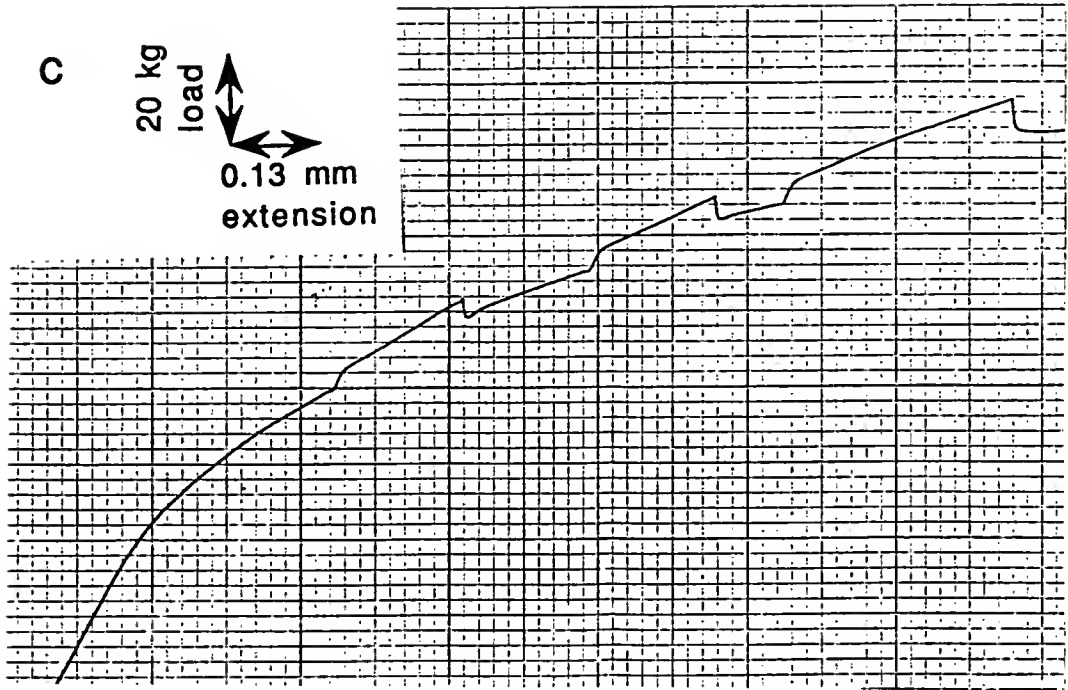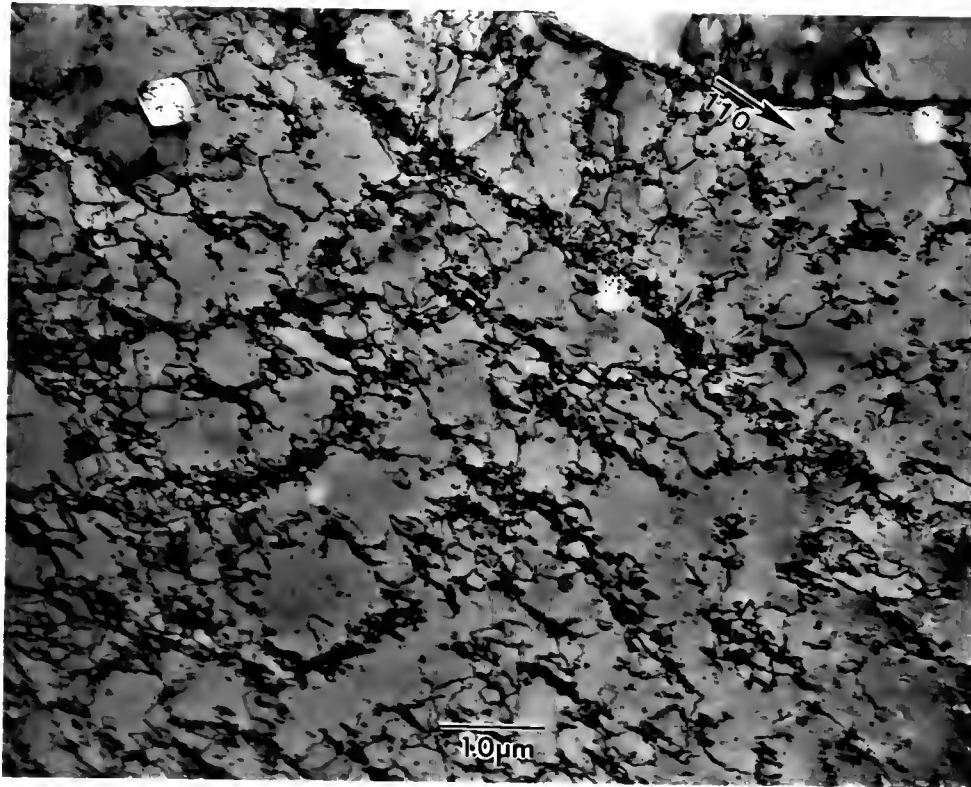
Figure 50 -- continued

Figure 51. BFTEM of dislocation structure observed in NiAl-100C after 11.5% deformation at 800 K illustrating the transition of a dislocation cell structure to a banded structure.

CHAPTER 7
MANIFESTATIONS OF DYNAMIC STRAIN AGING IN SOFT-ORIENTED NiAl SINGLE CRYSTALS

Introduction

As mentioned in the preceding chapters, the mechanical properties of the intermetallic compound NiAl exhibit an extreme sensitivity to (1) point defects introduced during processing and/or heat treatment, (2) the level and type of prestrain in the material, and (3) minute additions of interstitials that can lead to strain aging phenomena. Several manifestations of strain aging have been identified as playing a role in the deformation of polycrystalline and single crystal NiAl. They are: (1) the occurrence of yield points [23,167-169] ; (2) serrated stress-strain curves [15,22,23,26,28,164,165]; (3) strain rate sensitivity minima [12,166]; (4) yield stress plateaus as a function of temperature [18]; (5) the occurrence of local maxima or plateaus in plots of work hardening rate (WHR) as a function of temperature [12,27]; and (6) flow stress transients on changes in strain rate [139,166]. Despite these observations, the significance of strain aging and its influence on the mechanical properties of NiAl has been, until recently, largely ignored. The purpose of this chapter is to describe the dynamic strain aging (DSA) behavior observed in NiAl single crystals. To accomplish this objective, stoichiometric NiAl single crystals with differing interstitial contents were studied. Since dilute additions of reactive elements have been reported to retard the strain aging behavior in BCC metals, an alloy intentionally doped with Mo was also investigated to analyze the role of a strong gettering agent on the strain aging behavior of NiAl single crystals.

136

Experimental

One Mo-doped (NiAl-Mo), one Si-doped (NiAl-Si) and three nominally stoichiometric NiAl (CPNiAl-1, CPNiAl-2 and UF-NiAl1) single crystal slabs were grown in argon by a modified Bridgman procedure. Slabs CPNiAl-1, CPNiAl-2, and NiAl-Mo were produced at General Electric Aircraft Engines and measured 25 mm × 32 mm × 1000 mm. Slabs UF-NiAl1 and NiAl-Si were produced at the University of Florida and measured 25 mm diameter × 60 mm length. A low interstitial, high purity ingot of stoichiometric NiAl (HP-NiAl), 25 mm diameter × 50 mm length, was produced via a containerless electromagnetic levitating zone process at the University of Tennessee. All slabs were homogenized at 1589 K for at least 1 hour in argon followed by furnace cooling to room-temperature prior to machining into test specimens.

Post-processing chemical analyses were conducted using the techniques deemed the most accurate for the particular elements. The results of these analyses are listed in Table 10. The crystals were oriented using the back reflection Laue technique and either ground into round button-head tensile specimens parallel to the <123> axis or EDM wire cut into cylindrical compression specimens parallel to the <123> or <110> axis. Specimen dimensions were: (1) 3.1 mm and 30.0 mm for the for the tensile gage diameter and gage length; and (2) 3.0 mm and 6.4 mm for the compression sample diameter and height, respectively. All tensile specimens were electropolished prior to testing in a 10% perchloric acid-90% methanol solution that was cooled to 208 K.

All mechanical tests were performed on an Instron Model 1125 load frame at constant crosshead velocities corresponding to an initial strain rate of 2.8×10^{-5} s^{-1}. Tests were run in air between 300 and 1100 K by heating the samples in a clamshell type resistance furnace. Testing below room temperature was accomplished in compression by cooling in liquid baths. True stress-strain data were calculated from the load-time plots and yield stresses were determined by the 0.2% offset method. During some of these tests, the

strain rate sensitivity (SRS) was also determined by increasing the strain rate by a factor of ten from the base strain rate at fixed plastic strain intervals. The quantity extracted from these experiments was the SRS, $s = \Delta\sigma/\Delta\ln\dot{\varepsilon}$.

Table 10. Chemical Compositions of Single Crystal Alloys Examined in This Study

Alloy (ingot)	[hkl]	at.%				Impurities (appm)		
		Ni	Al	Mo	Si	C	O	N
HP-NiAl UT-HP2	[123]	50.2±0.2	49.8±0.2	----	0.04	76	24	40
CPNiAl-1 D5-553	[123]	50.6±0.2	49.2±0.2	----	0.17	112	87	<6
CPNiAl-2 D5-1273	[110]	50.4±0.2	49.4±0.2	----	0.15	209	612	<6
UF-NiAl1 UF-001	[123]	50.3±0.2	49.9±0.2	----	0.01	161	558	15
NiAl-Mo D52-783	[123]	50.0±0.2	49.8±0.2	0.11	0.23	558	830	25
NiAl-Si UF-003	[110]	50.4±0.2	49.3±0.2	----	0.29	220	95	12

Ni & Al   Analysis performed using wet chemistry/titration techniques, relative accuracy ±1%.

Mo   Analysis performed on a Flame Atomic Absorption/Emission Spectrophotometer, Perkin Elmer Model 5000, relative accuracy ±5%.

C & S   Analysis performed on a Simultaneous Carbon/Sulfur Determinator, LECO Corp., Model CS-244, relative accuracy ±10%. Sulfur concentrations were always less than 0.001 at.%.

N & O   Analysis Performed on a Simultaneous Nitrogen/Oxygen Determinator, LECO Corp., Model TC-136 or Model TC-436, relative accuracy ±10%.

Si   Analysis performed on an Ultraviolet/Visible Spectrophotometer, Shimadzu, Model UV-160, relative accuracy ±10%.

Samples for transmission electron microscopy (TEM) were cut from the tested tensile or compression specimens with a low-speed diamond saw and twin jet-electropolished in a solution of 70% ethanol, 14% distilled water, 10% butylcellusolve, and 6% perchloric acid at 273 K, 25V, and 0.15 mA. TEM examinations were conducted in a JEOL 100C microscope operating at an accelerating voltage of 120 kV.

Results

Composition and Microstructure

The results of the chemical analyses indicated that, within experimental accuracy, the Ni and Al contents of the five alloys are not significantly different from each other. The major differences between the materials are the residual Si, C, O and N contents and the addition of 0.1 at.%Mo to NiAl-Mo, which resulted in the formation of coarse precipitates (Figure 52). Energy dispersive spetroscopic analysis and TEM microdiffraction indicated that these particles were Mo_2C. The presence of silicon in NiAl-Mo, CPNiAl-1 and CPNiAl-2 has been attributed to reaction with the ceramic shell mold walls during processing. The lack of Si in UF-NiAl1 has been attributed to the use of arc-melted as opposed to vacuum induction melted feed stock and the use of higher purity crucibles during directional solidification.

Mechanical Properties

The temperature dependent properties (*i.e.*, critical resolved shear stress (CRSS), work hardening rate, and SRS) are summarized in Figures 53-55. Figure 53 shows the temperature dependence of the CRSS at 0.2% plastic strain. In agreement with prior studies [18,44], the CRSS decreased gradually with increasing temperature until reaching an apparent plateau in the temperature range 650 to 1000 K in CPNiAl-1, CPNiAl-2, UF-NiAl1, NiAl-Mo and NiAl-Si. In HP-NiAl, however, no such plateau was observed in agreement with the previous observations from Chapter 2 on a similarly processed material.

The work hardening characteristics between 0.2 and 1.8% plastic strain have been evaluated from the average work hardening rate ($\theta = \Delta\sigma/\Delta\varepsilon$) and work hardening exponent ($n=dln\sigma/dln\varepsilon$) normalized with respect to the elastic modulus and are summarized in Figure 54. Much like the CRSS, both θ/E and n/E decrease steadily with increasing temperature

until reaching an anomalous region in the temperature range 600 to 900 K in CPNiAl-1, CPNiAl-2, UF-NiAl1 and NiAl-Mo. No anomalous behavior was observed in HP-NiAl.

The occurrence of serrated flow has been previously reported in NiAl [14,15,28,164]. Since serrated flow can be associated with DSA and the Portevin-Le Chatelier (PLC) effect, the SRS, s, has been deduced from strain rate change tests. The temperature dependence of the strain rate sensitivity is presented in Figure 55. For all six alloys, s exhibits a distinct minimum in the range 600 to 800 K with s actually becoming negative for CPNiAl-1, CPNiAl-2 and NiAl-Si. In addition, the local maximum in the flow stress, in the plateau region, occurs at higher temperatures than the SRS minimum. Coincident with those temperatures where a negative SRS was observed was the occurrence of serrated yielding (Figure 56). Serrated yielding typically occurred after a small critical plastic strain, ε_c. The T and $\dot{\varepsilon}$ dependence of ε_c for CPNiAl-1, CPNiAl-2 and NiAl-Si is shown in Figure 57. Serrations occur in only certain $\dot{\varepsilon}$ and T regimes. Within these regions, increasing $\dot{\varepsilon}$ and decreasing temperature, generally caused a decrease in the magnitude of ε_c to some minimum followed by a further increase. Figure 58 maps the regime of serrated flow in CPNiAl-1 and NiAl-Si. Using the classification scheme of Rodriguez [104], the serrations in the region where a negative temperature dependence of the critical strain was observed could be predominantly classified as type C while the lower temperature serrations could be classified as type B (Figure 56). Both types of serrations are characteristic of unlocking of pinned dislocations and are associated with discontinuous deformation band propagation.

In this investigation Q for serrated flow was ascertained via three distinct methods. In the first method, the critical plastic strain can be related to $\dot{\varepsilon}$ and T by the following equation:

$$\varepsilon_c^{(m+\beta)} = K\dot{\varepsilon}\exp(Q/RT) \tag{42}$$

where m and β are exponents related to the variation in vacancy concentration C_v and mobile dislocation density ρ_m (*i.e.*, $C_v \propto \varepsilon^m$ and $\rho_m \propto \varepsilon^\beta$), K is a constant, Q is the

activation energy and R and T have their usual meanings. The exponent $(m+\beta)$, as determined from the slope of the plot of ln $\dot{\epsilon}$ versus ln ϵ_c at a constant temperature (Figure 57a), was in the range 0.98 to 1.27 for CPNiAl-1, CPNiAl-2, and NiAl-Si. Typical values for the exponent $(m+\beta)$ are between 2 and 3 for substitutional alloys and between 0.5 and 1 for interstitial alloys [104] which indicates that an interstitial specie is likely responsible for serrated yielding. The activation energy is determined by applying the derived exponent to a plot of ln ϵ_c versus 1/RT (Figure 57b) [187,188] which yields Q as its slope $\times$ $(m+\beta)$. This method gives activation energies in the range 75 to 90 kJ/mol for the onset of serrated flow.

In the second method, Q can be determined from the slope of an Arrhenius plot of $\dot{\epsilon}$ versus 1/RT. In this case the onset lines on Figure 58, which shows the regime of serrated flow for CPNiAl-1 and NiAl-Si, can be used [188]. This method yields an activation energies ranging from 66 to 100 kJ/mol.

Finally, the magnitude of the stress drop, $\Delta\sigma$, accompanying serrated flow is measured at a given strain for a range of $\dot{\epsilon}$ and T and plotted as indicated in Figure 59a; a constant value for $\Delta\sigma$ is selected from which the $\dot{\epsilon}$ corresponding to this $\Delta\sigma$ is determined for each temperature. The resulting $\dot{\epsilon}$ is then plotted as a function of 1/T and Q is determined from it's slope (*i.e.*, Q =-(ln $\dot{\epsilon}$RT/lne)). Detailed descriptions of this method are provided in references [188] and [189]. Figures 59a-c show the $\Delta\sigma$ versus $\dot{\epsilon}$ and $\dot{\epsilon}$ versus 1/T plots for CPNiAl-1, CPNiAl-2, and NiAl-Si from which activation energies of approximately 70 kJ/mol were ascertained for all three alloys.

Activation energies determined using these methods are summarized in Table 11 and are in reasonable agreement with the activation energies for SSA in polycrystalline NiAl (Chapter 5) and the activation energy for serrated flow in NiAl reported by Brzeski and co-workers [29,164].

Table 11. Summary of activation energy values for serrated flow evaluated using different methods for conventional purity and Si-doped single crystals.

Method employed to evaluate Q	Activation energy, Q (kJ/mol)		
	CPNiAl-1 <123>	CPNiAl-2 <110>	NiAl-Si <110>
1 From log ε_c vs. 1/T plots	94 (m+β) = 1.27	82 (m+β) = 0.98	75 (m+β) = 0.98
2 From log $\dot{\varepsilon}$ - 1/T map	onset = 66 end = 139	onset = 100* end = - na -	onset = 66 end = 138
3 Using stress drop method	72	73	73
Average Q for the onset of serrations using methods 1 to 3	77±14	85±14	71±5

* This value obtained from a plot of $\dot{\varepsilon}$ versus 1/T for the onset of serrations at two strain rates. A complete serration map for CPNiAl-2 was not available.

TEM observations of deformed samples

Representative TEM bright-field images of the NiAl alloys deformed at room temperature, in the DSA regime, and above the DSA regime are shown in Figures 60 through 63. Diffraction contrast analysis revealed that deformation occurred by the motion of <001> type dislocations at all temperatures. Figure 60a shows the deformation microstructures of CPNiAl-2 samples deformed at room temperature. In agreement with previous observations in Chapter 3, the microstructure consists of jogged and curved dislocation segments and dislocation debris in the form of elongated loops. At high strains (Figure 60b) the dislocations arrange themselves into cellular networks containing a low volume fraction of intercellular dislocations or debris. Such structures are attributed to the easy cross-slip of screw dislocations during room-temperature deformation [71,154,171,173].

Figure 61 shows the deformation microstructure of a CPNiAl-2 sample deformed in the DSA regime. The microstructure of CPNiAl-2 consists of poorly-defined cells or the beginning of a channel structure with the densest cell walls oriented parallel to the <110>

crystallographic direction. Coincident with this deformation structure was a relatively high density of dislocations within the cell walls Figure 61a. Similar observations have been reported previously for <110> oriented conventional purity single crystals [80,190,191]. Cell walls in non-<110> directions were particularly poorly defined indicating some sort of localized deformation in this temperature regime. This structure is reminiscent of the structures developed during low cycle fatigue testing in the DSA regime [192-194]. Similar deformation microstructures were observed in NiAl-Si following deformation at its SRS minimum with the cell walls oriented parallel to the <100> direction (Figure 61b).

Figure 62 shows the deformation substructure observed in CPNiAl-2 following deformation at 1000 K. This structure was characterized by a lower dislocation density than that observed at 300 K or at the SRS minimum and the general lack of a cell structure. This is attributed to the greater relaxation and recovery effects which become important at this temperature.

In NiAl-Mo following deformation at the SRS minimum (Figure 63), structures consisting of poorly defined cells and dislocation tangles were also observed. However, the channel structures observed in CPNiAl-2 were not as evident. In addition, a lower density of intercellular debris and dislocations was observed even after levels of deformation equivalent to those in CPNiAl-2. In HP-NiAl (Figure 64a), cellular structures characterized by large loosely packed cell walls with very little intercellular debris were observed indicating a much greater ease of cross-slip in this alloy compared to either CPNiAl-2 or NiAl-Mo. On occasion, single slip bands were observed propagating across the sample (Figure 64b) indicating some localized slip processes but not to the same degree as in the other alloys.

Discussion

The yield stress and WHR versus temperature curves for each alloy exhibit several common features. First, the temperature dependencies of the yield stress and θ/E generally

decrease with increasing temperature. In the case of the CPNiAl-1, CPNiAl-2, UF-NiAl1, NiAl-Mo, and NiAl-Si alloys, however, anomalous regions in the form of local peaks or plateaus are observed in the temperature range 650 to 1000 K. No such feature was observed for HP-NiAl. Secondly, the temperature dependence of the SRS exhibited distinct minima for all six alloys in the temperature range 600 to 800 K with SRS actually becoming negative for CPNiAl-1, CPNiAl-2, and NiAl-Si. Coincident with this region of negative SRS was the observation of serrated flow during mechanical testing which directly supports the premise that DSA does occur in this intermediate temperature range in NiAl. In HP-NiAl, NiAl-Mo, and in UF-NiAl1, SRS always remained positive and serrated flow was not observed. However, flow stress transients on changes in strain rate in the form of sharp upper yield points were consistently observed during testing near the SRS minimum in UF-NiAl1 and NiAl-Mo which are indicative of DSA. No flow stress transients were observed in HP-NiAl.

The dislocation substructures formed during deformation at temperatures both above and below the regime where serrated flow occurs are characterized by elongated cell structures, dense tangles and debris. The substructure formed in the DSA regime was typified by a dislocation vein structure. An important additional feature in samples exhibiting serrated flow is that the regions between the dislocation walls often contain a rather uniform dislocation distribution. It is proposed that these inter-wall dislocations result from solute locking of slow moving dislocations between slip bands. Inhomogeneous deformation occurs as a result of differential movement of dislocations within and in between the dislocation walls.

The anomalous mechanical behaviors observed in this study are attributed to DSA or the migration of interstitial solutes to mobile dislocations. Confirmation is provided by SSA studies performed on polycrystalline NiAl (chapters 4 and 5) and by the observance of localized slip in the conventional purity and Si-doped NiAl single crystal alloys. The lack

of serrated flow in UF-NiAl1, which has the same general composition as CPNiAl-2, is attributed to its lower silicon concentration.

Once again, the species responsible for DSA can be identified by comparison of the deformation behavior for the six single crystal alloys and the results from the previous six chapters. Serrated flow was observed in CPNiAl-1, CPNiAl-2, and NiAl-Si, but, not in HP-NiAl, UF-NiAl1, or NiAl-Mo. In HP-NiAl, the C and Si concentrations were much lower than those observed in CPNiAl-1, CPNiAl-2, or NiAl-Si (*i.e.*, 76 appm C versus >150 appm C and 500 appm Si versus >1500 appm Si) which suggests that the lack of serrated flow in HP-NiAl is related to reductions in the C and Si contents. This is supported by the results of Chapters 4 and 6 which show that yield point formation is enhanced and that serrated flow is observed in conventional purity alloys containing >1500 appm Si in addition to normal levels of C (approximately 150 appm). When C is maintained at levels comparable to the conventional purity alloys but Si is reduced to less than 100 appm, as in the case of UF-NiAl1, serrated flow is not observed but yield stress transients upon an increase in strain rate and a yield stress plateau are observed between 600 and 900 K, which would indicate that C still causes some strain aging behaviors but that Si somehow enhances the effect. Finally, in NiAl-Mo, the bulk Si levels were equivalent to those in NiAl-Si (*i.e.*, 0.23 versus 0.25 at.% Si) while the bulk interstitial levels were higher than those observed in CPNiAl-1, CPNiAl-2, and NiAl-Si, the three alloys that exhibited serrated flow. However, no serrated flow was observed in NiAl-Mo. The microstructural analysis presented in this chapter showed that this alloy contains a distribution of coarse Mo_2C stringers and no silicide precipitates; this suggests that the lack of serrated flow in NiAl-Mo is due to the gettering of C from the NiAl matrix. Once again, this suggests that C causes strain aging in NiAl and that the strain aging kinetics can be enhanced by the presence of Si in sufficient quantities. Were Si the cause for the serrated yielding, instead of C, then it is expected that serrated yielding would also be observed in NiAl-Mo since it contains nearly as much Si as NiAl-Si. In addition, if C alone were the

cause, then it is expected that serrated yielding would be observed in UF-NiAl1 which contains more C than CPNiAl-2 but only 69 appm Si. These results strongly suggest that the serrated yielding in NiAl is a result of interactions between dislocations and solute atoms, namely C and Si but that C is the main cause for the manifestations of DSA observed in the NiAl investigated in this dissertation.

The mechanism by which Si and C can cause serrated flow remains unknown, however two possibilities come to mind: First, it is possible that Si simply modifies the activity coefficient of C in NiAl. It has been observed in austenitic Fe-Mn-C alloys [195,196] that the addition of aluminum raised the activation energy for the onset of serrated flow by reducing the carbon activity, and thus its diffusivity, in these alloys. The opposite effect could occur in the case of NiAl where Si, increases the activity and diffusivity of C in NiAl and thus decreases the activation energy for the onset of serrated flow. However, the results collected in this study indicate that the activation energies for the onset of serrated flow in CPNiAl-1 (0.17 at.% Si), CPNiAl-2 (0.15 at.% Si), and in NiAl-Si (0.25 at.% Si) are similar whereas no activation energy could be calculated for NiAl containing lower Si concentrations.

Second, DSA could be the result of an interaction solid solution hardening (ISSH) effect as described in references [197-201]. This process is attributed to the strengthening that arises from the simultaneous presence in solid solution of substitutional and interstitial atoms that exhibit an affinity for each other. The exact reasons for ISSH are unknown but depend upon whether the interstitial atoms bind more strongly to the substitutional solute atoms or to dislocations [199]. For example, if interstitials bind more strongly to dislocations then strain aging effects will be extended to higher temperatures due to the reduced mobility of the dislocations and dislocation atmospheres. Whereas, if interstitials bind more strongly to substitutional solutes, solid solution strengthening due to interstitials will be extended to higher temperatures than in more pure metals due to a reduction in the mobility of the interstitials due to their association with substitutional solute atoms or due to

the formation of clusters of interstitial and substitutional solute atoms. Diffusion couple studies between NiAl, Ni₃Al, and SiC [202,203] have suggested that Si may diffuse as fast as or faster than C in NiAl and may result in the formation of complex Ni-Al-Si-C phases. This suggests that some clustering of C with Si, Ni, and Al does occur resulting in an expansion of the DSA regime and stronger pinning.

In light of the fact that Si is frequently present in conventional purity NiAl single crystals grown by the Bridgman method due to interactions with the ceramic mold walls, the possible synergistic effect of Si and C on the deformation behavior of NiAl certainly deserves more attention.

Conclusions

Five of the six alloys examined in the present study exhibit yield stress and work hardening plateaus in the temperature range 650 to 1000 K which are indicative of DSA. In HP-NiAl and in UF-NiAl1, such regions were not as obvious.

Pronounced regions of negative SRS have been observed in conventional purity alloys (CPNiAl-1 and CPNiAl-2) in the temperature range 600 to 800 K. Coincident with this temperature regime was the occurrence of serrated flow (*i.e.*, the PLC effect).

In the temperature range where serrated flow occurs, the dislocation distribution consists mainly of dislocation walls or the beginning of a vein structure indicating localized slip. In HP-NiAl and NiAl-Mo, the dislocations maintain cellular networks indicating more abundant and therefore, easier cross slip. At temperatures above or below the regime of serrated flow, well-developed cell structures dominate for all alloys.

Activation energies for serrated flow have been calculated using three methods: 84±10 kJ/mol (ε_c vs. T), 73±1 kJ/mol (stress drop method [188]) and 77±19 kJ/mol (Arrhenius method). All values are reasonable order of magnitude estimates which agree with the prior observations in this dissertation and with Hack and co-workers [14,15,28,29,164]. These results suggest that a combination of interstitial and

substitutional solutes, namely C and Si, cause serrated flow in soft oriented NiAl. Small additions of Mo to NiAl caused a dramatic increase in yield stress and eliminated serrated yielding. This latter effect is attributed to the gettering of C by Mo.
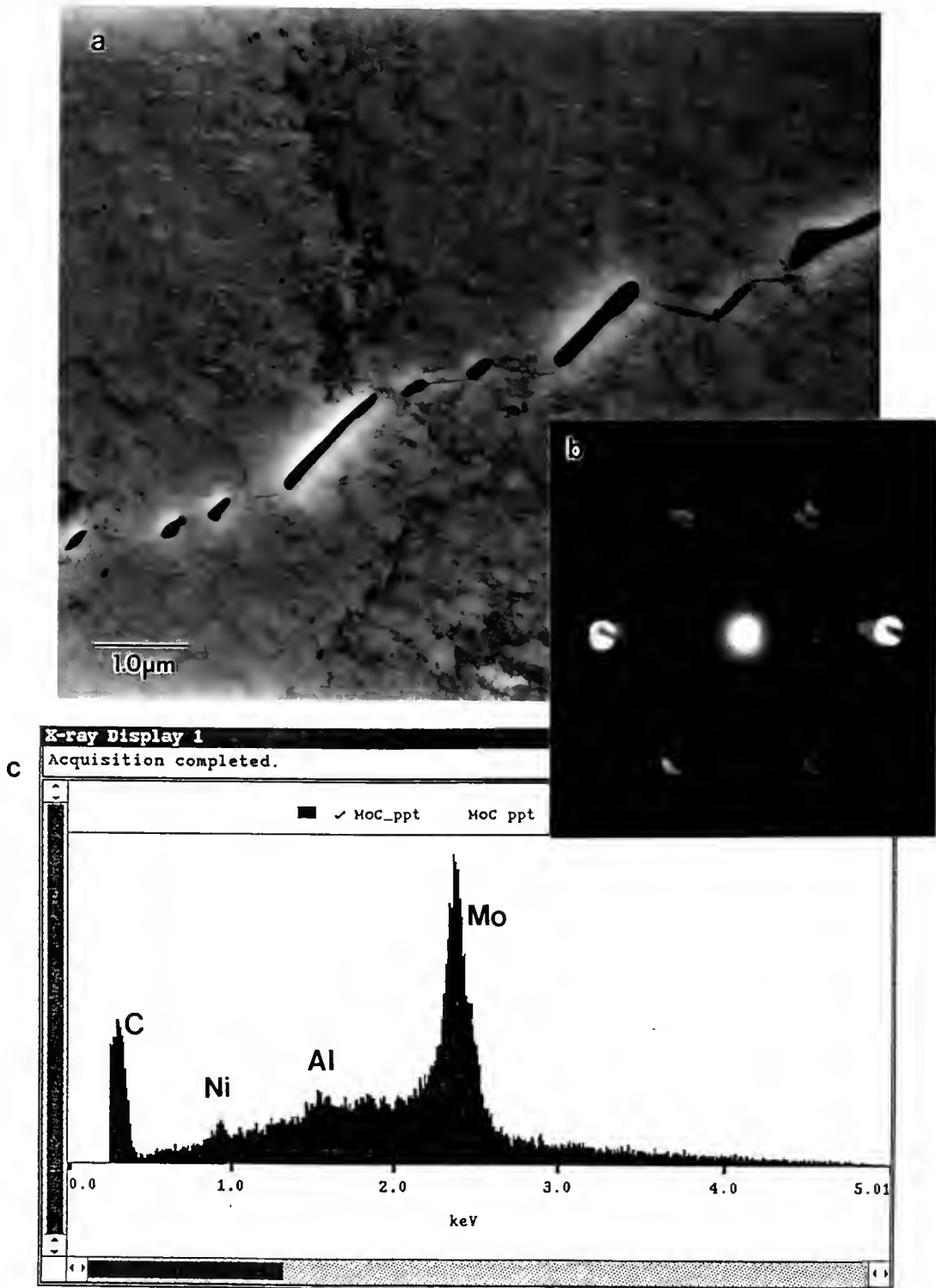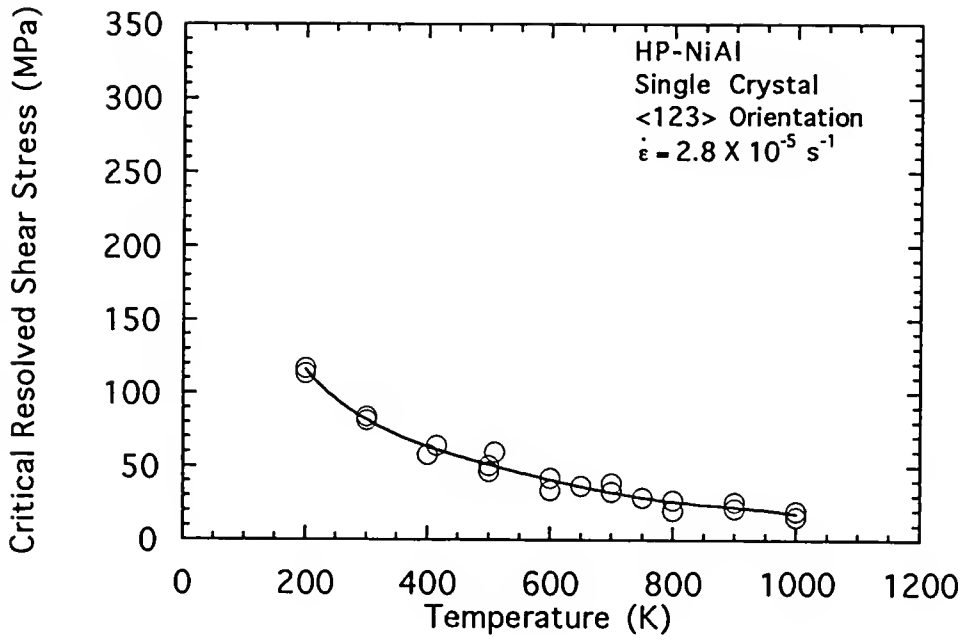
Figure 52.   Precipitates observed in NiAl-Mo: (a) BFTEM micrograph of Mo_2C precipitates in NiAl-Mo; (b) TEM microdiffraction pattern illustrating an orientation relationship ($[112](11\bar{1})_{Mo_2C}$ //$[111](10\bar{1})_{NiAl}$) between the Mo_2C precipitate and NiAl matrix ; and (c) SEM EDS spectra for one of the precipitates indicating that they are indeed Mo_2C.

(a)

(b)
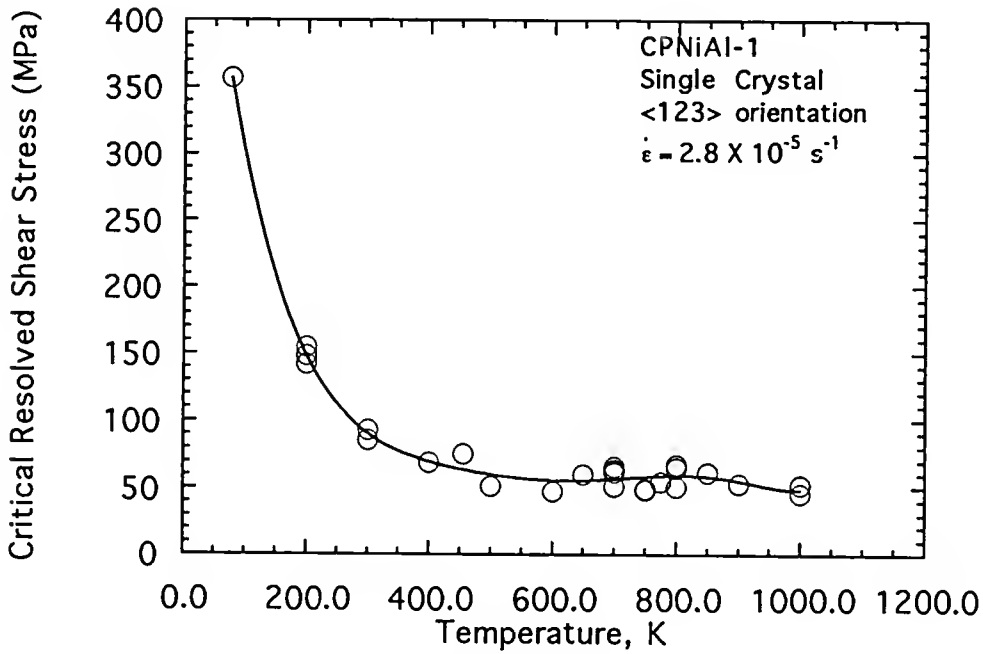
Figure 53.   Temperature dependence of the CRSS at 0.2% strain for NiAl single crystals: (a) HP-NiAl; (b) CPNiAl-1; (c) CPNiAl-2; (d) NiAl-Mo; (e) UF-NiAl1; and (f) NiAl-Si.
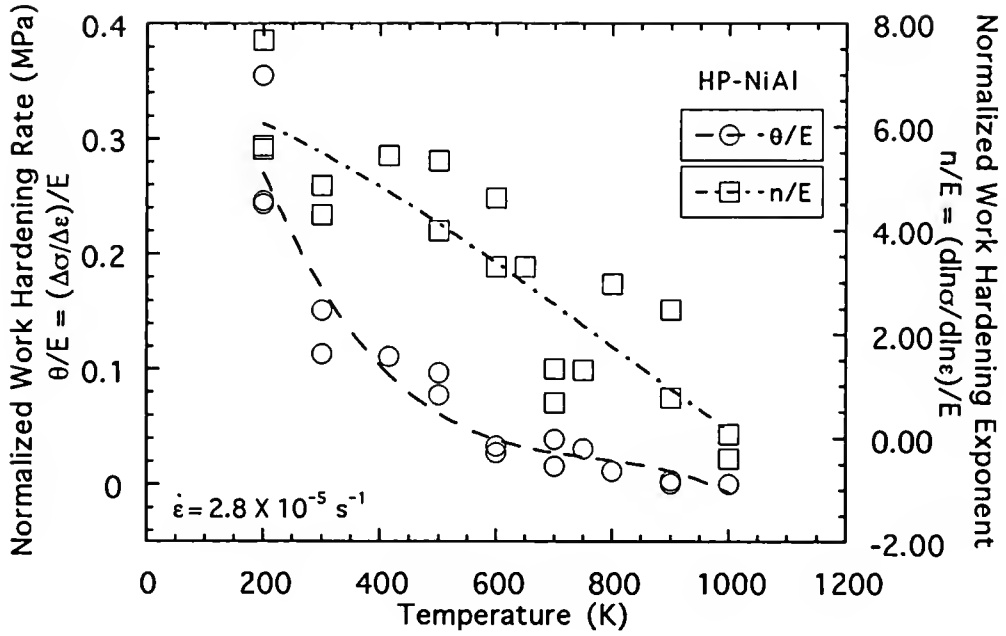
(c)
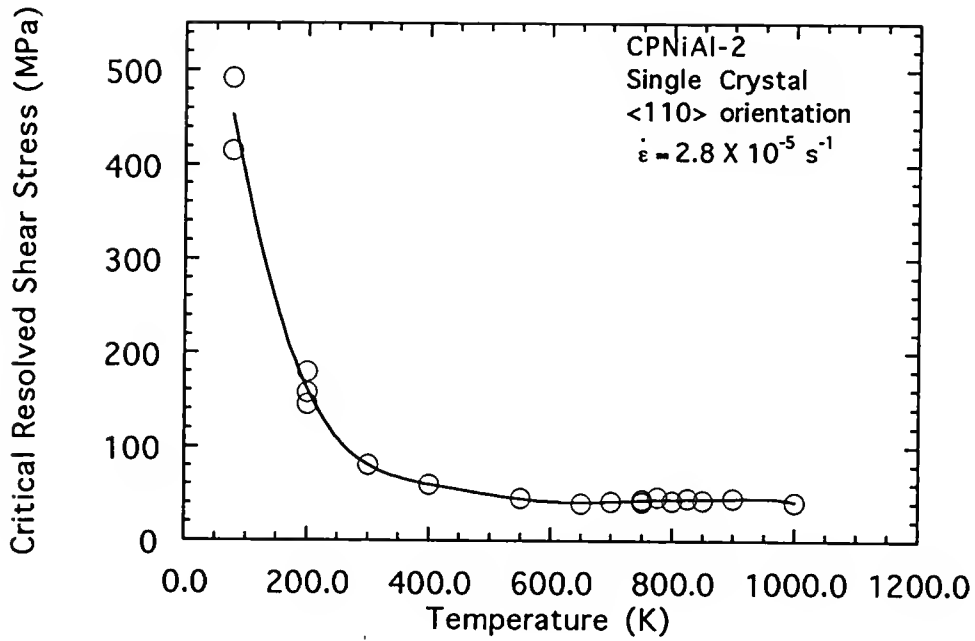
(d)
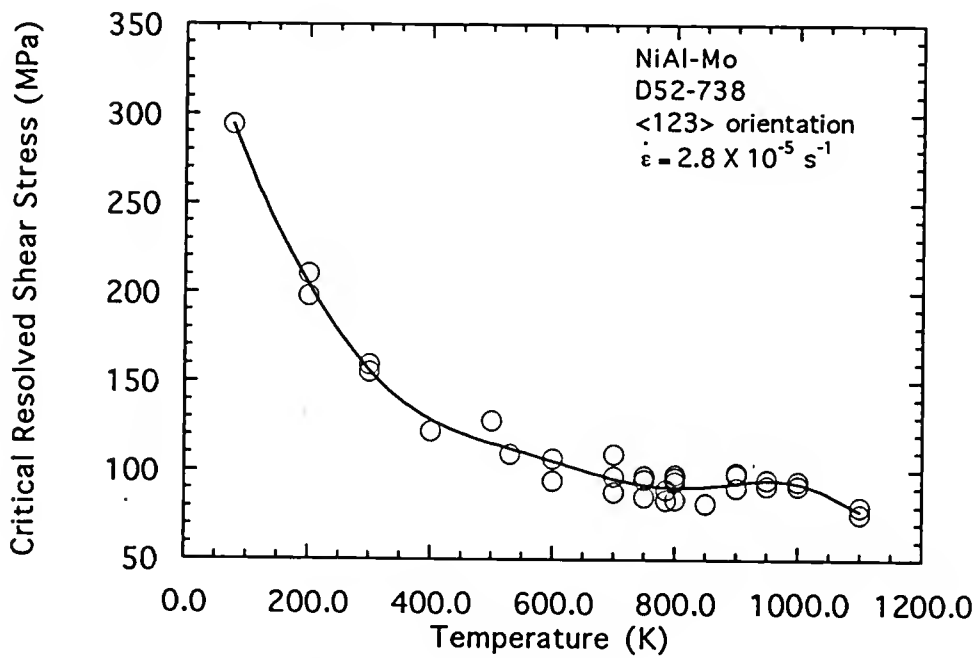
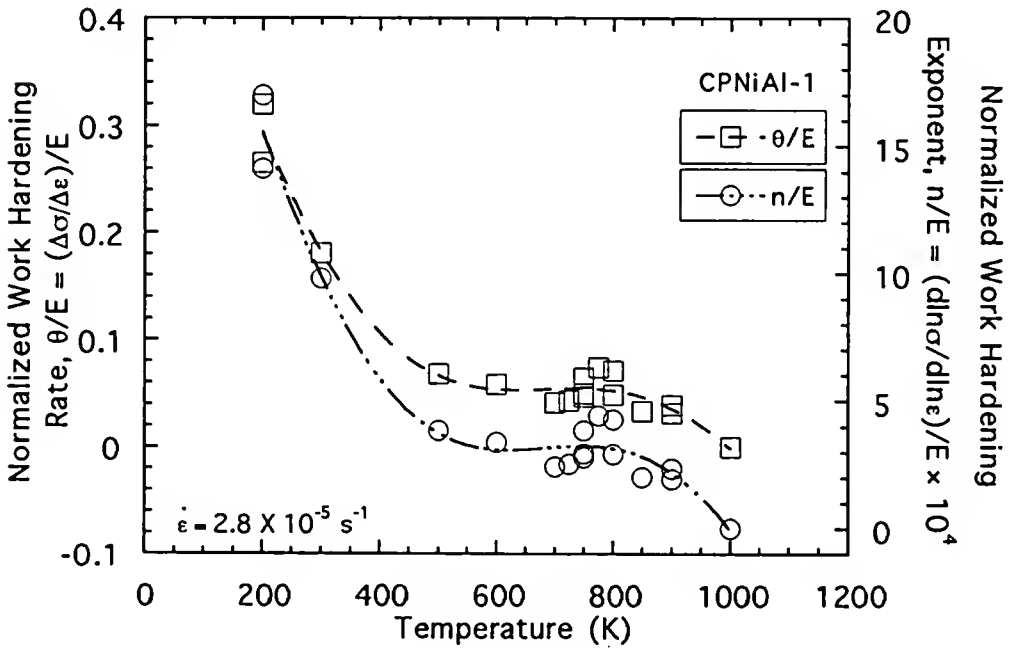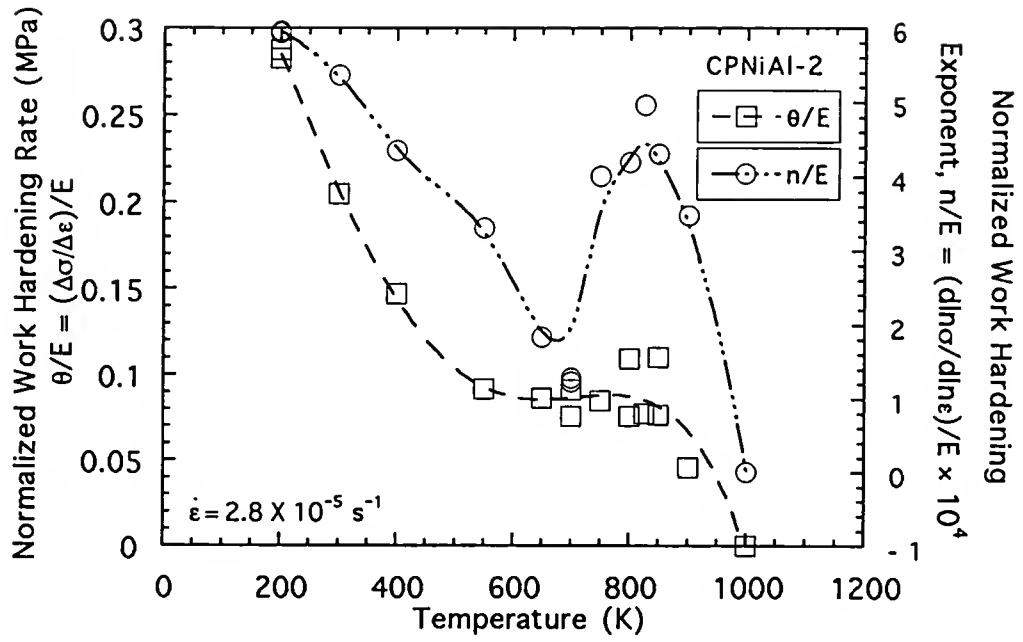Figure 53 -- continued

(e)
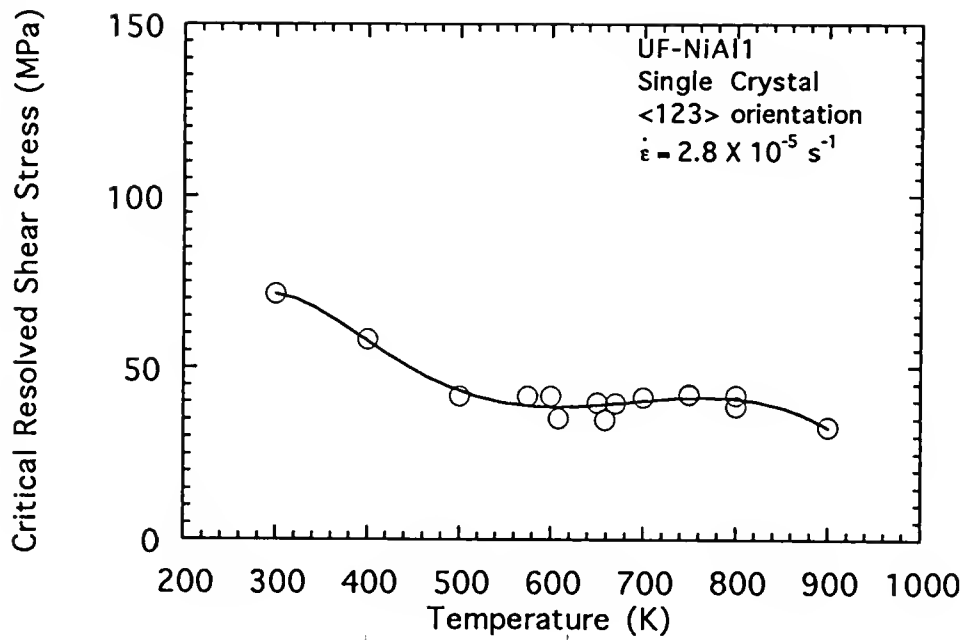
(f)
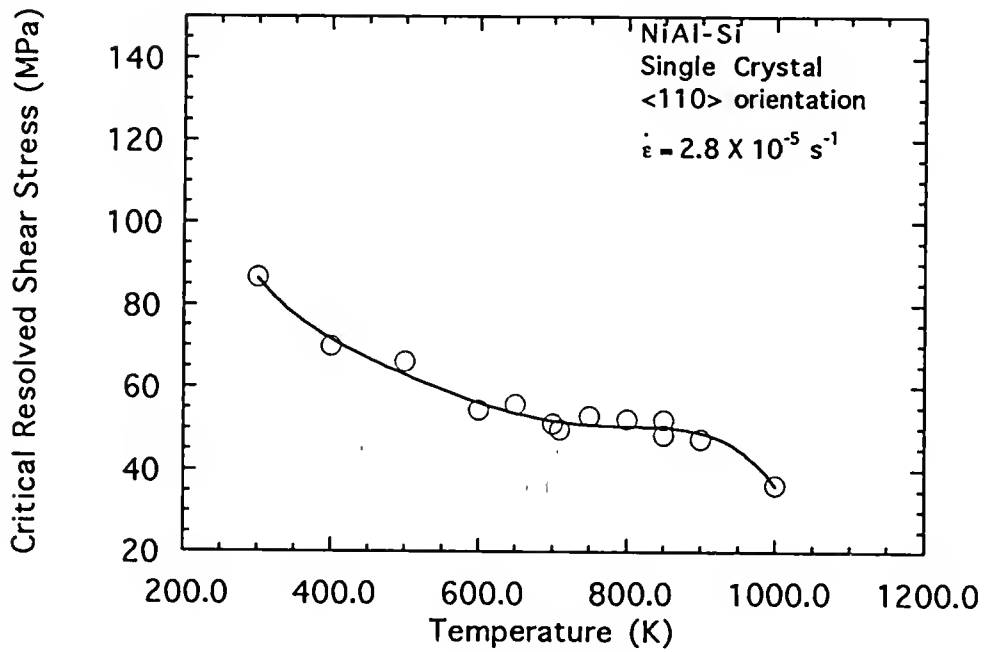
Figure 53 -- continued

Figure 54. Temperature dependence of the normalized work hardening rates, θ/E, and work hardening exponents, n/E, for NiAl single crystals: (a) HP-NiAl; (b) CPNiAl-1; (c) CPNiAl-2; (d) NiAl-Mo; (e) UF-NiAl1; and (f) NiAl-Si.
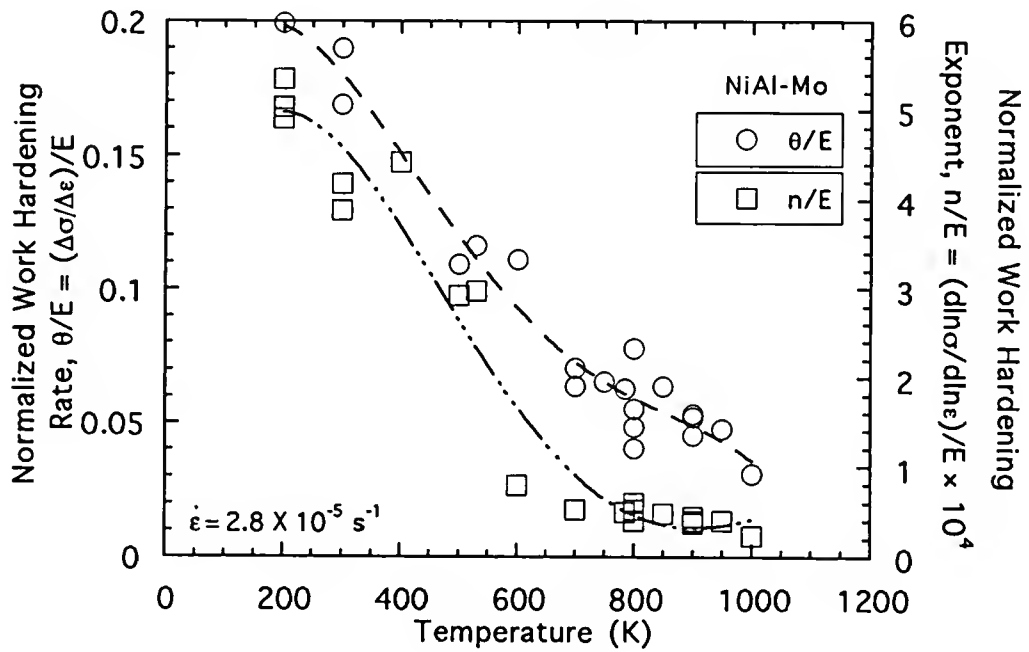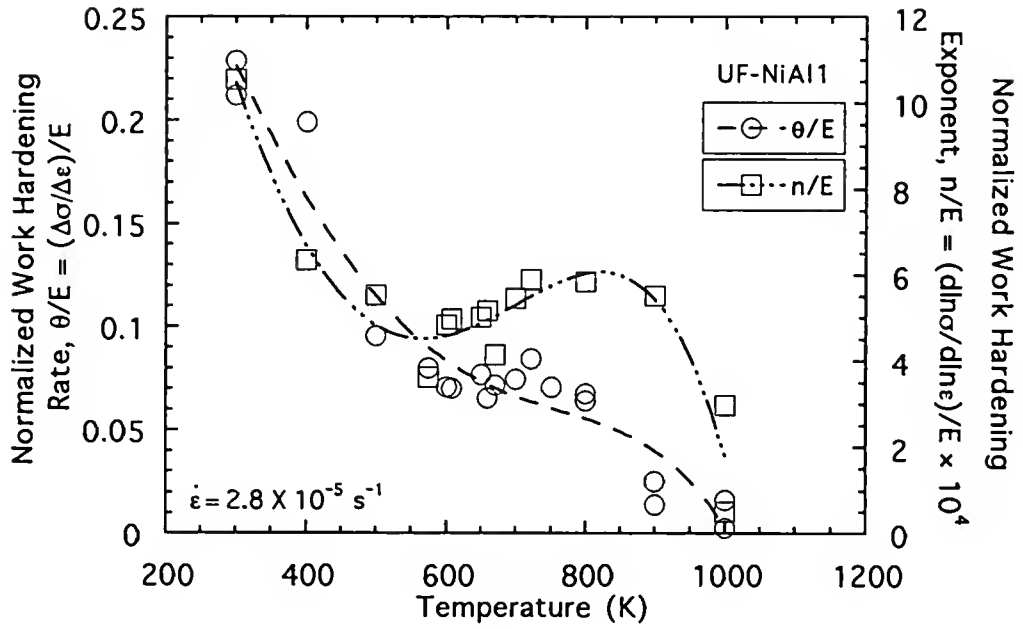
(c)

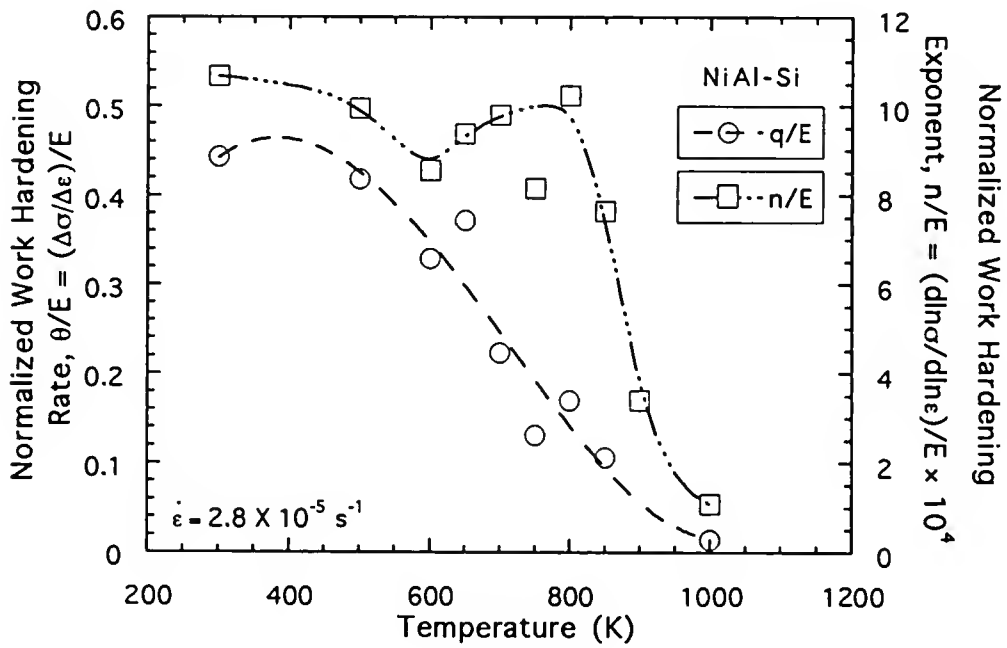(d)

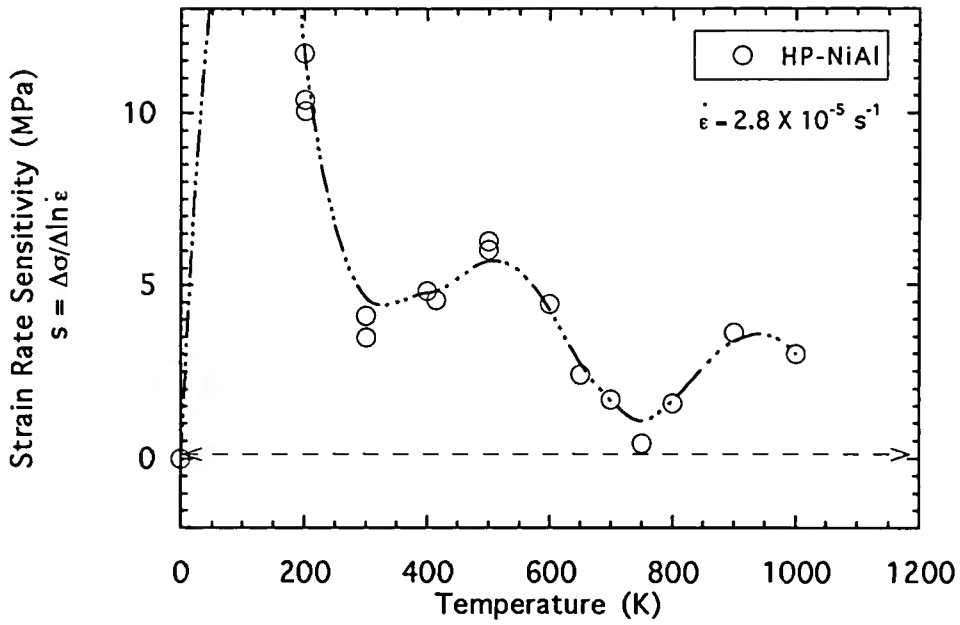
Figure 54 -- continued

(e)

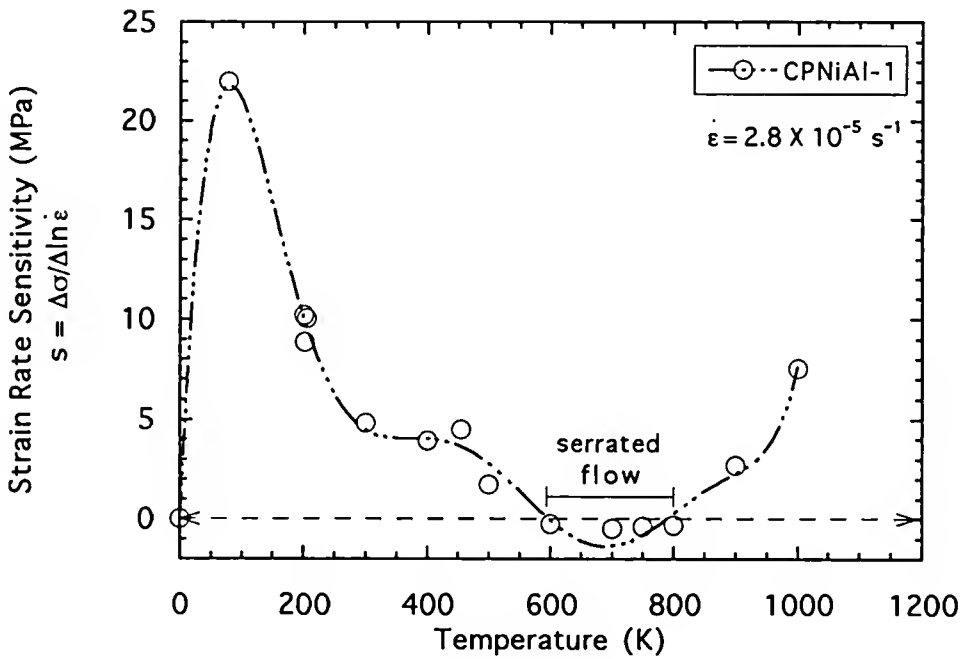

(f)

Figure 54 -- continued

(a)

(b)

Figure 55.   Temperature dependence of SRS for NiAl single crystal: (a) HP-NiAl; (b) CPNiAl-1; (c) CPNiAl-2; (d) NiAl-Mo; (e) UF-NiAl1; and (f) NiAl-Si.

(c)
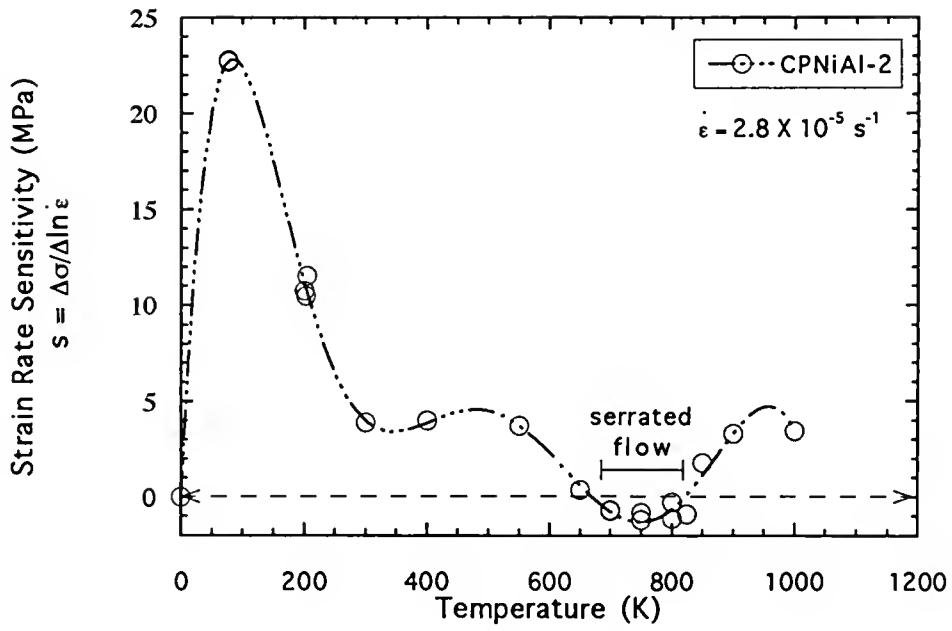
(d)

Figure 55 -- continued

(e)

(f)

Figure 55 -- continued
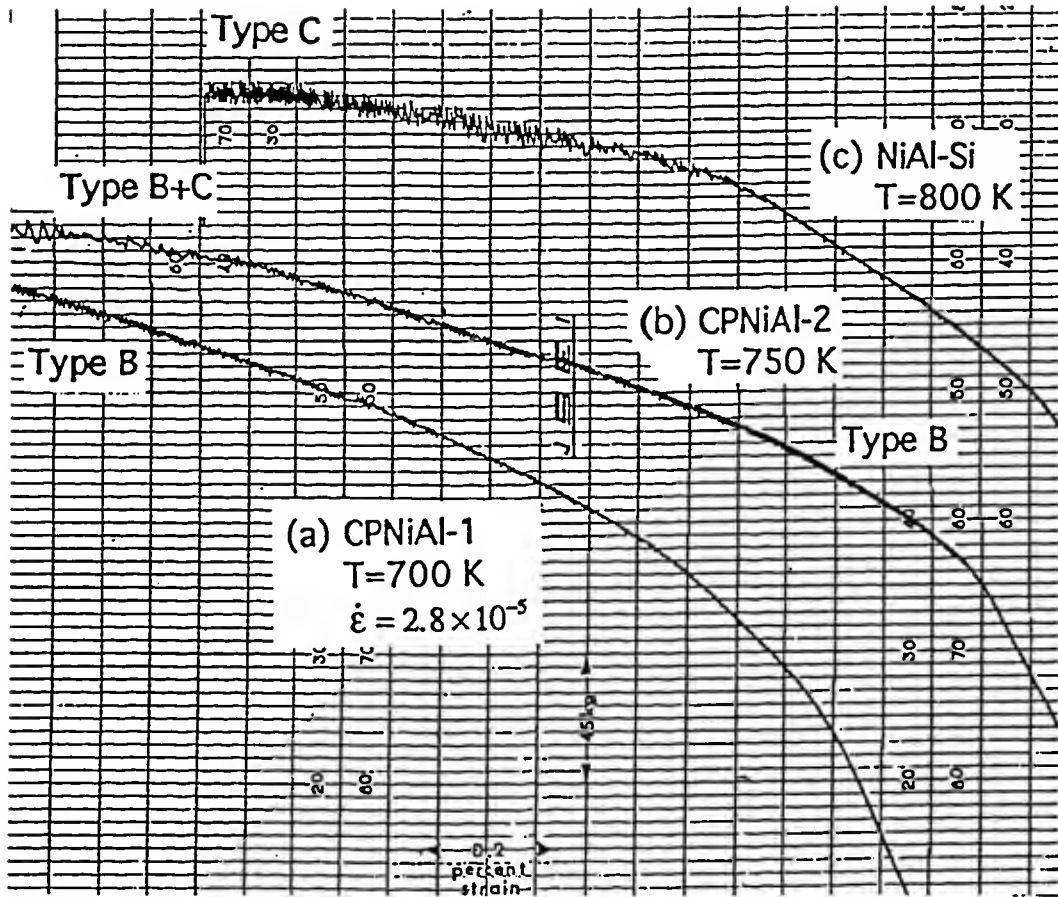
Figure 56.   Examples of flow stress serrations observed in CPNiAl-1, CPNiAl-2, and NiAl-Si deformed in the negative SRS regime. (a) CPNiAl-1, T=700 K; (b) CPNiAl-2, T=750 K; and (c) NiAl-Si, T=800 K (strain rate = 2.8×10^{-5} s^{-1}). Note the transition from type B serrations at lower temperatures to type C serrations at higher temperatures.

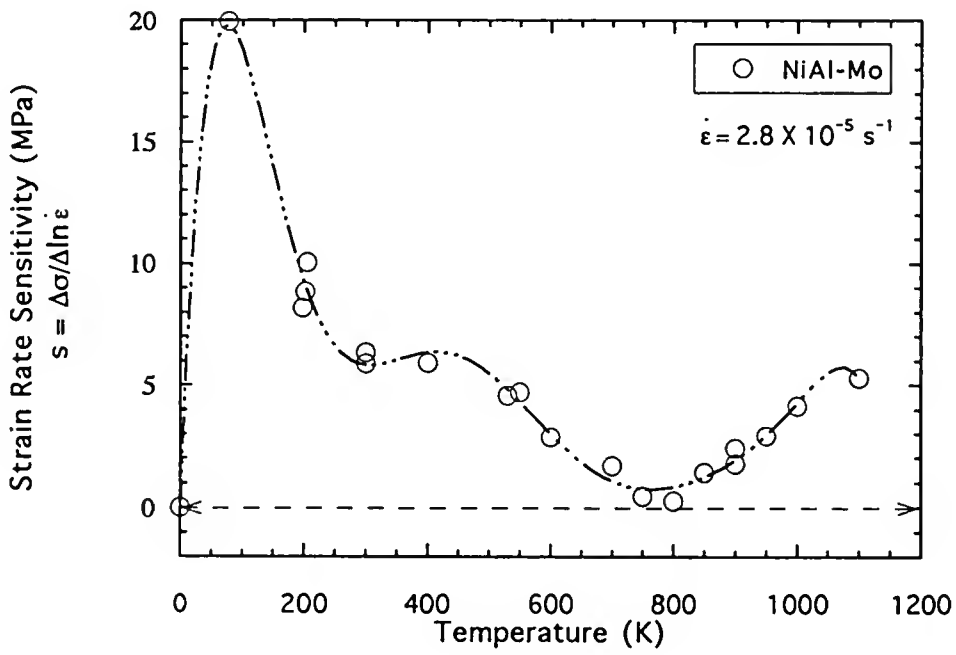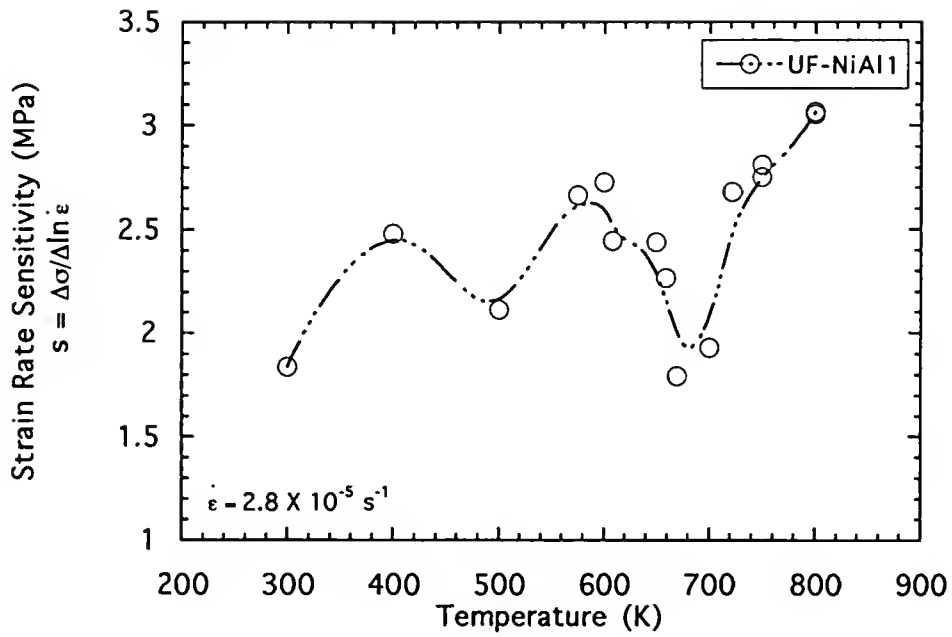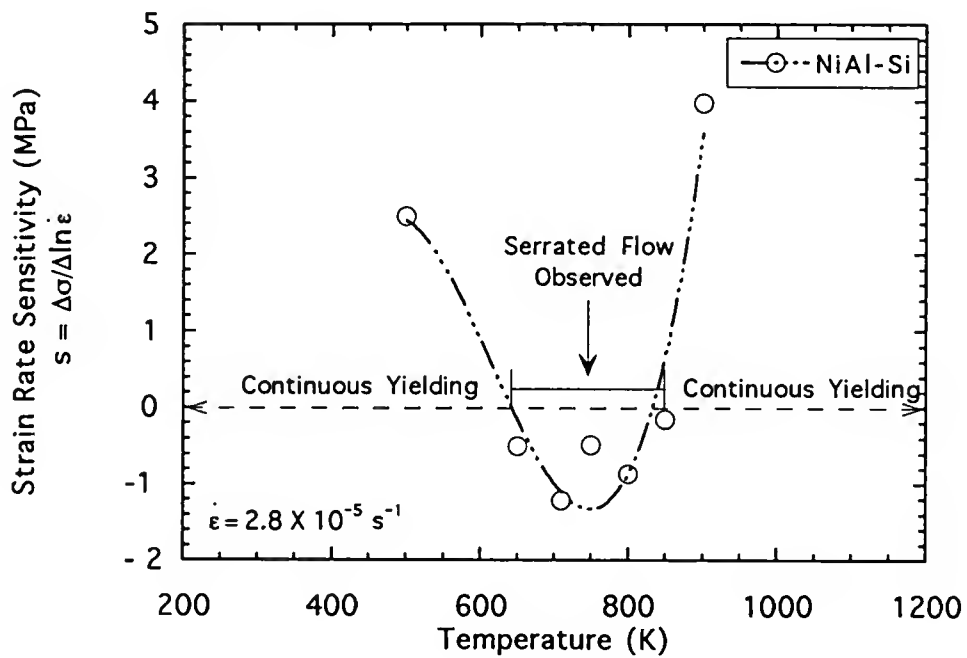$$\dot{\varepsilon} = \varepsilon_c^{m+\beta} \times KC^n \exp(-Q/RT)$$

(a)

CPNiAl-1
T = 750 K
m + β = 1.27

NiAl-Si
T = 800 K
m + β = 0.98

CPNiAl-2
T = 750 K
m + β = 0.98

Legend: CPNiAl-1, CPNiAl-2, NiAl-Si

Strain Rate (s^{-1}) vs Critical Strain

(b)

CPNiAl-1
Q = 94 kJ/mol

CPNiAl-2
Q = 82 kJ/mol

NiAl-Si
Q = 75 kJ/mol

$\dot{\varepsilon} = 2.8 \times 10^{-5} \, s^{-1}$

Legend: CPNiAl-1, CPNiAl-2, NiAl-Si

Critical Strain (%) vs $1/T$ (K^{-1})
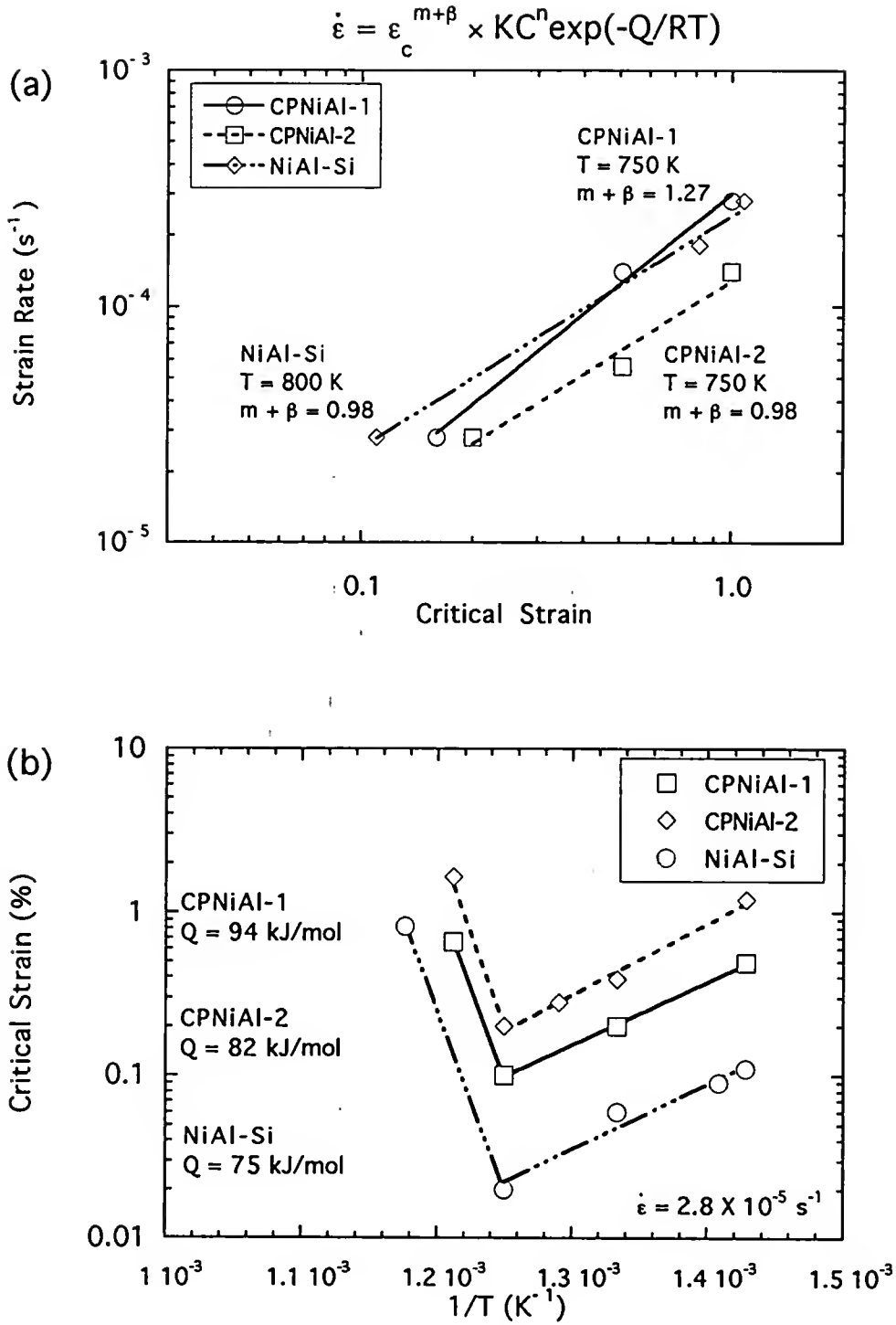
Figure 57.   The influence of $\dot{\varepsilon}$ and T on the critical strain for the onset of serrated flow, ε_c for CPNiAl-1, CPNiAl-2, and NiAl-Si: (a) ln $\dot{\varepsilon}$ versus ln ε_c and (b) ln ε_c versus 1/T.
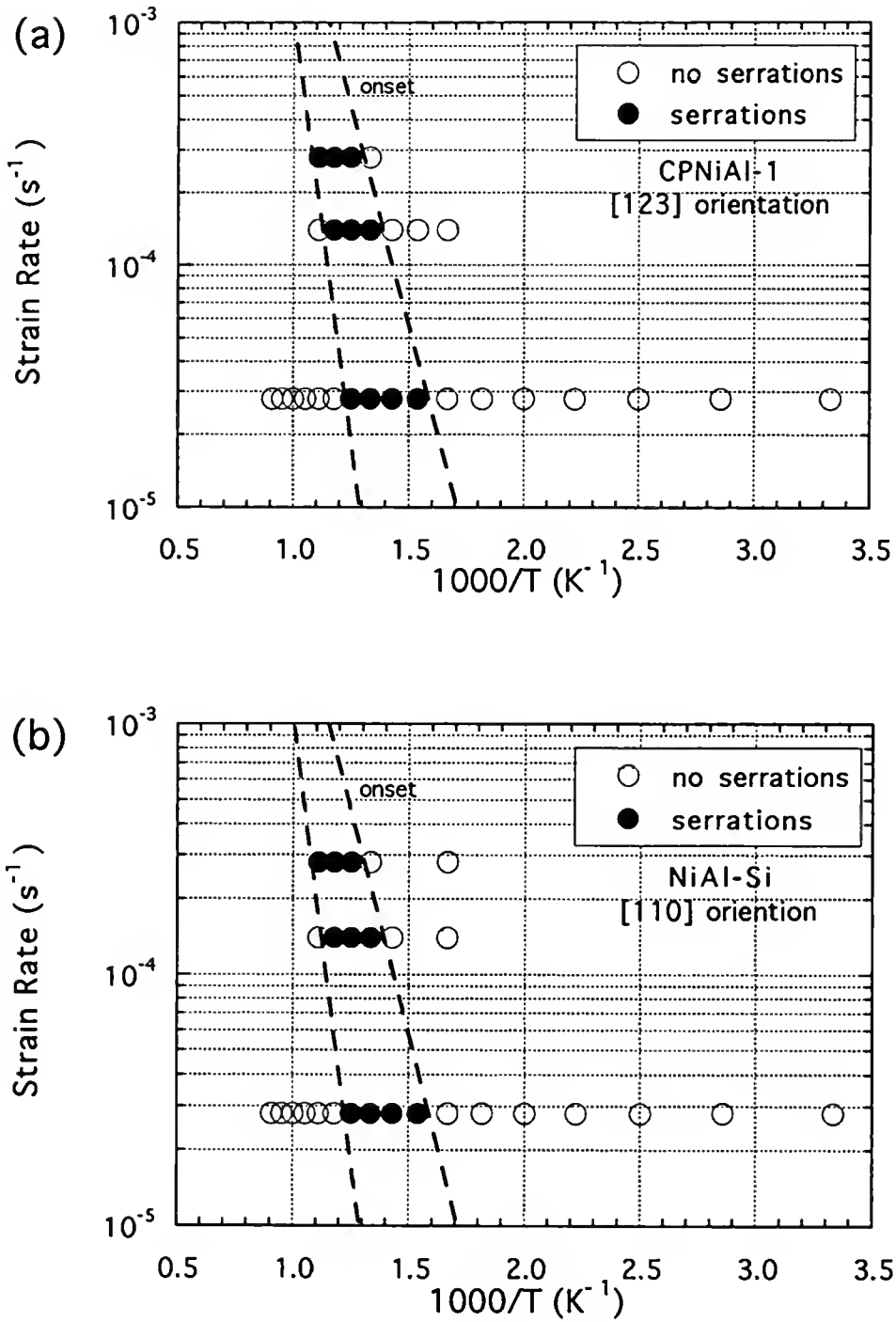
Figure 58. Plots of ln $\dot{\varepsilon}$ versus 1/T for CPNiAl-1 and NiAl-Si illustrating the T-$\dot{\varepsilon}$ regimes for serrated flow. (a) CPNiAl-1 and (b) NiAl-Si.
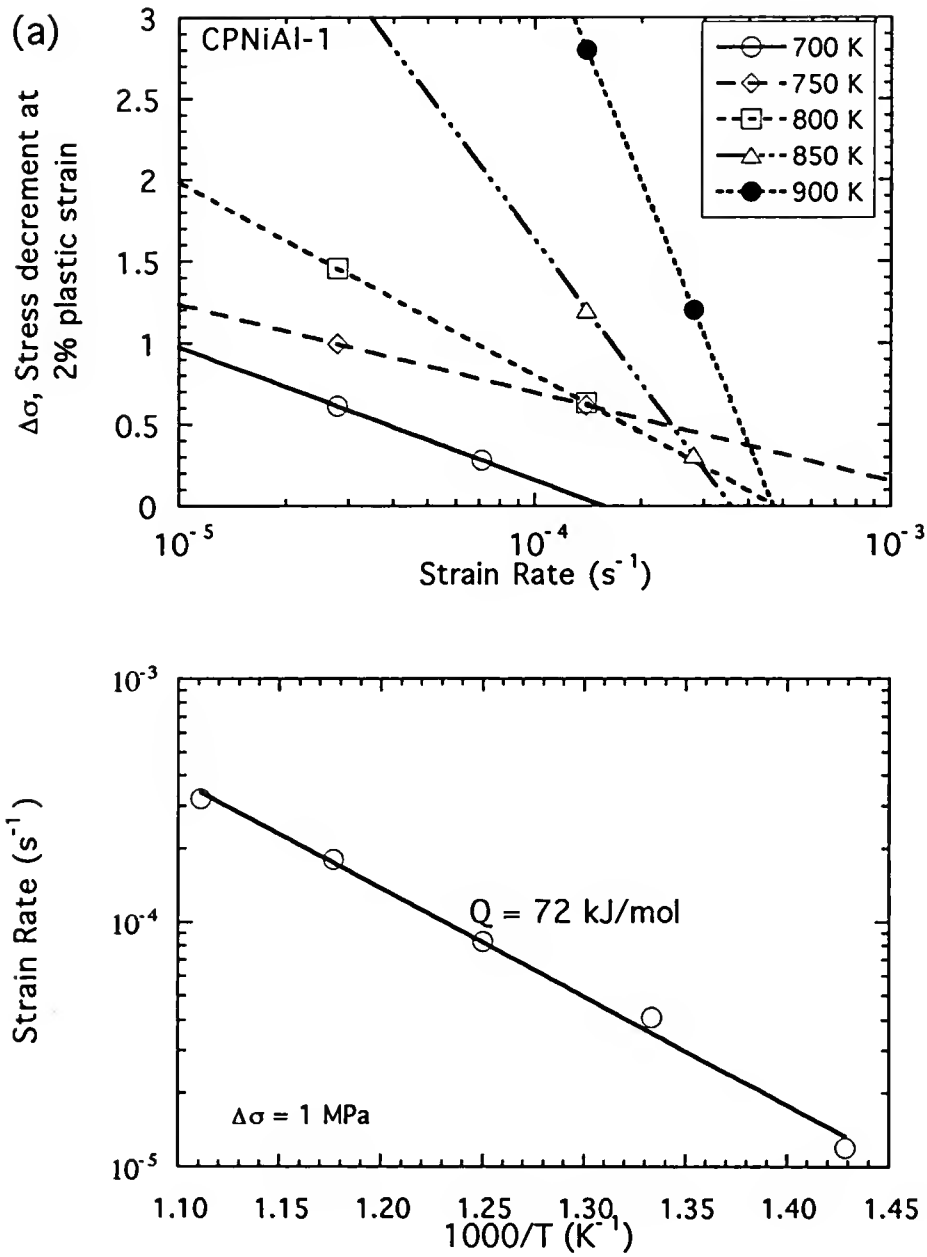
Figure 59.   Plots of the stress drop at 2% plastic strain versus $\dot{\varepsilon}$ at constant T and $\dot{\varepsilon}$ versus 1/T for CPNiAl-1, CPNiAl-2, and NiAl-Si illustrating use of the stress drop method for determining activation energy [188]. (a) CPNiAl-1, (b) CPNiAl-2, and (c) NiAl-Si.
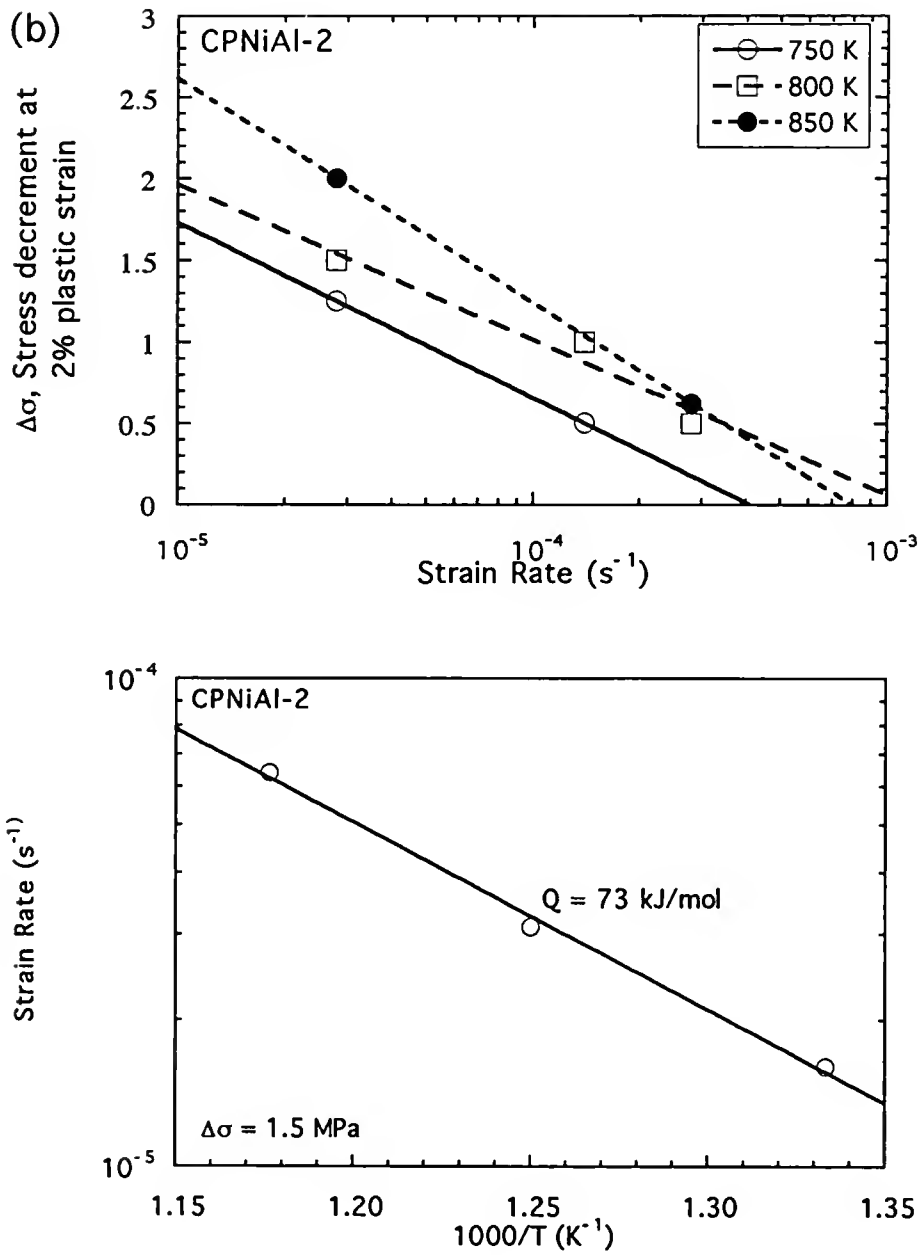
Figure 59 -- continued
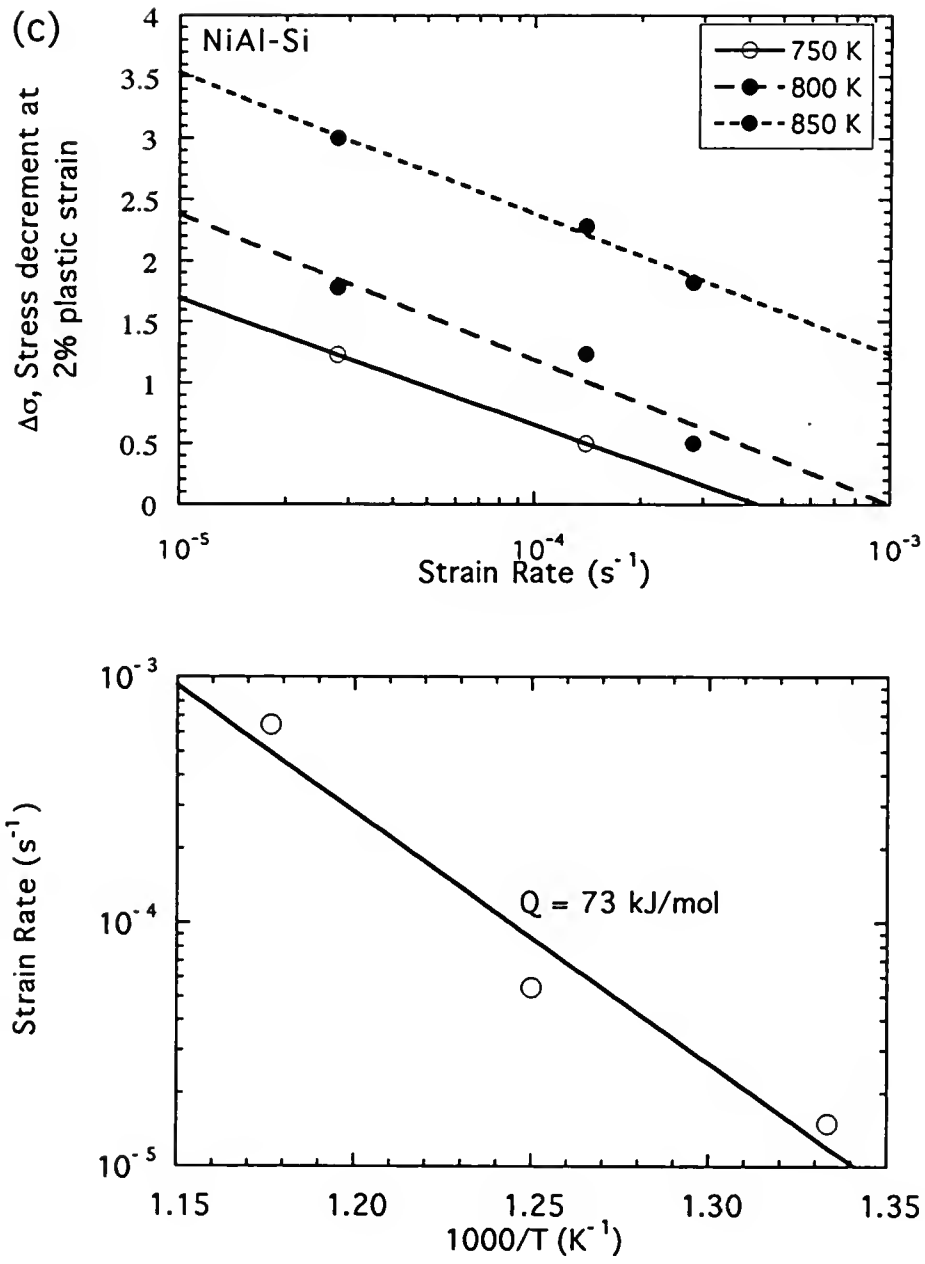
Figure 59 -- continued
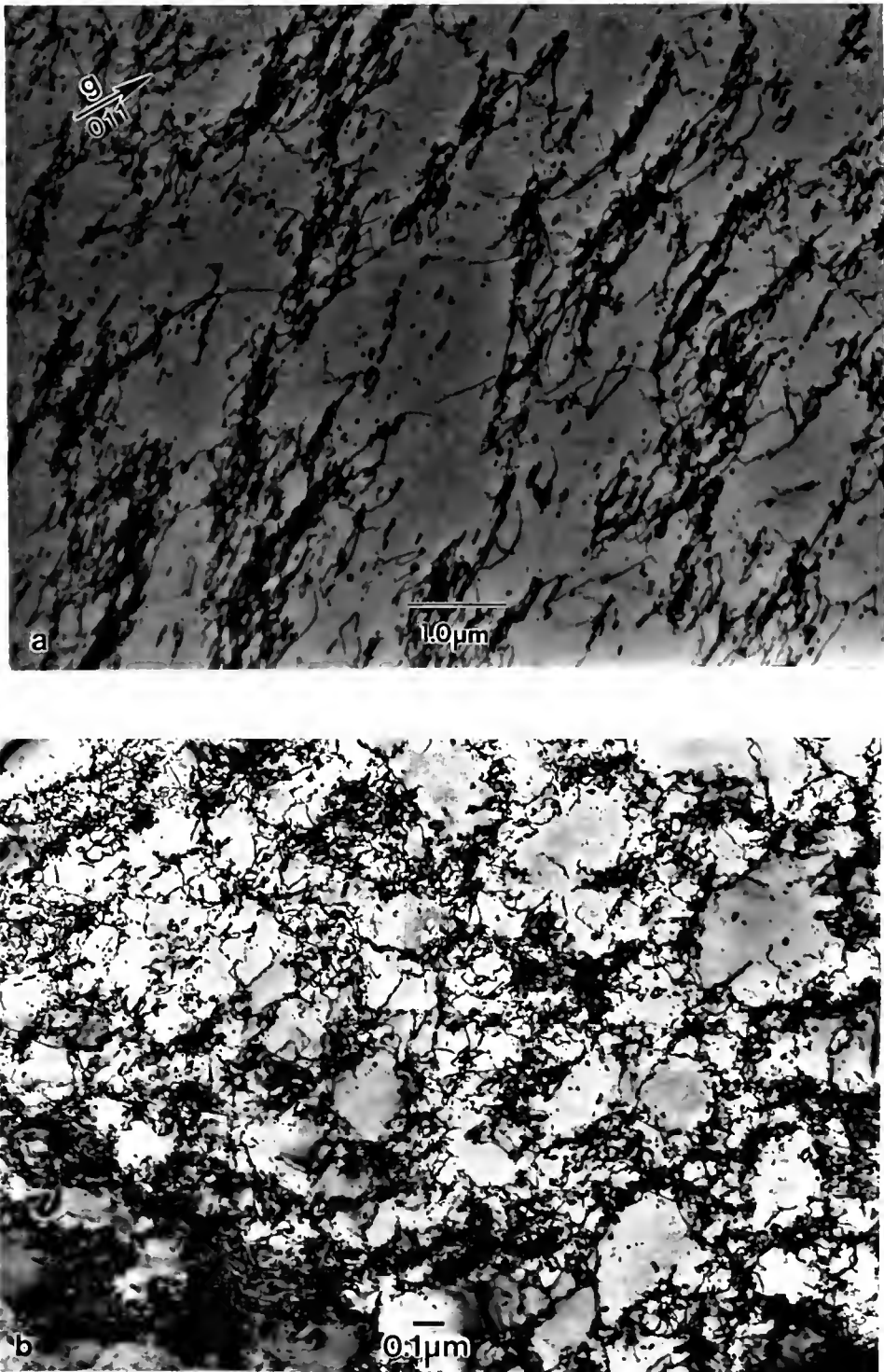
Figure 60.   Room-temperature deformation structure observed in CPNiAl-2: (a) after ~0.2% plastic deformation, and (b) after ~2% plastic deformation.
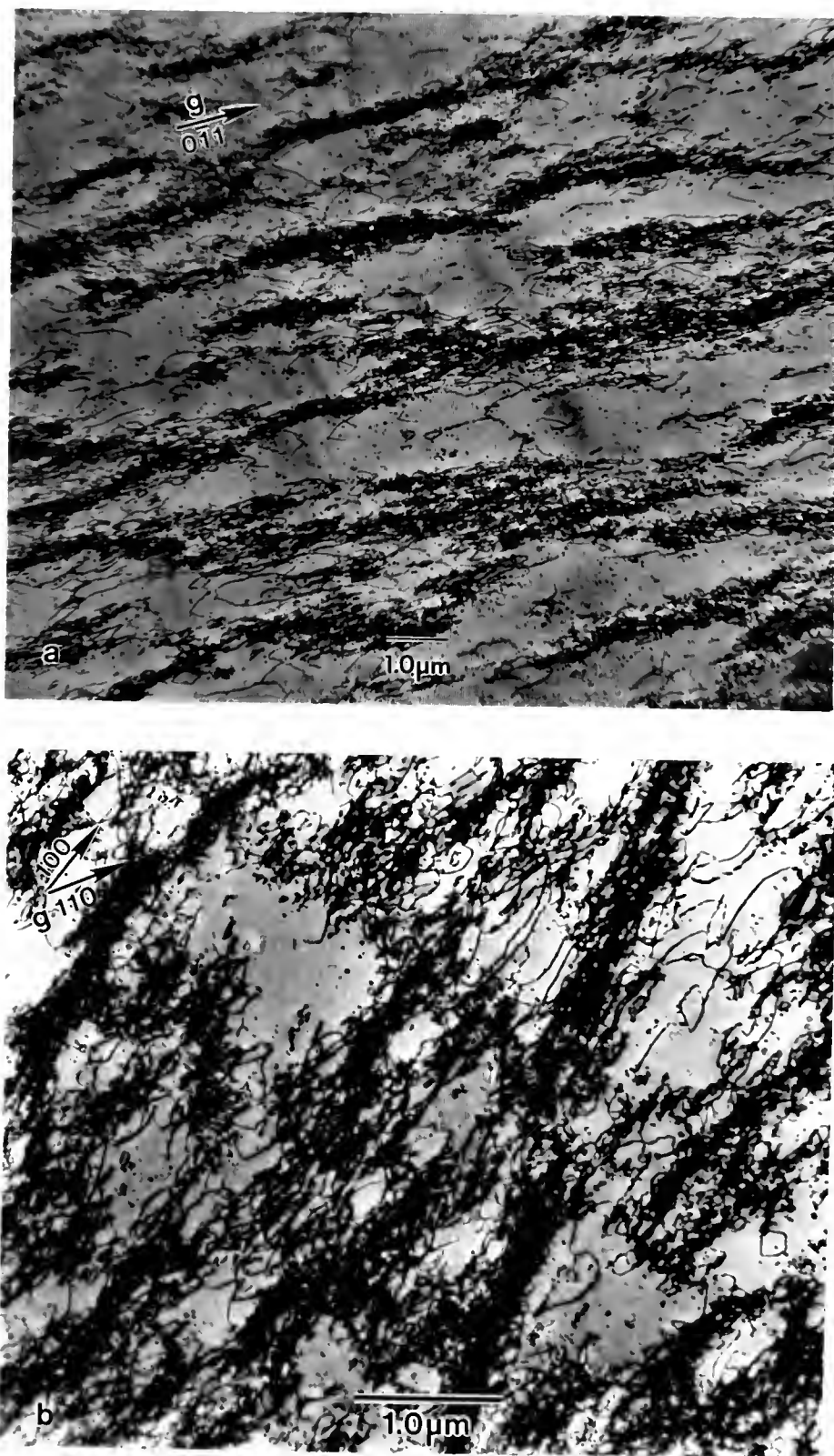
Figure 61.   Deformation structures observed in CPNiAl-2 and NiAl-Si after ~17% plastic deformation at 700 and 800 K. (a) CPNiAl-2 at 700 K and (b) NiAl-Si at 800 K.
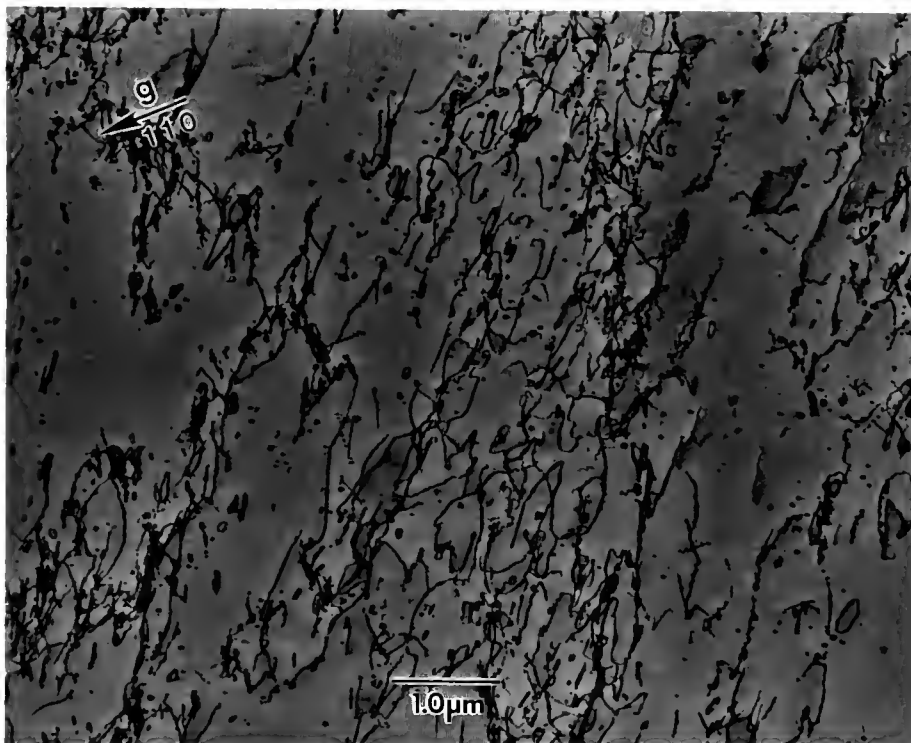
Figure 62.   Dislocation morphology observed in CPNiAl-1 after 11% deformation at 1000 K.
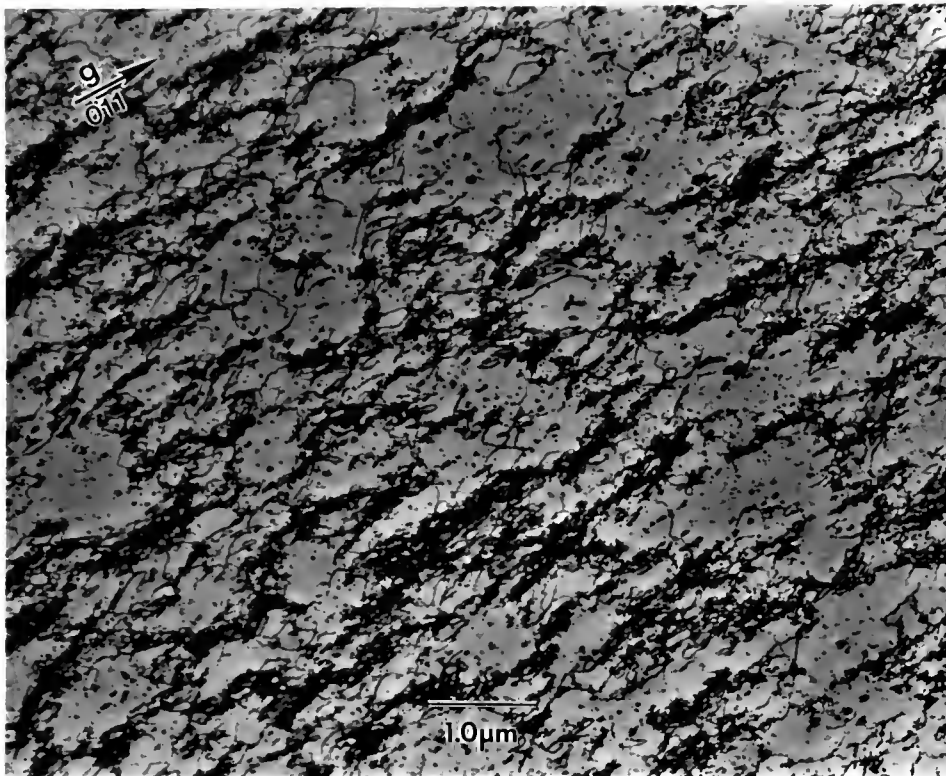
Figure 63.   Deformation structure observed in NiAl-Mo after 9% plastic deformation at 700 K.
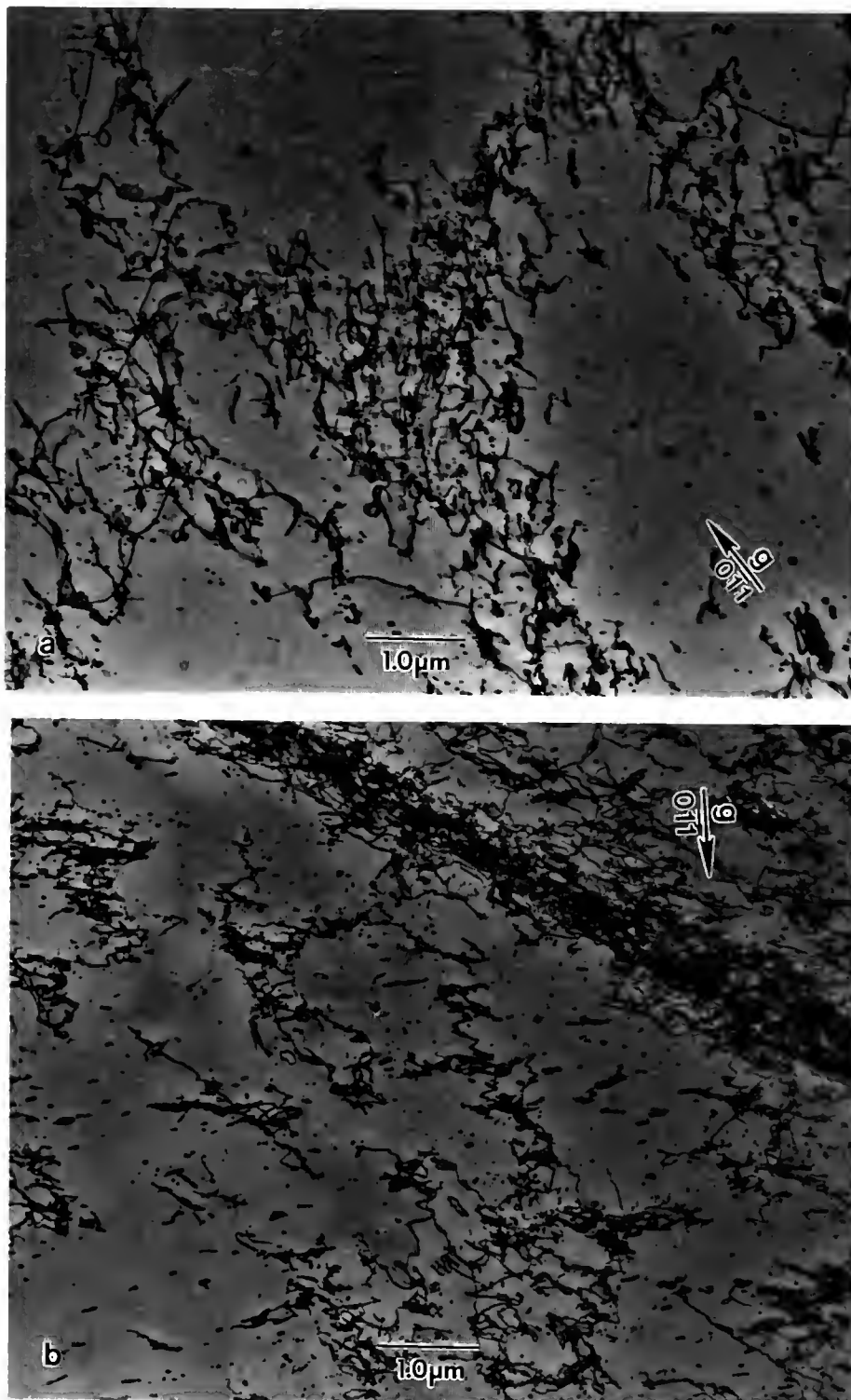
Figure 64.   Deformation structure observed in HP-NiAl after 9% plastic deformation at 725 K. (a) Cellular morphology observed in most samples and (b) a single deformation band observed in one of the foils.

CHAPTER 8
MODELLING DSA EFFECTS IN SINGLE AND POLYCRYSTALLINE NiAl

The results and discussions provided in the previous seven chapters have shown that behavior consistent with the occurrence of strain aging is observed in conventional purity NiAl alloys and that this phenomenon can be reduced, but not necessarily eliminated, by microalloying with reactive ternary additions such as Ti or Mo, or by zone refining to decrease impurity levels. All alloys investigated in this study exhibited a dramatic SRS minimum near 750 K and a smaller minimum near 400 K.

These manifestations can be rationalized using the phenomenological model for DSA developed by Reed-Hill and co-workers [1-3,115,116]. The basic assumptions of this model are: (1) The total flow stress consists of two parts, one that is independent of DSA and one that is DSA dependent; (2) the thermal component (*i.e.*, the effective stress) of the DSA-independent stress obeys a power law relationship:

$$\sigma^* = \sigma_0^* \left(\frac{\dot{\varepsilon}}{\dot{\varepsilon}_0} \right)^{RT/H^o} \tag{43}$$

where the exponent RT/H^o is the strain rate sensitivity measured under conditions where ε is directly proportional to the dislocation velocity, v, H^o is a material parameter with units of energy, σ^* is the effective component of the flow stress, σ_o^* is the effective stress at 0 K, $\dot{\varepsilon}$ is the base strain rate, and $\dot{\varepsilon}_0$ is a constant equal to $\rho_m \bar{b} v_0$. The universal gas constant, R, has been used rather than Boltzmann's constant to yield results with units of energy. It is further assumed that: (3) sufficient strain rate sensitivity and flow stress versus temperature data must exist at temperatures below the plateau region (*i.e.*, where DSA does not occur); (4) the temperature dependence of the elastic modulus must be

known; (5) the temperature dependence of the internal stress is related to that of the elastic modulus, E, by the equation

$$\sigma_E = \frac{\sigma_{E_o} \cdot E}{E_o}$$ (44)

where E_o represents the elastic modulus at 0 K and $\sigma_{E_\bullet}$ represents the internal stress at 0 K. Finally, (6) it is assumed that the applied stress is assumed to be the sum of its internal, σ_E, and effective, σ^*, components. Thus,

$$\sigma = \sigma_E + \sigma^*.$$ (45)

At temperatures where DSA occurs, a DSA component, σ_{DSA}, which itself consists of two components (*i.e.*, $\sigma_{DSA} = \sigma_{snoek} + \sigma_{cottrell}$) is added to equation (44). In studies of strain aging the strain rate sensitivity, which was expressed above as n, may also be expressed as $s = d\sigma/d\ln\dot{\varepsilon}$. Considering the assumptions listed above, it can be shown that the strain rate sensitivity, s, is related to the flow stress and the strain rate by the following equation

$$s = \frac{RT}{H^o}\sigma_o^*\left(\frac{\dot{\varepsilon}}{\dot{\varepsilon}_o}\right)^{RT/H^o}$$ (46)

where σ_o^* is the effective stress at 0 K. Plotting s versus temperature yields a curve containing a single maximum as illustrated in Figure 65. At the maximum of this curve it can be shown that the following relationships apply:

$$T_{max} = -\frac{1}{\left(R/H^o\right)\ln(\dot{\varepsilon}/\dot{\varepsilon}_o)}$$ (47)

$$S_{max} = -\frac{\sigma_o^*}{e \times \ln(\dot{\varepsilon}/\dot{\varepsilon}_o)}$$ (48)

$$\sigma_{max}^* = \sigma_o^*/e$$ (49)

$$H^o = \frac{RT_{max}\sigma_{max}^*}{s_{max}}$$ (50)

$$\dot{\epsilon}_0 = \dot{\epsilon}\exp\left(\frac{\sigma^*_{max}}{s_{max}}\right) \qquad (51)$$

where e is the base of the natural logarithm, s_{max} the strain rate sensitivity peak, T_{max} the temperature at s_{max}, σ_{max} the effective stress at T_{max}, and σ_0 the effective stress at 0 K. These relationships can be used in conjunction with equation (44) to derive the following expression for the internal stress at 0 K:

$$\sigma_{E_0} = \frac{\sigma_0 - e\sigma_{max}}{\left(1 - \frac{e \cdot E_{max}}{E_0}\right)} \qquad (52)$$

where σ_0 and σ_{max} can be extrapolated from the experimental data. Thus, only data concerning the temperature dependence of the elastic modulus is required to determine σ_{E_0}.

Examples of the application of this model to the polycrystalline NiAl data of Pascoe and Newey [12,166] and to the polycrystalline NiAl-100CO and single crystal CPNiAl-2 (<110> orientation) data presented in Chapters 6 and 7 are presented in Figures 66-69.

Pascoe and Newey [12,166] used a base strain rate of 2.2×10^{-4} s^{-1}. For Ni-48.9 at.%Al, the maximum in the strain rate sensitivity plot was judged to occur at $s_{max} = 23.6$ MPa and $T_{max} = 103$ K. For Ni-43.0 at.%Al, no definite maximum was given but it was assumed to occur at $s_{max} = 32.1$ MPa and $T_{max} = 150$ K which represents the first data point for this alloy. Extrapolating the flow stress data to 0 K we find $\sigma_0 = 2000$ MPa and $\sigma_{max} = 750$ MPa at 103 K for Ni-48.9 at.% Al and $\sigma_0 = 3100$ MPa and $\sigma_{max} = 1380$ MPa at 150 K for Ni-43.0 at.%Al.

In this dissertation, base strain rates of 1.4×10^{-4} and 2.8×10^{-5} s^{-1} were used for the NiAl-100CO and the CPNiAl-2 single crystal respectively. For NiAl-100CO, the actual SRS maximum was not determined. It was determined, however, using the method outlined by Iswaran et al. [115] to occur at $s_{max} = 21$ MPa at $T_{max} = 114$ K. Similarly, for CPNiAl-2, the values were determined to be $s_{max} = 23$ MPa and $T_{max} = 109$ K.

Extrapolating the flow stress data to 0 K yielded $\sigma_0 \cong 2100$ MPa and $\sigma_{max} \cong 800$ MPa for both alloys. The temperature dependence of the elastic modulus has been found to vary significantly with processing technique but not with composition [7,18]. For this analysis we have adopted the recent equation of Hellman *et al.* [204] which was derived for a powder-processed alloy of Ni-50.6 at.%Al. Assuming that this equation may be applied to off-stoichiometry extruded alloys, we describe the modulus as follows:

$$E \text{ (GPa)} = 249.3 - 0.031T + 1 \times 10^{-5}T^2 \qquad (53)$$

which yields values of $E_0 = 249.3$ GPa for the Pascoe and Newey alloys and for NiAl-100CO and $E_{max} = 246.2$ GPa for Ni-48.9 at.%Al, $E_{max} = 244.9$ GPa for Ni-43.0 at.%Al, and $E_{max} = 245.9$ for NiAl-100CO. For analysis of CPNiAl-2, which is a <110> oriented single crystal, the equation of Wasilewski [57], which describes the principal elastic moduli over the temperature range 123-1073 K, has been adopted:

$$E \text{ (GPa)} = 184.6-0 - 0.035 \times (T-298) \qquad (54)$$

which yields values of $E_0 = 195$ GPa and $E_{max} = 191$ GPa. Substituting these values into equations (43)-(52) it was possible to determine internal stresses for all four alloys as summarized in Table 12.

A second method for determining the constants H_0 and $\dot{\epsilon}_0$ is from a plot of the strain-rate sensitivity n versus T. A plot of n versus temperature should be linear where DSA is not a factor. Using the n versus temperature data of Pascoe and Newey [32,205], we determined H_0 to be 58,561 J/mol for Ni-43.0 at.% Al and 23,077 J/mol for Ni-48.9 at .% Al which, for Ni-48.9 at.%Al, compares favorably with the data presented in Table 12. The poor correlation for Ni-43.0 at.%Al is attributed to a lack of sufficient low temperature data for this alloy.

In Chapter 2 it was shown that the DSA component of the flow stress is given by the equation:

$$\sigma_{DSA} = \exp(B \times (T - 400)) \times$$

$$\times \left\langle \sigma_{s_{max}} \left\{ 1 - \exp\left[-\left(\frac{t_w}{\tau_s} \right) \right] \right\} + \sigma_{c_{max}} \left\{ 1 - \exp\left[-\left(\frac{t_w}{\tau_c} \right)^{2/3} \right] \right\} \right\rangle \qquad (55)$$

Table 12. Calculated values of σ_{E_0}, H^o and $\dot{\varepsilon}_0$ for the NiAl alloys.

Alloy	σ_{E_0} (MPa)	H^o J/mole	$\dot{\varepsilon}_0$ s^{-1}
Ni-43.0 at.% Al	389.9	38,442.4	5.4×10^9
Ni-48.9 at.% Al	35.0	26,927.6	9.1×10^9
NiAl-100CO	44.07	33,985.8	6.1×10^{11}
CPNiAl-2	44.75	30,129.9	7.9×10^9

where $\sigma_{s_{max}}$ and $\sigma_{c_{max}}$ are the isothermal maximum obtainable magnitudes of the Snoek and Cottrell contributions to the flow stress, respectively; τ_s and τ_c are the relaxation times for Snoek and Cottrell aging, respectively; and B is defined by:

$$B = \frac{R}{H^o} \times \ln\left(\frac{\dot{\varepsilon}}{\dot{\varepsilon}_0} \right) \qquad (56)$$

By substituting the activation energies calculated for yield point return and/or the onset of serrated yielding, it is possible to estimate the component of the flow stress attributed to DSA. Assuming, as described in Chapter 5, that interstitials occupy octahedral atom positions in the B2 lattice and that diffusion occurs by jumps between the appropriate adjacent octahedral positions, then the diffusion coefficient, calculated above, may be related to the relaxation time, τ_σ, by the equation [206]:

$$D = \frac{a_o^2}{24 \cdot \tau} = \frac{a_o^2}{36 \cdot \tau_\sigma} \qquad (57)$$

where a_o is the lattice parameter and τ is the mean time of stay of a solute atom at an interstitial site. This equation was derived for BCC metals. In B2 alloys, Koiwa [207-210] has shown that the actual relationship between τ and τ_σ is more complex because two

types of octahedral interstices exist. For the qualitative approximations presented here, the use of equation (57) is justified. Substitution of the diffusion equation derived in Chapter 5 into equation (57) yields the following expression for the relaxation time:

$$\tau_\sigma = (3.9 \times 10^{-9}) \exp\left(\frac{Q}{RT}\right) \tag{58}$$

This theoretical relaxation time corresponds to the one that would be observed in a torsion pendulum experiment. A prior investigation [211] showed that τ_s in BCC metals is normally equal to $0.25\tau_\sigma$, whereas, τ_c has been found to be approximately 5,000 times larger than τ_s [212]. Assuming that a single species is causing strain aging and that the activation energies for strain aging correspond to the average of those derived in this study and those reported previously by Brzeski and Hack [29,164], only t_w, $\sigma_{s_{max}}$ and $\sigma_{c_{max}}$ remain unknown. In this case t_w was selected so as to make the start of the analytical plot of the DSA stress with the temperature at which the experimental evidence for DSA begins. This yielded a waiting time of 1 s. In strain aging under stress experiments performed in niobium, Delobelle et al. [212] indicated that the oxygen Cottrell amplitude was approximately 4.3 times larger than the oxygen Snoek amplitude. Assuming the same ratio holds for the species causing strain aging in NiAl, the curves appearing in Figures 66-69 were obtained by insertion of the parameters listed in Table 12 and on the respective figures into the equations described above. The theoretical curves in Figures 66-69 are based upon original estimates of material parameters. No attempts have been made to improve the fit of the derived curves by adjustment of the original estimates of T_{max} and s_{max}. Considering the limited number of strain rate sensitivity measurements near the strain rate sensitivity peak in this study and in the work of Pascoe and Newey [12,166]; the lack of diffusion data for interstitial and substitutional solutes in NiAl; the approximated relaxation times; and the assumption that NiAl behaves like a BCC metal, there is a reasonable agreement between the analytical flow stress curves and the experimental data. However, the fit for

the SRS is poor at best. Further refinement of the DSA parameters, in particular the relaxation time, will be required to achieve a better fit.
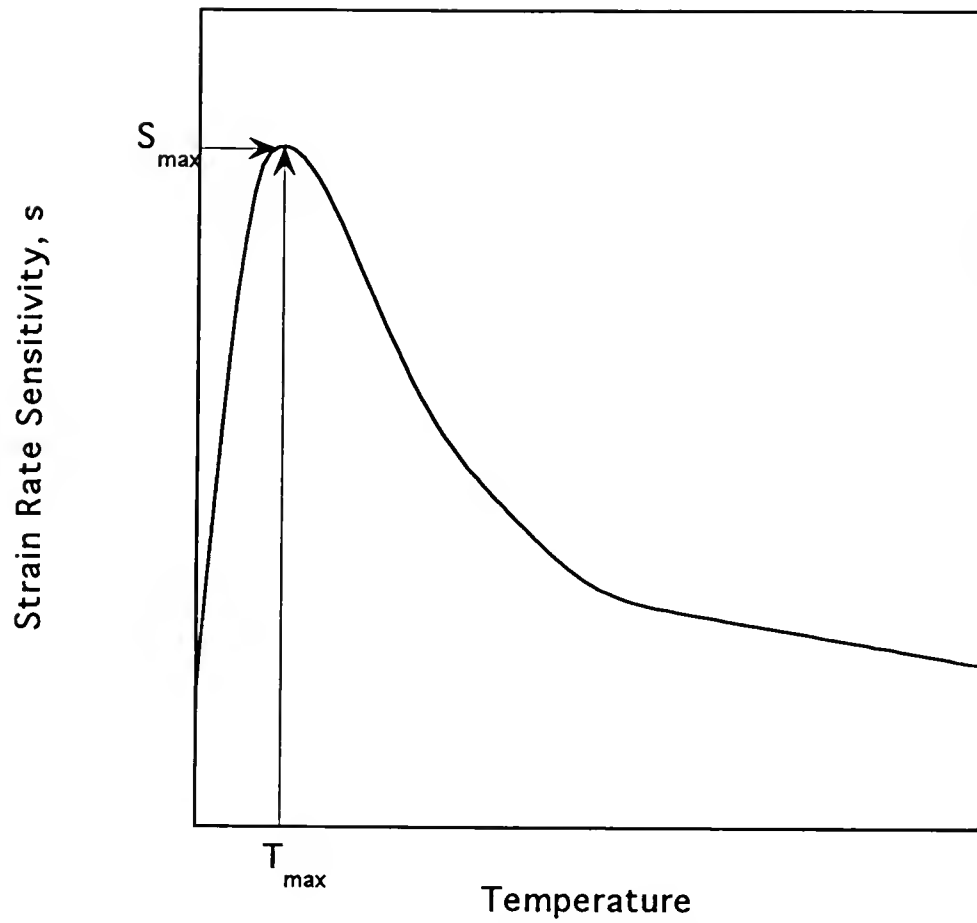
Figure 65.   Schematic representation of the strain rate sensitivity, s (= dσ/dln ε̇) versus T curve.
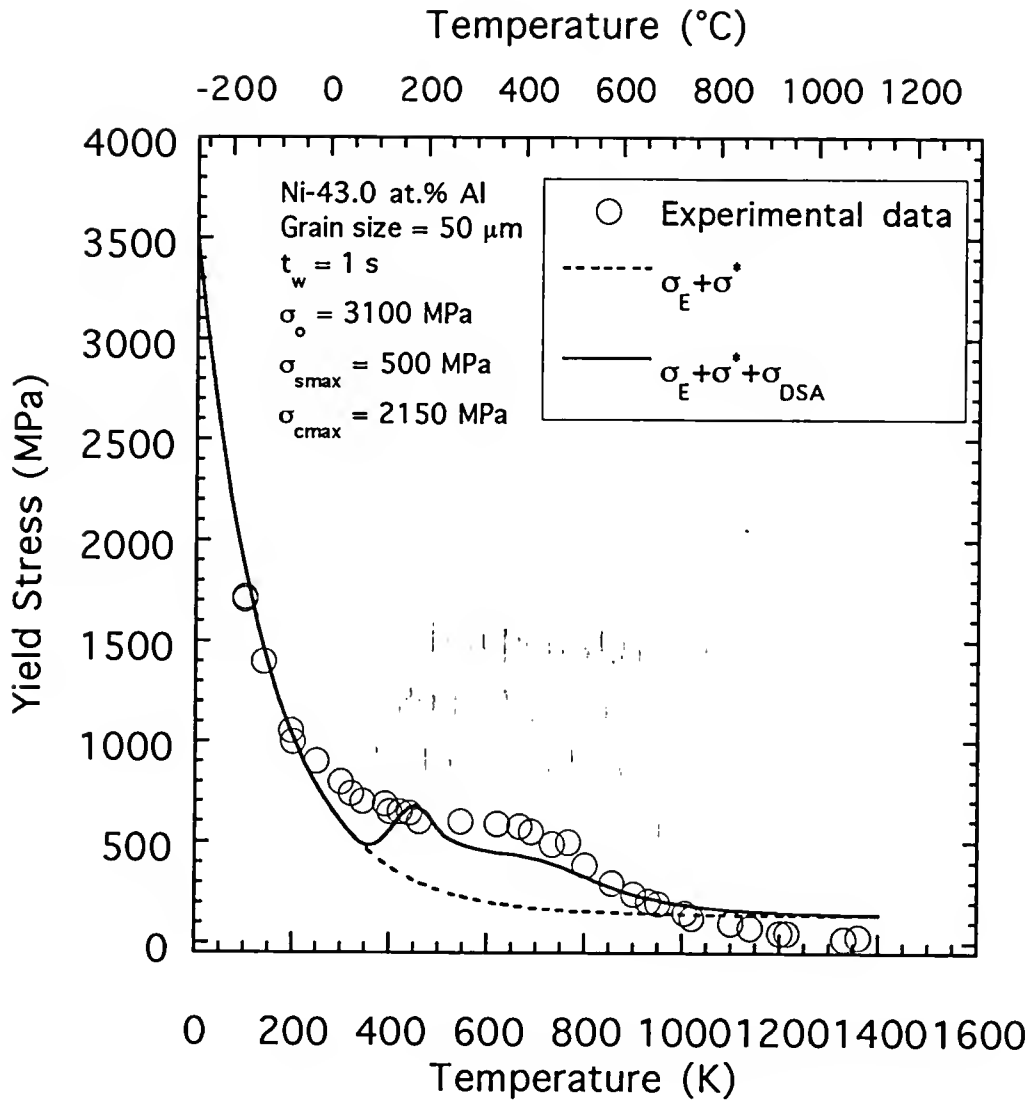
Figure 66. The analytical 0.2% yield stress versus temperature curve for Ni-43Al deduced from the data of Pascoe and Newey [12,166]. Base strain rate = 2.2 × 10⁻⁴ s⁻¹. Their experimental data are also shown.
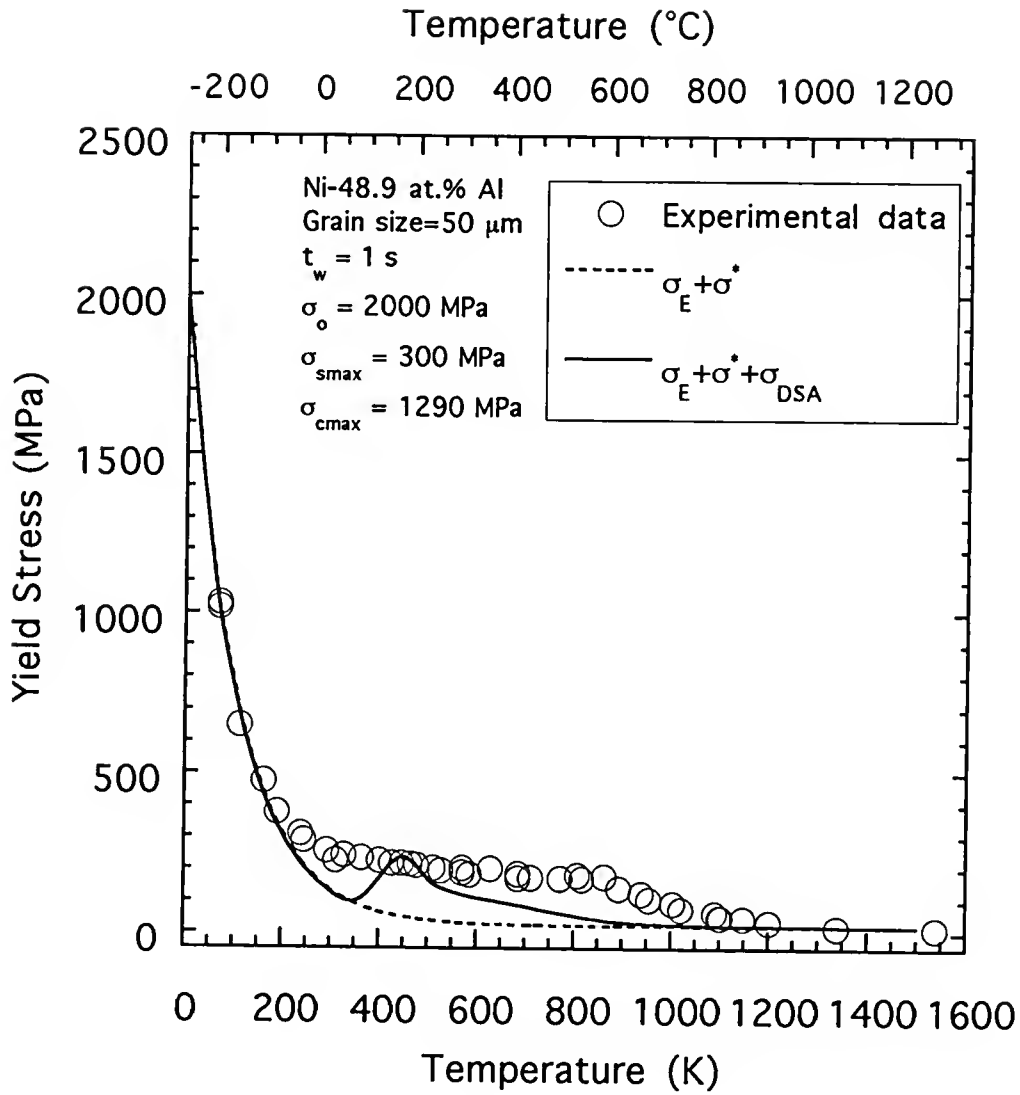
Figure 67. The analytical 0.2% yield stress versus temperature curve for Ni-48.9Al deduced from the data of Pascoe and Newey [12,166]. Base strain rate = 2.2×10^{-4} s^{-1}. Their experimental data are also shown.

Figure 68. The analytical 0.2% yield stress versus temperature curve for NiAl-100CO deduced from the data of presented in Chapters 4-7. Base strain rate = 1.4×10^{-4} s^{-1}.

Figure 69.   The analytical 0.2% yield stress versus temperature curve for CPNiAl-2 deduced from the data of presented in Chapters 4-7. Base strain rate = 2.8×10^{-5} s^{-1}.

CHAPTER 9
CONCLUSIONS

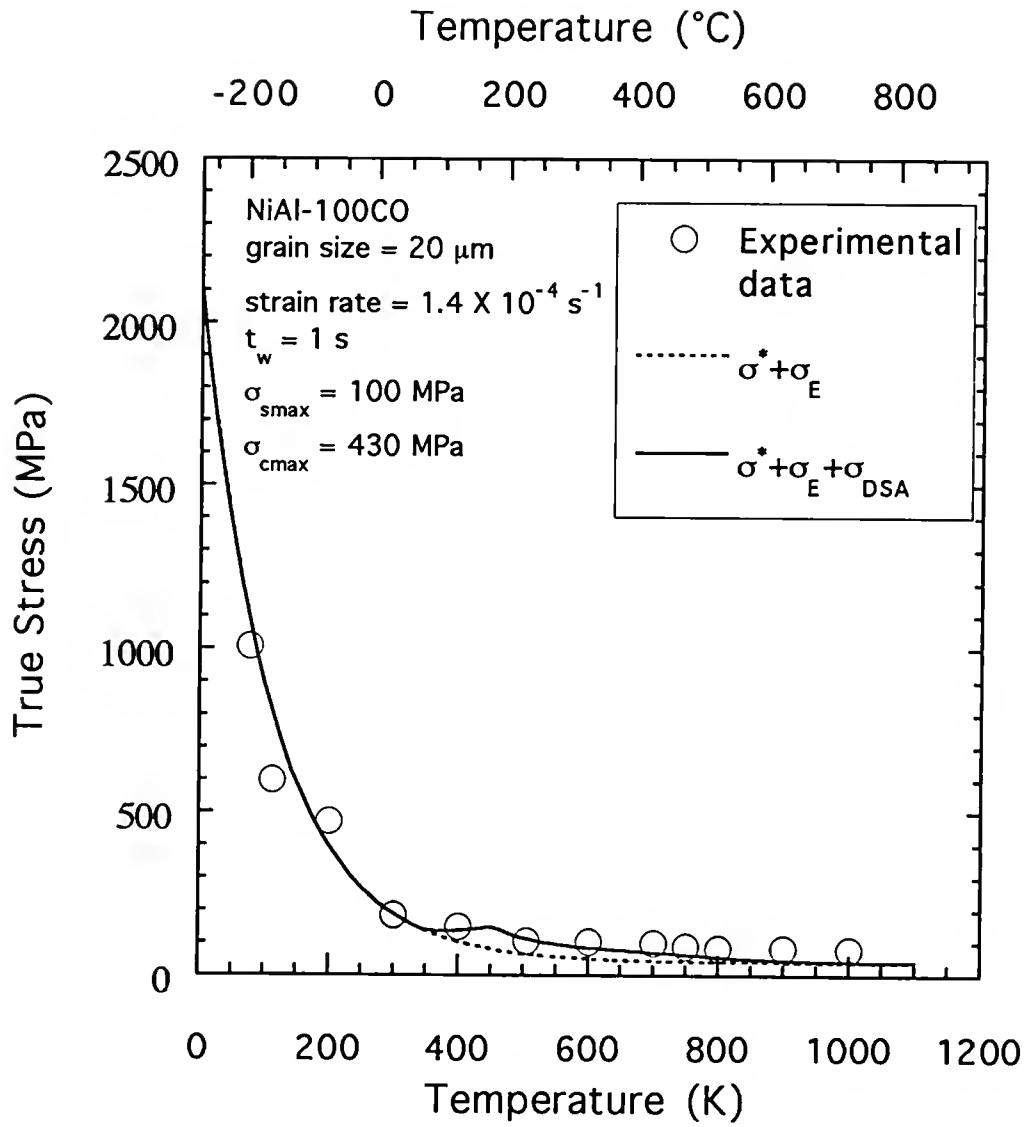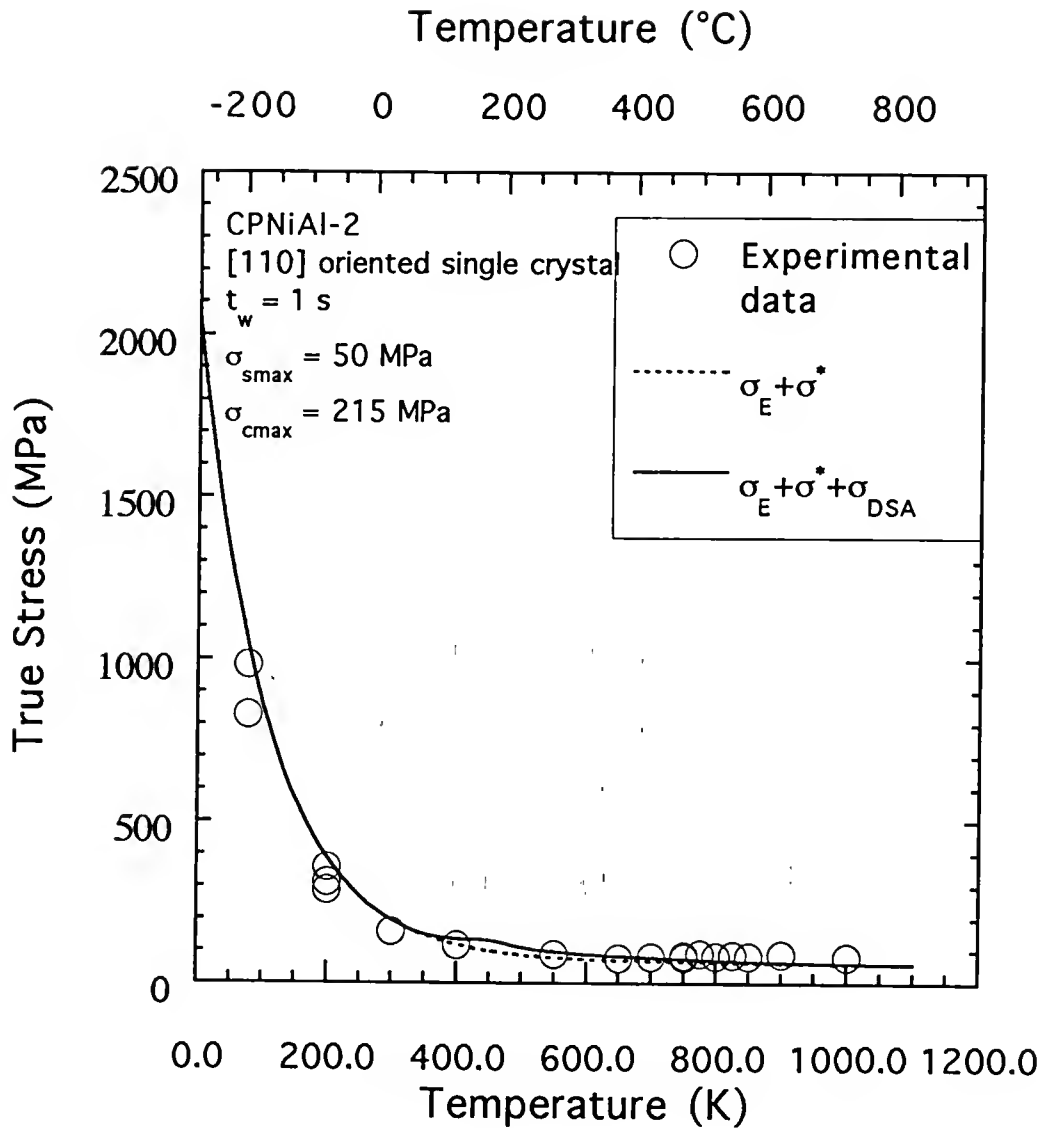The phenomenon of strain aging and its effects on the mechanical properties of NiAl-base alloys has been characterized using both single crystals and polycrystalline material covering a wide range of compositions and purity levels. The results indicate that:

Strain aging does occur at intermediate temperature regimes in NiAl, typically resulting in increased yield strengths, discontinuous yielding and anomalous work hardening. In conventional purity single crystals and in conventional purity polycrystals doped with sufficient quantities of silicon, this phenomenon results in negative strain rate sensitivities and the Portevin-Le Chatelier effect whereas in higher purity or doped single crystals, strain rate sensitivity exhibited a minimum but stayed positive. Coincident with this SRS decrease were yield stress transients upon an increase in strain rate in all alloys. In the higher purity alloys, however, these flow stress transients quickly vanished after small amounts of strain indicating that a reduction in the concentration of C in the alloy can result in a decrease in the propensity for DSA.

TEM observations of single crystals deformed in the DSA regime revealed evidence of localized slip in conventional purity materials in this temperature range but similarly tested high purity material exhibited extensive cross slip. Activation energies for SSA in polycrystals and DSA in single crystals have been calculated and are within the range for the diffusion of interstitial solutes in BCC metals.

Comparative analysis of alloys with equivalent carbon concentrations but different concentrations of other interstitial and/or substitutional dopants indicates that carbon is the species responsible for strain aging in NiAl and that the addition of silicon enhances the strain aging effect.

182

Based on the experimental observations collected in this study, it is proposed that the anomalous temperature dependence of yield stress and work hardening rate, and the minima in strain rate sensitivity are associated with Snoek strain aging and the formation of Cottrell atmospheres around mobile dislocations.

The generated data can be modeled reasonable well with the phenomenological DSA model developed by Reed-Hill *et al.* [1-3,115,116].

LIST OF REFERENCES

1. R.E. Reed-Hill and T. Zhu, *High Temp. Mater. Proc.* **6**, 93 (1984).

2. R.E. Reed-Hill, C.V. Iswaran and M.J. Kaufman, *Scripta Metall. Mater.* , in press (1995).

3. R.E. Reed-Hill and M.J. Kaufman, *Acta Metall. Mater.* **43**, 1731 (1995).

4. R. Darolia, *JOM* **43(3)**, 44 (1991).

5. R.D. Noebe, C.L. Cullers and R.R. Bowman, *J. Mater. Res.* **7**, 605 (1992).

6. D.F. Lahrman, R.D. Field and R. Darolia, in High-Temperature Ordered Intermetallic Alloys IV, L.A. Johnson, D.P. Pope and J.O. Stiegler, Eds., Materials Research Society, Pittsburgh, PA, p. 603 (1991).

7. R.D. Noebe, R.R. Bowman and M.V. Nathal, in Physical Metallurgy and Processing of Intermetallic Compounds, N.S. Stoloff and V.K. Sikka, Eds., Van Nostrand Reinhold, New York, NY (1994).

8. G.W. Groves and A. Kelly, *Phil. Mag.* **81**, 877 (1963).

9. K.H. Hahn and K. Vedula, *Scripta Metall.* **23**, 7 (1989).

10. I. Baker and P.R. Munroe, *JOM* **40(2)**, 28 (1988).

11. E.M. Grala, Investigation of the NiAl Phase of Nickel-Aluminum Alloys, National Advisory Committee for Aeronautics, Cleveland, OH, January (1957).

12. R.T. Pascoe and C.W.A. Newey, *Metal. Sci. J.* **2**, 138 (1968).

13. K. Vedula, K.H. Hahn and B. Boulogne, in High-Temperature Ordered Intermetallic Alloys III, C.T. Liu, A.I. Taub, N.S. Stoloff and C.C. Koch, Eds., Materials Research Society, Pittsburgh, PA, p. 299 (1989).

14. J.E. Hack, J.M. Brzeski and R. Darolia, *Scripta Metall. Mater.* **27**, 1259 (1992).

15. J.E. Hack, J.M. Brzeski, R. Darolia and R.D. Field, in High-Temperature Ordered Intermetallics V, I. Baker, R. Darolia, J.D. Whittenberger and M.H. Yoo, Eds., Materials Research Society, Pittsburgh, PA, p. 1197 (1993).

16. R. Darolia, D. Lahrman and R. Field, *Scripta Metall. Mater.* **26**, 1007 (1992).

17. J.W. Christian, *Metall. Trans. A* **14A**, 1237 (1983).

18. R.D. Noebe, R.R. Bowman and M.V. Nathal, *Int. Mater. Rev.* **38**, 193 (1993).

184

19. D.R. Johnson, S.M. Joslin, B.F. Oliver, R.D. Noebe and J.D. Whittenberger, in First International Conference on Processing Materials for Properties, H. Henein and T. Oki, Eds., TMS, Warrendale, PA, p. 865 (1993).

20. H.K. DeMarco and A.J. Ardell, in High-Tempature Ordered Intermetallic Alloys V, I. Baker, R. Darolia, J.D. Whittenberger and M.H. Yoo, Eds., Materials Research Society, Pittsburgh, PA, p. 641 (1993).

21. G.T. Hahn, *Acta Metall.* **10**, 727 (1962).

22. E.P. Lautenschlager, D.A. Kiewit and J.O. Brittain, *Trans. AIME* **233**, 1297 (1965).

23. R.W. Margevicius and J.J. Lewandowski, *Scripta Metall. Mater.* **25**, 2017 (1991).

24. S. Dymek, M. Dollar, S.J. Hwang and P. Nash, in High-Temperature Ordered Intermetallic Alloys V, I. Baker, R. Darolia, J.D. Whittenberger and M.H. Yoo, Eds., Materials Research Society, Pittsburgh, PA, p. 1117 (1992).

25. M. Dollar, S. Dymek, S.J. Hwang and P. Nash, *Metall. Trans. A* **24A**, 1993 (1993).

26. R.D. Field, D.F. Lahrman and R. Darolia, in High-Temperature Ordered Intermetallic Alloys V, I. Baker, R. Darolia, J.D. Whittenberger and M.H. Yoo, Eds., Materials Research Society, Pittsburgh, PA, p. 423 (1993).

27. M.L. Weaver, V. Levit, M.J. Kaufman and R.D. Noebe, in High-Temperature Ordered Intermetallic Alloys VI, J.A. Horton, I. Baker, S. Hanada, R.D. Noebe and D.S. Schwartz, Eds., Materials Research Society, Pittsburgh, PA, p. 425 (1995).

28. J.M. Brzeski, J.E. Hack, R. Darolia and R.D. Field, *Mater. Sci. Eng.* **A170**, 11 (1993).

29. J.M. Brzeski, J.E. Hack and R. Darolia, in High-Temperature Ordered Intermetallic Alloys VI, J.A. Horton, I. Baker, S. Hanada, R.D. Noebe and D.S. Schwartz, Eds., Materials Research Society, Pittsburgh, PA, p. 419 (1995).

30. P.R. Strutt, R.S. Polvani and B.H. Kear, *Scripta Metall.* **7**, 949 (1973).

31. R.W. Margevicius, J.J. Lewandowski and I. Locci, *Scripta Metall. Mater.* **26**, 1733 (1992).

32. G.W. Ardley and A.H. Cottrell, *Proc. R. Soc. (London)* **A219**, 328 (1953).

33. D.L. Wood and J.H. Westbrook, *Trans. AIME* **224**, 1024 (1962).

34. J.H. Westbrook and D.L. Wood, *J. Inst. Metals* **91**, 174 (1962-63).

35. A.S. Keh, Y. Nakada and W.C. Leslie, in Dislocation Dynamics, A.R. Rosenfield, G.T. Hahn, A.L. Bement and R.I. Jaffee, Eds., McGraw-Hill Book Company, p. 381 (1968).

36. S.C. Park, L.P. Beckerman and R.E. Reed-Hill, *Metall. Trans. A* **14A**, 463 (1983).

37. R.E. Reed-Hill, S.C. Park and L.P. Beckerman, *Acta Metall.* **31**, 1715 (1983).

38. S. Hartley, *Acta Metall.* **14**, 1237 (1966).

39. J.W. Edington, T.C. Lindley and R.E. Smallman, *Acta Metall.* **12**, 1025 (1964).

40. J.W. Edington and R.E. Smallman, *Acta Metall.* **12**, 1313 (1964).

41. S.A. Bradford and O.N. Carlson, *Trans. AIME* **224**, 738 (1962).

42. H.E. Rosinger, *Metal. Sci. J.* **9**, 1 (1975).

43. A.H. Cottrell and B.A. Bilby, *Proc. Phys. Soc. (London)* **A62**, 49 (1949).

44. D.B. Miracle, *Acta Metall. Mater.* **41**, 649 (1993).

45. M.F. Singleton, J.L. Murray and P. Nash, in Binary Alloy Phase Diagrams, T.B. Massalski, Eds., American Society for Metals, Metals Park, OH, p. 140 (1986).

46. W.S. Walston and R. Darolia, in High-Temperature Ordered Intermetallic Alloys V, I. Baker, R. Darolia, J.D. Whittenberger and M.H. Yoo, Eds., Materials Research Society, Pittsburgh, PA, p. 237 (1993).

47. E.-T. Henig and H.L. Lukas, *Z. Metalkde.* **66**, 98 (1975).

48. A.J. Bradley and A. Taylor, *Proc. R. Soc. (London)* **A159**, 66 (1937).

49. A. Taylor and N.J. Doyle, *J. Appl. Cryst.* **5**, 201 (1972).

50. K. Vedula and P.S. Khadkikar, in High Temperature Aluminides and Intermetallics, S.H. Whang, C.T. Liu, D.P. Pope and J.O. Stiegler, Eds., The Minerals, Metals and Materials Society, Warrendale, PA, p. 197 (1990).

51. A. Ball and R.E. Smallman, *Acta Metall.* **14**, 1349 (1966).

52. J.D. Whittenberger, R.D. Noebe, C.L. Cullers and K.S. Kumar, *Metall. Trans. A* **22A**, 1595 (1991).

53. R.R. Bowman, R.D. Noebe, S.V. Raj and I.E. Locci, *Metall. Trans. A* **23A**, 1493 (1992).

54. P. Nagpal and I. Baker, *Metall. Trans. A* **23A**, 2281 (1990).

55. M.L. Weaver, M.J. Kaufman and R.D. Noebe, *Scripta Metall. Mater.* **29**, 1113 (1993).

56. N. Rusovic and H. Warlimont, *Phys. Stat. Sol. (a)* **44**, 609 (1977).

57. R.J. Wasilewski, *Trans. AIME* **36**, 455 (1966).

58. N. Rusovic and H. Warlimont, *Phys. Stat. Sol. (a)* **53**, 283 (1979).

59. C.A. Moose,Interfacial Shear Studies of Sapphire Fiber-Reinforced Nickel Aluminide Matrix Composites, M.S. Thesis, Pennsylvania State University (1991).

60. M.R. Harmouche and A. Wolfenden, *JTEVA* **15**, 101 (1987).

61. P.S. Khadkikar, G.M. Michal and K. Vedula, *Metall. Trans. A* **21A**, 279 (1990).

62. T.R. Bieler, R.D. Noebe, J.D. Whittenberger and M.J. Luton, in Intermetallic Matrix Composites II, D.B. Miracle, D.L. Anton and J.A. Graves, Eds., Materials Research Society, Pittsburgh, PA, p. 165 (1992).

63. A. Ball and R.E. Smallman, *Acta Metall.* **14**, 1517 (1966).

64. R.J. Wasilewski, S.R. Butler and J.E. Hanlon, *Trans. AIME* **239**, 1357 (1967).

65. R.D. Field, D.F. Lahrman and R. Darolia, in High-Temperature Ordered Intermetallic Alloys IV, L.A. Johnson, D.P. Pope and J.O. Stiegler, Eds., Materials Research Society, Pittsburgh, PA, p. 255 (1991).

66. M.H. Loretto and R.J. Wasilewski, *Phil. Mag.* **23**, 1311 (1971).

67. M.J. Mills and D.B. Miracle, *Acta Metall. Mater.* **41**, 85 (1993).

68. D.F. Lahrman, R.D. Field and R. Darolia, in High-Temperature Ordered Intermetallic Alloys V, I. Baker, R. Darolia, J.D. Whittenberger and M.H. Yoo, Eds., Materials Research Society, Pittsburgh, PA, p. 679 (1993).

69. K.R. Forbes, U. Glatzel, R. Darolia and W.D. Nix, in High-Temperature Ordered Intermetallic Alloys V, I. Baker, R. Darolia, J.D. Whittenberger and M.H. Yoo, Eds., Materials Research Society, Pittsburgh, PA, p. 45 (1993).

70. J.D. Cotton, R.D. Noebe and M.J. Kaufman, *Intermetallics* **1**, 3 (1993).

71. P. Nagpal and I. Baker, *J. Mater. Lett.* **11**, 1209 (1992).

72. M. Dollar, S. Dymek, S.J. Hwang and P. Nash, *Scripta Metall. Mater.* **26**, 29 (1992).

73. C.H. Loyd and M.H. Loretto, *Phys. Stat. Sol.* **39**, 163 (1970).

74. I. Baker and E.M. Schulson, *Metall. Trans. A* **15A**, 1129 (1984).

75. W. Wunderlich, L. Machon and G. Sauthoff, *Z. Metalkde.* **83**, 679 (1992).

76. D.B. Miracle, *Acta Metall. Mater.* **39**, 1457 (1991).

77. J.T. Kim and R. Gibala, in High-Temperature Ordered Intermetallic Alloys IV, L.A. Johnson, D.P. Pope and J.O. Stiegler, Eds., Materials Research Society, Pittsburgh, PA, p. 261 (1991).

78. T. Takasugi, S. Watanabe and S. Hanada, *Mater. Sci. Eng.* **A149**, 183 (1992).

79. R.R. Bowman, R.D. Noebe and R. Darolia, Mechanical Properties and Deformation Mechanisms of NiAl. HITEMP Review-1989: Advanced High Temperature Engine Materials Technology Program, NASA, (1989).

80. T. Takasugi, J. Kishino and S. Hanada, *Acta Metall. Mater.* **41**, 1009 (1993).

81. H. Hu, V.I. Levit and M.J. Kaufman, in High-Temperature Ordered Intermetallic Alloys VI, J.A. Horton, I. Baker, S. Hanada, R.D. Noebe and D.S. Schwartz, Eds., Materials Research Society, Pittsburgh, PA, p. 297 (1995).

82. K. Matsugi, D.W. Wenman and N.S. Stoloff, *Scripta Metall. Mater.* **27**, 1633 (1992).

83. R.D. Noebe and M.K. Behbehani, *Scripta Metall. Mater.* **27**, 1795 (1992).

84. K.-M. Chang, R. Darolia and H.A. Lipsitt, *Acta Metall. Mater.* **40**, 2727 (1992).

85. H. Vehoff, in High-Temperature Ordered Intermetallic Alloys V, I. Baker, R. Darolia, J.D. Whittenberger and M.H. Yoo, Eds., Materials Research Society, Pittsburgh, PA, p. 71 (1993).

86. J.D. Rigney and J.J. Lewandowski, *Mater. Sci. Eng.* **A149**, 143 (1992).

87. K.S. Kumar, S.K. Mannan and R.K. Viswanadham, *Acta Metall. Mater.* **40**, 1201 (1992).

88. H.W. Doty, Reactive Processing to Form In-Situ Nickel Aluminide Microcomposites, Ph.D Dissertation, University of Florida (1994).

89. S. Reuss and H. Vehoff, *Scripta Metall. Mater.* **24**, 1021 (1990).

90. H.K. DeMarco, A.J. Ardell and R.D. Noebe, *Mater. Sci. Eng.* **A192/193**, 333 (1995).

91. C.T. Liu, J.A. Horton, E.H. Lee and E.P. George, Alloying Effects on Mechanical and Metallurgical Properties of NiAl, Oak Ridge National Laboratory, June 1993.

92. R.D. Noebe and A. Garg, *Scripta Metall. Mater.* **30**, 815 (1994).

93. W.C. Leslie, Eds., Quench and Strain Aging , vol. 5, MIT Press, Cambridge, MA, 1986.

94. J.D. Baird, *Metall. Rev.* **16**, 1 (1971).

95. J. Snoek, *Physica* **8**, 711 (1941).

96. J. Snoek, *Physica* **6**, 591 (1939).

97. G. Schoeck and A. Seeger, *Acta Metall.* **7**, 469 (1959).

98. Y. Nakada and A.S. Keh, *Acta Metall.* **15**, 879 (1967).

99. L.P. Kubin, Y. Estrin and C. Perrier, *Acta Metall. Mater.* **40**, 1037 (1992).

100. E.O. Hall, Yield Point Phenomena in Metals and Alloys, Plenum Press, New York, (1970).

101. H.E. Rosinger, G.B. Craig and W.J. Bratina, *Mater. Sci. Eng.* **5**, 163 (1969/70).

102. Z.C. Szkopiak, *Acta Metall.* **16**, 381 (1968).

103. J.D. Lubahn, *Trans. ASM* **44**, 643 (1952).

104. P. Rodriquez, *Bull. Mat. Sci.* **6**, 653 (1984).

105. W.G. Johnston, *J. Appl. Phys.* **33**, 2716 (1962).

106. W.G. Johnston and J.J. Gilman, *J. Appl. Phys.* **30**, 129 (1959).

107. J.J. Gilman and W.G. Johnston, *J. Appl. Phys.* **31**, 687 (1960).

108. D.F. Stein and J.R. Low, *J. Appl. Phys.* **31**, 362 (1960).

109. R.E. Reed-Hill, *Rev. High Temp. Mat.* **2**, 217 (1974).

110. P.G. McCormick, *Acta Metall.* **19**, 463 (1971).

111. P.G. McCormick, *Acta Metall.* **20**, 351 (1972).

112. A. van den Beukel, *Phys. Stat. Sol. (a)* **30**, 197 (1975).

113. U.F. Kocks, *Prog. Mater. Sci.* **19**, 185 (1981).

114. U.F. Kocks, *Metall. Trans. A* **16A**, 2109 (1985).

115. C.V. Iswaran, R.E. Reed-Hill, V.I. Levit and M.J. Kaufman, *Scripta Metall. Mater.* **32**, 941 (1995).

116. C.V. Iswaran, R.E. Reed-Hill and M.J. Kaufman, submitted to *Acta Metall.Mater.* (1995).

117. A.H. Cottrell and M.A. Jawson, *Proc. R. Soc. A* **199**, 104 (1949).

118. A.H. Cottrell, Dislocations and Plastic Flow in Crystals, Oxford University Press, (1953).

119. A.H. Cottrell, in Vacancies and Other Point Defects in Metals and Alloys, Institute of Metals, London, p. 1 (1958).

120. A.W. Sleeswyk, *Acta Metall.* **6**, 598 (1958).

121. A. van den Beukel and U.F. Kocks, *Acta Metall.* **30**, 34 (1982).

122. J. Friedel, Dislocations, Pergamon Press, Oxford (1964).

123. H. Conrad and H. Wiedersich, *Acta Metall.* **8**, 128 (1960).

124. K.W. Qian and R.E. Reed-Hill, *Scripta Metall.* **16**, 807 (1982).

125. R.A. Mulford and U.F. Kocks, *Acta Metall.* **27**, 1125 (1979).

126. P. Wycliffe, U.F. Kocks and J.D. Embury, *Scripta Metall.* **14**, 1349 (1980).

127. L.P. Kubin and Y. Estrin, *J. Phys. III* **1**, 929 (1991).

128. Y. Estrin and L.P. Kubin, in <u>Continuum Models for Materials With Micro-Structure</u>, H.-B. Muhlhaus, Ed., John Wiley and Sons, New York (1995).

129. Y. Estrin and P.G. McCormick, *Acta Metall. Mater.* **39**, 2977 (1991).

130. L.P. Kubin and Y. Estrin, *Acta Metall. Mater.* **38**, 697 (1990).

131. P. Penning, *Acta Metall.* **20**, 1169 (1972).

132. P.G. McCormick and Y. Estrin, *Scripta Metall.* **23**, 1231 (1989).

133. D.J. Gaydosh, S.L. Draper, R.D. Noebe and M.V. Nathal, *Mater. Sci. Eng.* **A150**, 7 (1992).

134. D.G. Morris, J.C. Joye and M. Leboeuf, *Phil. Mag. A* **69**, 961 (1994).

135. A.E. Vidoz, D.P. Lazarevic and R.W. Cahn, *Acta Metall.* **11**, 17 (1963).

136. A. Wolfenden, S.V. Raj and S.K.R. Kondlapudi, *J. Mater. Res.* **9**, 1166 (1994).

137. M.L. Weaver, M.J. Kaufman and R.D. Noebe, *Intermetallics* in press, (1995).

138. M.L. Weaver, R.D. Noebe, J.J. Lewandowski, B.F. Oliver and M.J. Kaufman, *Mater. Sci. Eng.* **A192/193**, 179 (1995).

139. M.L. Weaver, The Effect of Molybdenum Additions on the Mechanical Behavior of NiAl, University of Florida, Progress Report, August 1 to September 15 (1993).

140. H. Mabuchi, K. Hirukawa, K. Katayama, H. Tsuda and Y. Nakayama, *Scripta Metall. Mater.* **24**, 1553 (1990).

141. L. Potez, G. Lapasset and L.P. Kubin, *Scripta Metall. Mater.* **26**, 841 (1992).

142. R. Lerf and D.G. Morris, *Acta Metall. Mater.* **39**, 2419 (1991).

143. Z.L. Wu, D.P. Pope and V. Vitek, *Acta Metall. Mater.* **42**, 3577 (1994).

144. K. Hashimoto, S. Kajiwara, T. Kikuchi and M. Nakamura, *Scripta Metall. Mater.* **32**, 417 (1995).

145. A. Bartels, C. Koeppe, L. Schmidt, C. Hartig and H. Mecking, presented at <u>T.S. Meeting</u>, Las Vegas (1995).

146. D.G. Morris, S. Gunther and R. Lerf, in <u>High-Temperature Ordered Intermetallic Alloys V</u>, I. Baker, R. Darolia, J.D. Whittenberger and M.H. Yoo, Eds., Materials Research Society, Pittsburgh, PA, p. 177 (1993).

147. R. Lerf and D.G. Morris, *Acta Metall. Mater.* **42**, 1091 (1994).

148. Z.L. Wu and D.P. Pope, in Structural Intermetallics, R. Darolia, J.J. Lewandowski, C.T. Liu, P.L. Martin, D.B. Miracle and M.V. Nathal, Eds., The Minerals, Metals and Materials Society, Warrendale, PA, p. 107 (1993).

149. D.G. Morris, S. Gunter, R. Lerf and J.C. Joye, in Structural Intermetallics, R. Darolia, J.J. Lewandowski, C.T. Liu, P.L. Martin, D.B. Miracle and M.V. Nathal, Eds., The Minerals, Metals and Materials Society, Warrendale, PA, p. 97 (1993).

150. E.M. Savitskii, G.S. Burdhanov and I.M. Zalivin, *Strength of Materials* **4**, 1406 (1972).

151. E.P. George and C.T. Liu, *J. Mater. Res.* **5**, 754 (1990).

152. E.P. George, C.T. Liu and J.J. Liao, in Alloy Phase Stability and Design, G.M. Stock, G.P. Pope and A.F. Giamei, Eds., Materials Research Society, Pittsburgh, PA, p. 375 (1991).

153. R.D. Reviere, B.F. Oliver and D.D. Bruns, *Mater. Manuf. Proc* **4**, 103 (1989).

154. J.T. Kim, On the Slip Behavior and Surface film Effects in B2 Ordered NiAl Single Crystals, Ph.D. Dissertation, The University of Michigan (1990).

155. T. Takasugi, J. Kishino and S. Hanada, *Acta Metall. Mater.* **41**, 1021 (1993).

156. I.E. Locci, R.D. Noebe, J.A. Moser, D.S. Lee and M.V. Nathal, in High-Temperature Ordered Intermetallic Alloys III, C.T. Liu, A.I. Taub, N.S. Stoloff and C.C. Koch, Eds., Materials Research Society, Pittsburgh, PA, p. 639 (1989).

157. W.J. Yang and R.A. Dodd, *Scripta Metall.* **8**, 237 (1974).

158. W. Yang, R.A. Dodd and P.R. Strutt, *Metall. Trans. A* **3**, 2049 (1972).

159. M.S. Wechsler and K.L. Murty, *Metall. Trans. A* **20A**, 2637 (1989).

160. A. Lawley, J.V.d. Sype and R. Maddin, *J. Inst. Metals* **91**, 23 (1962-63).

161. N. Rusovic and E.-T. Henig, *Phys. Stat. Sol. (a)* **57**, 529 (1980).

162. K.S. Kumar, *Int. Mater. Rev.* **35**, 293 (1990).

163. J.D. Cotton, R.D. Noebe and M.J. Kaufman, in Structural Intermetallics, R. Darolia, J.J. Lewandowski, C.T. Liu, P.L. Martin, D.B. Miracle and M.V. Nathal, Eds., The Minerals, Metals and Materials Society, Warrendale, PA, p. 513 (1993).

164. J.E. Hack, J.M. Brzeski and R. Darolia, *Mater. Sci. Eng.* **A192/193**, 268 (1995).

165. C.T. Liu, E.H. Lee, E.P. George and A.J. Duncan, *Scripta Metall. Mater.* **30**, 387 (1994).

166. R.T. Pascoe and C.W.A. Newey, *Metal. Sci. J.* **5**, 50 (1971).

167. R.W. Margevicius, J.J. Lewandowski, I.E. Locci and R.D. Noebe, *Scripta Metall. Mater.* **29**, 1309 (1993).

168. R.W. Margevicius and J.J. Lewandowski, *Acta Metall. Mater.* **41**, 485 (1993).

169. R.W. Margevicius, J.J. Lewandowski and I.E. Locci, in Structural Intermetallics, R. Darolia, J.J. Lewandowski, C.T. Liu, P.L. Martin, D.B. Miracle and M.V. Nathal, Eds., The Minerals, Metals and Materials Society, Warrendale, PA, p. 577 (1993).

170. R.W. Margevicius and J.J. Lewandowski, *Metall. Mater. Trans. A* **25A**, 1457 (1994).

171. J.T. Kim, R.D. Noebe and R. Gibala, in Proceedings of the International Symposium of Intermetallic Compounds--Structural and Mechanical Properties, O. Izumi, Eds., Japan Institute of Metals, Sendai, Japan, p. 591 (1991).

172. R.R. Bowman and R.D. Noebe, in Superalloys 1992, S.D. Antolovich, R.W. Stusrud, R.A. MacKay, D.L. Anton, T. Khan, R.D. Kissinger and D.L. Klarstrom, Eds., The Minerals, Metals & Materials Society, Warrendale, PA, p. 341 (1992).

173. P. Nagpal, I. Baker and J.A. Horton, *Intermetallics* **2**, 23 (1994).

174. D.V. Wilson and G.R. Ogram, *JISI* **206**, 911 (1968).

175. H. Suzuki, in Dislocations and Mechanical Properties of Crystals, John Wiley and Sons, (1957).

176. J.F. Dinhut, T. Bonou and P. Moine, *Acta Metall.* **24**, 445 (1976).

177. J.F. Dinhut, P. Lepinay and J.C. Desoyer, *Phys. Stat. Sol. (a)* **55**, 621 (1979).

178. R.T. Pascoe and C.W.A. Newey, *Phys. Stat. Sol.* **29**, 357 (1968).

179. K. Kitano and T.M. Pollock, in Structural Intermetallics, R. Darolia, J.J. Lewandowski, C.T. Liu, P.L. Martin, D.B. Miracle and M.V. Nathal, Eds., The Minerals, Metals and Materials Society, Warrendale, PA, p. 591 (1993).

180. K. Kitano, T.M. Pollock and R.D. Noebe, *Scripta Metall. Mater.* **31**, 397 (1994).

181. H. Schultz, *Mater. Sci. Eng.* **3**, 189 (1968/69).

182. I. Baker, *J. Mater. Res.* **8**, 1203 (1993).

183. A.J. Duncan, M.J. Kaufman and M.K. Miller, *Appl. Surf. Sci.* **76/77**, 160 (1994).

184. R. Jayaram and M.K. Miller, *Acta Metall. Mater.* **42**, 1561 (1994).

185. W.C. Leslie, The Physical Metallurgy of Steels, McGraw-Hill, New York, (1981).

186. G.E. Dieter, Mechanical Metallurgy, McGraw-Hill, New York, (1986).

187. S. Venkadesan, C. Phaniraj, P.V. Sivaprasad and P. Rodriguez, *Acta Metall. Mater.* **40**, 569 (1992).

188. E. Pink, *Scripta Metall.* **17**, 847 (1983).

189. R.W. Hayes and W.C. Hayes, *Acta Metall.* **30**, 1295 (1982).

190. M.A. Crimp, S.C. Tonn and Y. Zhang, *Mater. Sci. Eng.* **A170**, 95 (1993).

191. Y. Zhang, S.C. Tonn and M.A. Crimp, in High-Temperature Ordered Intermetallic Alloys V, I. Baker, R. Darolia, J.D. Whittenberger and M.H. Yoo, Eds., Materials Research Society, Pittsburgh, PA, p. 379 (1993).

192. M. Weisse, C.K. Wamukwamba, H.J. Christ and H. Mughrabi, *Acta Metall. Mater.* **41**, 2227 (1993).

193. K.B.S. Rao, M. Valsan, R. Sandhya, S.L. Mannan and P. Rodriguez, *Met. Mater. Proc.* **2**, 17 (1990).

194. C.L. Cullers, S.D. Antolovich and R.D. Noebe, in High-Temperature Ordered Intermetallic Alloys V, I. Baker, R. Darolia, J.d. Whittenberger and M.H. Yoo, Eds., Materials Research Society, Pittsburgh, PA, p. 531 (1993).

195. B.K. Zuidema, D.K. Subramanyam and W.C. Leslie, *Metall. Trans. A* **18A**, 1629 (1987).

196. T. Shun, C.M. Wan and J.G. Byrne, *Acta Metall. Mater.* **40**, 3407 (1992).

197. J.D. Baird and C.R. MacKenzie, *JISI* **202**, 427 (1964).

198. J.D. Baird and A. Jamieson, *JISI* **204**, 793 (1966).

199. J.D. Baird and A. Jamieson, *JISI* **210**, 841 (1972).

200. R.L. Klueh and R.E. Oakes Jr., *J. Eng. Mater. Tech.* **98**, 361 (1976).

201. R.L. Klueh, *J. Nucl. Mat.* **68**, 294 (1977).

202. T.C. Chou and T.G. Nieh, *Scripta Metall. Mater.* **25**, 2059 (1991).

203. T.C. Chou and T.G. Nieh, in High-Temperature Ordered Intermetallic Alloys IV, L.A. Johnson, D.P. Pope and J.O. Stiegler, Eds., Materials Research Society, Pittsburgh, PA, p. 1045 (1991).

204. J.R. Hellman, D.A. Koss, C.A. Moose, R.R. Petrich and M.N. Kallas, in HITEMP Review-1990, NASA CP-10051, Cleveland, p. 41 (1990).

205. R.W. Guard and J.H. Westbrook, *Trans. AIME* **215**, 807 (1959).

206. R.E. Reed-Hill and R. Abbaschian, Physical Metallurgy Principles, PWS-Kent, Boston, (1992).

207. M. Koiwa, *Phil. Mag.* **24**, 81 (1971).

208. M. Koiwa, *Phil. Mag.* **24**, 799 (1971).

209. M. Koiwa, *Phil. Mag.* **24**, 107 (1971).

210. M. Koiwa, *Phil. Mag.* **24**, 539 (1971).

211. R.E. Reed-Hill, in Proceedings of the International Conference on Dislocation Modeling of Physical Systems, M.F. Ashby, R. Bullough, C.S. Hartley and J.P. Hirth, Eds., Acta Metallurgica Inc., Oxford, p. 163 (1981).

212. P. Delobelle, C. Oytana and D. Varchon, *Mater. Sci. Eng.* **29**, 261 (1977).

BIOGRAPHICAL SKETCH

Mark Lovell Weaver was born on 6 October 1965 in Seattle, Washington, USA. Upon completing high school, he enrolled at the University of Washington, Seattle, Washington, where he received a Bachelor of Science degree in Metallurgical Engineering in December 1988. He then interned at the Goodyear Tire and Rubber Company's Tech Center in Akron, Ohio for five months.

In September 1989 he enrolled at the University of Florida where he received a Master of Science degree in Materials Science and Engineering in May 1992. During the course of his studies, he was awarded a Graduate Student Researchers Fellowship from the National Aeronautics and Space Administration (NASA) and has spent over 20 months in residence at the NASA-Lewis Research Center in Cleveland, Ohio under the direction of Drs. Mike Nathal and Ron Noebe.
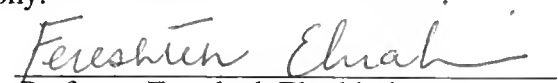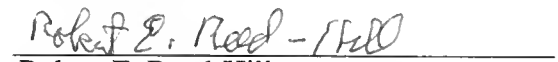
I certify that I have read this study and that in my opinion it conforms to acceptable standards of scholarly presentation and is fully adequate, in scope and quality, as a dissertation for the degree of Doctor of Philosophy.

Michael J. Kaufman, Chairman
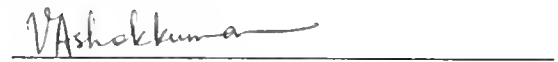Associate Professor of Materials Science
and Engineering

I certify that I have read this study and that in my opinion it conforms to acceptable standards of scholarly presentation and is fully adequate, in scope and quality, as a dissertation for the degree of Doctor of Philosophy.

Professor Reza Abbaschian
Professor of Materials Science and
Engineering

I certify that I have read this study and that in my opinion it conforms to acceptable standards of scholarly presentation and is fully adequate, in scope and quality, as a dissertation for the degree of Doctor of Philosophy.

Professor Fereshteh Ebrahimi
Associate Professor of Materials Science
and Engineering

I certify that I have read this study and that in my opinion it conforms to acceptable standards of scholarly presentation and is fully adequate, in scope and quality, as a dissertation for the degree of Doctor of Philosophy.
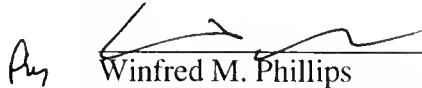
Robert E. Reed-Hill
Emeritus of Materials Science and
Engineering

I certify that I have read this study and that in my opinion it conforms to acceptable standards of scholarly presentation and is fully adequate, in scope and quality, as a dissertation for the degree of Doctor of Philosophy.

Ashok V. Kumar
Assistant Professor of Mechanical
Engineering

This dissertation was submitted to the Graduate Faculty of the College of Engineering and to the Graduate School and was accepted as partial fulfillment of the requirements for the degree of Doctor of Philosophy.

May, 1995

Winfred M. Phillips
Dean, College of Engineering

Karen A. Holbrook
Dean, Graduate School